



CENTRO BRASILEIRO DE PESQUISAS FÍSICAS
DOCTORATE PROGRAM

Lucas Nicholas Falcão Ferreira

**Investigation of CP Violation and S-Wave in $B^\pm \rightarrow K^\mp K^\pm \pi^\pm$ decay via
Amplitude Analysis with LHCb Run II data**

Rio de Janeiro/RJ

2024

"Investigation of CP Violation and S-Wave in $B \rightarrow K K \pi$ decay via Amplitude Analysis with LHCb Run II data"

LUCAS NICHOLAS FALCAO FERREIRA

Tese de Doutorado em Física apresentada no Centro Brasileiro de Pesquisas Físicas do Ministério da Ciência Tecnologia e Inovação. Fazendo parte da banca examinadora os seguintes professores:

Documento assinado digitalmente
 **ANDRE MASSAFFERRI RODRIGUES**
Data: 14/04/2025 16:43:34-0300
Verifique em <https://validar.iti.gov.br>

André Massafferri Rodrigues - Presidente/CBPF

Firmado por DALSENO JEREMY PETER - ****9429* el día 24/03/2025 con un certificado emitido por AC FNMT Usuarios

Jeremy Peter Dalseno – UDC - ESPANHA

Documento assinado digitalmente
 **SANDRA FILIPPA AMATO**
Data: 25/03/2025 11:36:12-0300
Verifique em <https://validar.iti.gov.br>

Sandra Amato - UFRJ

Documento assinado digitalmente
 **ANTONIO VILELA PEREIRA**
Data: 09/04/2025 05:34:41-0300
Verifique em <https://validar.iti.gov.br>

Antonio Vilela Pereira – UERJ

Documento assinado digitalmente
 **JUAN MARTIN OTALORA GOICOCHEA**
Data: 11/04/2025 18:37:05-0300
Verifique em <https://validar.iti.gov.br>

Juan Martin Otálora Goicochea – UFRJ

Rio de Janeiro, 20 de fevereiro de 2025.

Dedico este trabalho à minha esposa e à minha mãe.

"Lembre-se de quem você é."

Mufasa — O Rei Leão

Agradecimentos

Escrevo este agradecimento como um registro eterno da minha memória, para que eu nunca me esqueça de quem sou e de todo o amparo que recebi ao longo da minha trajetória

Meu trabalho de doutorado foi concluído em quatro anos, mas o caminho que me trouxe até aqui é, na verdade, a construção de uma vida inteira. Por isso, os agradecimentos que faço não se limitam a este breve período, mas abrangem todas as pessoas que, de alguma forma, contribuíram para que eu chegasse a este momento. Ainda assim, sei que nomes importantes ficarão de fora, não por falta de importância, mas pela imensidão de pessoas que marcaram minha história. Entre tantos, lembro com carinho de “tios e tias” do coração — Lu, Graça, Sílvia, Miriam, Walter, Edna, Cláudio, Eliane, entre outros — que representam o apoio inestimável que recebi ao longo da vida. Essa rede de afeto se tornou ainda mais necessária diante da ausência de meu pai biológico. Minha mãe, uma mulher de coragem e determinação, me criou sozinha, contando apenas com a ajuda de muitos amigos. A todos que não têm seus nomes citados diretamente aqui, deixo minhas desculpas e minha profunda gratidão.

Agradeço a Deus por tudo, especialmente por colocar em minha vida três mulheres extraordinárias: minha mãe, Ivany, minha tia Marília e minha esposa, Cloe. Sem elas, nada eu seria.

Sou também abençoado por ter acumulado grandes amizades ao longo da vida. Seria impossível listar todas as pessoas queridas que cruzaram meu caminho, vindas dos mais variados contextos — faculdade, grupos musicais, religião, infância e até mesmo os amigos feitos fora do Brasil. A todos vocês, meu muito obrigado pela parceria, pelo apoio e por fazerem parte da minha caminhada.

Família, para muitos, é definida por laços de sangue, mas a minha é formada pelos laços do coração. Agradeço profundamente ao meu sogro Cláudio, minha sogra Lara, minha cunhada Nicole e meu padrasto Edson. Vocês têm sido um pilar de apoio, manifestado de inúmeras formas ao longo dos anos, e sou imensamente grato por isso.

Ao meu grupo de pesquisa, deixo meu sincero reconhecimento pela paciência com as minhas limitações e pela confiança depositada em meu potencial. Sou especialmente grato ao meu orientador André Massafferri, assim como a Jussara Miranda, Ignacio Bediaga, Melissa Cruz, Patrícia Camargo, Juan Otalora e Fernando Luiz. A todos vocês, meu profundo agradecimento pela orientação, pelas lições e por acreditarem em mim.

Gostaria também de expressar minha gratidão aos meus futuros leitores e deixar

meus votos de esperança. Sejam vocês estudantes de pós-graduação em física ou não, nunca deixem de acreditar em seus sonhos. Quem poderia imaginar que um menino criado por uma mãe solo, de pouca instrução, que entregava alho para ajudar no sustento de casa, um dia se tornaria doutor? Que este testemunho sirva para lembrar que, com determinação, apoio daqueles que caminham ao nosso lado e paixão pelo conhecimento, nenhum obstáculo é intransponível

Resumo

Esta tese descreve a análise de amplitude para o canal de decaimento $B^\pm \rightarrow K^\mp K^\pm \pi^\pm$ utilizando dados coletados durante 2015, 2016, 2017 e 2018 em colisões pp a uma energia de centro de massa de $\sqrt{s} = 13$ TeV, correspondendo a uma luminosidade integrada de $5,9 \text{ fb}^{-1}$. A seleção dos eventos é baseada nas características topológicas do decaimento, seguida pela aplicação de um critério baseado em análise multivariada. O conjunto final de dados preparado para análise inclui cerca de 35.000 eventos.

A primeira análise de amplitude do canal $B^\pm \rightarrow K^\mp K^\pm \pi^\pm$, realizada durante o Run I, revelou uma das maiores assimetrias de CP em uma única amplitude já observada, em aproximadamente -66% . O modelo base do Run I incorporou componentes como $K(892)^0$, $K^{*0}(1430)$, $\rho(1450)^0$, $f_2(1270)$, $\phi(1020)$, Rescattering e uma contribuição não ressonante.

Este estudo se concentra em revisitar a análise de amplitude utilizando o modelo Isobárico para $B^\pm \rightarrow K^\mp K^\pm \pi^\pm$ com os dados do Run II, refinando a compreensão das contribuições dominantes da onda S, que correspondem a aproximadamente 60% da amplitude do decaimento. Além disso, ressonâncias de charmonium são exploradas.

Apresentamos dois modelos que diferem no tratamento das contribuições não ressonantes: um inclui δ_{Pol2} e o outro utiliza o componente PolarFFNR. O modelo base incorpora $K^{*0}(892)$, $K^{*0}(1430)$ e PolarFFNR como componentes do sistema KK , juntamente com as ressonâncias $\rho^0(1700)$, $\rho^0(1450)$, $f_2(1270)$, Rescattering, $\phi(1020)$ e χ_{c0} para o sistema $K\pi$. O segundo modelo introduz essencialmente o movimento de fase permitido por δ_{Pol2} , que oferece uma representação mais dinâmica da região de baixa massa de $K\pi$.

Key-words: B sem charme. Decaimento em 3 corpos. Violação de CP.

Abstract

This thesis describes the amplitude analysis for the $B^\pm \rightarrow K^\mp K^\pm \pi^\pm$ decay channel using data collected during 2015, 2016, 2017, and 2018 from pp collisions at a center-of-mass energy $\sqrt{s} = 13$ TeV, corresponding to an integrated luminosity of 5.9 fb^{-1} . The event selection is based on the topological features of the decay, followed by the application of a multivariate analysis-based criterion. The final dataset prepared for analysis includes around 35,000 events.

The first amplitude analysis of the $B^\pm \rightarrow K^\mp K^\pm \pi^\pm$ channel, performed during Run I, revealed one of the largest single-amplitude CP asymmetries observed, at approximately -66% . The baseline model for Run I incorporated components such as $K^*(892)^0$, $K_0^*(1430)^0$, $\rho(1450)^0$, $f_2(1270)$, $\phi(1020)$, Rescattering, and a non-resonant contribution.

This study focuses on revisiting the amplitude analysis using the Isobar model of $B^\pm \rightarrow K^\mp K^\pm \pi^\pm$ using Run II data, refining the understanding of the dominant S-wave contributions, which account for approximately 60% of the decay amplitude. Additionally, charmonium resonances are explored.

We present two models differing in their treatment of non-resonant contributions: one includes the δ_{Pol2} and the other uses PolarFFNR component. The baseline model incorporates $K^{*0}(892)$, $K^{*0}(1430)$, and PolarFFNR as components of the KK system, alongside $\rho^0(1700)$, $\rho^0(1450)$, $f_2(1270)$, Rescattering, $\phi(1020)$, and χ_{c0} resonances for the $K\pi$ system. The second model essentially introduces the phase motion allowed by δ_{Pol2} , which offers a more dynamic representation of the $K\pi$ low-mass region.

Key-words: B charmless. 3-body decay. CP violation.

Contents

	List of Figures	13
	List of Tables	25
1	INTRODUCTION	1
2	THEORY OVERVIEW	5
2.1	The Standard Model	5
2.2	The Cabibbo-Kobayashi-Maskawa Matrix	6
2.3	CP Violation	7
2.3.1	CP violation aspects for $B^\pm \rightarrow h^\pm h^+ h^-$ decays	8
2.3.1.1	The final-state interactions	9
2.3.2	The Direct CP violation measurements in $B^\pm \rightarrow h^\pm h^+ h^-$ decays	10
3	THE LHCb EXPERIMENT	13
3.1	The Large Hadron Collider	13
3.2	The LHCb Detector	15
3.2.1	The tracking system	17
3.2.1.1	The Vertex Locator - VELO	17
3.2.1.2	Tracking Stations	18
3.2.1.3	The Magnet	21
3.2.2	The particle identification system	21
3.2.2.1	Ring-Imaging Cherenkov System (RICH)	22
3.2.2.2	Calorimeter System	24
3.2.2.3	Muon System	25
3.2.3	The trigger system	28
3.2.3.1	The L0 trigger	29
3.2.3.2	The High-Level Trigger	30
3.2.3.3	The LHCb tracks	31
3.3	The LHCb Upgrade I	33
3.3.1	The trigger and software update	35
4	THE SCIFI TRACKER AND THE ROB TEST SYSTEM	37
4.1	A new tracker for the LHCb Experiment	37
4.1.1	Detector Performance	38
4.1.2	Scintillating Fibres	39
4.1.3	Silicon Photomultipliers (SiPM)	39

4.1.4	The Read-out Box (ROB)	40
4.1.5	The front-end electronics	41
4.2	The Read-out Box test system	43
4.2.1	Charge injection device	44
4.2.2	The test bench	44
4.2.3	The RoB test sequence	45
5	MASS FIT AND EVENT SELECTION	49
5.1	Variables definition	49
5.2	Data set	51
5.2.1	Trigger requirements	52
5.2.2	Stripping selection	52
5.2.3	B-mass constraint	53
5.2.4	Offline selection	53
5.2.5	Loose preselection	53
5.2.6	Boosted Decision Trees	53
5.2.7	Final PID selection	56
5.2.8	Mass vetoes	60
5.3	B^\pm mass fit	62
5.3.1	Fit model	63
5.3.1.1	Signal fit model	64
5.3.1.2	Background fit models	65
5.3.2	Fit procedure and results	67
5.3.2.1	Signal region	67
6	THE DALITZ PLOT: TOOLS AND THEORIES	71
6.1	The Dalitz Plot description	71
6.2	$B^\pm \rightarrow K^\mp K^\pm \pi^\pm$ decay amplitude	75
6.2.1	The Isobar model	75
6.2.1.1	Limitations of the Isobar Model	76
6.2.2	Expected resonances	78
6.2.3	Dynamical functions	80
6.2.3.1	Breit-Wigner	80
6.2.3.2	Flatté	81
6.2.3.3	Gounaris-Sakurai	81
6.2.3.4	Non-resonant contribution	82
6.2.3.5	The δ formulation	83
6.2.3.6	The $\pi\pi \rightarrow KK$ Rescattering	84
7	DALITZ PLOT FIT	88

7.1	Acceptance	88
7.2	Selection and PID	89
7.2.1	Trigger correction	90
7.2.2	Total Acceptance Maps	90
7.3	Background Models	91
7.3.1	Total background model	93
7.4	Quantitative metrics for evaluation	94
7.4.1	The probability density function	94
7.4.2	The coefficient c_i	96
7.4.3	Fit Fractions and CP Asymmetry	97
7.4.4	Multiple solutions	98
7.4.5	Wilks' Theorem and the Likelihood Ratio Test	98
8	DALITZ PLOT FIT RESULTS	101
8.1	Preliminary observations	101
8.2	Methodology for evaluating fit quality	104
8.3	Fit Results	106
8.3.1	The baseline model	119
8.4	Summary	144
9	FUTURE SYSTEMATIC UNCERTAINTIES STUDIES	145
10	CONCLUSIONS	146
	References	148
A	APPENDIX: COMPONENTS	155
B	APPENDIX: FITS PER BIN	160
C	APPENDIX: COMPARATIVE ANALYSIS OF RESCATTERING PARAMETER SETS	163
D	APPENDIX: POLARFFNR Δ FITTING	165
E	APPENDIX: CROPPED DALITZ PLOT FIT STUDIES	167
E.1	First approach: generated toys and individual contributions	167
E.2	“Square” cropped region	171
E.3	Upper cropped region	175
E.4	Middle cropped region	179
E.4.1	Studies with a realistic model for the Middle cropped region	180
E.5	Limitations and insights from Cropped Dalitz Plot Analysis	181

F	APPENDIX: IMPACT OF RESCATTERING MODEL VARIATIONS ON NLL	183
G	APPENDIX: TESTING WILK'S THEOREM WITH TOYS	188
G.1	The vector $J/\psi(1S)$ resonance	188
G.1.1	Adding no $J/\psi(1S)$	190
G.2	The tensor $f_2'(1525)$ resonance	190
H	APPENDIX: ALTERNATIVE MODELS	192

List of Figures

Figura 1 – Measured A_{cp} in bins of the $B^\pm \rightarrow K^\mp K^\pm \pi^\pm$ Dalitz plot. The distribution comes from background-subtracted and acceptance-corrected events [1].	2
Figura 2 – Tree (left) and penguin (right) diagrams for the $B^\pm \rightarrow K^\mp K^\pm \pi^\pm$ decay.	2
Figura 3 – Tree (left, where $q_1, q_2 \in \{u, c, s\}$) and QCD penguin (right, where $q_1 = q_2 \in \{u, d, c, s\}$) diagrams [2].	9
Figura 4 – The distribution of asymmetry in the bins of the Dalitz plot is presented for the following decays: (a) $B^\pm \rightarrow \pi^\pm \pi^+ \pi^-$, utilizing 400 bins with an average of 229 events per bin; (b) $B^\pm \rightarrow K^\pm \pi^+ \pi^-$, with 1728 bins and an average of 276 events per bin; (c) $B^\pm \rightarrow \pi^\pm K^+ K^-$, using 256 bins averaging 127 events per bin; and (d) $B^\pm \rightarrow K^\pm K^+ K^-$, consisting of 729 bins with approximately 461 events per bin [3].	12
Figura 5 – The CERN accelerator complex.	14
Figura 6 – 3D sketch of the LHCb detector, including all its subdetectors [4].	16
Figura 7 – Schematic illustration of the VELO r and ϕ strips (left) alongside an image of the VELO sensors.	18
Figura 8 – Schematic illustration of the VELO r and ϕ strips (left) alongside an image of the VELO sensors.	18
Figura 9 – Layout of the TT, with the LHC beam pipe passing through an opening in the center of the detection layers. The four detection layers are labeled TTaX, TTaU, TTbV, and TTbX. Different types of readout sectors are indicated by varying shading: the sectors closest to the beam pipe consist of a single silicon sensor, while other sectors are made up of two, three, or four silicon sensors connected in series [5].	19
Figura 10 – Arrangement of OT straw-tube modules in layers and stations [6].	20
Figura 11 – Perspective view of the LHCb dipole magnet with its current and water connections (units in mm). The interaction point lies behind the magnet [6].	21
Figura 12 – Cherenkov angle versus particle momentum for the RICH radiators [6].	23
Figura 13 – (a) Side view schematic layout of the RICH1 detector. (b) Cut-away 3D model of the RICH1 detector, shown attached by its gas-tight seal to the VELO tank. (c) Photo of the RICH1 gas enclosure containing the flat and spherical mirrors [6].	23
Figura 14 – (a) Top view schematic of the RICH2 detector. (b) A schematic layout of the RICH2 detector. (c) A photograph of RICH2 with the entrance window removed [6].	23

Figura 15 – Lateral segmentation of the SPD/PS and ECAL (left) and the HCAL (right). One-quarter of the detector’s front face is shown. In the left figure, the cell dimensions are given for the ECAL [6].	25
Figura 16 – Side view of the muon system [6].	27
Figura 17 – Station layout with the four regions R1-R4 [6].	27
Figura 18 – 4 muon station regions [6].	27
Figura 19 – Overview of the LHCb trigger system. Out of the LHC bunch crossing rate of 40 MHz, the LHCb subdetector’s maximum read-out rate was about 1 MHz, constrained by the bandwidth and frequency of the front-end electronics. [7].	29
Figura 20 – A schematic illustration of the various track types: long, upstream, downstream, VELO and T tracks. For reference, the main B-field component is plotted above as a function of the z coordinate [6].	32
Figura 21 – Left: Trigger yields normalized to $\mathcal{L} = 2 \times 10^{32} \text{ cm}^{-2} \text{ s}^{-1}$ as a function of instantaneous luminosity. Right: Reconstructed decay rates within the LHCb acceptance as a function of the p_T cut for decaying particles with $\tau > 0.2 \text{ ps}$ [8].	33
Figura 22 – Layout of the upgraded LHCb detector.	34
Figura 23 – The three stations of the scintillating fibre tracker shown between the dipole magnet on the left and RICH2 on the right [9].	38
Figura 24 – 3D model of the SciFi [8].	38
Figura 25 – Side and front views of the end of a scintillating fiber module, displaying the SiPM arrays, cooling pipe, flexible cables, and front-end electronics [8].	41
Figura 26 – Photograph of assembled Master, Clusterization, and PACIFIC boards [8].	42
Figura 27 – Diagram illustrating the functional data flow within the FE electronics [8].	43
Figura 28 – Photo of the injector module.	45
Figura 29 – Current source plot of all channels for all RoBs tested.	46
Figura 30 – HV Fit Slope plot of all channels for all RoBs tested.	47
Figura 31 – Profile of the HV Fit Slope plot of all channels for all RoBs tested.	47
Figura 32 – From left to right, distributions of (a) pedestal, (b) Q_{inj} , and (c) ENL from a ThScan.	48
Figura 33 – Topology of a three-body decay. The acronyms are defined in the text.	49
Figura 34 – Distribution of ANN probabilities for $B^+ \rightarrow K^+(d1)\pi^+(d2)K^-(d3)$	54
Figura 35 – Invariant mass distributions $B^\pm \rightarrow K^\mp K^\pm \pi^\pm$ decays. The histogram in red has the candidates rejected by the minimal PID cut. Sample plots made with MagUp data only.	54

Figura 36 – Invariant mass distributions for the decays retained after the minimal PID cut for $B^\pm \rightarrow K^\mp K^\pm \pi^\pm$ decays. Sample plots made with MagUp data only.	55
Figura 37 – The distributions of outputs variables from BDT. Left curves are background and right ones are signal. Red lines are for the optimization specific to $B^\pm \rightarrow K^\mp K^\pm \pi^\pm$ while blue lines are for the optimization common to all channels.	55
Figura 38 – The background rejection efficiency against signal selection efficiency (ROC curves). Red lines is for the optimization specific for $B^\pm \rightarrow K^\mp K^\pm \pi^\pm$ and blue line is for the optimization common to all channels.	56
Figura 39 – The background rejection efficiency against signal selection efficiency (The significance $S/\sqrt{(S+N)}$ and the signal efficiency for the specific optimizations. The green line indicate the maximum of the significance. The pink line indicate the location of the cut on the BDT output variables we chose.	57
Figura 40 – The invariant mass distribution of $B^\pm \rightarrow K^\mp K^\pm \pi^\pm$ before (black) and after (blue) BDT selection, for the optimization specific to each channel. The shaded region corresponds to the signal region $ (B_m - 5284 \text{ MeV}/c^2) < 40 \text{ MeV}/c^2$	57
Figura 41 – The $K^+K^+K^-$ (left) and $K^+\pi^+\pi^-$ (right) invariant mass distributions from the $B^+ \rightarrow K^+\pi^+K^-$ sample. The plot has the 2015+2016 data and includes both polarities.	58
Figura 42 – The $B^+ \rightarrow \bar{D}^0 K^+(\pi^+)$ signal from the $B^+ \rightarrow K^+\pi^+K^-$ sample. The plot has the 2015+2016 data and includes both polarities.	58
Figura 43 – The $B^+ \rightarrow K^+K^+K^-$ signal from the $B^+ \rightarrow K^+\pi^+K^-$ sample. Histograms in, red, magenta, green and brown correspond to the requirement of $\text{ProbNNk} < 0.4, 0.3, 0.2$ and 0.1 , respectively. The plot has the 2015+2016 data and includes both polarities.	59
Figura 44 – The $B^+ \rightarrow \pi^+K^+\pi^-$ signal from the $B^+ \rightarrow K^+\pi^+K^-$ sample. Histograms in, red, magenta, green and brown correspond to the requirement of $\text{ProbNNpi} < 0.4, 0.3, 0.2$ and 0.1 , respectively. The plot has the 2015+2016 data and includes both polarities.	59
Figura 45 – The $B^+ \rightarrow \bar{D}^0 K^+(\pi^+)$ signal from the $B^+ \rightarrow K^+\pi^+K^-$ sample. Histograms in, red, magenta, green and brown correspond to the requirement of $\text{ProbNNpi} > 0.3, 0.4, 0.5$ and 0.6 , after the negative PID is applied respectively. The plot has the 2015+2016 data and includes both polarities.	60
Figura 46 – The $B^+ \rightarrow K^+\pi^+K^-$ signal sample with final PID requirements. The plots has the 2015+2016 data and includes both polarities.	60

Figura 47 – Comparison between the KK (right) and $K\pi$ (left) projections before and after the application of the new vetoes. The red represents the data before the new vetoes, and the blue represents the data after their application.	61
Figura 48 – The $\bar{D}^0 \rightarrow K^+\pi^-$ signal from the $\pi^+K^+\pi^-$ sample after final PID requirements. On the left panel, the $\bar{D}^0 \rightarrow K^+\pi^-$ signal with no misID (combination of particles 2 and 3). On the right $\bar{D}^0 \rightarrow K^+\pi^-$ signal (combination of particle 1 and 3). The candidate is selected when particle 1, a true kaon, is misidentified as a pion. The plots have the 2016 data and include both polarities.	62
Figura 49 – The $\bar{D}^0 \rightarrow hh$ signal from the $\pi^+K^+\pi^-$ sample after final PID requirements. On the left panel, the $\bar{D}^0 \rightarrow \pi^+\pi^-$ signal with no misID. On the right $\bar{D}^0 \rightarrow K^+K^-$ signal where particle 3 is kaon misidentified as a pion. The plots have the 2016 data and include both polarities. . . .	62
Figura 50 – Invariant mass fits for $B^\pm \rightarrow K^\mp K^\pm \pi^\pm$: (top) MC mass fit result plot using logarithmic scale and pull, (middle) data sample mass fit result plot using logarithmic scale and pull and (bottom) data sample mass fit.	70
Figura 51 – The scheme for three-body decays. Figure extracted from PDG [10]. . .	71
Figura 52 – Kinematic boundaries of the three-body decay phase space, along with a depiction of various kinematic configurations for the final-state particles at representative points on the Dalitz plot. This figure illustrates the phase space for the decay process $B^0 \rightarrow \pi^- \bar{D}^0 K^+$, where $a = \pi^-$, $b = \bar{D}^0$, and $c = K^+$ [11].	72
Figura 53 – Simulated data projections in the nominal Dalitz plot (left) and Square Dalitz plot (right) highlighting how each region of the phase space maps from one representation for $B^\pm \rightarrow K^\mp K^\pm \pi^\pm$	74
Figura 54 – The S -wave phase as a function of the $K\pi$ invariant mass, extracted from the QMI-PWA analysis of the $D^+ \rightarrow K^+\pi^+\pi^-$ Dalitz plot, is presented in [12]. The shaded region represents the results obtained from the Isobar model fit conducted in a prior study [13] The dashed vertical line indicates the elastic range as determined by the LASS experiment [14]	77
Figura 55 – The OZI rule states that if a Feynman diagram can be divided into two disconnected parts by cutting only gluon lines (without slicing through any external lines), the process is highly suppressed [15]	79
Figura 56 – $B \rightarrow \phi(\rightarrow KK)\pi$ diagram considering the ϕ meson is subject to suppression according to the OZI rule [16].	80
Figura 57 – Upper panel: the modulus of $\pi\pi - KK$ scattering. Lower panel: the phase for $\pi\pi - KK$ scattering. Figure extracted from [17].	87

Figura 58 – Overall acceptance map for $B^+ \rightarrow \pi^+ K^+ K^-$	91
Figura 59 – Overall acceptance map for $B^- \rightarrow \pi^- K^- K^+$	91
Figura 60 – Background model for $B^- \rightarrow \pi^- K^- K^+$	93
Figura 61 – Background model for $B^+ \rightarrow \pi^+ K^+ K^-$	93
Figura 62 – (a) $m^2(K^+ \pi^-)$ projection for the rescattering region with the $B^\pm \rightarrow$ $K^\mp K^\pm \pi^\pm$ mass fits for the (b) region 1 (B^- on the left) [1].	103
Figura 63 – Dalitz plot distribution for $B^+ \rightarrow K^- K^+ \pi^+$, the color scale indicates the number of events.	103
Figura 64 – Dalitz plot distribution for $B^- \rightarrow K^+ K^- \pi^-$, the color scale indicates the number of events.	103
Figura 65 – Colored Dalitz Plot with indications of regions of highest interest. . . .	105
Figura 66 – Colored Dalitz Plot with indications of regions of highest interest. . . .	105
Figura 67 – Fit 1 results, for each plot B^- (top), B^+ (middle) and the difference ($B^- - B^+$, bottom). The a) ($\cos Hel23 < 0$), b) ($\cos Hel > 0$), and c) are showing the $m_{K^\pm \pi^\mp}^2$ in a different region. The d) ($\cos Hel13 > 0$), e) ($\cos Hel13 < 0$), and f) are the projections for the $m_{K^+ K^-}^2$. For the g) and h) we have the diagonal projections $m_{K^+ \pi^+}^2$. The line in blue represents the model, the black dots represent the data, and the region in red is the background estimation. All plots were produced using 40 bins.	108
Figura 68 – Fit 1 results, for each plot B^- (top), B^+ (middle) and the difference ($B^- - B^+$, bottom). The a) ($m_{K^\pm \pi^\mp}^2 > 4$, specially for the $\chi_{c0}(1P)$), b) ($m_{K^\pm \pi^\mp}^2 > 4$) are showing the $m_{K^+ K^-}^2$ in different regions. The c) ($m_{K^+ K^-}^2 < 1.4$), d) ($1.4 < m_{K^+ K^-}^2 < 3.5$), and e) ($4 < m_{K^+ K^-}^2 <$ 5) are the projections for the $m_{K^\pm \pi^\mp}^2$. For the f) ($m_{K^+ \pi^+}^2 < 5$), g) ($0.5 < m_{K^\pm \pi^\mp}^2 < 1.2$) and h) ($1.2 < m_{K^\pm \pi^\mp}^2 < 3$) we have the $m_{K^+ K^-}^2$ - projections. The line in blue represents the model, the black dots represent the data, and the region in red is the background estimation. All plots were produced using 40 bins.	109
Figura 69 – Fit 1 results, for each plot B^- (top), B^+ (middle) and the difference ($B^- - B^+$, bottom). The a) and b) show the full projections of $m_{K^\pm \pi^\mp}$ and $m_{K^+ K^-}$ produced using 100 bins, respectively. It is important to note that in these two cases, the mass is not squared. The c) is the $0.9 < m_{K^+ K^-}^2 < 1.2$ to zoom in on the $\phi(1020)$, using 40 bins. The line in blue represents the model, the black dots represent the data, and the region in red is the background estimation.	110
Figura 70 – Magnitude and phase of the $K\pi$ S-wave resulting from Fit 1 using $K_0^*(1430)$ and PolarFFNR.	110

Figura 71 – Magnitude and phase of the KK S-wave resulting from Fit 1 using Rescattering.	111
Figura 72 – Fit 2 results for the $m_{K^+K^-}^2$ projection with the $m_{K^\pm\pi^\mp}^2 > 4$. Signature of $J/\psi(1S)$ and $\chi_{c0}(1P)$ around $9.5 \text{ GeV}^2/c^4$ and $11.6 \text{ GeV}^2/c^4$, respectively.	112
Figura 73 – Fit 4 using UFD_b parameters, for each plot B^- (top), B^+ (middle) and the difference ($B^- - B^+$, bottom). The a) ($\cos\text{Hel}23 < 0$), b) ($\cos\text{Hel} > 0$), and c) are showing the $m_{K^\pm\pi^\mp}^2$ in a different region. The d) ($\cos\text{Hel}13 > 0$), e) ($\cos\text{Hel}13 < 0$), and f) are the projections for the $m_{K^+K^-}^2$. For the g) and h) we have the diagonal projections $m_{K^+\pi^+}^2$. The line in blue represents the model, the black dots represent the data, and the region in red is the background estimation. All plots were produced using 40 bins.	115
Figura 74 – Fit 4 using UFD_b parameters, for each plot B^- (top), B^+ (middle) and the difference ($B^- - B^+$, bottom). The a) ($m_{K^\pm\pi^\mp}^2 > 4$, specially for the $\chi_{c0}(1P)$), b) ($m_{K^\pm\pi^\mp}^2 > 4$) are showing the $m_{K^+K^-}^2$ in different regions. The c) ($m_{K^+K^-}^2 < 1.4$), d) ($1.4 < m_{K^+K^-}^2 < 3.5$), and e) ($4 < m_{K^+K^-}^2 < 5$) are the projections for the $m_{K^\pm\pi^\mp}^2$. For the f) ($m_{K^+\pi^+}^2 < 5$), g) ($0.5 < m_{K^\pm\pi^\mp}^2 < 1.2$) and h) ($1.2 < m_{K^\pm\pi^\mp}^2 < 3$) we have the $m_{K^+K^-}^2$ projections. The line in blue represents the model, the black dots represent the data, and the region in red is the background estimation. All plots were produced using 40 bins.	116
Figura 75 – Fit 4 using UFD_b parameters, for each plot B^- (top), B^+ (middle) and the difference ($B^- - B^+$, bottom). The a) and b) show the full projections of $m_{K^\pm\pi^\mp}$ and $m_{K^+K^-}$ produced using 100 bins, respectively. It is important to note that in these two cases, the mass is not squared. The c) is the $0.9 < m_{K^+K^-}^2 < 1.2$ to zoom in on the $\phi(1020)$, using 40 bins. The line in blue represents the model, the black dots represent the data, and the region in red is the background estimation.	117
Figura 76 – Magnitude and phase of the $K\pi$ S-wave resulting from Fit 6 using $K_0^*(1430)$ and PolarFFNR.	120
Figura 77 – Magnitude and phase of the KK S-wave resulting from Fit 6 using Rescattering and χ_{c0}	120
Figura 78 – Fit 6, for each plot B^- (top), B^+ (middle) and the difference ($B^- - B^+$, bottom). The a) ($\cos\text{Hel}23 < 0$), b) ($\cos\text{Hel} > 0$), and c) are showing the $m_{K^\pm\pi^\mp}^2$ in a different region. The d) ($\cos\text{Hel}13 > 0$), e) ($\cos\text{Hel}13 < 0$), and f) are the projections for the $m_{K^+K^-}^2$. For the g) and h) we have the diagonal projections $m_{K^+\pi^+}^2$. The line in blue represents the model, the black dots represent the data, and the region in red is the background estimation. All plots were produced using 40 bins.	121

Figura 79 – Fit 6, for each plot B^- (top), B^+ (middle) and the difference ($B^- - B^+$, bottom). The a) ($\cos Hel23 < 0$), b) ($\cos Hel > 0$), and c) are showing the $m_{K^\pm\pi^\mp}^2$ in a different region. The d) ($\cos Hel13 > 0$), e) ($\cos Hel13 < 0$), and f) are the projections for the $m_{K^+K^-}^2$. For the g) and h) we have the diagonal projections $m_{K^+\pi^+}^2$. The line in blue represents the model, the black dots represent the data, and the region in red is the background estimation. All plots were produced using 40 bins.	122
Figura 80 – Fit 6, for each plot B^- (top), B^+ (middle) and the difference ($B^- - B^+$, bottom). The a) and b) show the full projections of $m_{K^\pm\pi^\mp}$ and $m_{K^+K^-}$ produced using 100 bins, respectively. It is important to note that in these two cases, the mass is not squared. The c) is the $0.9 < m_{K^+K^-}^2 < 1.2$ to zoom in on the $\phi(1020)$, using 40 bins. The line in blue represents the model, the black dots represent the data, and the region in red is the background estimation.	123
Figura 81 – Magnitude and phase of the $K\pi$ S-wave resulting from Fit 7 using $K_0^*(1430)$ and δ_{Pol2}	126
Figura 82 – Fit 7, for each plot B^- (top), B^+ (middle) and the difference ($B^- - B^+$, bottom). The a) ($\cos Hel23 < 0$), b) ($\cos Hel > 0$), and c) are showing the $m_{K^\pm\pi^\mp}^2$ in a different region. The d) ($\cos Hel13 > 0$), e) ($\cos Hel13 < 0$), and f) are the projections for the $m_{K^+K^-}^2$. For the g) and h) we have the diagonal projections $m_{K^+\pi^+}^2$. The line in blue represents the model, the black dots represent the data, and the region in red is the background estimation. All plots were produced using 40 bins.	127
Figura 83 – Fit 7, for each plot B^- (top), B^+ (middle) and the difference ($B^- - B^+$, bottom). The a) ($\cos Hel23 < 0$), b) ($\cos Hel > 0$), and c) are showing the $m_{K^\pm\pi^\mp}^2$ in a different region. The d) ($\cos Hel13 > 0$), e) ($\cos Hel13 < 0$), and f) are the projections for the $m_{K^+K^-}^2$. For the g) and h) we have the diagonal projections $m_{K^+\pi^+}^2$. The line in blue represents the model, the black dots represent the data, and the region in red is the background estimation. All plots were produced using 40 bins.	128
Figura 84 – Fit 7, for each plot B^- (top), B^+ (middle) and the difference ($B^- - B^+$, bottom). The a) and b) show the full projections of $m_{K^\pm\pi^\mp}$ and $m_{K^+K^-}$ produced using 100 bins, respectively. It is important to note that in these two cases, the mass is not squared. The c) is the $0.9 < m_{K^+K^-}^2 < 1.2$ to zoom in on the $\phi(1020)$, using 40 bins. The line in blue represents the model, the black dots represent the data, and the region in red is the background estimation.	129
Figura 85 – Fit 9 results for the $m_{K^+K^-}^2$ projection with the $m_{K^\pm\pi^\mp}^2 > 4$. Signature of $J/\psi(1S)$ around $9.5 \text{ GeV}^2/c^4$	130

- Figura 86 – Fit 10 replacing the $f_2(1270)$ with $f'_2(1525)$, for each plot B^- (top), B^+ (middle) and the difference ($B^- - B^+$, bottom). The a) ($\cos Hel23 < 0$), b) ($\cos Hel > 0$), and c) are showing the $m_{K^\pm\pi^\mp}^2$ in a different region. The d) ($\cos Hel13 > 0$), e) ($\cos Hel13 < 0$), and f) are the projections for the $m_{K^+K^-}^2$. For the g) and h) we have the diagonal projections $m_{K^+\pi^+}^2$. The line in blue represents the model, the black dots represent the data, and the region in red is the background estimation. All plots were produced using 40 bins. 133
- Figura 87 – Fit 10 replacing the $f_2(1270)$ with $f'_2(1525)$, for each plot B^- (top), B^+ (middle) and the difference ($B^- - B^+$, bottom). The a) ($\cos Hel23 < 0$), b) ($\cos Hel > 0$), and c) are showing the $m_{K^\pm\pi^\mp}^2$ in a different region. The d) ($\cos Hel13 > 0$), e) ($\cos Hel13 < 0$), and f) are the projections for the $m_{K^+K^-}^2$. For the g) and h) we have the diagonal projections $m_{K^+\pi^+}^2$. The line in blue represents the model, the black dots represent the data, and the region in red is the background estimation. All plots were produced using 40 bins. 134
- Figura 88 – Fit 10 replacing the $f_2(1270)$ with $f'_2(1525)$, for each plot B^- (top), B^+ (middle) and the difference ($B^- - B^+$, bottom). The a) and b) show the full projections of $m_{K^\pm\pi^\mp}$ and $m_{K^+K^-}$ produced using 100 bins, respectively. It is important to note that in these two cases, the mass is not squared. The c) is the $0.9 < m_{K^+K^-}^2 < 1.2$ to zoom in on the $\phi(1020)$, using 40 bins. The line in blue represents the model, the black dots represent the data, and the region in red is the background estimation. 135
- Figura 89 – Fit 10 adding the $f_2(1270)$ together with $f'_2(1525)$, for each plot B^- (top), B^+ (middle) and the difference ($B^- - B^+$, bottom). The a) ($\cos Hel23 < 0$), b) ($\cos Hel > 0$), and c) are showing the $m_{K^\pm\pi^\mp}^2$ in a different region. The d) ($\cos Hel13 > 0$), e) ($\cos Hel13 < 0$), and f) are the projections for the $m_{K^+K^-}^2$. For the g) and h) we have the diagonal projections $m_{K^+\pi^+}^2$. The line in blue represents the model, the black dots represent the data, and the region in red is the background estimation. All plots were produced using 40 bins. 136

- Figura 90 – Fit 10 adding the $f_2(1270)$ together with $f'_2(1525)$, for each plot B^- (top), B^+ (middle) and the difference ($B^- - B^+$, bottom). The a) ($\cos Hel23 < 0$), b) ($\cos Hel > 0$), and c) are showing the $m_{K^\pm\pi^\mp}^2$ in a different region. The d) ($\cos Hel13 > 0$), e) ($\cos Hel13 < 0$), and f) are the projections for the $m_{K^+K^-}^2$. For the g) and h) we have the diagonal projections $m_{K^+\pi^+}^2$. The line in blue represents the model, the black dots represent the data, and the region in red is the background estimation. All plots were produced using 40 bins. 137
- Figura 91 – Fit 10 adding the $f_2(1270)$ together with $f'_2(1525)$, for each plot B^- (top), B^+ (middle) and the difference ($B^- - B^+$, bottom). The a) and b) show the full projections of $m_{K^\pm\pi^\mp}$ and $m_{K^+K^-}$ produced using 100 bins, respectively. It is important to note that in these two cases, the mass is not squared. The c) is the $0.9 < m_{K^+K^-}^2 < 1.2$ to zoom in on the $\phi(1020)$, using 40 bins. The line in blue represents the model, the black dots represent the data, and the region in red is the background estimation. 138
- Figura 92 – Fit 11 using $f_0(980)$ in place of Rescattering and δ_{Pol4} for PolarFFNR, for each plot B^- (top), B^+ (middle) and the difference ($B^- - B^+$, bottom). The a) ($\cos Hel23 < 0$), b) ($\cos Hel > 0$), and c) are showing the $m_{K^\pm\pi^\mp}^2$ in a different region. The d) ($\cos Hel13 > 0$), e) ($\cos Hel13 < 0$), and f) are the projections for the $m_{K^+K^-}^2$. For the g) and h) we have the diagonal projections $m_{K^+\pi^+}^2$. The line in blue represents the model, the black dots represent the data, and the region in red is the background estimation. All plots were produced using 40 bins. 140
- Figura 93 – Fit 11 using $f_0(980)$ in place of Rescattering and δ_{Pol4} for PolarFFNR, for each plot B^- (top), B^+ (middle) and the difference ($B^- - B^+$, bottom). The a) ($\cos Hel23 < 0$), b) ($\cos Hel > 0$), and c) are showing the $m_{K^\pm\pi^\mp}^2$ in a different region. The d) ($\cos Hel13 > 0$), e) ($\cos Hel13 < 0$), and f) are the projections for the $m_{K^+K^-}^2$. For the g) and h) we have the diagonal projections $m_{K^+\pi^+}^2$. The line in blue represents the model, the black dots represent the data, and the region in red is the background estimation. All plots were produced using 40 bins. 141

Figura 94 – Fit 11 using $f_0(980)$ in place of Rescattering and δ_{Pol4} for PolarFFNR, for each plot B^- (top), B^+ (middle) and the difference ($B^- - B^+$, bottom). The a) and b) show the full projections of $m_{K^\pm\pi^\mp}$ and $m_{K^+K^-}$ produced using 100 bins, respectively. It is important to note that in these two cases, the mass is not squared. The c) is the $0.9 < m_{K^+K^-}^2 < 1.2$ to zoom in on the $\phi(1020)$, using 40 bins. The line in blue represents the model, the black dots represent the data, and the region in red is the background estimation.	142
Figura 95 – Amplitude and phase of the $K\pi$ S-wave resulting from Fit 11 using $K_0^*(1430)$ and δ_{Pol4}	142
Figura 96 – Amplitude and phase of the KK S-wave resulting from Fit 11 using $f_0(980)$ and χ_{c0}	143
Figura 97 – Possible components contributions in the $B^\pm \rightarrow K^\mp K^\pm \pi^\pm$ phase space. Components are parameterized using the Breit-Wigner lineshape. The first line shows $\chi_{c0}(1P)$, the second line shows $\rho(1700)$, the third line shows $K^*(892)$, the fourth line shows κ , and the fifth line shows $K_0^*(1430)$	156
Figura 98 – Possible components contributions in the $B^\pm \rightarrow K^\mp K^\pm \pi^\pm$ phase space. Components are parameterized using the Breit-Wigner lineshape. The first line shows $f_2(1270)$, the second line shows $f_2'(1525)$, the third line shows $\phi(1020)$, and the fourth line shows $\rho(1450)$	157
Figura 99 – Possible components contributions in the $B^\pm \rightarrow K^\mp K^\pm \pi^\pm$ phase space. Components are parameterized using different lineshapes. The first line shows a Non-Resonant using LASS, the second line shows the PolarFFNR, the third line shows $f_0(980)$ using Flattè, and the fourth line shows the Rescattering.	158
Figura 100 – Possible components contributions in the $B^\pm \rightarrow K^\mp K^\pm \pi^\pm$ phase space. Components are parameterized using different lineshapes. The first line shows $\rho(770)$ using Gounaris-Sakurai, the second line shows the BelleNR, the third line shows J/ψ , and the fourth line shows the δ_{Pol2}	159
Figura 101 – Fits for B^+ for all 64 bins of the background model.	161
Figura 102 – Fits for B^- for all 64 bins of the background model.	162
Figura 103 – Scatter plot showing the relationship between NLL and Λ from PolarFFNR from a total of 100 fits. Each point represents a different local minimum for each fitted value of Λ	166
Figura 104 – Histogram showing the distribution of Λ from PolarFFNR values from a total of 100 fits. This histogram highlights that the preferred value for Λ is around 1.22	166
Figura 105 – Resonances generated without background contributions, proportional to their respective fit fractions.	168

Figura 106–Cropped regions of the Dalitz Plot.	169
Figura 107–Fitted A_{CP} distribution from the 100 generated toys, with the reference value shown in red.	170
Figura 108–Fitted positive fit fraction distribution from the 100 generated toys, with the reference value shown in red.	170
Figura 109–Fitted negative fit fraction distribution from the 100 generated toys, with the reference value shown in red.	171
Figura 110–Fitted A_{CP} distribution from the 100 generated toys for the square cropped region of the Dalitz Plot. There is a clear bias between the reference value shown in red and the distribution of the fits depicted in blue.	172
Figura 111–Fitted positive fit fraction distribution from the 100 generated toys for the square cropped region of the Dalitz Plot. There is a clear bias between the reference value shown in red and the distribution of the fits depicted in blue.	172
Figura 112–Fitted negative fit fraction distribution from the 100 generated toys for the square cropped region of the Dalitz Plot. There is a clear bias between the reference value shown in red and the distribution of the fits depicted in blue.	173
Figura 113–Fitted A_{CP} distribution from the 100 generated toys for the square cropped region of the Dalitz Plot. There is no bias between the reference value shown in red and the distribution of the fits depicted in blue after correcting the background level.	174
Figura 114–Fitted positive fit fraction distribution from the 100 generated toys for the square cropped region of the Dalitz Plot. There is no bias between the reference value shown in red and the distribution of the fits depicted in blue after correcting the background level.	174
Figura 115–Fitted negative fit fraction distribution from the 100 generated toys for the square cropped region of the Dalitz Plot. There is no bias between the reference value shown in red and the distribution of the fits depicted in blue after correcting the background level.	175
Figura 116–Fitted A_{CP} distribution from the 100 generated toys for the Upper cropped region of the Dalitz Plot. The impact of removing three resonances on the fitted values (in blue) can be observed by comparing them with the reference values (in red).	176
Figura 117–Fitted positive fit fraction distribution from the 100 generated toys for the Upper cropped region of the Dalitz Plot. The impact of removing three resonances on the fitted values (in blue) can be observed by comparing them with the reference values (in red).	176

Figura 118–Fitted negative fit fraction distribution from the 100 generated toys for the Upper cropped region of the Dalitz Plot. The impact of removing three resonances on the fitted values (in blue) can be observed by comparing them with the reference values (in red).	177
Figura 119–Fitted A_{CP} distribution from the 100 generated toys for the Upper cropped region of the Dalitz Plot. After removing only the rescattering, the distributions (in blue) align consistently with the reference values (in red).	177
Figura 120–Fitted positive fit fraction distribution from the 100 generated toys for the Upper cropped region of the Dalitz Plot. After removing only the rescattering, the distributions (in blue) align consistently with the reference values (in red)..	178
Figura 121–Fitted negative fit fraction distribution from the 100 generated toys for the Upper cropped region of the Dalitz Plot. After removing only the rescattering, the distributions (in blue) align consistently with the reference values (in red).	178
Figura 122–Fitted A_{CP} distribution from the 100 generated toys for the Middle cropped region of the Dalitz Plot. Keeping only PolarFFNR, χ_c , and J/ψ , there appears to be a bias in the A_{CP} values when comparing the reference value (in red) with the distribution (in blue).	180
Figura 123–Fitted A_{CP} distribution from the 100 generated toys for the Middle cropped region of the Dalitz Plot, after adding the $\rho(1450)$	180
Figura 124–Fitted A_{CP} distribution from the new 100 generated toys for the Middle cropped region of the Dalitz Plot.	181
Figura 125–NLL distribution for the mother solution (in blue) and the parameters after one shaking (in red).	185
Figura 126–NLL distribution for the mother solution (in blue) and the parameters after 500 shakings (in red).	186
Figura 127–Distribution of NLL values calculated for four different cases: 500 simulations generated with Rescattering(2018), calculated with Rescattering(2018) and Rescattering(2023) shown in blue and red, respectively. 500 simulations generated with Rescattering(2023), calculated with Rescattering(2018) and Rescattering(2023) shown in green and pink, respectively.	187

List of Tables

Tabela 1	– Approximate values of the conditions for LHCb data-taking [18].	15
Tabela 2	– Summary of luminosity, stripping and reconstruction for run II data set.	51
Tabela 3	– General level requirements for large MC signal samples.	51
Tabela 4	– Stripping line selection criteria for charmless B^\pm decays to three light hadrons.	52
Tabela 5	– List of variables used as input for BDT training.	56
Tabela 6	– Final PID requirements for $B^+ \rightarrow \pi^+ K^+ \pi^-$	60
Tabela 7	– The \bar{D}^0 mass veto.	61
Tabela 8	– Summary of all selection stages applied in this analysis.	63
Tabela 9	– Branching ratios and fractions of the peaking backgrounds for $B^\pm \rightarrow K^\mp K^\pm \pi^\pm$	66
Tabela 10	– Peaking background parameters extracted from MC studies for $B^\pm \rightarrow K^\mp K^\pm \pi^\pm$	66
Tabela 11	– Fractions of the partially-reconstructed backgrounds, obtained from MC.	67
Tabela 12	– Parameters extracted from the mass fits distribution of MC samples.	68
Tabela 13	– Parameters extracted from the mass fits distributions of data samples. The numbers followed by a “(C)” were fixed in the corresponding fit. This table presents only the signal and combinatorial components of the fit. This table does not take into account the mass vetoes applied to address the D^0 contamination described in Sec. 5.2.8.	68
Tabela 14	– Integral of each component in the signal region of 5247 to 5315 MeV/ c^2	69
Tabela 15	– Angular distribution using Zemach tensor formalism.	76
Tabela 16	– Blatt-Weisskopf barrier factor used to correct the amplitude for penetration effects where z_0 represents the value of z when the invariant mass is equal to the pole mass of the resonance.	76
Tabela 17	– Parameters and their values extracted from Tables 3 and 4 of [17].	86
Tabela 18	– Description of various resonances including their line shapes, masses, and widths.	101
Tabela 19	– Signal and background events set on the Dalitz plot fit.	102
Tabela 20	– Results of the Dalitz plot fit for the Run I data used as the starting point model, table extracted from [19].	107
Tabela 21	– Results of the Dalitz plot Fit 1 for the Run II data using the starting point model.	107
Tabela 22	– Results of the Dalitz plot Fit 2 considering the addition of $\chi_{c0}(1P)$	112
Tabela 23	– Results of the Dalitz plot Fit 3 fitting $\Lambda = 1.22 \pm 0.03$	113

Tabela 24 – Dalitz Plot Fit 4 results using UFD_b parameters for the Rescattering component.	114
Tabela 25 – Dalitz Plot Fit 5 results with mass and width of the $\rho^0(1450)$ floating.	118
Tabela 26 – Dalitz Plot Fit 6 results after adding the $\rho^0(1700)$	119
Tabela 27 – Dalitz Plot Fit 7 results using the $\delta_{S_{K\pi}}$ as parametrization for the $K\pi$ low mass.	124
Tabela 28 – Dalitz Plot Fit 7 results using the δ_{Pol2} as parametrization for the $K\pi$ low mass.	125
Tabela 29 – Dalitz Plot Fit 9 results including the J/ψ	130
Tabela 30 – Dalitz Plot Fit 10 results replacing $f_2(1270)$ with $f'_2(1525)$	131
Tabela 31 – Dalitz Plot Fit 10 results adding $f_2(1270)$ together with $f'_2(1525)$	132
Tabela 32 – Dalitz Plot Fit 11 results using $f_0(980)$ replacing the Rescattering and the δ_{Pol4} replacing the PolarFFNR.	139
Tabela 33 – Dalitz Plot fit results using CFD_c parameters for the Rescattering component.	163
Tabela 34 – Dalitz Plot fit results using CFD_b parameters for the Rescattering component.	163
Tabela 35 – Dalitz Plot fit results using UFD_c parameters for the Rescattering component.	163
Tabela 36 – Dalitz Plot fit results using UFD_b parameters for the Rescattering component.	164
Tabela 37 – Model given as input for the generation of 100 toys.	169
Tabela 38 – Results of the square cropped Dalitz Plot after the correction of the background level.	173
Tabela 39 – Results of the upper cropped Dalitz Plot after removing only the Rescattering.	179
Tabela 40 – A more realistic model used as input for the generation of the new set of toys.	181
Tabela 41 – Dalitz Plot fit results using the Rescattering(2018).	184
Tabela 42 – Dalitz Plot fit results using the Rescattering(2023).	184
Tabela 43 – Dalitz Plot fit result for a toy dataset generated with the $J/\psi(1S)$ having an increased width and not included in the fit model.	188
Tabela 44 – Dalitz Plot fit result for a toy dataset generated with the $J/\psi(1S)$ having an increased width and included in the fit model.	189
Tabela 45 – Dalitz Plot fit result for a toy dataset generated with the $J/\psi(1S)$ having the real width and not included in the fit model.	189
Tabela 46 – Dalitz Plot fit result for a toy dataset generated with the $J/\psi(1S)$ having the real width and included in the fit model.	189

Tabela 47 – Dalitz Plot fit result for a toy dataset generated without the $J/\psi(1S)$ and not included in the fit model.	190
Tabela 48 – Dalitz Plot fit result for a toy dataset generated without the $J/\psi(1S)$ and included in the fit model.	190
Tabela 49 – Dalitz Plot fit result for a toy dataset generated with the $f'_2(1525)$ and included in the fit model.	191
Tabela 50 – Dalitz Plot fit result for a toy dataset generated with the $f'_2(1525)$ and not included in the fit model.	191
Tabela 51 – Dalitz Plot Fit replacing the PolarFFNR with the BelleNR.	192
Tabela 52 – Dalitz Plot Fit replacing the PolarFFNR with the κ	192
Tabela 53 – Dalitz Plot Fit replacing the PolarFFNR with the LASS.	192
Tabela 54 – Dalitz Plot Fit replacing the PolarFFNR with the non-resonant flat contribution.	193

1 Introduction

Over the past few decades, charmless decays have proven to be an excellent environment for exploring the phenomenon of CP violation. The LHCb experiment, one of the four main detectors at the Large Hadron Collider (LHC), is specifically built to study particles containing bottom and charm quarks, emphasizing the asymmetry between matter and antimatter. CP violation (CPV), first detected in neutral kaon decays, is essential for understanding this asymmetry and provides crucial insights into the Standard Model, especially through the Cabibbo-Kobayashi-Maskawa (CKM) matrix. The CPV measurements performed by LHCb have been vital in refining CKM parameters and probing potential physics beyond the Standard Model. These advances push the limits of current theoretical frameworks, paving the way for future breakthroughs.

Using the data collected during the Run I period, the LHCb experiment measured significant integrated CP asymmetries in three-body B decays involving pions and kaons in the final state [20]. With the higher statistics from the Run II dataset, LHCb confirmed the CP violation in the $B^\pm \rightarrow \pi^\mp \pi^\pm \pi^\pm$ decays and further strengthened the evidence for CP violation [1]. Building on this, this analysis focuses on the $B^\pm \rightarrow K^\mp K^\pm \pi^\pm$ decay channel.

Significant CP asymmetries have been identified in particular regions of the phase space. Based on Run 2 data, their distribution can be qualitatively analyzed, as shown in Fig.1, spotting clear CP asymmetries across the bins. The sources of these asymmetries can be investigated through amplitude analysis, allowing measurements of the resonant structure, interference patterns, relative contributions of each component, and their associated CP asymmetry.

From a theoretical perspective, the dynamics of each process cannot be determined from first principles. In three-body decays, the standard procedure is to consider a superposition of two-body interaction channels plus a spectator particle, within the framework of the so-called Isobar model. In this approach, two-body interactions are represented as a coherent sum of resonances, which are usually described by Breit-Wigner functions.

In the Run 1 period, LHCb conducted the first amplitude analysis of the $B^\pm \rightarrow K^\mp K^\pm \pi^\pm$ channel [19] using the Isobar model approach. This study uncovered one of the largest CP asymmetries for a single amplitude observed up to that point, with a value near -66% . Resonant contributions are expected in the two pairs of oppositely charged particles: the KK and $K\pi$ systems. The production of resonances in the $B^\pm \rightarrow \pi^\pm K^+ K^-$ decay is constrained. Resonances in the $\pi^\pm K^\mp$ system are only accessible via penguin transitions,

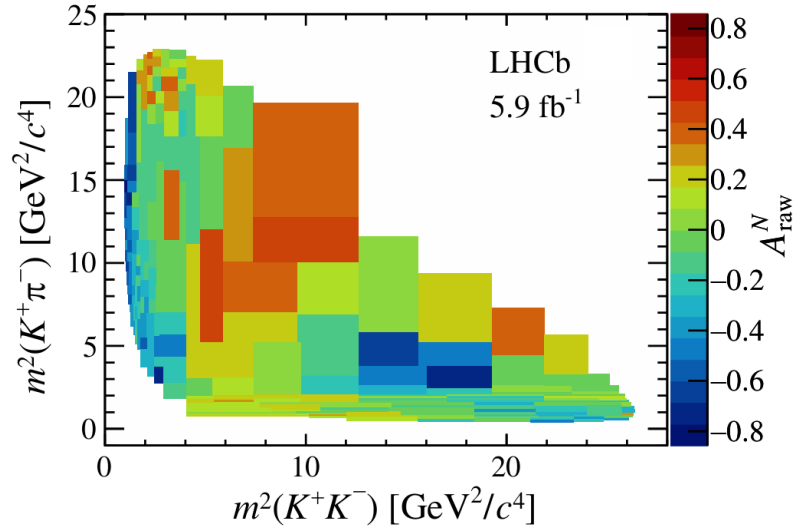


Figure 1 – Measured A_{cp} in bins of the $B^\pm \rightarrow K^\mp K^\pm \pi^\pm$ Dalitz plot. The distribution comes from background-subtracted and acceptance-corrected events [1].

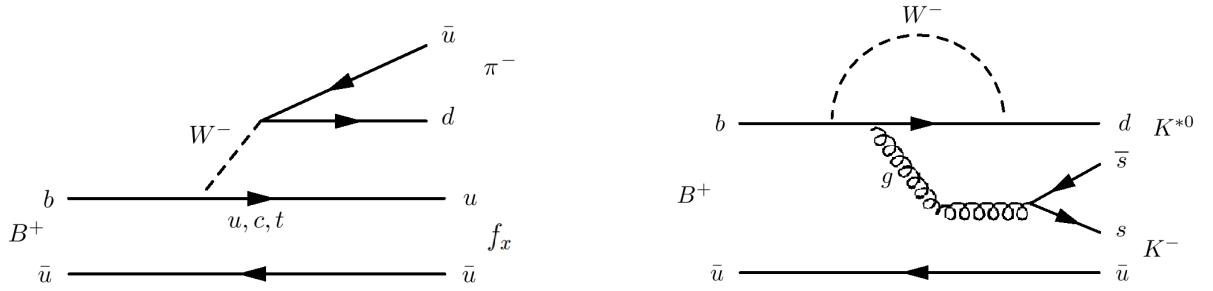


Figure 2 – Tree (left) and penguin (right) diagrams for the $B^\pm \rightarrow K^\mp K^\pm \pi^\pm$ decay.

whereas K^+K^- resonances may arise from tree-level transitions. One mechanism by which CP violation can occur is through the interference between resonance states, coming from the quark level due to different weak phases of penguin and tree transitions. The tree ($b \rightarrow u$) and the penguin ($b \rightarrow d$) level transitions diagrams for $B^\pm \rightarrow K^\mp K^\pm \pi^\pm$ are shown in the Fig. 2(a) and 2(b), respectively.

The amplitude analysis of $B^\pm \rightarrow K^\mp K^\pm \pi^\pm$ using the Run 2 data will be performed and, as a starting point, the previous results of the LHCb experiment will be used. The Run I baseline model included the following components: $K^*(892)$, $K_0^*(1430)$, and a non-resonant contribution for the $K\pi$ system, as well as $\rho(1450)$, $f_2(1270)$, a rescattering contribution, and $\phi(1020)$ for the KK system.

The rescattering $\pi\pi \leftrightarrow KK$ concept was introduced in the context of two-body interactions. In the context of three-body decays, rescattering transitions occur when a pair of mesons initially coming from one channel reappear in the final state of a coupled channel having the same flavor quantum numbers, which is the case of $B^\pm \rightarrow K^\mp K^\pm \pi^\pm$ and $B^\pm \rightarrow \pi^\mp \pi^\pm \pi^\pm$. The rescattering region needs improvements in its description so far.

The update of its modeling could lead to a better understanding of the significant difference between the fit fractions of this component associated with $B^\pm \rightarrow K^\mp K^\pm \pi^\pm$ ($\approx 16\%$) and $B^\pm \rightarrow \pi^\mp \pi^\pm \pi^\pm$ ($\approx 1 - 2\%$) [21].

The contributions of components such as rescattering, $\phi(1020)$, $\rho(1450)$, $f_2(1270)$, and other potential resonances will be analyzed. In practice, certain resonances are not expected in this decay. For instance, the $B^\pm \rightarrow \phi \pi^\pm$ decay, where $\phi \rightarrow K^+ K^-$, involves an $s\bar{s}$ resonance that is highly suppressed by the OZI rule, which states that diagrams with disconnected quark lines are less likely than those with connected ones, having $\mathcal{B}(B^\pm \rightarrow \phi \pi^\pm) < 1.5 \times 10^{-7}$. Additionally, other resonances exhibit contributions significantly exceeding predictions, such as $\rho(1450)$. While this resonance primarily decays into the $B^\pm \rightarrow \pi^\mp \pi^\pm \pi^\pm$ channel, where its fit fraction is approximately 5% [22], it shows a considerably higher contribution of around 30% in the $B^\pm \rightarrow K^\mp K^\pm \pi^\pm$ channel. The $f_2(1270)$ plays the role of the tensor contribution, however, the component that was expected for this role was $f'_2(1525)$, considering that the fraction of $f_2(1270) \rightarrow KK$ is 4.6% and for the $f'_2(1525) \rightarrow KK$ is 87.6%. The inclusion of $\phi(1020)$ was motivated by the lack of a good parametrization in the region near the threshold KK , as for the results of paper [23].

This study emphasizes the S-wave contribution to the decay, which accounts for approximately 60% of the total decay amplitude and is predominantly located near the most populated regions of events, along the edges of the Dalitz plot. A notable challenge in this analysis lies in parameterizing the $K\pi$ and KK S-wave, due to the absence of angular distribution information, components with well-defined angular properties are easier to identify. These are just some examples of situations that need to be better understood.

There is also a strong interest in the charmonium resonances, especially the $\chi_{c0}(1P)$ and $J/\psi(1S)$ components, as there seem to be indications of their presence. These are particularly intriguing because they involve $(c\bar{c})$, and the related decays are driven by the process $b \rightarrow c + \bar{c} + d$. According to the CKM matrix, the couplings involved (V_{bc} and V_{cd}) do not introduce a weak phase at λ^3 level, implying that there should not be CP violation within the Standard Model. This kind of component will be explored in the revisited resonant model for $B^\pm \rightarrow K^\mp K^\pm \pi^\pm$ with the Run II data.

In general, the aim of this study is, due to the abundance of resonant substructures and dynamical effects like rescattering, to perform a full amplitude analysis to shed light on the CP violation mechanisms in this channel, using the full Run II dataset, i.e, a total of $5.9fb^{-1}$ (higher luminosity if compared to the $3.0fb^{-1}$ from Run I) of pp collisions collected during 2015 - 2018 with around 35,000 events (7 times more than in Run I).

The organization of this thesis is as follows: Chapter 2 presents the essential theoretical foundations of the Standard Model and the type of physics relevant to this study. Chapter 3 provides an overview of the LHCb experiment, followed by Chapter

4, which details the technical contributions of this work to the experiment. Chapter 5 discusses the event selection process for the analysis. Chapter 6 introduces the Dalitz Plot formalism and fundamental concepts for analyzing the decay's phase space. Chapter 7 explores the technical aspects necessary for performing this analysis and describes the tools used to evaluate the results. Chapter 8 presents the main results of this study. Proposals for systematic studies are included in Chapter 9, and the thesis concludes with the findings and implications discussed in Chapter 10.

2 Theory Overview

In this chapter, a brief overview of the theoretical foundations of particle physics is presented, including an introduction to the Standard Model with a focus on flavor physics and CP violation. The published results for the CP violation in $B^\pm \rightarrow h^\pm h^+ h^-$ will be also discussed [20, 1].

2.1 The Standard Model

The Standard Model (SM) of particle physics is the theoretical framework that describes the fundamental particles and interactions in the universe, excluding gravity. It classifies particles into two main categories: fermions, which constitute matter, and bosons, which mediate interactions. The model successfully explains three of the four fundamental forces: electromagnetic, weak, and strong interactions, while organizing elementary particles into a structured framework. At its core, the SM is based on the symmetry group $SU(3)_C \times SU(2)_L \times U(1)_Y$, where each group corresponds to a fundamental interaction: $SU(3)_C$ for the strong force, $SU(2)_L$ for the weak force, and $U(1)_Y$ for electromagnetism.

The quark sector of the SM is particularly relevant to flavor physics. Quarks come in six flavors: up, down, charm, strange, top, and bottom, each grouped into three generations. The first generation consists of the up and down quarks, the second generation includes the charm and strange quarks, and the third generation contains the top and bottom quarks. Flavor-changing interactions are central to flavor physics and are observed in the weak interaction. In contrast to the strong and electromagnetic interactions, which conserve flavor, the weak interaction can change quark flavors through processes mediated by the charged W^\pm bosons.

Quarks are bound together by the strong interaction, described by Quantum Chromodynamics (QCD), forming composite particles known as hadrons. These hadrons come in two main types: baryons, which are made of three quarks (such as protons and neutrons), and mesons, which are quark-antiquark pairs. Flavor physics experiments, like LHCb at CERN, focus on the properties and decays of hadrons containing bottom (or b) quarks, providing insights into fundamental symmetries and potential new physics beyond the SM.

2.2 The Cabibbo-Kobayashi-Maskawa Matrix

A key element in understanding flavor physics within the Standard Model (SM) is the Cabibbo-Kobayashi-Maskawa (CKM) matrix, which describes the mixing and transitions between quark flavors due to the weak interaction. The CKM matrix elements V_{ij} represent the probability amplitude for a transition between quark flavors i and j , where $i = u, c, t$ and $j = d, s, b$. For example, V_{us} describes the transition of a strange quark to an up quark.

The CKM matrix is a unitary 3×3 matrix, ensuring the conservation of probability in flavor transitions. In general, any 3×3 unitary matrix has 9 parameters: 3 angles and 6 phases. However, due to the complex nature of the CKM matrix, there is freedom in the phase structure of the quark mass eigenstates. This allows the elimination of 5 of the 6 phases, leaving only 4 independent parameters: 3 angles and 1 complex phase. The CKM matrix can be expressed as:

$$\begin{pmatrix} d' \\ s' \\ b' \end{pmatrix} = \begin{pmatrix} V_{ud} & V_{us} & V_{ub} \\ V_{cd} & V_{cs} & V_{cb} \\ V_{td} & V_{ts} & V_{tb} \end{pmatrix} \begin{pmatrix} d \\ s \\ b \end{pmatrix} \equiv V_{CKM} \begin{pmatrix} d \\ s \\ b \end{pmatrix} \quad (2.1)$$

Written in terms of the three mixing angles and a complex phase, it can be expressed as:

$$V_{CKM} = \begin{pmatrix} c_{12}c_{13} & s_{12}c_{13} & s_{13}e^{-i\delta} \\ -s_{12}c_{23} - c_{12}s_{23}s_{13}e^{i\delta} & c_{12}c_{23} - s_{12}s_{23}s_{13}e^{i\delta} & s_{23}c_{13} \\ s_{12}s_{23} - c_{12}c_{23}s_{13}e^{i\delta} & -c_{12}s_{23} - s_{12}c_{23}s_{13}e^{i\delta} & c_{23}c_{13} \end{pmatrix},$$

Various parametrizations of the CKM matrix exist, with the Wolfenstein parametrization [24] being the most widely used. This parametrization relies on experimental measurements and expands in terms of $\lambda = \sin \theta_c \approx 0.225$, where θ_c is the Cabibbo angle. In this form, it is represented as follows:

$$V = \begin{pmatrix} 1 - \lambda^2/2 & \lambda & A\lambda^3(\rho - i\eta) \\ -\lambda & 1 - \lambda^2/2 & A\lambda^2 \\ A\lambda^3(1 - \rho - i\eta) & -A\lambda^2 & 1 \end{pmatrix} + O(\lambda^4), \quad (2.2)$$

where η expresses the complex nature of the matrix, responsible for CP violation.

2.3 CP Violation

The CP violation can occur through at least three distinct mechanisms. Direct CPV, also referred to as CPV in decay, takes place when the decay amplitude of a particle differs from that of its CP conjugate, impacting both charged and neutral particles. CPV in mixing appears as a difference in the oscillation rates between mesons and antimesons, occurring when the mass eigenstates of a neutral meson are not CP eigenstates. Lastly, CPV through the interplay of mixing and decay arises when a final state can be reached by both a neutral meson and its CP conjugate antimeson, allowing them to decay into the same final state either before or after mixing. Charged particles cannot undergo mixing due to charge conservation, that is why the last two forms of CP violation are limited to decays involving neutral mesons.

In the SM, CP violation originates from a complex phase in the CKM matrix. These phases can be classified into two types: CP-odd and CP-even. A CP-odd phase changes sign under CP conjugation — differing between particle and antiparticle — while a CP-even phase remains unchanged. These phases are associated with different interactions: CP-odd phases, often called weak phases, arise from weak interactions, whereas CP-even phases, referred to as strong phases, occur in strong or electromagnetic interactions. The origin of the weak and strong phases is not fully understood *a priori*. While weak phases are linked to the CKM matrix within the Standard Model (SM), strong phases may result from short-distance effects, such as those from penguin diagrams, or from long-distance effects due to final-state interactions (FSI) e.g. hadronic rescatterings in non-leptonic decays [25], which will be discussed in a further section.

For simplicity, let us consider an example of a decay $B^+ \rightarrow f$ and its conjugate $B^- \rightarrow \bar{f}$, where f is a possible final state that can be reached through two different amplitudes. The total amplitudes for B^+ and B^- are:

$$A_f = |a_1|e^{i(\delta_1+\phi_1)} + |a_2|e^{i(\delta_2+\phi_2)} \quad (2.3)$$

$$\bar{A}_{\bar{f}} = |a_1|e^{i(\delta_1-\phi_1)} + |a_2|e^{i(\delta_2-\phi_2)}, \quad (2.4)$$

where $\delta_{1,2}$ are the strong phases, $\phi_{1,2}$ are the weak phases, and $a_{1,2}$ are intermediate amplitudes. Under CP conjugation, the weak phase changes sign, while the strong phase remains unchanged. The asymmetry between the decay rates can be quantified by the quantity A_{CP} , given by:

$$A_{CP} = \frac{\Gamma(B^+ \rightarrow f^+) - \Gamma(B^- \rightarrow f^-)}{\Gamma(B^+ \rightarrow f^+) + \Gamma(B^- \rightarrow f^-)} = \frac{|A_f|^2 - |\bar{A}_{\bar{f}}|^2}{|A_f|^2 + |\bar{A}_{\bar{f}}|^2}. \quad (2.5)$$

By substituting Eqs. 2.3 and 2.4 into Eq. 2.5, we find:

$$A_{CP} = \frac{2|a_1 a_2| \sin(\delta_2 - \delta_1) \sin(\phi_2 - \phi_1)}{|a_1|^2 + |a_2|^2 + 2|a_1 a_2| \cos(\delta_2 - \delta_1) \cos(\phi_2 - \phi_1)}. \quad (2.6)$$

From Eq. 2.6, we can see that, as long as there is interference between amplitudes with different strong and weak phases, an observable CP asymmetry will arise.

2.3.1 CP violation aspects for $B^\pm \rightarrow h^\pm h^+ h^-$ decays

One of the reasons for performing the amplitude analysis of $B^\pm \rightarrow K^\mp K^\pm \pi^\pm$ is inspired by the findings reported in [1]. As already observed in this work, charmless three-body B decays represent an interesting scenario for exploring the sources of CP violation. The authors presented a study of the phase-space integrated CP -asymmetries for the decay modes $B^\pm \rightarrow K^\pm \pi^+ \pi^-$, $B^\pm \rightarrow K^\pm K^+ K^-$, $B^\pm \rightarrow \pi^\pm K^+ K^-$, and $B^\pm \rightarrow \pi^\pm \pi^+ \pi^-$. The distributions of CP asymmetries in the phase space of the four modes are also presented.

The four decay channels under investigation are highly sensitive to CP violation effects because their dominant diagrams involve $b \rightarrow s(d)$ (penguin diagrams) and $b \rightarrow u$ (tree diagrams), see Figure 3, producing different resonances. These processes can result in interference between these resonances denoted by distinct weak and strong phases. Consequently, the strong interaction between intermediate decay states could generate localized CP asymmetries in regions with weak phases.

Estimating direct CP violation asymmetries presents a significant challenge, from a theoretical perspective. These estimates heavily depend on the magnitude of the strong phases involved in the decays [26]. The Bander, Silverman, and Soni framework [27] (BSS mechanism) was the first theoretical proposal to study direct CP violation. It suggests that asymmetries in charged B meson decays arise from the interference between tree-level and penguin-level quark diagrams, which have distinct weak and strong phases. Since then, numerous studies have explored different mechanisms to understand the role of strong interaction phases. It is generally agreed that strong phases originating from short-distance effects are expected to be small. Under this assumption, the resulting level of direct CP violation would also be minimal. However, if long-distance effects are considered a significant source of strong phase shifts, much larger direct CP violation effects could be expected.

Even though the existence of a strong phase and a weak phase are necessary conditions for the occurrence of the direct CP violation, these should, in principle, not be the only ones, the influence of CPT symmetry is not explicitly evident and must be carefully considered. Together with the unitarity of the scattering matrix, CPT invariance imposes a significant constraint on direct CP violation. Specifically, in the absence of

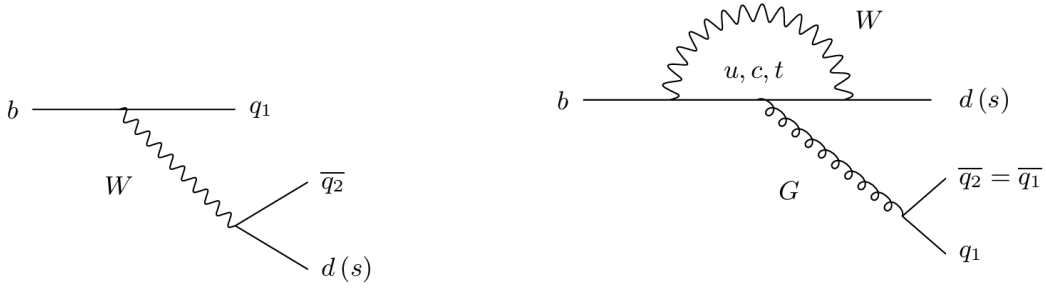


Figura 3 – Tree (left, where $q_1, q_2 \in \{u, c, \}$) and QCD penguin (right, where $q_1 = q_2 \in \{u, d, c, s\}$) diagrams [2].

rescattering processes, direct CP asymmetries cannot occur, even in the presence of weak phases [26].

2.3.1.1 The final-state interactions

The interaction that occurred at the quark level before hadronization is characterized as a short-distance phenomenon. Such interactions involve collisions between quarks and gluons governed by QCD. Conversely, the scattering takes place at the hadronic level and is identified as a long-distance process [28].

During the decay of B mesons, quarks produced in the weak transition experience strong interactions that persist even after the hadrons are formed. These interactions, referred to as FSI, play a crucial role in shaping the final particle states. Following the initial weak decay of a heavy meson, the hadrons generated can scatter into different particle configurations through non-perturbative strong interactions or electromagnetic processes, facilitated by various FSI mechanisms. This contributes to the complexity of the decay dynamics and can influence observable properties, such as CP asymmetries.

In the literature, the prevailing belief has been that FSI has a minimal impact regarding the asymmetries, due to the high energy released in such decays. The energy released causes the hadrons produced in the final state to move at such high speeds that they quickly exit the interaction region, leaving them with insufficient time to participate in meaningful final-state rescattering processes [29]. Thus, the FSI would have a negligible influence on the production of the strong phase. However, by examining the implications of the BSS mechanism for CP violation in the B -meson system, the FSI rescattering at the hadronic level increases with energy [30]. Moreover, it was demonstrated that relying solely on short-distance amplitudes in the BSS mechanism could potentially violate the CPT theorem in quark-level processes.

“communication”

According to CPT symmetry, the lifetimes, τ , and consequently the total decay

widths, Γ_{total} , of a particle and its antiparticle are identical. However, CP violation allows for differences in the partial decay widths, Γ_i . Maintaining equality in total widths between a particle and its antiparticle while permitting variations in their partial widths necessitates a “communication” between different decay modes. This communication can only occur among modes that share the same flavor quantum numbers. For final states with identical quantum numbers, the sum of partial decay widths must also be identical. In this context, CPV could be distributed among multiple channels through FSI. This implies, for example, that if a significant positive CP asymmetry is observed in one decay mode, it necessitates the presence of strongly coupled final states exhibiting negative CP asymmetry to maintain the overall balance.

In a nutshell, the final-state interactions play a critical role in providing the strong phases required for CP violation to manifest, and it is also a fundamental element in preserving the CPT symmetry. Thus, the CPT symmetry not only demands equality in the total decay widths of particles and antiparticles but also imposes the condition that the sum of partial widths to final states with identical quantum numbers must be equal. This constraint can be expressed as:

$$\sum_i \Delta\Gamma(P \rightarrow f_i) = 0$$

The hadronic rescattering in the final state, like $K^-K^+ \leftrightarrow \pi^-\pi^+$, which connects different final states, could introduce the necessary strong phase difference for CP violation. This mechanism plays a significant role in the specific decay $B^\pm \rightarrow K^\mp K^\pm \pi^\pm$, which is the focus of our interest [31, 32].

2.3.2 The Direct CP violation measurements in $B^\pm \rightarrow h^\pm h^+ h^-$ decays

The standard observable used when investigating CP violation in decays is the CP asymmetry (A_{cp}). The observed raw charge asymmetry is defined as:

$$A_{\text{RAW}} \equiv \frac{N_{\text{sig}}^- - N_{\text{sig}}^+}{N_{\text{sig}}^- + N_{\text{sig}}^+}, \quad (2.7)$$

where N_{B^-} and N_{B^+} represent the number of events for B^- and B^+ , respectively. However, experimentally, the value of A_{raw} is influenced not only by CP -violation but also by a series of effects stemming from production, reconstruction, and the final selection of events.

After performing a mathematical manipulation and considering other sources of asymmetries, we can express the physical CP violation asymmetry as:

$$A_{CP} = \frac{A_{RAW}^{ACC} - A_P}{1 - A_{RAW}^{ACC} A_P} \quad (2.8)$$

where the A_P is the production asymmetry and A_{RAW}^{ACC} is representing the detection and acceptance correction. The final results for the phase-space integrated CP-asymmetry of the four $B^\pm \rightarrow h^\pm h^+ h^-$ modes, including uncertainties, are:

$$\begin{aligned} A_{CP}(B^\pm \rightarrow K^\pm \pi^+ \pi^-) &= +0.011 \pm 0.002 \pm 0.003 \pm 0.003, \\ A_{CP}(B^\pm \rightarrow K^\pm K^+ K^-) &= -0.037 \pm 0.002 \pm 0.002 \pm 0.003, \\ A_{CP}(B^\pm \rightarrow \pi^\pm \pi^+ \pi^-) &= +0.080 \pm 0.004 \pm 0.003 \pm 0.003, \\ A_{CP}(B^\pm \rightarrow \pi^\pm K^+ K^-) &= -0.114 \pm 0.007 \pm 0.003 \pm 0.003. \end{aligned}$$

where the first uncertainty is statistical, the second is systematic and the third is due to the limited knowledge of the CP asymmetry of the $B^\pm \rightarrow J/\psi K^\pm$ control channel.

One of the benefits of three-body decays is that they enable the investigation of CP asymmetries in localized regions of the phase space. The Dalitz Plot is the phase-space graphical representation of the decay¹ and it provides direct insight into the decay dynamics allowing the exploration of CP asymmetry effects. To examine localized asymmetries, the A_{CP} distribution within phase space bins is constructed. Figure 4 illustrates a rich pattern of significant localized asymmetries, which arise from the interference between different contributions, with negative and positive asymmetries being observed in the same phase space. It is interesting to note how CP violation can manifest at higher levels - varying from 80% to -80% in some cases - in localized regions compared to the integrated value.

Notice that for the $B^\pm \rightarrow K^\pm K^+ K^-$ decay, the phase space can be divided into two regions: $1.1 < m_{KK,low}^2 < 2.25$ and $4 < m_{KK,high}^2 < 17$. Similarly, for the $B^\pm \rightarrow K^\pm \pi^+ \pi^-$ decay, the division can be applied as follows: $1.1 < m_{\pi^+ \pi^-}^2 < 2.25$ and $3.5 < m_{K^+ \pi^-}^2 < 19$. A striking difference is observed in the CP asymmetry between these decays: the asymmetry changes sign in opposite directions (blue-negative for $B^\pm \rightarrow K^\pm K^+ K^-$ and red-positive for $B^\pm \rightarrow K^\pm \pi^+ \pi^-$). The selected region corresponds to the rescattering region, and the difference in the sign of the asymmetries could be attributed to the ‘‘communication’’ facilitated by the rescattering phenomena, as previously mentioned.

As observed, the integrated asymmetry in $B^\pm \rightarrow K^\mp K^\pm \pi^\pm$ is predominantly concentrated in the rescattering region defined as $1 < m_{KK}^2 < 2.25$ and $4 < m_{K\pi}^2 < 19$, where an almost constant blue asymmetry is present. To explore the origin of these pronounced CP asymmetries, an amplitude analysis across all decay channels is essential. The substructures of the components, as well as their interferences, can provide

¹ Further details and discussions on this topic will be presented in the subsequent chapters.

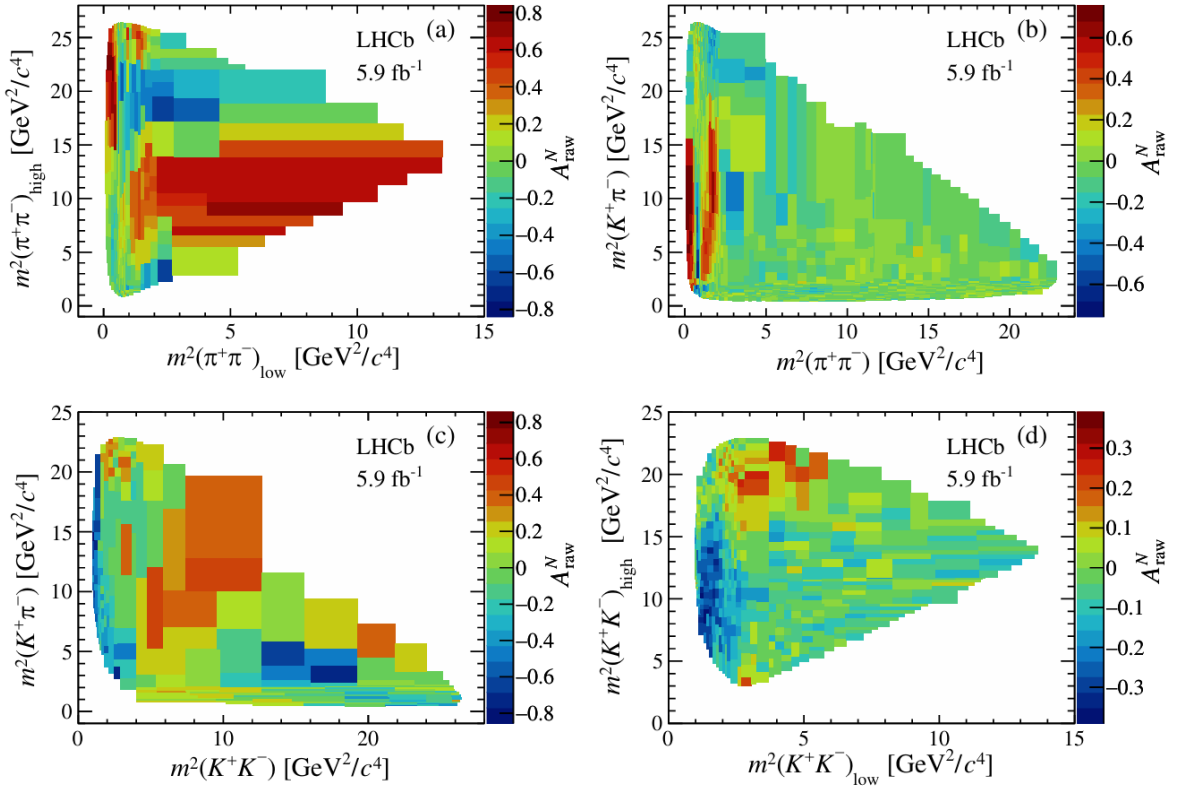


Figure 4 – The distribution of asymmetry in the bins of the Dalitz plot is presented for the following decays: (a) $B^\pm \rightarrow \pi^\pm \pi^+ \pi^-$, utilizing 400 bins with an average of 229 events per bin; (b) $B^\pm \rightarrow K^\pm \pi^+ \pi^-$, with 1728 bins and an average of 276 events per bin; (c) $B^\pm \rightarrow \pi^\pm K^+ K^-$, using 256 bins averaging 127 events per bin; and (d) $B^\pm \rightarrow K^\pm K^+ K^-$, consisting of 729 bins with approximately 461 events per bin [3].

valuable insights into the dynamic processes underlying the observed CP violation. The localized CP asymmetry detected in the rescattering region appears strongly connected to rescattering phenomena, particularly in $B^\pm \rightarrow K^\mp K^\pm \pi^\pm$, where a significant CP asymmetry is evident.

3 The LHCb Experiment

This chapter describes some of the main features of the LHC, its accelerator complex, and its collaborations. CERN has four main experiments: ALICE, ATLAS, CMS, and LHCb. The latter is an experiment dedicated to heavy flavor physics. Some of its primary objectives are the study of CP violation and rare processes involving hadrons containing b and c quarks [6].

3.1 The Large Hadron Collider

The LHC (Large Hadron Collider) is an accelerator located in a tunnel approximately 27 km in length, which was originally built between 1984 and 1989 for the LEP (Large Electron–Positron Collider). It lies around 100 meters below the surface on the border between Switzerland and France, near Geneva. The primary purpose of the LHC is to study elementary particles and their interactions, aiming to test the validity of theoretical models such as the Standard Model (SM) and to explore physics beyond it. This accelerator was designed to collide beams of protons and lead nuclei, achieving center-of-mass energies of up to 13 TeV.

The LHC is host to several experiments. The four main experiments are:

1. ALICE (A Large Ion Collider Experiment): This experiment is focused on heavy ion collisions and investigates QCD, the strong interaction sector of the Standard Model. According to QCD, a new phase of matter should exist at extreme values of density and temperature, which can be achieved in high-energy nucleus-nucleus collisions [33];
2. ATLAS (A Toroidal LHC Apparatus): This is the largest of the four experiments and, together with CMS, was involved in the discovery of the Higgs boson in 2012. Its research topics also include measurements of the Standard Model and phenomena beyond it, such as the search for extra dimensions and dark matter [34];
3. CMS (Compact Muon Solenoid): Like ATLAS, CMS is a general-purpose experiment, but it is designed to enhance the efficiency of muon reconstruction by detecting them before they decay into electrons and in a more compact form [35].
4. LHCb (Large Hadron Collider beauty experiment): This experiment explores the flavour physics. Its main objective is to search for indirect signs of new physics, meaning deviations from the Standard Model predictions caused by effects of yet-undiscovered phenomena, like CP violation and rare decays of beauty and charm

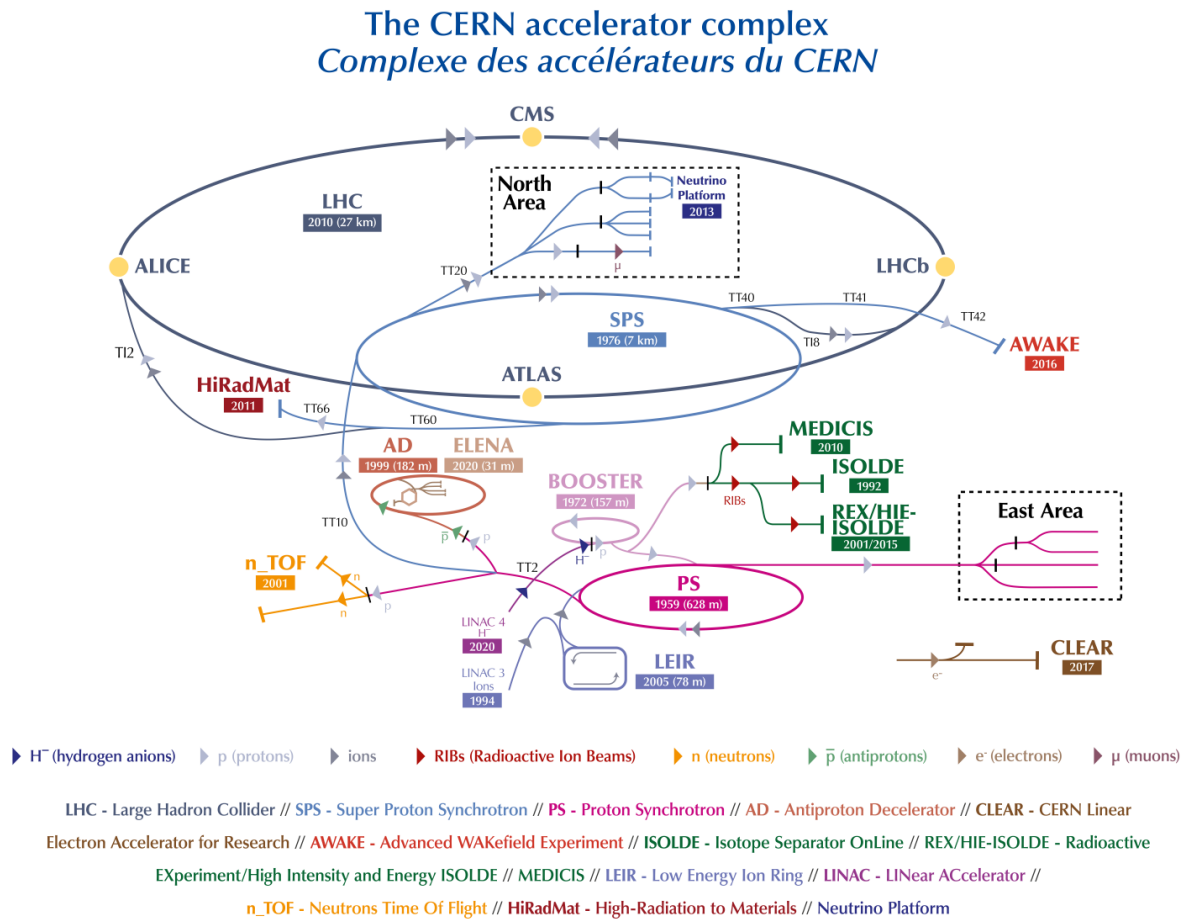


Figura 5 – The CERN accelerator complex.

hadrons[6]. Unlike ATLAS and CMS, which focus on direct searches for new particles, LHCb provides a complementary approach by probing the effects of potential new physics through measurements in the flavour sector;

Proton beams travel through the accelerator tunnel in opposite directions, in an ultra-high vacuum environment at a temperature of 2 K, and are guided and focused by superconducting magnetic dipoles and quadrupoles, respectively.

Figure 5 shows the accelerator complex that supports the LHC. These smaller accelerators are responsible for providing intermediate energies, ensuring beam stability, minimizing losses, and optimizing energy use. Each accelerator in the chain is designed to handle specific energy ranges, preparing the beam efficiently for the LHC’s high-energy collisions. Protons to be collided are obtained in LINAC2, where they are accelerated to 50 MeV by ionizing hydrogen gas with an electron bombardment. They then pass to the PSB (Proton Synchrotron Booster), where they are accelerated to 1.4 GeV. The beam is injected into the PS (Proton Synchrotron), where it is accelerated to 25 GeV. After this, the protons are directed to the SPS (Super Proton Synchrotron), where they reach 450

GeV, and finally, they enter the LHC. In this final stage, protons reach a center-of-mass energy of 13 TeV and collide at specific points where the experiments are located.

To conduct the type of physics we aim to study, increasing the number of events is essential. To achieve this, the LHC was designed to operate at high luminosity, maximizing the collision rate and facilitating the exploration of rare phenomena. Thus, in addition to the center-of-mass energy, luminosity (\mathcal{L}) is a fundamental factor. It represents a measure of the number of collisions that can occur per unit area per unit time: the higher the luminosity, the greater the number of collisions. Luminosity can be expressed as:

$$\mathcal{L} \approx \frac{N^2}{t \times S_{eff}}, \quad (3.1)$$

where N^2 represents the number of protons (with each cloud containing approximately 1.1×10^{11} protons), t is the time between the proton clouds, about 25×10^{-9} s, and S_{eff} is the effective collision cross-section, which depends on the cross-sectional area and has a value of approximately $4\pi(16 \times 10^{-4})^2$ cm². Thus, we arrive at a value of $\mathcal{L} \approx 10^{34}$ cm⁻² s⁻¹ [36], representing the potential for the LHC to produce 10^{34} collisions per cm² per second. Once luminosity is known, it can be integrated over time, and this integrated luminosity is a measure of the total amount of data collected. The instantaneous luminosity used by LHCb is lower, at 10^{32} cm⁻² s⁻¹, chosen to limit the number of interactions per beam crossing, which allows for the reconstruction of primary and secondary vertices and prevents premature aging of the detector [37]. Table 1 shows the values of integrated luminosity and energy for each year of data collection during LHCb runs I and II.

Tabela 1 – Approximate values of the conditions for LHCb data-taking [18].

Run	Year	\sqrt{s} (TeV)	Integrated Luminosity (fb^{-1})
I	2011	7	1.14
I	2012	8	2.19
II	2015	13	0.36
II	2016	13	1.88
II	2017	13	1.87
II	2018	13	2.46

3.2 The LHCb Detector

In high-energy proton-proton collisions, heavy flavor hadrons, such as those containing b-quarks or c-quarks, are predominantly produced in the forward or backward directions. This production mechanism, combined with the substantial mass of B mesons, results in particles characterized by high transverse momentum (p_T) and energy (E_T).

To optimize the study of heavy flavor hadrons, the LHCb detector is designed as a single-arm spectrometer covering the forward region, with an angular coverage of approximately 10–300 mrad in the horizontal plane and 10–250 mrad in the vertical plane. This corresponds to a pseudorapidity¹ range of $2 < \eta < 5$, where $\eta = -\ln(\tan(\theta/2))$ is defined in terms of θ , the angle relative to the beam axis. The LHCb detector consists of a series of sub-detectors, each with specific functions, as described below

Figure 6 shows some components of this detector. The VELO (Vertex Locator) is responsible for reconstructing the trajectories of charged particles together with the tracker stations, TT (Tracker Turicensis), T1, T2, and T3, allowing it to determine the interaction points, known as primary vertices, as well as decay points, or secondary vertices. The Magnet is responsible for deflecting the trajectories of charged particles, enabling the measurement of their momenta. The RICH detectors (Ring Imaging Cherenkov) provide particle identification. The calorimeters (ECAL, HCAL, SPD/PS) measure the positions and energies of particles, assisting in their identification as electrons, photons, or hadrons. The muon stations (M1–M5) are responsible for identifying muons.

The detectors described above are grouped into two main systems within LHCb: the Tracking System and the Particle Identification System. These components will be further explored in the following sections.

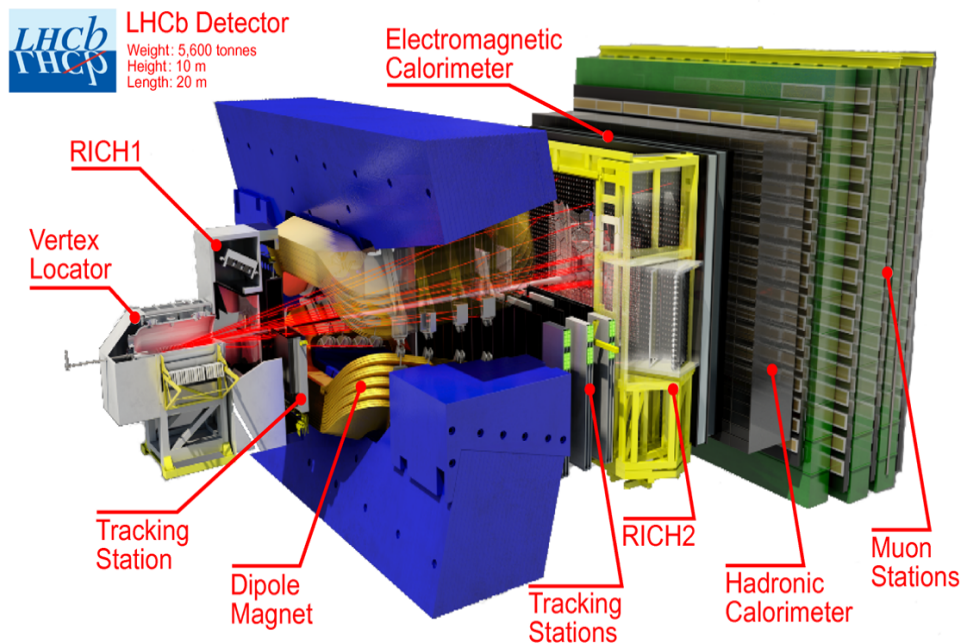


Figura 6 – 3D sketch of the LHCb detector, including all its subdetectors [4].

¹ Pseudorapidity is an approximation to Rapidity, which is a measure of a particle's angle relative to the beam axis, but easier to calculate from the polar angle and equivalent to Rapidity for massless particles.

3.2.1 The tracking system

The LHCb tracking system is essential for the precise reconstruction of particle vertices and achieving high momentum resolution, both critical to the detector's performance. It is composed of several key components: the Vertex Locator (VELO), positioned close to the interaction point; the Tracker Turicensis (TT), located upstream of the dipole magnet; the dipole magnet itself, used to measure the momentum of charged particles; and the Inner and Outer tracking stations (T1-T3), positioned downstream of the magnet. This system is responsible for reconstructing the trajectories of charged particles, known as tracks, which deposit a small amount of energy as they pass through the detector material. Designed for optimal accuracy, the tracking system provides excellent momentum resolution, from 0.5% at low momentum to 1.0% at 200 GeV/c.

3.2.1.1 The Vertex Locator - VELO

For data analysis, it is essential to precisely know the position of the interaction point, known as the primary vertex (PV), where colliding protons interact, as well as to identify secondary vertices (SV), which are the decay points of hadrons such as B and D mesons. These interactions occur within the region enclosed by the VELO. The distance between primary and secondary vertices is crucial for studying heavy hadrons, and the VELO provides information on particle coordinates, enabling the reconstruction and localization of the secondary vertex [38].

This sub-detector consists of 42 modules, with 21 on each side of the semi-circular structure surrounding the beam. These modules are made of silicon strips sensors grouped in two sectors: one for radial coordinates (r-sensor) and another for azimuthal coordinates (ϕ -sensor). The z-coordinate is determined from the position of each module along the experiment. This setup allows for the three-dimensional reconstruction of trajectories and vertices. This system provides spatial resolutions of 10 μm and 40 μm for ϕ and z coordinates, respectively, at the primary vertex, and 300 μm and 150 μm for ϕ and z coordinates at the secondary vertex. Figure 7 shows the geometry of the VELO sensors.

The accuracy of the reconstructed vertex position decreases as the distance from the initial measurement point to the interaction region increases. Therefore, the detector is positioned as close as possible to the collision point, with the sensitive area of the sensors starting just 8 mm from the beam axis. To protect the detector, the VELO is equipped with a retractable system, allowing each half to remain at a distance of 3 cm from the operating position during beam injection and acceleration - named VELO open -, and at 8 mm away - named VELO closed - when the beam is collimated and stable, as shown in Figure 8.

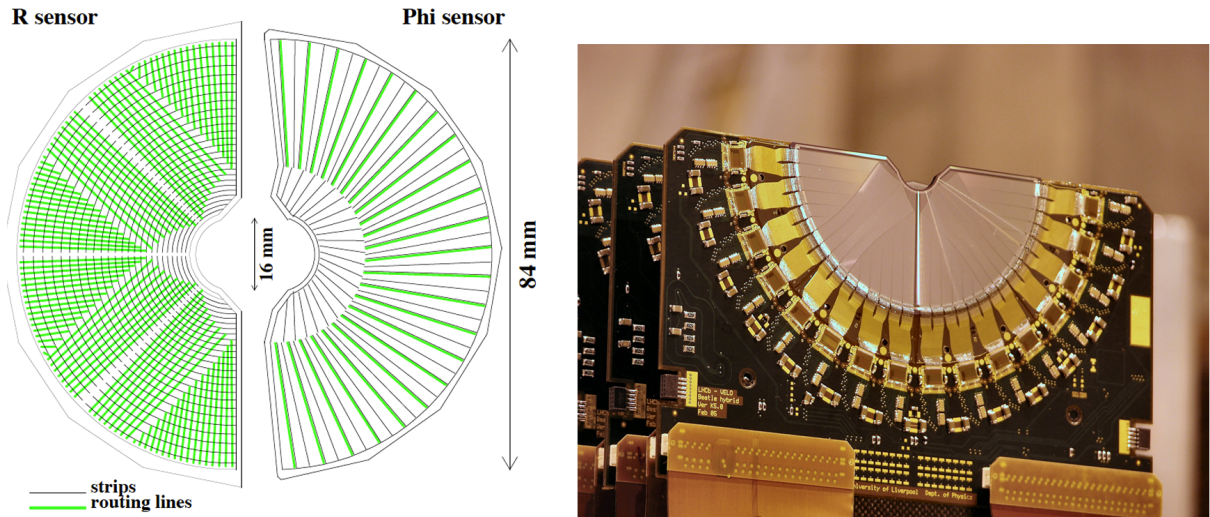


Figura 7 – Schematic illustration of the VELO r and ϕ strips (left) alongside an image of the VELO sensors.

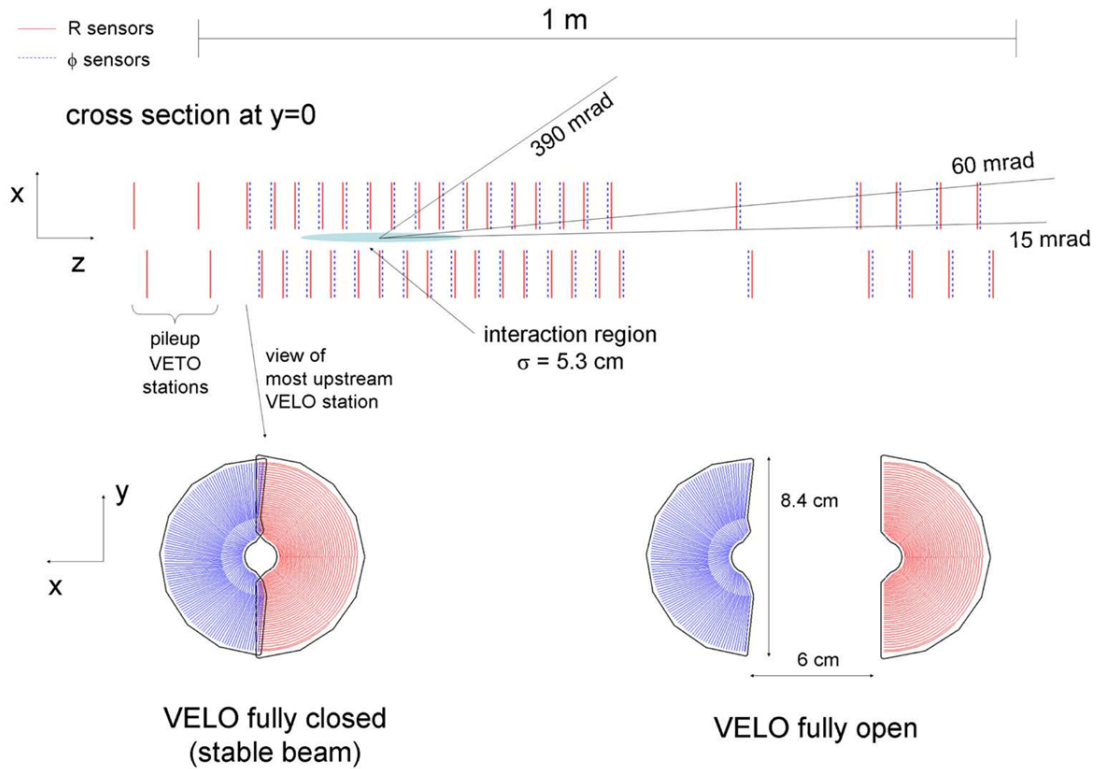


Figura 8 – Schematic illustration of the VELO r and ϕ strips (left) alongside an image of the VELO sensors.

3.2.1.2 Tracking Stations

Together with the VELO, the TT and T1, T2, T3 tracking stations form the particle tracking system. These stations are divided into Inner (IT) and Outer (OT) regions [39], as explained below.

- Tracker Turicensis (TT)

The primary purpose of the TT is to provide information on the trajectories of low-momentum particles. It fully covers the angular acceptance of LHCb and has dimensions of 150 cm in width and 130 cm in height. Like the VELO, this detector also uses silicon strips, arranged in four layers, and is located between the RICH1 detector and the magnet. These layers are organized in an “x-u-v-x” configuration, as shown in Figure 9, with vertical strips in the “x” layers and strips rotated by -5° and $+5^\circ$ in the “u” and “v” layers, respectively. This configuration enhances transverse momentum resolution. Each silicon strip has a spatial resolution of approximately $200 \mu\text{m}$.

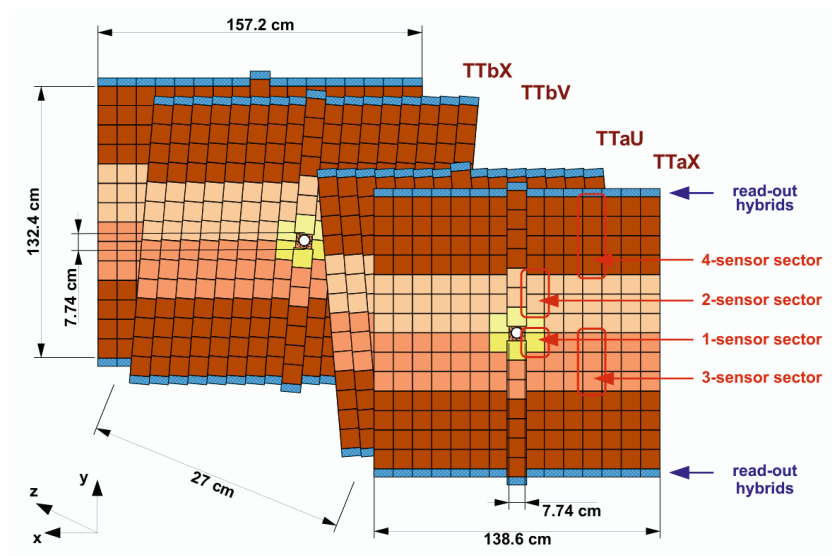


Figura 9 – Layout of the TT, with the LHC beam pipe passing through an opening in the center of the detection layers. The four detection layers are labeled TTaX, TTaU, TTbV, and TTbX. Different types of readout sectors are indicated by varying shading: the sectors closest to the beam pipe consist of a single silicon sensor, while other sectors are made up of two, three, or four silicon sensors connected in series [5].

- Inner Tracker (IT) and Outer Tracker (OT)

The design of the IT detector is similar to that of the TT, also utilizing silicon strips with an “x-u-v-x” layer arrangement. The IT covers the inner regions of the T1, T2, and T3 stations, each of which contains four boxes surrounding the particle beam, with each box containing seven modules. The boxes are arranged in a cross shape, with each module equipped with one sensor if located at the top or bottom, or two sensors if positioned on the sides. Like the TT, this system also has a spatial resolution of approximately $200 \mu\text{m}$ [40].

The OT covers the outer regions of the tracking stations. It is a straw-tube gas detector that uses the drift-time to track charged particles and measure their momentum across a wide coverage area. When a charged particle passes through the gas-filled environment, consisting of a mixture of Argon (70%) and CO_2 (30%), the gas atoms become ionized and the resulting charges are collected by an anode wire at the center of each tube. Like the previous detectors, the OT also consists of four layers aligned in the “x-v-u-x” configuration. The drift time is approximately 50 ns, due to the tube diameter of 4.9 mm and the specific gas mixture [41]. An illustration of these detectors is shown in Figure 10.

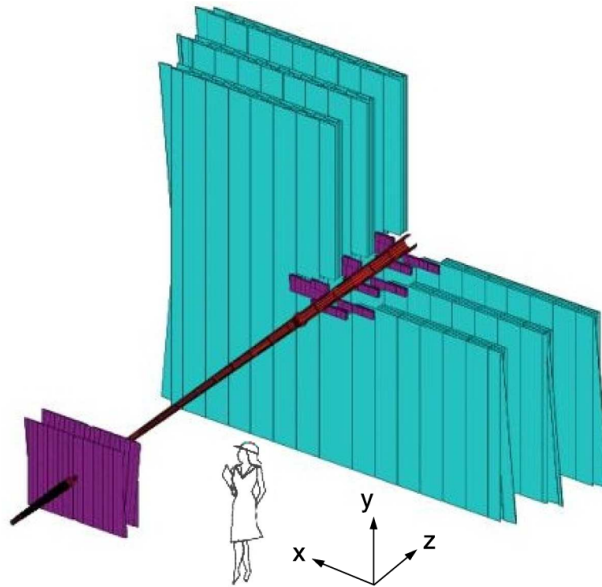


Figura 10 – Arrangement of OT straw-tube modules in layers and stations [6].

3.2.1.3 The Magnet

A dipole magnet is responsible for bending the trajectories of charged particles by generating a vertical dipole magnetic field in the “y” direction, providing an integrated field of 4 Tm over a length of 10 m [42]. It is located near the first tracking station, TT, and is composed of saddle-shaped coils. This magnetic field generates a perpendicular force that depends on the particle’s momentum, allowing the momentum to be measured based on the deflection caused by the dominant component of the field in its direction of action.

The magnet’s polarity is periodically reversed, enabling the field direction to point either upward or downward. These configurations are referred to as MagUp and MagDown, respectively. This polarity reversal is essential for controlling systematic effects related to charge asymmetries within the detector.

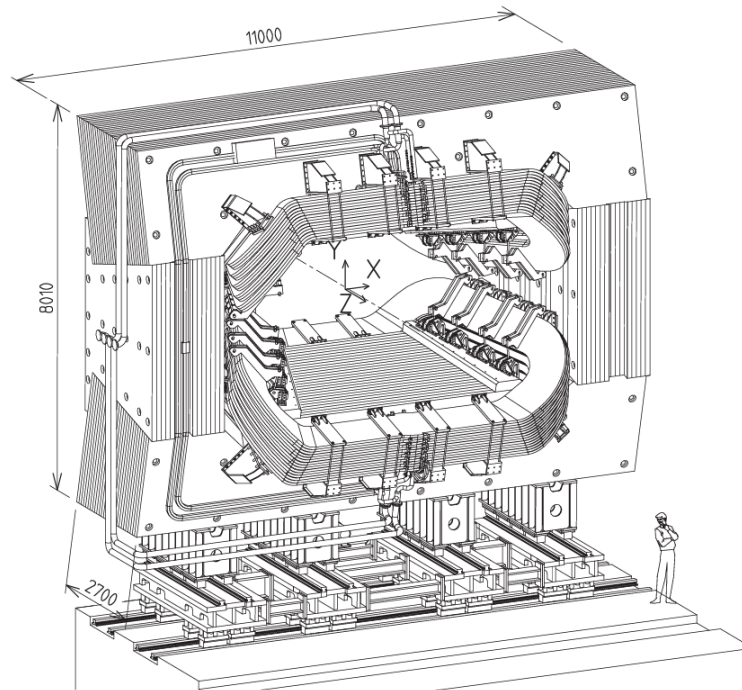


Figura 11 – Perspective view of the LHCb dipole magnet with its current and water connections (units in mm). The interaction point lies behind the magnet [6].

3.2.2 The particle identification system

Particle Identification (PID) is crucial for studying the weak decays of B and D mesons, as it enables the accurate reconstruction of heavy-flavor decay products. A precise PID system is also essential for distinguishing between decays with similar topologies, reducing background from random track combinations, and identifying hadronic decays that involve one or more muons in the final state. The LHCb PID system comprises two

ring-imaging Cherenkov detectors (RICH1 and RICH2), an electromagnetic calorimeter (ECAL), a hadronic calorimeter (HCAL), and a dedicated muon detection system.

3.2.2.1 Ring-Imaging Cherenkov System (RICH)

For the study of heavy hadron decays, it is crucial to identify the particles in the final state. To achieve this, the collaboration employs RICH detectors, which are responsible for particle identification, distinguishing between kaons, pions, and protons. The RICH detector operates based on the Cherenkov radiation phenomenon. By combining the particle's speed with the momentum information provided by the tracking system, it is possible to determine its mass. The cone formed by the photons emitted as the particle passes through the medium has an angle θ relative to the trajectory, such that:

$$\cos\theta_c = \frac{1}{vn}, \quad (3.2)$$

where n is the refractive index of the medium, θ_c is the Cherenkov angle, and v is the particle's velocity. Two types of RICH detectors are used depending on the particle momenta. Larger angles correspond to low-momentum particles, while high-momentum particles are associated with smaller angles.

The first detector, RICH1, positioned upstream, is designed for low-momentum charged particle identification in the range of approximately 1–60 GeV/c, using C₄F₁₀ as radiators. RICH1 has a wide angular acceptance, fully covering the LHCb range, with a horizontal acceptance of ± 300 mrad and a vertical acceptance of ± 250 mrad. A schematic, 3D model, and photo of the RICH1 detector are shown in Figure 13.

The second detector, RICH 2, positioned downstream between the final tracking station (T3) and the first muon station (M1), is designed for high-momentum particle identification, covering a range from approximately 15 GeV/c up to and beyond 100 GeV/c. It achieves this using a CF₄ radiator (see Figure 12). The detector's acceptance spans a horizontal range of ± 15 mrad to ± 120 mrad and a vertical range of ± 15 mrad to ± 100 mrad, effectively covering the region where high-momentum particles are detected. Two schematic layouts of RICH2 are illustrated in Figure 14.

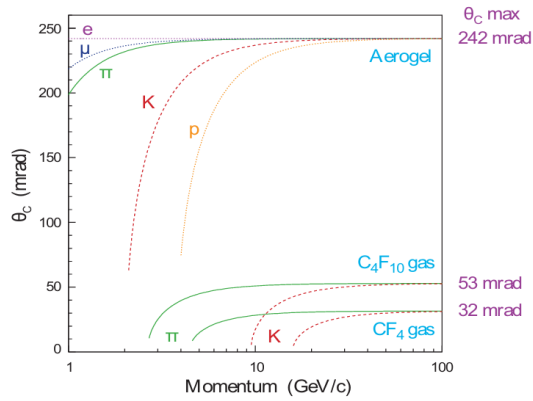


Figura 12 – Cherenkov angle versus particle momentum for the RICH radiators [6].

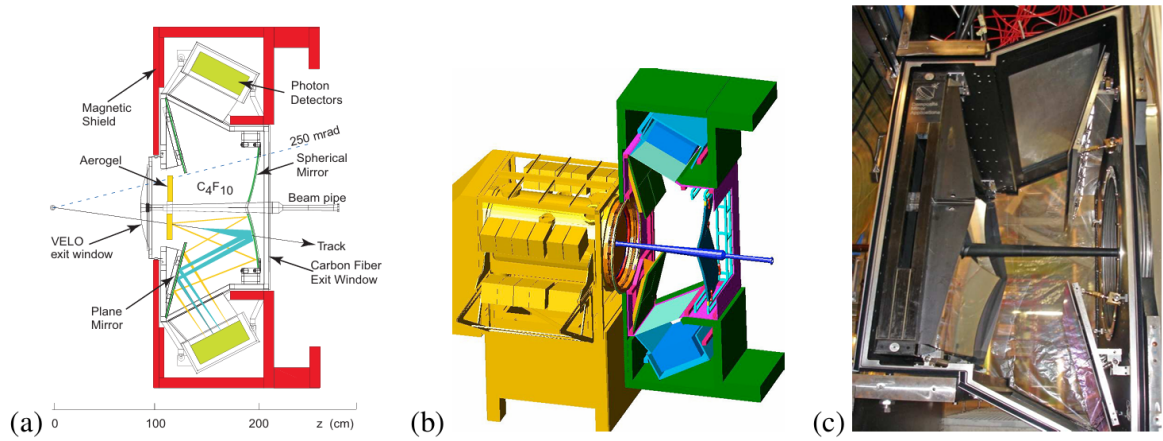


Figura 13 – (a) Side view schematic layout of the RICH1 detector. (b) Cut-away 3D model of the RICH1 detector, shown attached by its gas-tight seal to the VELO tank. (c) Photo of the RICH1 gas enclosure containing the flat and spherical mirrors [6].

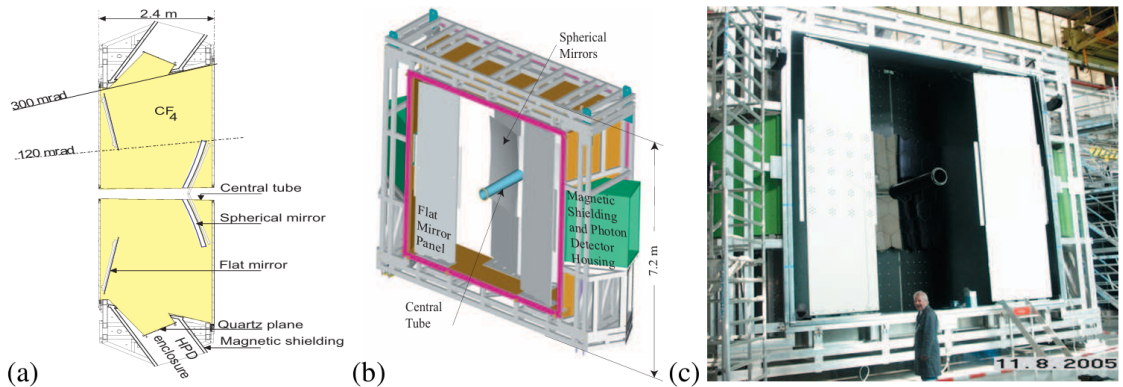


Figura 14 – (a) Top view schematic of the RICH2 detector. (b) A schematic layout of the RICH2 detector. (c) A photograph of RICH2 with the entrance window removed [6].

3.2.2.2 Calorimeter System

The calorimeter system in LHCb consists of several sub-detectors: the electromagnetic calorimeter (ECAL), the hadronic calorimeter (HCAL), the Scintillator Pad Detector (SPD), and the PreShower (PS) detector. This system primarily assists in identifying particles such as electrons, photons, and hadrons by measuring their energies and positions [43], and it also contributes to the trigger system.

The system follows a classic setup, with the ECAL placed in front of the HCAL. The main challenge is accurately identifying electrons among the particles, which is crucial for enriching b events in the sample. To this end, the Level 0 electron trigger is designed to reject 99% of inelastic pp interactions while enhancing b events by a factor of at least 15, achieved by selecting electrons with high transverse energy (E_T). A section about the LHCb trigger will be presented soon.

Each calorimeter shares a fundamental design feature: alternating layers of absorbers and scintillators. The absorbers, composed of dense materials of lead (in ECAL) and iron (in HCAL), induce particle showers by breaking down the incident particle into lighter particles with lower energies. The scintillators, made of materials that emit photons when charged particles pass through, detect part of this energy. The emitted light are guided to photomultiplier tubes (PMTs) via wavelength-shifting fibers, where they are converted into electrons, producing a measurable electrical signal.

- **ECAL:** The electromagnetic calorimeter measures the energy of electrons and photons². To separate electrons from the high background of charged pions, the ECAL is longitudinally segmented and includes a preshower detector (PS) positioned in front of the main ECAL section. This structure aids in refining electron selection by detecting early signals in the development of the particle shower. The thickness of the lead used in the ECAL, set at 25 radiation lengths, is chosen to balance trigger performance and energy resolution. The ECAL achieves an energy resolution of $\sigma_E/E = 10\%\sqrt{E} \oplus 1\%$.
- **HCAL:** The hadronic calorimeter is used to measure the energies of hadrons such as protons, neutrons, pions, and kaons. Due to the larger size of hadronic showers, the HCAL has a lower containment requirement than the ECAL, with a thickness of 5.6 interaction lengths. It consists of 16 mm iron plates interleaved with 4 mm scintillators, aligned parallel to the particle beam, providing an energy resolution of $\sigma_E/E = 80\%\sqrt{E} \oplus 10\%$. The HCAL modules emit about 30 times less light than those in the ECAL, so the phototubes in HCAL operate at a higher gain.

² Photon identification is crucial for the reconstruction of particles such as π^0 .

- **SPD and PS:** The SPD (Scintillator Pad Detector) and PS (PreShower) help filter out background particles. The SPD, positioned in front of the PS, is essential for discriminating between showers from electrons and photons and for rejecting high- E_T electrons. The PS further assists in rejecting charged pion background, enhancing electron candidate selection.

To account for the varying density of particle hits across the calorimeter surface, the ECAL and SPD/PS are divided into three sections with different lateral segmentations, while the HCAL is divided into two larger zones, each with larger cell sizes. The segmentation is designed to match the distribution of hit density, as shown in Figure 15.

Overall, all calorimeters operate on the principle of capturing scintillation light via wavelength-shifting fibers and channeling it to PMTs. In the SPD/PS, individual fibers connect to multianode PMTs (MAPMTs) for each cell, while in the ECAL and HCAL, fiber bundles connect to single phototubes. The gain of each phototube is adjusted according to its distance from the beamline to maintain a consistent E_T scale across the calorimeters, ensuring uniform response throughout the detector.

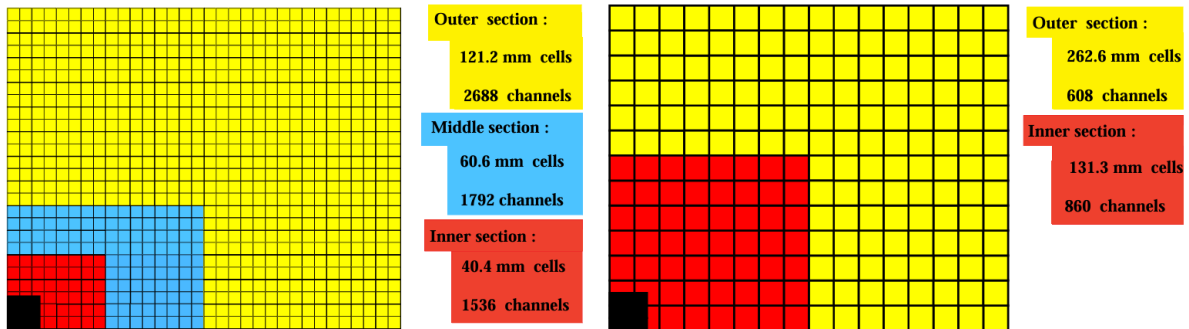


Figure 15 – Lateral segmentation of the SPD/PS and ECAL (left) and the HCAL (right). One-quarter of the detector’s front face is shown. In the left figure, the cell dimensions are given for the ECAL [6].

3.2.2.3 Muon System

A crucial particle for identification at the LHCb detector is the muon - a long-lived, charged quasi-stable particle frequently produced in decays of b and c-hadrons. As an elementary charged lepton, it is heavier than the electron and can travel through the entire detector, generating only minimal ionization signals in each subdetector with a low probability of being absorbed. Muons play a vital role in numerous decays that are either CP-sensitive or rare, holding the potential to provide insights into new physics. Additionally, they are employed to determine the flavor of neutral B and D mesons in CP asymmetry and oscillation studies.

The muon system consists of five rectangular stations (M1-M5) arranged along the beam axis, covering an area of 435 m^2 , as illustrated in Figure 16. The system includes a total of 1380 chambers, with an angular acceptance ranging from 20 (16) mrad to 306 (258) mrad in the bending (non-bending) plane, providing approximately 20% acceptance for muons from inclusive semileptonic b decays.

To optimize muon identification, the area is divided into four regions (R1 to R4), with dimensions that increase progressively to manage the particle flux and occupancy uniformly across the detector. The layout of each station follows a projective geometry, meaning their transverse dimensions and pad resolution scale with their distance from the interaction point, as shown in Figure 17.

Station M1 is located in front of the calorimeter and uses Gas Electron Multiplier (GEM) detectors to handle high occupancy rates. The remaining stations (M2 to M5) are placed downstream of the calorimeters, separated by 80 cm thick iron absorbers. These absorbers are designed to block hadrons and allow only high-penetration particles, as muons, to pass, helping to reduce hadronic background [44]. Muons must have a minimum momentum of around $6 \text{ GeV}/c$ to pass through all five stations, as the combined absorber thickness is roughly 20 interaction lengths.

The detectors in M2 to M5 utilize Multi Wire Proportional Chambers (MWPCs) with a gas mixture of Ar (40%), CO_2 (55%), and CF_4 (5%). As muons pass through, they ionize the gas, generating a signal by driving ions toward the cathode and electrons toward the anode. GEM detectors, used in M1, consist of three GEM plates placed between cathode and anode planes, filled with a gas mixture of Ar (45%), CO_2 (15%), and CF_4 (40%). This setup enables the system to track muon paths accurately, as depicted in Figure 18.

The muon trigger relies on independent muon track reconstruction and transverse momentum (p_T) estimation. It requires aligned hits across all five stations, with stations M1-M3 providing high spatial resolution along the x -axis (bending plane). This configuration allows for precise track direction determination and p_T calculation for candidate muons, achieving a 20% p_T resolution. Stations M4 and M5 primarily serve to confirm the identification of penetrating particles.

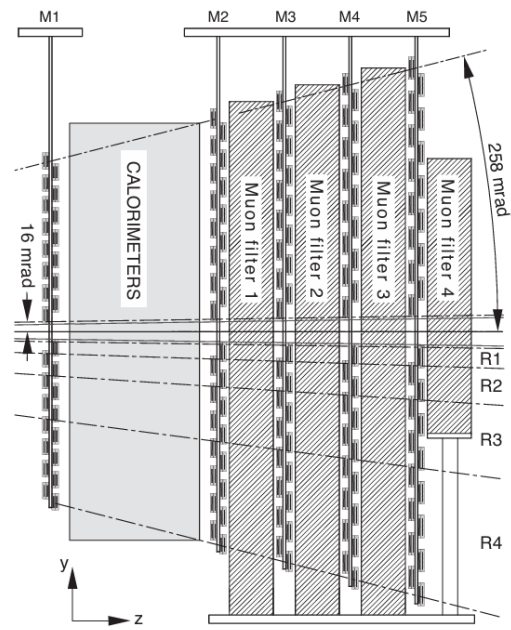


Figura 16 – Side view of the muon system [6].

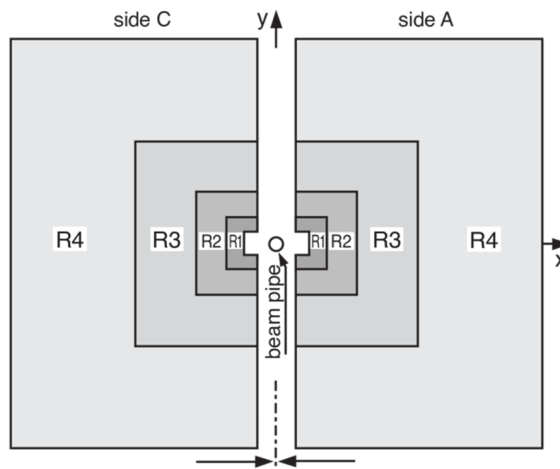


Figura 17 – Station layout with the four regions R1-R4 [6].

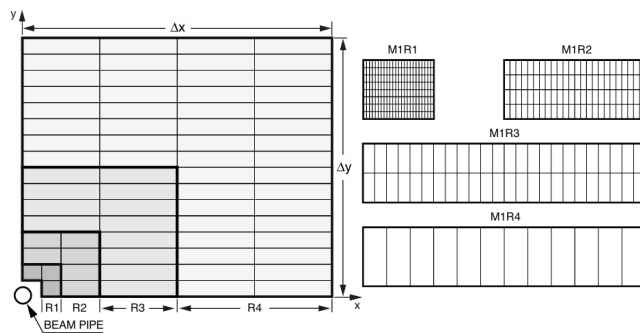


Figura 18 – 4 muon station regions [6].

3.2.3 The trigger system

Many people unfamiliar with the subject might assume that all data generated from proton collisions is stored for analysis. However, the volume of information far exceeds both storage capacity and the limited readout rate from the subdetector’s front-end electronics. Consequently, only a fraction of the events can be recorded for subsequent analysis.

The trigger system’s work comprises a collection of algorithms designed to filter events that may be of interest for analysis. Its function is to reduce the data rate to a manageable level by retaining only those events or parts of events considered significant. Within the LHC framework, each classification algorithm is typically called a “line,” making the trigger system a compilation of various trigger lines.

The LHCb trigger system used during Run 1 operated with a simplified, two-stage approach that mirrored offline reconstruction. In the first stage, only charged particles with transverse momentum (p_T) above 1 GeV/c and displaced from the primary vertex (PV) were selected. For muons, a lower p_T threshold was set, and they did not require displacement. In the second stage, most charged particles with p_T over 300 MeV/c became available to classify events more fully. Additionally, particle identification information and neutral particles, such as photons or π^0 mesons, could be accessed by specific algorithms as needed.

While this trigger system supported the majority of the LHCb physics goals, it posed some limitations. The absence of low-momentum charged particles in the first stage and incomplete particle identification in the second stage restricted its effectiveness, particularly in studies involving c-hadrons. Furthermore, differences in resolution between the online and offline reconstructions made it challenging to determine absolute trigger efficiencies accurately.

The LHCb trigger system was restructured for Run 2, to allow for complete offline event reconstruction within the trigger itself. The entire data processing framework was overhauled to facilitate unified real-time detector alignment and calibration, as well as direct real-time analysis using information from the trigger system. This change significantly enhanced the efficiency of selecting charm- and strange-hadron decays and also achieved the same level of alignment and calibration quality in the trigger as was reached offline in Run 1, allowing final signal selection to occur at the trigger stage.

The LHCb trigger is designed to facilitate data-taking with minimal dead time at the full LHC bunch crossing rate of 40 MHz. The maximum rate at which all LHCb subdetectors can be read out is limited by the bandwidth³ and frequency of the front-end electronics, corresponding to around 1.1 MHz when operating at the intended rate of visible interactions per bunch crossing, $\mu = 0.4$, in LHCb. During Run 2, LHCb operated

³ The amount of data that can be transmitted over a network or communication channel per unit time.

at $\mu \approx 1.62$ to collect a higher integrated luminosity, which effectively limited the readout rate to about 1 MHz. Figure 19 presents a diagram showing the trigger data flow in Run 2. The trigger system is organized into two stages: the hardware trigger (L0) and the high-level trigger (HLT).

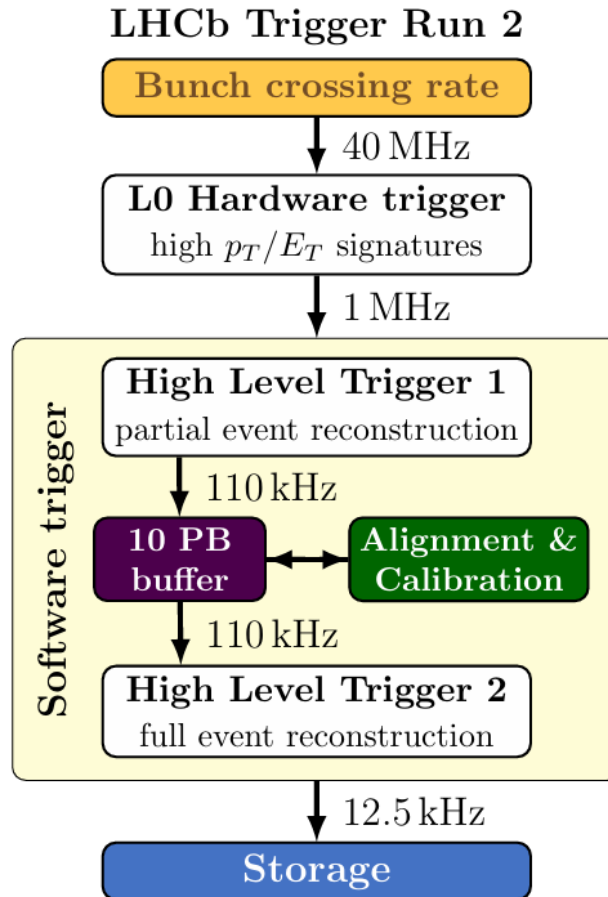


Figura 19 – Overview of the LHCb trigger system. Out of the LHC bunch crossing rate of 40 MHz, the LHCb subdetector’s maximum read-out rate was about 1 MHz, constrained by the bandwidth and frequency of the front-end electronics. [7].

3.2.3.1 The L0 trigger

The L0 trigger uses information from both the calorimeter and muon systems to select events. Events are chosen if they include a muon with high p_T or a hadron, photon, or electron with substantial transverse energy in the calorimeters. The energies deposited in the SPD, PS, ECAL, and HCAL detectors are used by the L0-calorimeter system for event selection. Each calorimeter component is segmented into cells of varying sizes across the plane perpendicular to the beam axis, while data from SPD and PS detectors helps distinguish between hadron, photon, and electron candidates.

The L0-muon trigger searches for straight-line tracks in the five muon stations, with each station divided into logical pads in the x - y plane, where pad size increases with

distance from the beamline. The track direction is used to estimate the p_T of a muon candidate, assuming the particle originated at the interaction point and was deflected by the magnetic field. The p_T resolution of the L0-muon trigger averages around 25% over the relevant p_T range. The trigger decision is based on the two muon candidates with the highest p_T : either the highest p_T must exceed the L0Muon threshold, or the product of the two highest p_T values must exceed the L0DiMuon threshold.

3.2.3.2 The High-Level Trigger

The high-level trigger (HLT) operates entirely through software and is divided into two stages: HLT1 and HLT2. Events selected by the L0 trigger are transferred to the Event Filter Farms (EFF), a network of computers where the software-based trigger steps are executed. The first stage of the software trigger, HLT1, reconstructs the trajectories of charged particles passing through the entire LHCb tracking system, referred to as long tracks, with p_T greater than 500 MeV/c. Additionally, a precise reconstruction of the primary vertex (PV) is carried out.

In the second stage, HLT2, the full event reconstruction is performed, which consists of three main phases: track reconstruction of charged particles, reconstruction of neutral particles, and particle identification (PID). HLT2 track reconstruction leverages complete information from the tracking sub-detectors, performing additional pattern recognition steps not feasible in HLT1 due to strict time limitations. This enables the identification of high-quality long and downstream tracks with the most precise momentum estimation achievable. Similarly, the most accurate neutral cluster reconstruction algorithms are executed within HLT2.

In addition to the muon identification available in HLT1, HLT2 utilizes the full particle identification capabilities of the RICH detectors and calorimeter system. All reconstruction algorithms have been optimized for Run 2 to better harness the processing power of modern CPUs. Combined with the algorithmic improvements described in subsequent sections, this optimization results in a twofold increase in execution speed while achieving the same or, in several cases, superior physics performance compared to the offline reconstruction in Run 1.

Approximately 40% of the trigger output rate is allocated to inclusive topological trigger (discussed in the Chapter 5) lines, another 40% is devoted to exclusive c -hadron trigger lines, with the remaining portion divided among dimuon lines, trigger lines for electroweak physics, searches for exotic particles, and other exclusive lines tailored for specific analyses. In total, there are around 20 HLT1 and 500 HLT2 trigger lines.

Events that pass the trigger selections are sorted into categories based on whether the signal candidate or another part of the event activated a specific trigger line. The categories include Triggered on Signal (TOS), Triggered Independent of Signal (TIS), and

Triggered on Both.

In TOS events, the signal candidate’s tracks directly trigger the line, providing higher signal efficiency, though these samples may have charge biases that are challenging to simulate accurately. For TIS, other event components activate the trigger, capturing the signal candidate as a byproduct. While more abundant, TIS events tend to include additional background. The “Triggered on Both” category applies when both the signal candidate and other event elements contribute to the trigger.

3.2.3.3 The LHCb tracks

In the track reconstruction process at LHCb, data from multiple detectors, including the VELO, TT, IT, and OT, are combined to reconstruct particle trajectories from the interaction point near the VELO through to the calorimeters. This computational procedure starts by clustering hit points in these detectors to form segments. Segments containing VELO hits are reconstructed under the assumption that their origin lies along the z -axis, where the pp collision point is centered within the VELO.

The reconstruction algorithm aims to identify all tracks within an event that leave sufficient detector hits, not only those resulting from b -hadron decays. It employs both direct and reverse search techniques: the direct search algorithm identifies potential trajectories starting from segments detected in the TT, while the reverse search algorithm extrapolates segments identified in the T stations back to the pp collision point to complete valid track formation.

Depending on their paths inside the detector, the following categories of tracks are defined, as shown in Figure 20:

- Longtracks: traverse the complete tracking system, from the VELO to the T stations, offering the highest momentum resolution. This accuracy makes them the most essential track type for reconstructing b -hadron decays.
- Upstreamtracks: tracks that pass through only the VELO and TT stations are typically lower-momentum and are bent out of the detector acceptance by the magnetic field. Despite their limited momentum resolution, these tracks are useful for analyzing backgrounds in the RICH particle identification algorithm. They can also contribute to b -hadron decay reconstruction and flavor tagging when needed.
- Downstream tracks: tracks that cross only the TT and T stations are typically the decay products of long-lived hadrons, like K_S^0 and Λ , which decay outside the VELO acceptance.
- VELO tracks: measured in the VELO, they are useful for the primary vertex reconstruction.

- T tracks: cross only the T stations are generally produced in secondary interactions and are valuable for global pattern recognition in RICH2.

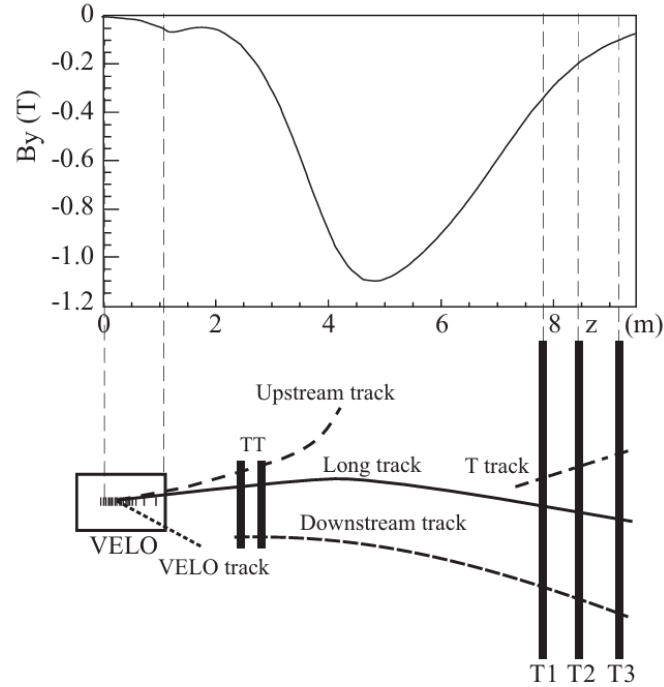


Figure 20 – A schematic illustration of the various track types: long, upstream, downstream, VELO and T tracks. For reference, the main B-field component is plotted above as a function of the z coordinate [6].

3.3 The LHCb Upgrade I

This section outlines the main modifications introduced in LHCb Upgrade I. Technical contributions made as part of this work will be discussed in Chapter 4.

Initially designed for CP violation studies and precision measurements in heavy-flavor physics, the LHCb experiment has proven effective across a wide range of fields, including electroweak physics, heavy-ion studies, and fixed-target experiments. To further expand its physics program and take advantage of the fivefold increase in LHC luminosity in Run 3, the LHCb detector underwent significant hardware and software upgrades, transforming it into a general-purpose experiment focused on the forward region. Operated successfully from 2010 to 2018 during Run 1 (2010–2012) and Run 2 (2015–2018), LHCb collected an extensive dataset comprising 9 fb^{-1} of proton-proton data [8].

The design of the LHCb system during Runs 1 and 2 imposed constraints on the ability to significantly increase statistical data, particularly for fully hadronic final state decays. The maximum allowed output rate of the initial trigger level, L0, represents the main limitation. The inclusive selection criteria employed in the L0 trigger, primarily relying on particle transverse momentum, led to a notable reduction in efficiency as luminosity increased. This was especially pronounced for the most prevalent processes involving hadrons in the final state, ultimately resulting in the saturation of the event yield, as illustrated in the left panel of Figure 21.

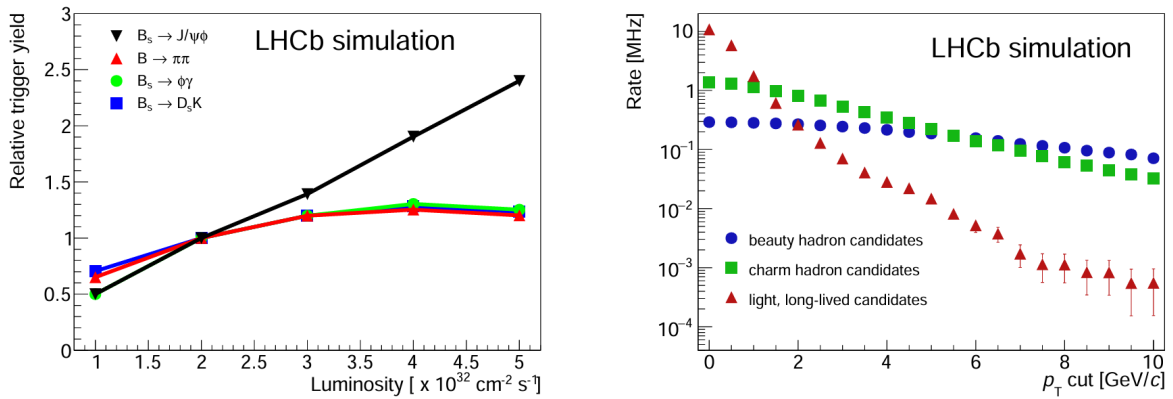


Figure 21 – Left: Trigger yields normalized to $\mathcal{L} = 2 \times 10^{32} \text{ cm}^{-2} \text{ s}^{-1}$ as a function of instantaneous luminosity. Right: Reconstructed decay rates within the LHCb acceptance as a function of the p_T cut for decaying particles with $\tau > 0.2 \text{ ps}$ [8].

Key upgrades include a new tracking system with a silicon-pixel vertex detector, a silicon-strip tracker positioned upstream of the dipole magnet, and a scintillating-fibre tracker downstream of the magnet. The photon detection system of the Cherenkov detectors has been enhanced with multianode photomultiplier tubes, while the calorimeter and muon detector electronics have been redesigned and updated. Additionally, an all-

software trigger utilizing GPUs and a dedicated computing farm has been implemented, along with a completely renewed online system. To align with this new trigger approach, the software and computing framework have been entirely restructured and reengineered.

The particle tracking system consists of the vertex locator (VELO), an array of pixel silicon detectors surrounding the interaction region; the silicon-strip upstream tracker (UT) positioned before the large-aperture dipole magnet; and three scintillating fibre tracker (SciFi Tracker) stations located downstream of the magnet. The upgraded VELO uses hybrid silicon pixel detectors, and the SciFi Tracker replaces the former straw-tube Outer Tracker and silicon-strip Inner Tracker in the downstream tracking stations.

Particle identification (PID) is handled by two ring-imaging Cherenkov detectors using C_4F_{10} and CF_4 gases, an electromagnetic calorimeter (ECAL), a hadronic calorimeter (HCAL), and four muon chamber stations (M2–5) interspersed with iron shielding. The previous Scintillating Pad Detector and Pre-Shower, as well as the most upstream muon station, have been removed, as their roles have reduced with the new full software trigger replacing the former hardware L0. Figure 22 shows the layout of the upgraded detector.

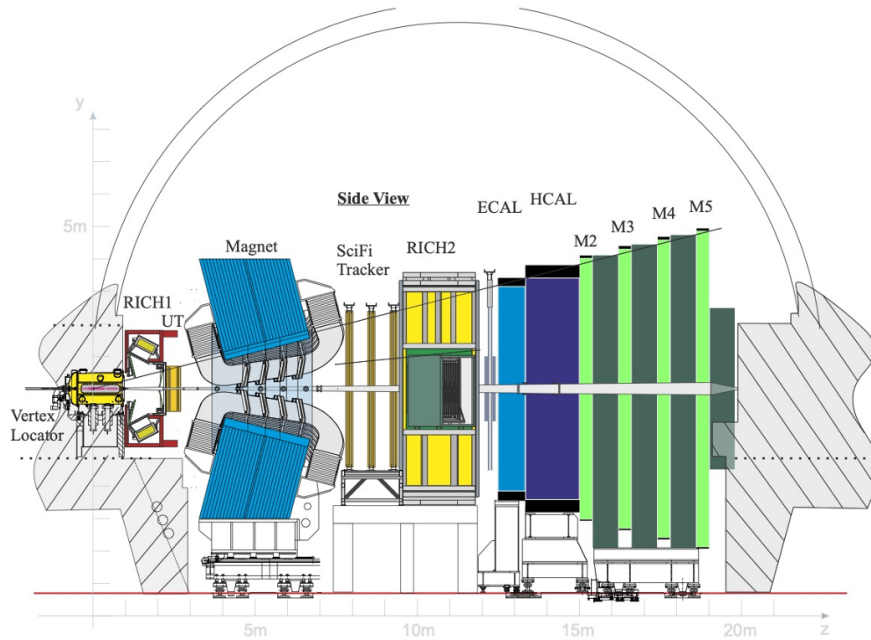


Figura 22 – Layout of the upgraded LHCb detector.

The VELO has undergone an extensive upgrade, now incorporating hybrid silicon pixel detectors arranged in modules and cooled by a silicon microchannel cooling system. Only the primary vacuum vessel and motion mechanisms from the original VELO structures used in Run 1 and Run 2 have been retained. The RF boxes, which connect the detector to the LHC beams, have been completely redesigned to reduce material usage and decrease the VELO's inner radius along the beamline. Additionally, a new storage cell has been installed upstream of the VELO within the beam vacuum to support further fixed-target

physics studies. This upgraded VELO is anticipated to significantly enhance performance while also enduring a radiation dose approximately ten times higher than before.

The TT has been replaced by the Upstream Tracker (UT), which consists of four planes of silicon detectors with a central circular gap allowing space for the beam pipe. The UT is a crucial part of the upgraded tracking system, providing essential data for the first processing algorithm in the software trigger. It is designed to maintain a single-hit efficiency of 99% and to withstand radiation damage, ensuring reliable performance through the end of Run 4.

The T1-T3 tracking stations were upgraded to new stations utilizing scintillating fiber technology with SiPM readout. These stations handle the tracking of charged particles and measure momentum, achieving performance levels for b - and c -hadrons comparable to those in Run 1 and Run 2, despite operating in an environment with increased particle density.

The photon detection system in both RICH1 and RICH2 previously relied on hybrid photon detectors (HPDs) with embedded front-end electronics, restricted to a 1 MHz output rate, which necessitated replacement for the upgrade. The updated system now utilizes multi-anode photomultiplier tubes (MaPMTs) paired with new front-end electronics capable of a 40 MHz readout rate. Additionally, RICH1 underwent significant optical redesigns to manage the anticipated increase in hit occupancy within the detector's central region. The upgraded calorimeter system no longer includes the Scintillating Pad Detector (SPD) and PreShower detector (PS), while the M1 station has been removed from the upgraded muon system. The ECAL, HCAL, and the remaining muon stations underwent no major structural changes, although their front-end and readout electronics were redesigned to support a 40 MHz readout frequency.

3.3.1 The trigger and software update

Increasing the quantity of acquired data is, therefore, essential for advancing the studies conducted at LHCb. Such an increase involves raising the beam luminosity, leading to more collisions and more events per unit time. However, any attempt to operate the current LHCb experiment at higher luminosity results in the saturation of the L0 trigger. This saturation is caused by limitations in the detector layout and data acquisition hardware, which impose a maximum rate for data accumulation from the experiment. During the Run 2, the average number of detectable proton-proton (pp) collisions per bunch-crossing is $\mu \approx 1.62$.

At the nominal instantaneous luminosity for pp collisions during Run 3, the LHCb experiment will generate data at a rate close to 4 TB/s. However, only a maximum of 10 GB/s can be permanently saved for physics analyses. To address this limitation, the

LHCb detector has been extensively upgraded to implement a trigger system that relies on software. The LHCb has also undergone a redesign of its trigger system. This system is intended to carry out real-time analysis, executing a complete reconstruction with offline-level quality by providing full detector raw data to the decision-making processes, while alignment and calibration are conducted in near real-time.

After the upgrade, the experiment will be able to take advantage of the new available luminosity, which will be 5 times greater than the Runs 1 and 2 together. It is expected that, in this way, the LHCb experiment will be capable of collecting 50 fb^{-1} of data over the course of Run 3. The expected number of detectable pp interactions per bunch-crossing after the upgrade is $\mu \approx 5$.

The new two-stage trigger system consists of an initial inclusive stage, HLT1, focused on charged particle reconstruction and reducing data volume by a factor of 20. This is followed by HLT2, which performs a full offline-quality reconstruction and selection of physics events. A 30 PB disk buffer sits between these stages to store data while real-time alignment and calibration occur.

HLT1's main objective is to lower the event rate to allow data buffering for alignment, calibration, and further processing in HLT2, while ensuring high efficiency across LHCb's physics goals. The HLT1 output rate, capped at 2 MHz for Run 3, is optimized based on HLT2's reconstruction throughput and the disk buffer's write speed, ensuring minimal selection of false tracks or random track combinations.

4 The SciFi Tracker and the ROB test system

Part of the work conducted during my PhD is related to the commissioning of the SciFi detector. Further details on this detector will be presented in this chapter. The test system for the front-end electronics housed in the SciFi readout boxes (ROB) will also be discussed.

4.1 A new tracker for the LHCb Experiment

The tracking detectors upstream and downstream of the LHCb dipole magnet enable precise momentum measurements of charged particles, ensuring accurate mass resolution for particles undergoing decay. The reconstructed particle trajectories are crucial inputs for photon-ring searches in the RICH detectors, which are used for particle identification. Momentum resolution for tracks is primarily limited by multiple scattering at momenta up to about 80 GeV/c [9], while detector resolution is the main constraint for tracks with higher momentum. This chapter focuses on the upgrades to the downstream tracking detectors, specifically the Scintillating Fiber Detector (SciFi), which is now the primary tracker in the LHCb spectrometer.

The SciFi detector, designed to measure charged-particle tracks with over 99% efficiency and spatial resolution better than $70\ \mu\text{m}$ (with $100\ \mu\text{m}$ sufficient for the required momentum resolution), plays a key role in track reconstruction by providing the hit data necessary to determine the momentum of charged particles. It also supplies positional information to the RICH system for particle identification.

The SciFi consists of three tracking stations positioned between the magnet and the RICH2 detector (see Figure 23), each with four detection layers arranged in a “XUVX” configuration. These layers are spaced approximately 20 cm apart and oriented at angles of 0° , $+5^\circ$, -5° , and 0° relative to the vertical axis. The stations are centered around the LHC beam pipe, with a circular opening in the center allowing the detection layers to approach as close as 20 mm to the beam pipe.

The $\pm 5^\circ$ layer orientation maximizes resolution in the plane of magnetic field deflection while reducing the number of hit combinations needed for pattern recognition, with a minor trade-off in vertical resolution. The entire detector covers an area of 5 meters in height and 6 meters in width within the X-Y plane. Altogether, the SciFi detector consists of 144 modules. Figure 24 illustrates the arrangement of these modules.

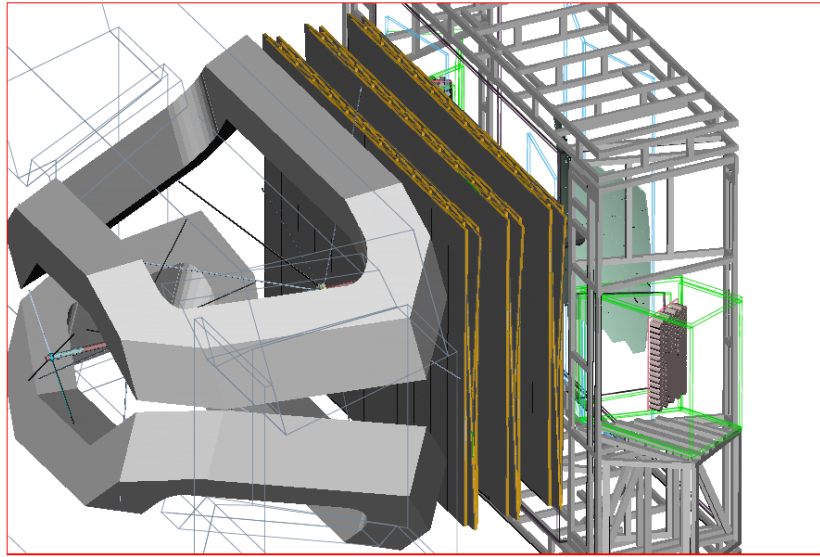


Figura 23 – The three stations of the scintillating fibre tracker shown between the dipole magnet on the left and RICH2 on the right [9].

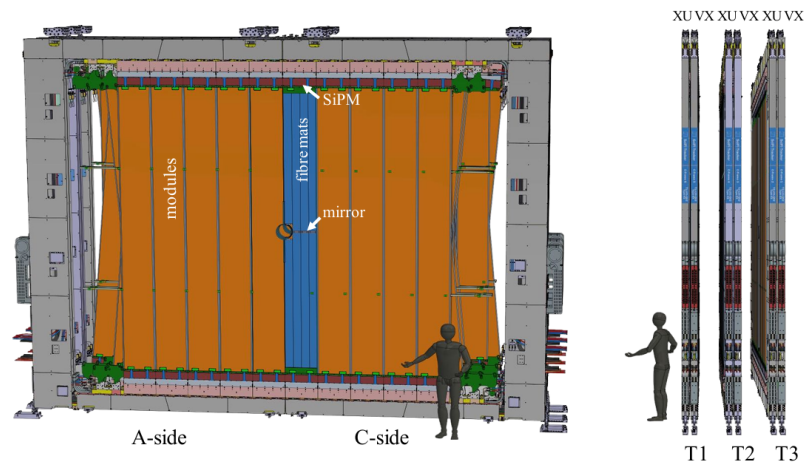


Figura 24 – 3D model of the SciFi [8].

4.1.1 Detector Performance

The main requirements for the upgraded tracking detector are outlined below:

- **Hit Detection Efficiency:** The detector should achieve a high hit detection efficiency, aiming for approximately 99%. Additionally, the rate of reconstructed noise clusters at any location in the detector should remain significantly lower than the signal rate at the same location, specifically less than 10% of the signal rate.
- **Spatial Resolution:** In the bending plane of the magnet, the spatial resolution for single hits should be no more than 100 μm . Higher precision is not necessary, as the

extrapolation of tracks from the VELO is mainly affected by multiple scattering in the upstream detectors.

- **Material Minimization:** The material in the detector's acceptance region should be minimized to reduce multiple scattering effects in the tracker. This ensures that scattering effects are less significant than those caused by upstream materials.
- **Read-Out Electronics:** The electronics should operate at a 40 MHz frequency, with a short recovery time for each read-out channel to minimize inefficiencies caused by dead time.
- **Operational Performance:** The detector must maintain the required performance levels for data collection at an integrated luminosity of up to 50 fb^{-1} .

4.1.2 Scintillating Fibres

Scintillating plastic fibers are used as the active elements in the SciFi Tracker project. Optical photons are generated through a multi-step process. Initially, ionization energy is deposited in the fiber's polymer core, where only a few eV of energy is needed to excite the polymer molecules. However, the base material alone has a low light yield and slow relaxation time. To enhance the scintillation efficiency, an organic fluorescent dye with a compatible excitation energy level is mixed into the polystyrene base, at around 1% by weight. This enables rapid (sub-nanosecond) energy transfer from the polymer to the dye through a non-radiative dipole-dipole interaction called Förster Transfer, after which the dye releases a photon as it returns to a lower energy state.

4.1.3 Silicon Photomultipliers (SiPM)

Silicon photomultipliers (SiPMs) are solid-state devices designed for photon detection, encompassing all necessary features for capturing photons in high-resolution scintillating fiber trackers. These specialized devices offer high photon detection efficiency across a wide wavelength spectrum, high reliability due to their straightforward mechanical design, and are packaged in dense multi-channel formats. Their cost-effectiveness enables their use in constructing large-area tracking detectors.

SiPMs must meet several demanding requirements, including resilience to neutron radiation and efficient operation with the relatively low light yield from long scintillating fibers. One of the crucial aspects of the SciFi project is the necessity to control the noise generated by the SiPMs, which directly impacts the detector's performance. To address this challenge, custom-designed SiPMs are employed to match the detector channel dimensions and packaging, and a low-temperature operation is implemented to significantly reduce

noise. The cooling of the SciFi Tracker is, therefore, a critical feature, as it ensures optimal SiPM performance and supports the overall efficiency and reliability of the detector.

The tracker’s primary performance metrics are hit detection efficiency and spatial resolution, which are largely influenced by the overall light yield of the detector and fiber module, given that mechanical parameters such as channel size and fiber diameter are predetermined. The SiPM noise has three main components: dark noise, pixel cross-talk, and after-pulsing. Dark noise, resulting from random avalanches in the silicon amplification region, produces signals equivalent to a single photon. The Dark Count Rate (DCR) — the measure of dark noise — significantly rises post-irradiation, which is the primary form of radiation damage observed at the levels required for LHCb. Each avalanche may trigger a neighboring pixel, a phenomenon known as pixel cross-talk. Both cross-talk and after-pulsing are highly dependent on the detector technology. After-pulsing contributes to the DCR by introducing after-pulses with enough amplitude to mimic a single-pixel signal, which can only occur after a substantial portion of the pixel recovery time (over 10 ns). Thanks to advancements in technology, after-pulsing has been considerably reduced and now accounts for only a small part of the overall noise.

4.1.4 The Read-out Box (ROB)

The Read-out Box is a compact device designed to read the SiPM signals of the SciFi detector module. Located at both ends of the module, the RoB interfaces with the scintillating fiber ribbons linked to the SiPM arrays and connects to the front-end electronics. The RoB handles 2048 input channels, divided into two independent Half RoBs. Each Half RoB houses one Master Board (MB), four Cluster Boards (CB), and four PACIFIC Boards (PB), with each PB accommodating 256 input channels.

The *low-Power Asic for the sCIntillating FIBres traCker* (PACIFIC) boards [45] is an application-specific integrated circuit (ASIC) with around a 64-channel, which is responsible for amplifying and digitizing the input signals. This ASIC includes 8-bit DACs (digital-to-analogical converter) for fine-tuning the SiPM high voltage and the analog threshold for the comparators. The Cluster Boards contain two Microsemi FPGAs, each handling 128 channels, and one slow control adapter (SCA) ASIC. The Master Board integrates key components such as four DataGBT ASICs for data transmission, one MasterGBT (Giga-Bit Transceiver) for control interface, an SCA ASIC for slow control, DC-DC power provided by FeastMPs, and one Housekeeping FPGA. Data is transmitted to the acquisition system via eight unidirectional data links and one bidirectional control link. The cooling system, known as the “Cold box” cools the 16 SiPM arrays to a temperature of -40°C . It employs dry gas, maintaining frost and dew points below -70°C at the inlet and -50°C at the exhaust. Additionally, for slow control, the RoB contains ten SCA ASICs equipped devices enabling voltage measurements.

The RoB design, shown schematically in Figure 25, exemplifies the integration of functionality and precision required to support the SciFi detector’s performance within the LHCb experiment.

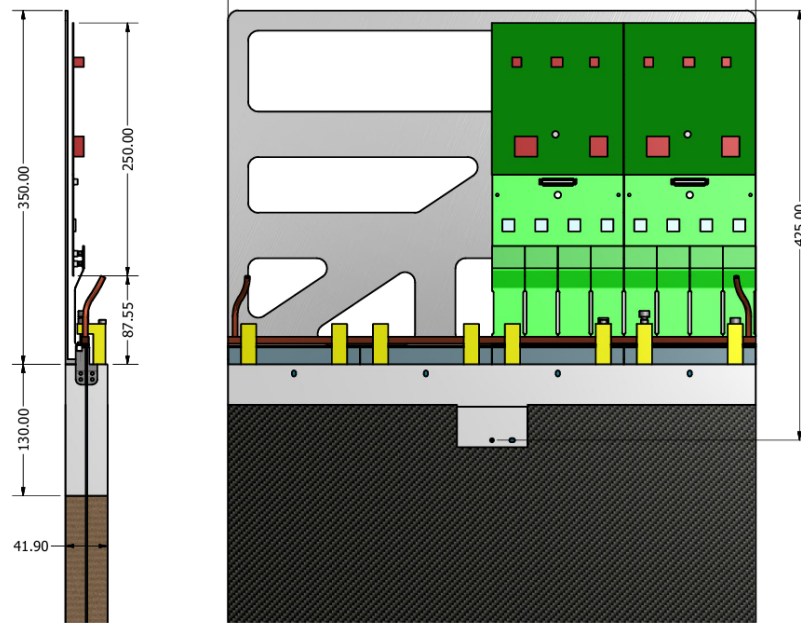


Figura 25 – Side and front views of the end of a scintillating fiber module, displaying the SiPM arrays, cooling pipe, flexible cables, and front-end electronics [8].

Access to the ROB is provided through two panels on its front face: one for the front-end electronics and another for the cold volume housing the SiPMs. The modular design of the electronic cards and SiPM super-arrays is intended to facilitate easy replacement with minimal adjustments. Connectors for electronics and power supplies will be routed through the top end of the ROB.

Significant insulation (around 5 cm) will be required to separate the cold area containing the SiPMs from the warmer region with the front-end electronics. Additionally, the limited 2 cm space between the cooling pipe and the ROB faces presents a challenge in preventing condensation and frost formation inside and outside the ROB.

4.1.5 The front-end electronics

The front-end electronics (FEE) in the SciFi Tracker function as the interface between the SiPM signals and the Back-End Electronics (BE) modules, facilitating data acquisition and control. Positioned on the warm side of the ROB, the FEE is attached directly to the detector, connecting to the SiPMs on one side and to the experiment’s data acquisition and control system on the other. The FEE is responsible for reading detector signals and transferring the data to the BE electronics. Additionally, it controls and monitors the detector, receives commands, and reports the status of various components.

Each FEE board includes an interface to distribute bias voltages to both the integrated circuits and the SiPMs, manages Timing and Fast Control (TFC) signals, and communicates with the Experiment Control System (ECS).

The SciFi FEE consists of three types of modules that handle data readout, processing, and transmission (see Figure 26):

- **Pacific Board:** is the module responsible for reading, amplifying, and digitizing the data from the SiPMs. It includes four PACIFIC.
- **Clusterization Board:** performs zero-suppression, organizes the data into clusters, and prepares it for transmission to the back end.
- **Master Board:** coordinates the other boards, supplying power and clock signals, and is responsible for data serialization and transmission to the counting room.

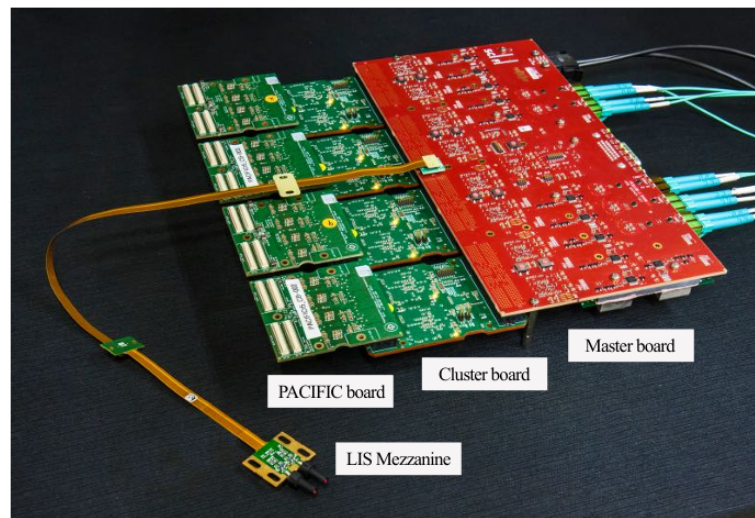


Figura 26 – Photograph of assembled Master, Clusterization, and PACIFIC boards [8].

The architecture of the SciFi Tracker’s FE electronics follows [46]. Its functional operation is summarized in the block diagram shown in Figure 27. The data path in the FE electronics begins when light reaching the SiPM pixels generates electrical pulses. The PACIFIC chip reads these pulses and outputs a 2-bit digital signal representing the pulse’s threshold level. Clusterization FPGAs then process signals from all 128 SiPM channels, creating clusters and formatting them according to the GBTx protocol. The data is subsequently passed to the GBTx chips on the Masterboard, which serializes it and sends it to the Back-End (BE) electronics via VTTx modules. Each GBTx channel transmits data through specific VTTx modules, as shown in the block diagram for a half FE Box.

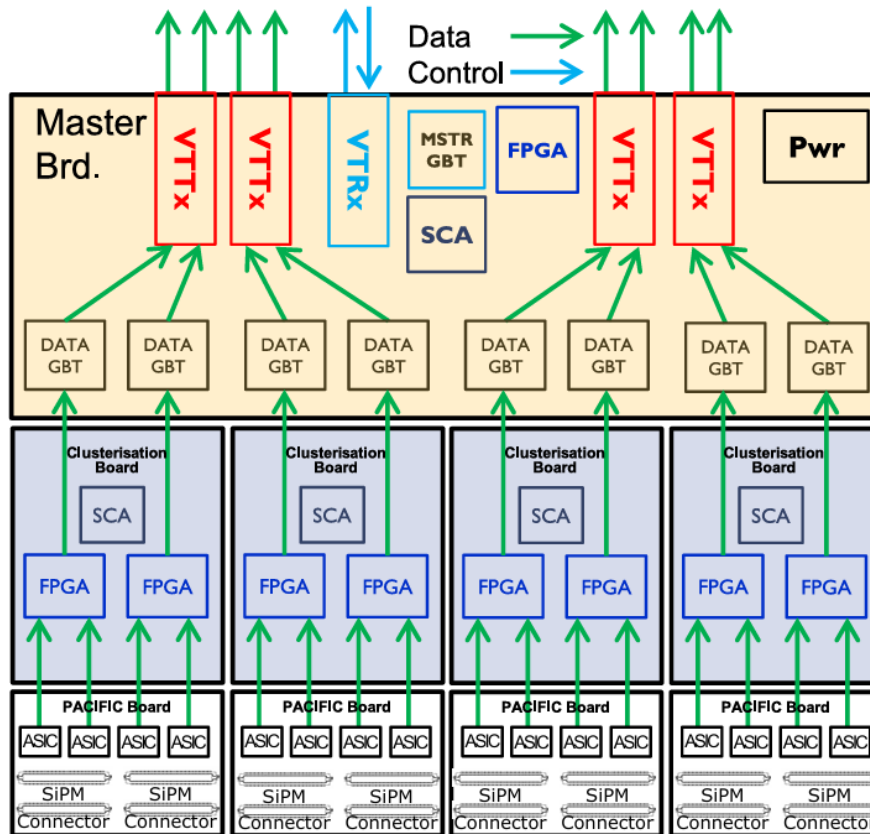


Figura 27 – Diagram illustrating the functional data flow within the FE electronics [8].

4.2 The Read-out Box test system

The SciFi layout consists of 144 detector modules, each with two readout boxes, one on each end. This setup results in the production of 288 readout boxes for assembly, plus approximately 10% additional units as spares, totaling over 300 boxes. The front-end electronics in the SciFi readout boxes are required to pass a series of functional tests before installation to guarantee optimal performance for the LHCb experiment. Given the scale of production and the time constraints, manual testing is impractical. To address this, the Charge Injection Device, which consists of using FPGAs to generate pulses with binary amplitude, was proposed as a key tool for automating the testing of the SciFi ROB front-end electronics. The tests conducted and the development of the testing system was entirely the responsibility of the CBPF group.

The test system is designed to ensure quality control of the front-end electronics by identifying potential issues that may arise from manufacturing or assembly processes. It should be capable of detecting defective (dead) and noisy channels, as well as pinpointing interference (crosstalk) and phase differences (timing) between channels. Furthermore, it needs to verify the functionality of the PACIFIC, including assessments of DC level uniformity, input gains, and threshold voltages, in addition to the performance of shapers,

integrators, comparators, and digital logic. An essential aspect of this system is its ability to validate the integrity of an emulated physical measurement by injecting charge levels comparable to those generated by photomultipliers during real events. This validation confirms the functionality of the entire acquisition chain, covering clustering mechanisms, data transmission, and data storage. Ultimately, this test system is intended to support the reliability and performance of the SciFi front-end electronics, ensuring each component meets the operational standards required for the LHCb experiment.

One of the main contributions of this work lies in the enhancement and utilization of the RoB test system. Over 10% of the total RoBs available for the SciFi detector were tested during the course of this project.

4.2.1 Charge injection device

The Charge Injector is a device designed to emulate the electrical signals produced by four SiPM super-arrays when excited by photons generated by scintillating fibers under the effect of ionizing radiation. The purpose of this emulation is to systematically stimulate the readout mechanism. The emulation of the SiPM channels is achieved by replacing the photomultiplier elements with output channels from the Charge Injector Device. These channels are capable of injecting into the PACIFIC ASIC inputs a charge amount equivalent to that generated by an SiPM. A full evaluation of a Readout Box requires 2048 injection channels, each functioning as an independent pulse generator.

4.2.2 The test bench

The Test Bench includes an injection system, the RoB under test, and a back-end data acquisition and control unit named miniDAQ, equipped with a monitor, keyboard, and mouse. Additionally, it requires a high-precision high-voltage module and a 4-channel power supply capable of delivering 10A. The power supply provides two +12 V lines for the injection system and two +6.5 V lines for the RoB.

The injection system features a control board connected to the miniDAQ, and eight injector modules, each with 256 channels (see Figure 28). These modules are capable of individually injecting calibrated charge pulses into any of the 2048 inputs of the RoB through the standard SiPM connectors. Due to the high-density design of the connector, which has a maximum insertion limit of 50 cycles—far less than the number of RoBs requiring testing.

The combination of the miniDAQ and the injection system ensures a robust and efficient testing setup for the RoBs. The test procedure is fully automatized by the WINCC control panel, which can be used by non-experts.



Figura 28 – Photo of the injector module.

4.2.3 The RoB test sequence

A brief summary of the steps involved in the RoB Test Procedure is provided below:

- Download file configuration and RoB IDs: The initial step involves downloading the configuration files from the database and obtaining the production and hardware IDs for all MB, CB, and PB components of the RoB being tested.
- Current Verification I: Verification of the RoB current before configuration, measured on the Power Supply.
- Optical Control Link synchronization: Before initiating the configuration process, the error lock counters in the miniDAQ firmware are reset. Once the RoB configuration is complete (as detailed in the following step), these counters are used to detect and report any errors present in the control fiber connections.
- RoB configuration: in the MB, we configure the MasterGBTs, DataGBTs and MasterSCA. In the CB, we configure the SCA.
- Check LEDs status: following a successful configuration, the software checks the status of the RoB LEDs to identify any potential configuration issues with the DataGBTs.
- Light Power Verification of Optical Fiber Links: verification of the light intensity of the optical links.
- House-keeping FPGA: the procedure loads the firmware of the two FPGAs located in MBs, and records the firmware version.

- Cluster Board FPGA: the procedure loads the firmware of sixteen FPGAs located in CBs, and records the firmware version.
- RoB configuration II: once the firmware for the HK and CB FPGAs is successfully loaded, the configuration process is repeated to ensure the proper setup of the PB.
- Optical Data Link synchronization: checks if all DataLinks are properly locked. The process is the same as the control links.
- Current Verification II and Voltage: measures the RoB current following the configuration and firmware loading process. Additionally, it records the voltages from the MB SCA ADCs (analog-to-digital converter) and the power supply.
- IDs verification: the MasterGBT IDs are read to identify the MB, and the MasterSCA ID from the MB is uploaded to the data. For the CBs, this step compares the SCA IDs with those already stored in the data base to ensure consistency.
- Current Source Calibration: This step involves determining the current values generated by the eight current sources. The current measurements are averaged and then uploaded to the data base, as shown in Fig. 29.

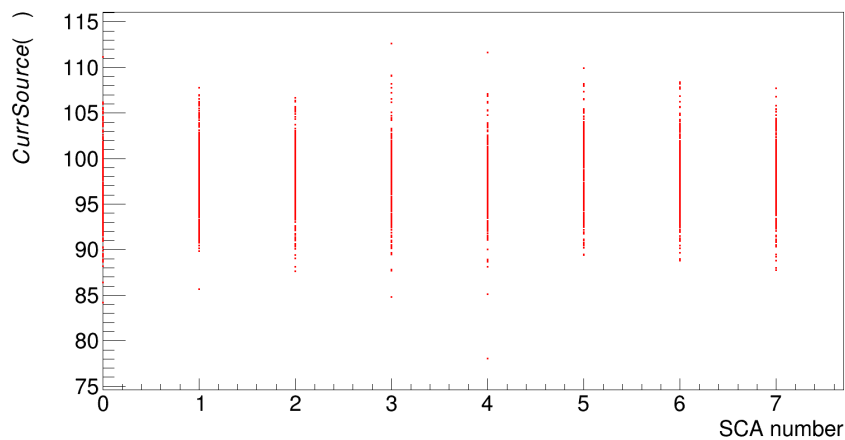


Figure 29 – Current source plot of all channels for all RoBs tested.

- Temperature measurements: once the current source values are determined, the test measures the temperatures of all sensors.
- Calibration of HV measurement: Each HalfRoB is supplied with 16 high-voltage lines from an external HV power supply. During data acquisition, the HV bias is monitored by reading the ADC values from multiplexed ¹ channels on the SCA chip after passing through a voltage divider. For calibration, this process involves applying a high-precision power supply voltage ranging from 5 V to 70 V in 1 V

¹ Combining multiple signals into a single transmission medium or channel, allowing multiple data sources to share a single communication resource.

increments and averaging the measurements 20 times. The voltage readings from the ADC are then used to perform a linear fit, mapping the applied voltage to the measured ADC values. Although the theoretical relationship is described by $V_{\text{bias}} = (72.43 \pm 0.09) \cdot V_{\text{ADC}}$, the fit is modeled as a first-degree polynomial (with two parameters) to account for minor variations in millivolts caused by grounding fluctuations, as illustrated in Figures 30 and 31. The calibration parameters are stored in a database for comparison with future calibration data.

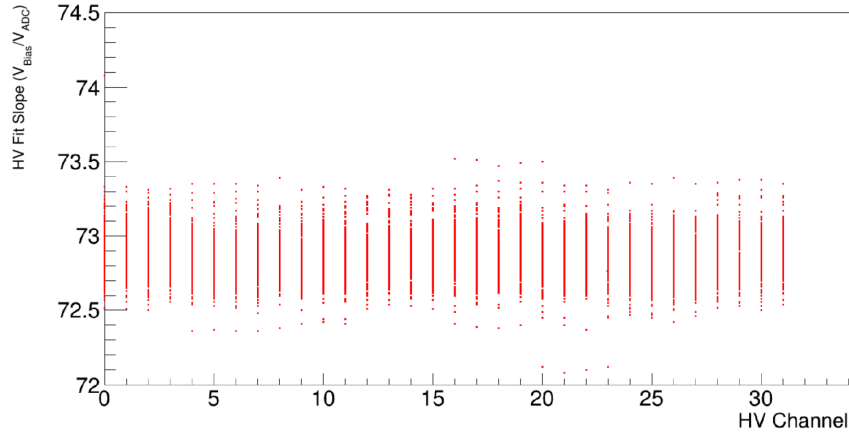


Figure 30 – HV Fit Slope plot of all channels for all RoBs tested.

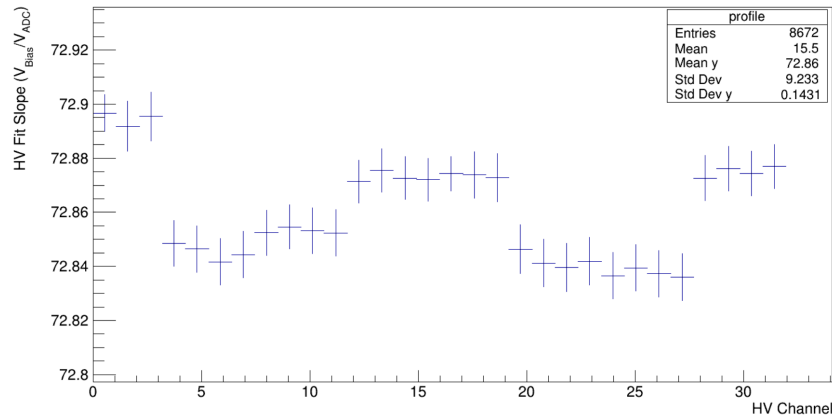


Figure 31 – Profile of the HV Fit Slope plot of all channels for all RoBs tested.

- **Threshold-Scan Test:** the ThScan test determines key parameters of the system, such as the pedestal, injected charge (Q_{inj}), and Equivalent-Noise-like (ENL). This procedure consists of a powerful tool to search for dead and noisy channels

Figure 32 presents an example of the distributions of the pedestal, Q_{inj} , and ENL (pedestal) for a Rob. In this example, all channels are working as expected.

- **Short-Circuit Test:** this test aims is to identify short circuits and crosstalk between adjacent channels. These channels are grouped into blocks of 128, sharing the same SiPM connector and two PACIFIC ASICs on the PB.

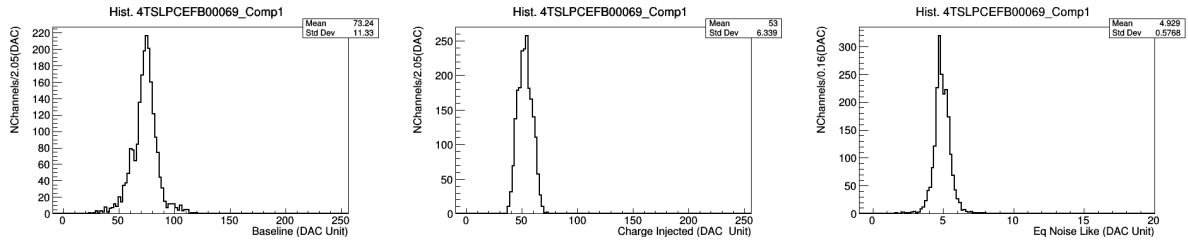


Figura 32 – From left to right, distributions of (a) pedestal, (b) Q_{inj} , and (c) ENL from a ThScan.

- Link Stability Test: the purpose of this test is to monitor communication errors caused by clock failures in the control links.
- PACIFIC Bit Error Rate (BER): this test is designed to confirm proper communication between the PACIFIC output and the back-end system. This is achieved by transmitting a predefined pattern sequence through a specific route. The process begins in the CB FPGA, which sends digital data to the PACIFIC chip. The PACIFIC chip then returns the data to the back-end, where any discrepancies in the sequence are detected and counted.

5 Mass fit and event selection

This chapter presents the event selection process for this analysis, building upon the strategy detailed in [1], which discusses the selection criteria and the mass fit for the four $B^\pm \rightarrow h^\mp h'^\pm h''^\pm$ channels. A concise summary of the event selection and B -mass fit specifically for $B^\pm \rightarrow K^\mp K^\pm \pi^\pm$ is provided here for both completeness and to reflect the updates made.

5.1 Variables definition

B -meson decays are identified based on their topological characteristics and reconstructed from the signatures left in the detector. Selecting signal events (B^\pm candidates) involves analyzing these features, which correspond to physical quantities measured precisely by the LHCb sub-detectors. Distinguishing signal from background is a crucial aspect of the analysis and is accomplished by setting thresholds on key discriminating variables.

A substantial part of the data selection process focuses on evaluating variables related to the identification of final state particles and the decay's topology. The typical topology of a $B^\pm \rightarrow K^\mp K^\pm \pi^\pm$ decay, illustrated in Fig. 33, shows the B meson being produced at the primary vertex (PV), traveling a certain distance (flight distance, FD), and decaying at the secondary vertex (SV). Important selection features include high transverse momentum (P_T), a large impact parameter (IP) for the tracks, and a requirement that they originate from the PV. These variables serve as effective discriminators, allowing us to separate signal from background. Below, we describe some of these variables in detail:

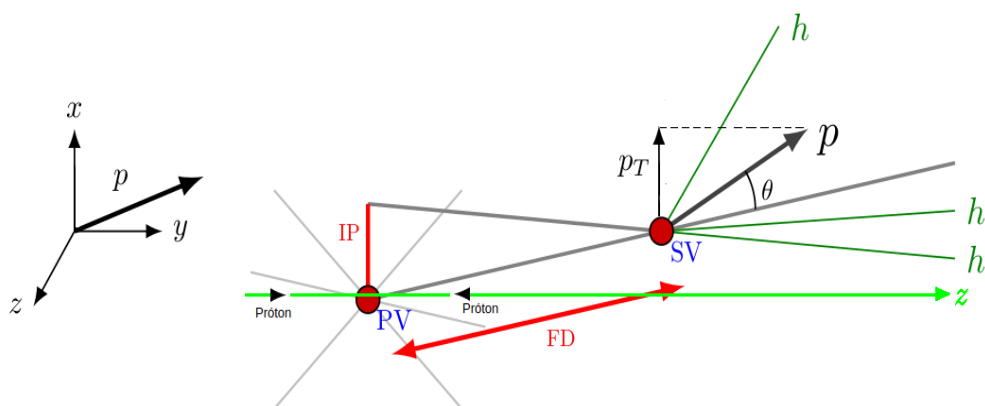


Figura 33 – Topology of a three-body decay. The acronyms are defined in the text.

- **Invariant Mass:** Using the masses of the three daughter particles, we can reconstruct the mass of the meson in question, as we have the momentum vectors of the

reconstructed tracks. The four-momentum can be expressed as $p_B^\mu = p_1^\mu + p_2^\mu + p_3^\mu$, and the invariant mass is given by:

$$m_{hhh} = \sqrt{(p_1^\mu + p_2^\mu + p_3^\mu)^2}$$

- **Flight Distance (FD)**: This is the distance between the primary vertex (PV), where the proton-proton interaction and typically the B^+ meson production occurs, and the secondary vertex (SV), where the decay happens.
- **Transverse Momentum (p_T)**: This is the momentum of the particle perpendicular to the z -axis.
- **PTsum**: This is the scalar sum of the transverse momenta of the daughter particles.
- **Momentum (P)**: The momentum P of the mother particle B is defined as the sum of the daughters momenta.
- **Impact Parameter (IP)**: Defined as the shortest distance between the reconstructed particle trajectory and the associated primary vertex.
- **DOCA**: The minimum distance of closest approach between the reconstructed trajectories of two final state particles. In the case of a three-body decay, we have DOCA12, DOCA13, and DOCA23.
- **Maximum DOCA**: Refers to higher DOCA among the three possibilities mentioned above.
- **Flight Distance χ^2 (FDCHI2)**: This is the ratio of the square of the flight distance to the quadratic sum of the uncertainties of the PV and SV.
- **Impact Parameter χ^2 (IPCHI2)**: This represents the difference in χ^2 of the PV fit with and without the evaluated particle (or track).
- **ProbNN**: This variable is used for particle identification, employing neural networks to assign an ID to each particle being analyzed. It is particularly useful in reducing background from kaon and pion misidentification. The information utilized comes from the RICH detectors, calorimeters, and the muon system.
- **Track IP χ^2** : Is defined as the difference in the vertex-fit χ^2 of the PV reconstructed with and without the inclusion of the track being considered.
- **Track P_T** : Is the component of the momentum transverse to the beam for each daughter particle.
- **Secondary vertex χ^2** : A good quality of the secondary vertex is required by imposing that the three daughter tracks form a good vertex.

5.2 Data set

Given that this analysis represents a follow-up from the previous work [1], a few other new requirements have been included. Namely, modifications to the veto cut in the two-body invariant masses $m_{K^+K^-}$ and $m_{\pi^+K^-}$, in order to avoid remnant structures from charm decays. The whole selection process can be divided into the following steps: trigger, stripping, and offline selection criteria. All of them will be discussed in the following.

This analysis uses the Run II data collected in 2015 - 2018, with a total integrated luminosity of 5.9 fb^{-1} and energy of 13TeV at the center-of-mass energy. The luminosity achieved per year is the total comprised by magnet polarity, namely, 0.33 fb^{-1} for 2015, 1.67 fb^{-1} for 2016, 1.71 fb^{-1} for 2017, and 2.19 fb^{-1} for 2018. Table 2 shows the summary of luminosity, Stripping and reconstruction version per year.

Tabela 2 – Summary of luminosity, stripping and reconstruction for run II data set.

Year	Luminosity	Stripping	Reco
2015	0.33 fb^{-1}	Stripping24r1	Reco15a
2016	1.67 fb^{-1}	Stripping28r1	Reco16a
2017	1.71 fb^{-1}	Stripping29r2	Reco17
2018	2.19 fb^{-1}	Stripping34	Reco18

LHCb Monte Carlo (MC) samples are generated for 2015 Stripping24r1, 2016 Stripping28r1 and 2017 Stripping29r2 signal simulated samples using Sim09, Pythia 8 and Reco15a/Reco16a/Reco17h respectively, are used for efficiency studies (the 2018 MC was unavailable during the period in which the efficiency was being determined).

The signal large simulated samples were generated uniformly distributed in the denominated squared Dalitz plot (SDP), without CP violation. The use of the uniform distribution in the SDP aims to improve the determination of the efficiency variation across the phase space if compared with nominal Dalitz plot representation, since events are located near of the curved borders in the latter. The generation criteria for the large MC samples are listed in Table 3.

Tabela 3 – General level requirements for large MC signal samples.

Variables	Selection cuts
Tracks P_T	$>90 \text{ MeV}/c$
Tracks P	$>1400 \text{ MeV}/c$
$B^\pm P_T$	$>1000 \text{ MeV}/c$
$B^\pm P$	$>17000 \text{ MeV}/c$

Tabela 4 – Stripping line selection criteria for charmless B^\pm decays to three light hadrons.

Variables	Selection cuts
Tracks P_T	0.1 GeV/c
Tracks P	>1.5 GeV/c
Tracks IP_{χ^2}	>1
Tracks $\chi^2/n.d.f$	<3
Tracks GhostProb	<0.5
Sum of P_T of tracks	>4.5 GeV/c
Sum of P of tracks	>20 GeV/c
Sum of IP_{χ^2} of tracks	>500
P_T of the highest- P_T track	>1.5 GeV/c
Maximum DOCA	<0.2 mm
B^\pm candidate M_{KKK}	5.05 - 6.30 GeV/c ²
B^\pm candidate M_{KKK}^{COR}	4 - 7 GeV/c ²
B^\pm candidate IP_{χ^2}	<10
B^\pm candidate P_T	>1. GeV/c
Distance from SV to any PV	>3 mm
Secondary Vertex χ^2	<12
B^\pm candidate $\cos(\theta)$	>0.99998
B^\pm Flight Distance χ^2	>500

5.2.1 Trigger requirements

Trigger decisions are applied at all levels to select hadronic decays. At the L0 trigger stage, events are required to pass either the hadron line (L0_Hadron_T0S) or any L0 line independent of the signal (L0_Global_TIS). At the software trigger stage, the selections include Hlt1TrackMVADecision_T0S and Hlt2Topo(2-,3-)_T0S [47].

5.2.2 Stripping selection

For all $B^\pm \rightarrow h^\pm h^+ h^-$ decay modes, particles are assigned the kaon mass and selected using an inclusive stripping line. Due to the topological similarities between the channels, the stripping lines rely on StdAllNoPIDKaons and are designed to capture all four charmless B^\pm decays within a wide three-body invariant mass window. A summary of the stripping criteria can be found in Table 4.

The stripping selection applies initial constraints on track parameters, such as IP_{χ^2} , momentum (P), transverse momentum (P_T), and the maximum distance of closest approach (DOCA) between tracks. The three tracks must form a common secondary vertex (SV) with a good χ^2 , displaced from the primary vertex (PV) due to the significant flight distance (FD) of the B^\pm meson before decay. The reconstructed B^\pm momentum vector is required to align with the primary vertex, typically resulting in a small impact parameter and a minimal angle θ between the momentum and flight direction. Additionally, B^\pm

candidates must satisfy a corrected mass (M^{COR}) range criterion, calculated assuming all daughters have kaon masses (M_{KKK}^{COR}).

5.2.3 B-mass constraint

All Dalitz plot analyses utilize a B-mass constraint applied through `DecayTreeFitter`. This algorithm parametrizes the entire decay chain in terms of vertex positions, decay lengths, and momentum parameters, fitting these parameters simultaneously while enforcing relevant constraints like measured final state track parameters and 4-momentum conservation at each vertex. A Kalman filter is employed for efficient fitting, as detailed in [48].

5.2.4 Offline selection

The multivariate method (e.g., Boosted Decision Trees) was employed during the offline procedures to improve the selection of B^\pm candidates, suppress combinatorial background, and utilize particle identification to mitigate contamination from other b-hadron decays. Events with multiple candidates passing the final selection were discarded randomly ($\approx 1\%$), as only one signal B candidate per event is expected due to the low branching ratio of the decay channel.

5.2.5 Loose preselection

To reduce the large size of the various $B^\pm \rightarrow h^\pm h^+ h^-$ subsamples, loose preselection criteria are applied before the multivariate selection. Vetoes were imposed in the two-body invariant mass to eliminate background contributions from $B^+ \rightarrow \bar{D}^0 K^+ (\pi^+)$ decays. A muon veto is implemented by requiring `Track_isMuon = 0` for all decay products. Additionally, loose PID requirements are employed, which are highly efficient for signal retention while significantly reducing background. These requirements are based on the Artificial Neural Network (ANN) PID algorithm.

The probability distributions for all tracks in the $B^\pm \rightarrow K^\mp K^\pm \pi^\pm$ decay are shown in Figs. 34. A large number of entries with low values of the corresponding `ProbNN` variable can be observed. For further analysis, only kaon and pion candidates with `ProbNNk/pi > 0.1` are retained. The impact of this loose PID preselection is illustrated in Fig. 35, where the rejected candidates are highlighted in red. The mass spectra of the retained candidates are presented in Fig. 36.

5.2.6 Boosted Decision Trees

To train the boosted decision trees (BDT), we selected ten input variables with strong signal-background discrimination and minimal inter-variable correlation. These

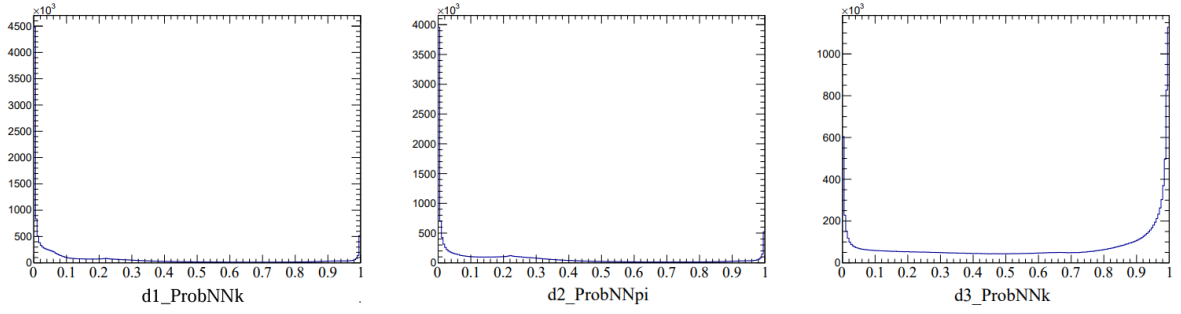


Figura 34 – Distribution of ANN probabilities for $B^+ \rightarrow K^+(d1)\pi^+(d2)K^-(d3)$.

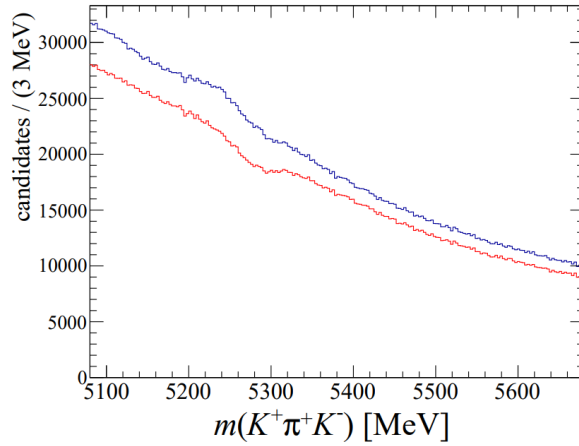


Figura 35 – Invariant mass distributions $B^\pm \rightarrow K^\mp K^\pm \pi^\pm$ decays. The histogram in red has the candidates rejected by the minimal PID cut. Sample plots made with MagUp data only.

variables demonstrated good consistency between their distributions in data and simulation. Signal samples were obtained from Monte Carlo simulations, while background samples were taken from high-mass sideband data ($m_B > 5.4 \text{ GeV}/c^2$) from 2015 and 2016, with comparable event counts in both.

Due to discrepancies in PID variable distributions between data and simulation, weights from the PIDCalib package [49] were applied to the simulation to correct for PID pre-selection efficiency. The variables used for BDT training are detailed in Table 5. Among them, the pointing variable is particularly effective in suppressing combinatorial background, defined as:

$$Pointing = \frac{P \sin \theta}{P \sin \theta + \sum_i P_T^i}, \quad (5.1)$$

where the sum is over the transverse momenta of the daughter particles, $P_T^i = P_i \sin(\theta_i)$, and θ_i denotes the angle between the particle's momentum and the parent's displacement from the specified vertex. This variable corresponds to a normalized transverse momentum relative to the flight displacement, rescaled to lie within the range $[0, 1]$.

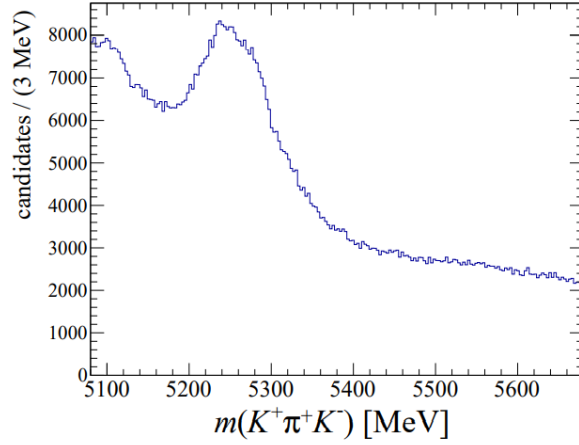


Figure 36 – Invariant mass distributions for the decays retained after the minimal PID cut for $B^\pm \rightarrow K^\mp K^\pm \pi^\pm$ decays. Sample plots made with MagUp data only. .

Figure 37 displays the distribution of the BDT output variable, contrasting the optimization specific for $B^\pm \rightarrow K^\mp K^\pm \pi^\pm$ with the one applied to all channels. Similarly, Figure 38 illustrates the Receiver Operating Characteristic (ROC) curve, showing background rejection efficiency versus signal selection efficiency, again comparing the $B^\pm \rightarrow K^\mp K^\pm \pi^\pm$ -specific optimization with the channel-independent approach.

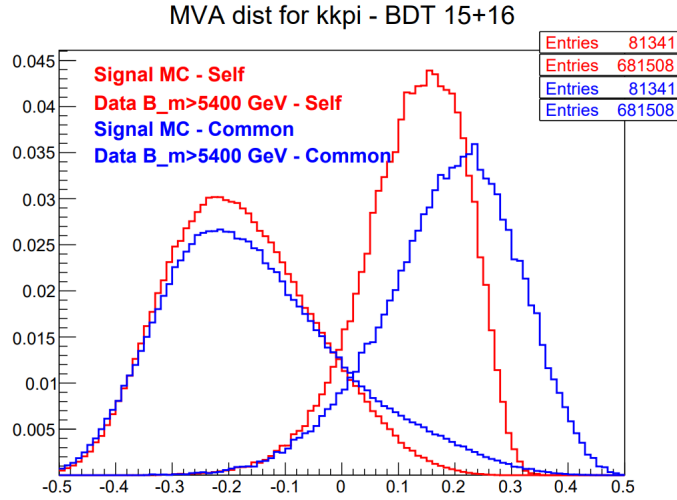


Figure 37 – The distributions of outputs variables from BDT. Left curves are background and right ones are signal. Red lines are for the optimization specific to $B^\pm \rightarrow K^\mp K^\pm \pi^\pm$ while blue lines are for the optimization common to all channels.

The optimal BDT output variable cuts are determined by maximizing the statistical significance, calculated as $\frac{S_{MC}}{\sqrt{(S+B)_{data}}}$. Here, S_{MC} represents signal events selected from simulated samples, and $(S+B)_{data}$ corresponds to the event count in the signal region $|(B_m - 5284 \text{ MeV}/c^2)| < 40 \text{ MeV}/c^2$ obtained from data. To improve signal efficiency with minimal loss of significance, the cuts are chosen slightly before the peak significance value.

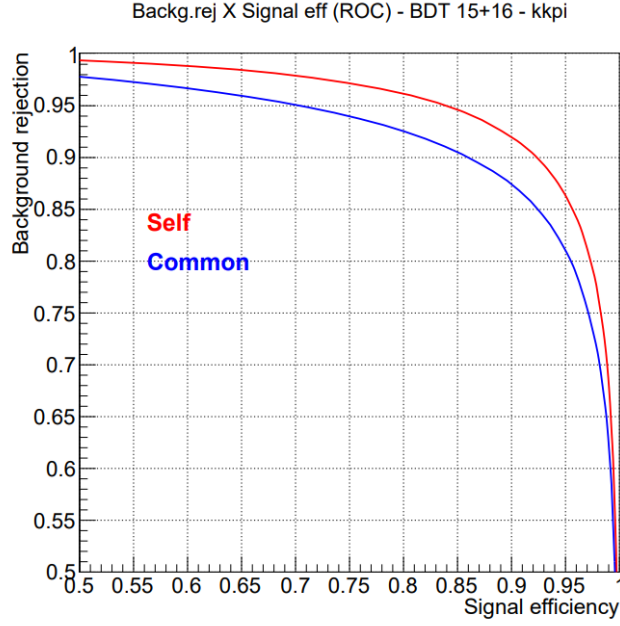


Figure 38 – The background rejection efficiency against signal selection efficiency (ROC curves). Red lines is for the optimization specific for $B^\pm \rightarrow K^\mp K^\pm \pi^\pm$ and blue line is for the optimization common to all channels.

Tabela 5 – List of variables used as input for BDT training.

Pointing [pointing_pt]
Maximum DOCA [B_AMAXDOCA]
Sum of the IP relative to PV of tracks [ipownpvsum]
Secondary Vertex χ^2 B_ENDVERTEX_CHI2]
PT asymmetry in a cone of 0.5 around the B^\pm candidates B_050_cc_CONEPTASYM_B
Mean of tracks P_T ptmed
Max of tracks P_T ptmax
B^\pm candidate B_P
B^\pm candidate IP_{χ^2} B_IPCHI2_OWNPV
P of track with opposite sign relative to B^\pm candidate d3_P

Figure 39 illustrates the signal significance and efficiency for this optimization, indicating the selected cut position. For $B^\pm \rightarrow K^\mp K^\pm \pi^\pm$, the chosen cut was $K^+ \pi^+ K^- > -0.07$.

Figure 40 shows the $B^\pm \rightarrow K^\mp K^\pm \pi^\pm$ invariant mass distribution both before and after the application of the BDT selection. One can observe how the multivariate selection significantly contributes to the reduction of the combinatorial background, enhancing the signal purity.

5.2.7 Final PID selection

Candidates are selected only if all their tracks meet the criteria of momentum below 100 GeV/ c and pseudorapidity within $1.5 < \eta < 5.5$ (this is also known as fiducial

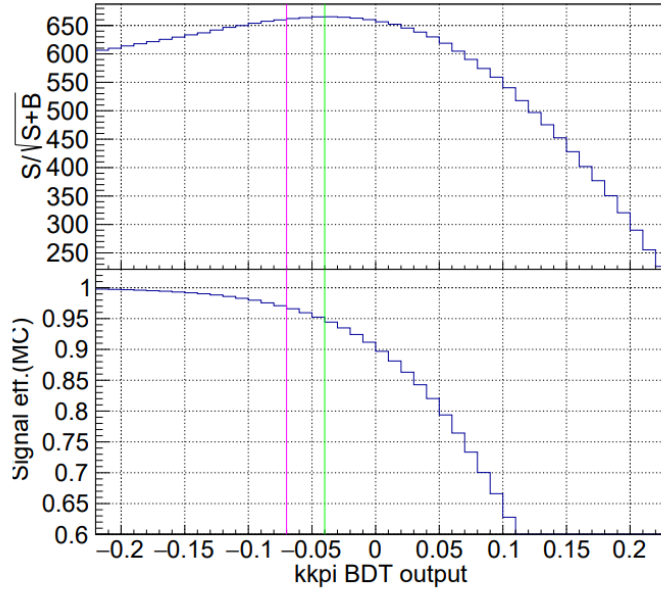


Figura 39 – The background rejection efficiency against signal selection efficiency (The significance $S/\sqrt{S+N}$ and the signal efficiency for the specific optimizations. The green line indicate the maximum of the significance. The pink line indicate the location of the cut on the BDT output variables we chose.

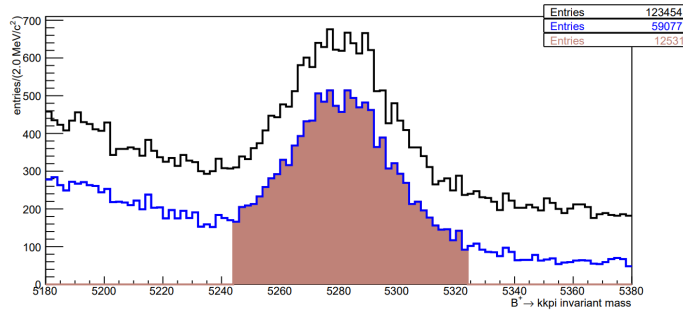


Figura 40 – The invariant mass distribution of $B^\pm \rightarrow K^\mp K^\pm \pi^\pm$ before (black) and after (blue) BDT selection, for the optimization specific to each channel. The shaded region corresponds to the signal region $|(B_m - 5284 \text{ MeV}/c^2)| < 40 \text{ MeV}/c^2$.

cuts) . This restriction minimizes cross-feed from other $B^\pm \rightarrow h^\mp h^\pm h^\pm$ modes by reducing the misidentification probability for high-momentum tracks, where the RICH system’s particle identification capability is limited.

The final PID selection combines “positive” requirements (identifying kaon and pion candidates as their respective particles) and “negative” requirements (kaon candidates not identified as pions, and vice versa). The decays $B^+ \rightarrow \bar{D}^0 K^+(\pi^+)$ and $\bar{D}^0 \rightarrow K^- \pi^+ / K^- K^+$ are used to establish these criteria when it is possible.

The PID selection aims to manage cross-feed background by balancing signal efficiency and background rejection. While PID cuts can significantly reduce cross-feed, they cannot eliminate it entirely. Tightening requirements sharply decreases signal

efficiency, so an optimal balance is necessary. Given the large signal yields, the PID requirements were determined by analyzing the behavior of $\bar{D}^0 \rightarrow K^- \pi^+ / K^- K^+$ signals relative to both positive and negative cuts. The $\text{ProbNN}_{\pi} < 0.4$ cut was also applied to remove residual contamination from $J/\psi \rightarrow e^+ e^-$, where electrons and positrons are misidentified as pions or kaons. This cut achieves an efficiency of approximately 99%.

For $B^\pm \rightarrow K^\mp K^\pm \pi^\pm$, the primary backgrounds are $B^+ \rightarrow K^+ \pi^+ \pi^-$ and $B^+ \rightarrow K^+ K^+ K^-$, caused by $\pi - K$ and $K - \pi$ misidentifications, respectively. Negative requirements are applied to ProbNN_{π} for particles 1 and 3 (kaon candidates in $B^+ \rightarrow K^+ \pi^+ K^-$) and to ProbNN_k for particle 2 (the pion candidate). Clear signals from both $B^+ \rightarrow K^+ K^+ K^-$ and $B^+ \rightarrow K^+ \pi^+ \pi^-$ are visible in the $B^+ \rightarrow K^+ \pi^+ K^-$ sample (see Fig. 41), providing a basis for the negative PID cuts. For positive requirements, the $B^+ \rightarrow \bar{D}^0 K^+(\pi^+)$ signal (Fig. 42) is used.

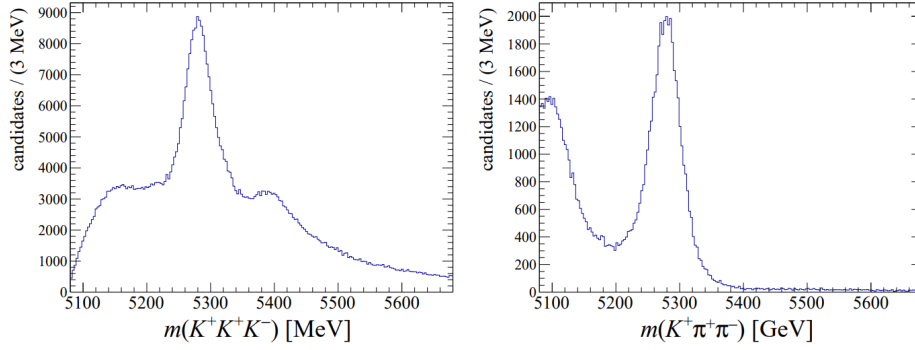


Figure 41 – The $K^+ K^+ K^-$ (left) and $K^+ \pi^+ \pi^-$ (right) invariant mass distributions from the $B^+ \rightarrow K^+ \pi^+ K^-$ sample. The plot has the 2015+2016 data and includes both polarities.

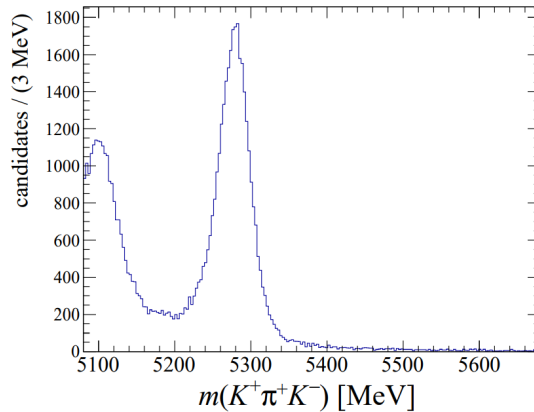


Figure 42 – The $B^+ \rightarrow \bar{D}^0 K^+(\pi^+)$ signal from the $B^+ \rightarrow K^+ \pi^+ K^-$ sample. The plot has the 2015+2016 data and includes both polarities.

Contamination from $B^+ \rightarrow K^+ K^+ K^-$ is mitigated by applying a negative PID cut ($\text{ProbNN}_k < x$) to particle 2, as shown in Fig. 43. The histograms in red, magenta, green, and brown correspond to cuts of $\text{ProbNN}_k < 0.4, 0.3, 0.2,$ and $0.1,$ respectively.

Similarly, Fig. 44 illustrates the reduction in $B^+ \rightarrow K^+\pi^+\pi^-$ contamination when a negative PID cut is applied to particles 1 and 3, with the same color scheme for $\text{ProbNN}\pi$. Final requirements of $\text{ProbNNk} < 0.05$ for particle 2 and $\text{ProbNN}\pi < 0.2$ for particle 3 effectively remove most of the contamination from $B^+ \rightarrow K^+K^+K^-$ and $B^+ \rightarrow K^+\pi^+\pi^-$.

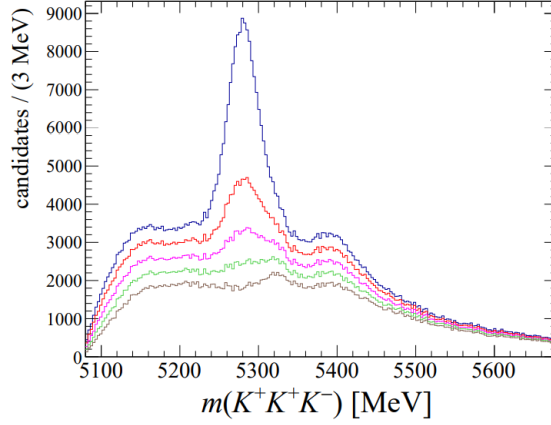


Figura 43 – The $B^+ \rightarrow K^+K^+K^-$ signal from the $B^+ \rightarrow K^+\pi^+K^-$ sample. Histograms in, red, magenta, green and brown correspond to the requirement of $\text{ProbNNk} < 0.4, 0.3, 0.2$ and 0.1 , respectively. The plot has the 2015+2016 data and includes both polarities.

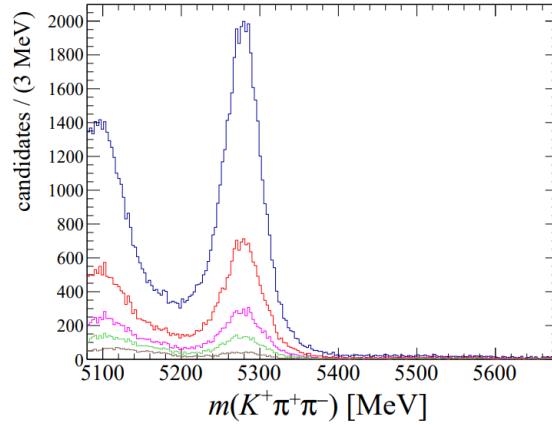


Figura 44 – The $B^+ \rightarrow \pi^+K^+\pi^-$ signal from the $B^+ \rightarrow K^+\pi^+K^-$ sample. Histograms in, red, magenta, green and brown correspond to the requirement of $\text{ProbNN}\pi < 0.4, 0.3, 0.2$ and 0.1 , respectively. The plot has the 2015+2016 data and includes both polarities.

In addition to the negative PID requirements, positive identification is applied to the three particles in $B^+ \rightarrow K^+\pi^+K^-$ candidates. After the negative PID cut, positive identification proves highly efficient. This is illustrated in Fig. 45, where simultaneous cuts of $\text{ProbNNk} > 0.3, 0.4, 0.5$, and 0.6 are applied to particles 1 and 3, and $\text{ProbNN}\pi > 0.3, 0.4, 0.5$, and 0.6 to particle 2, represented by the histograms in red, magenta, green, and brown. The selected values were $\text{ProbNNk} > 0.4$ for particle 1, $\text{ProbNN}\pi > 0.7$ for

Tabela 6 – Final PID requirements for $B^+ \rightarrow \pi^+ K^+ \pi^-$.

	K^+	π^+	K^-
ProbNNpi	-	>0.7	<0.2
ProbNNk	>0.4	<0.05	>0.6

particle 2, and ProbNNk > 0.6 for particle 3. The final spectrum is presented in Fig. 46, and the requirements are summarized in Table 6.

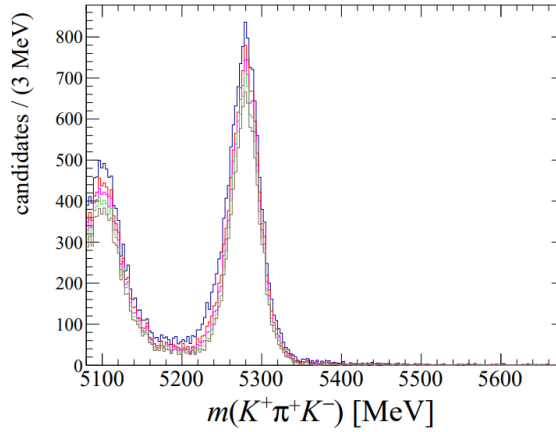


Figura 45 – The $B^+ \rightarrow \bar{D}^0 K^+(\pi^+)$ signal from the $B^+ \rightarrow K^+ \pi^+ K^-$ sample. Histograms in, red, magenta, green and brown correspond to the requirement of ProbNNpi > 0.3, 0.4, 0.5 and 0.6, after the negative PID is applied respectively. The plot has the 2015+2016 data and includes both polarities.

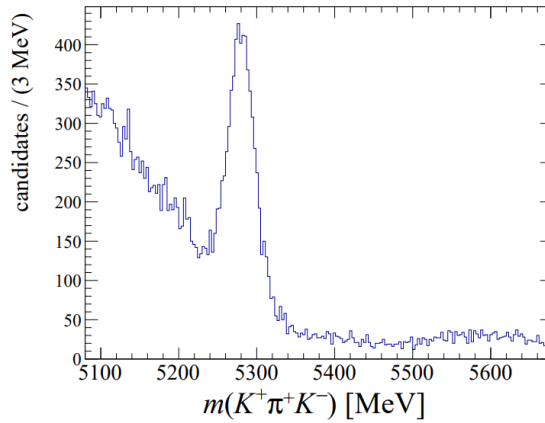


Figura 46 – The $B^+ \rightarrow K^+ \pi^+ K^-$ signal sample with final PID requirements. The plots has the 2015+2016 data and includes both polarities.

5.2.8 Mass vetoes

To isolate charmless B decay samples, contamination from $B^+ \rightarrow \bar{D}^0 h^+(h = K^+, \pi^+)$ must be removed using specific mass cuts in the two-body spectra. D^0 backgrounds can arise in two forms: with or without K - π misidentification. The $B \rightarrow \bar{D}^0(\rightarrow K^+ \pi^-) \pi^+$,

Tabela 7 – The \bar{D}^0 mass veto.

	m23_kpi	m23_pipi	m23_kk	m23_pik	m31_kk	m31_pipi	m31_pik
$K^+\pi^+K^-$	no	no	no	yes	yes	no	no

$B \rightarrow \bar{D}^0(\rightarrow \pi^+\pi^-)K^+$ (without misID), and $B \rightarrow \bar{D}^0(\rightarrow K^+K^-/\pi^+\pi^-)\pi^+$ (with K - π misID) contribute as backgrounds. Figures 48 and 49 illustrate the four possible \bar{D}^0 signals, while Table 7 summarizes the applied mass vetoes on the corresponding two-body invariant mass spectra. The veto nomenclature specifies combinations like m23_kpi (particle 2=kaon, particle 3=pion) and m23_kk (particle 2=kaon, particle 3=kaon). For the $\bar{D}^0 \rightarrow K^+\pi^-$ decay, the mass veto window is extended to $m_{D^0} \pm 0.060 \text{ GeV}/c^2$ to account for signal tail contributions, while other \bar{D}^0 decays use $m_{D^0} \pm 0.035 \text{ GeV}/c^2$, consistent with [1].

It was also identified that the vetoes in the D^0 region needed to be extended. Residual peaks of D^0 contamination were observed in both the KK mass and the $K\pi$ mass distributions. The final version of vetoes applied were: $1.70 < m_{K^\pm\pi^\mp}^2 < 2.0 \text{ GeV}^2/c^4$ and $1.83 < m_{K^+K^-}^2 < 2.1 \text{ GeV}^2/c^4$. Figure 47 compares the version of the data used in [1] and the data after the extension of the vetoes. As can be seen, after applying the cuts, the contamination peaks from the D^0 near 3 and 4 GeV^2/c^4 were removed.

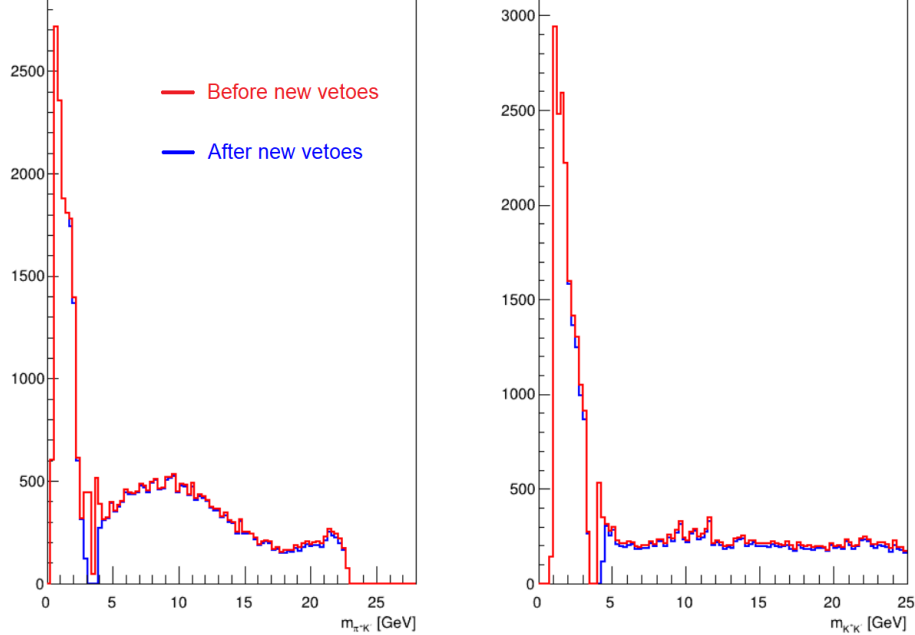


Figure 47 – Comparison between the KK (right) and $K\pi$ (left) projections before and after the application of the new vetoes. The red represents the data before the new vetoes, and the blue represents the data after their application.

Another type of background, found in the high-mass sideband of B^+ , does not affect the signal region but impacts the three-body mass fit. It originates from two-body decays, such as $B^0 \rightarrow K^+\pi^-/\pi^+\pi^-/K^+K^-$, combined with a random track. To address

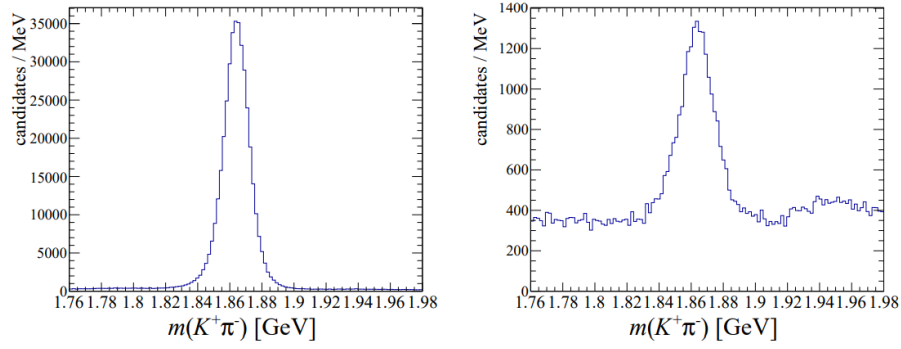


Figura 48 – The $\bar{D}^0 \rightarrow K^+\pi^-$ signal from the $\pi^+K^+\pi^-$ sample after final PID requirements. On the left panel, the $\bar{D}^0 \rightarrow K^+\pi^-$ signal with no misID (combination of particles 2 and 3). On the right $\bar{D}^0 \rightarrow K^+\pi^-$ signal (combination of particle 1 and 3). The candidate is selected when particle 1, a true kaon, is misidentified as a pion. The plots have the 2016 data and include both polarities.

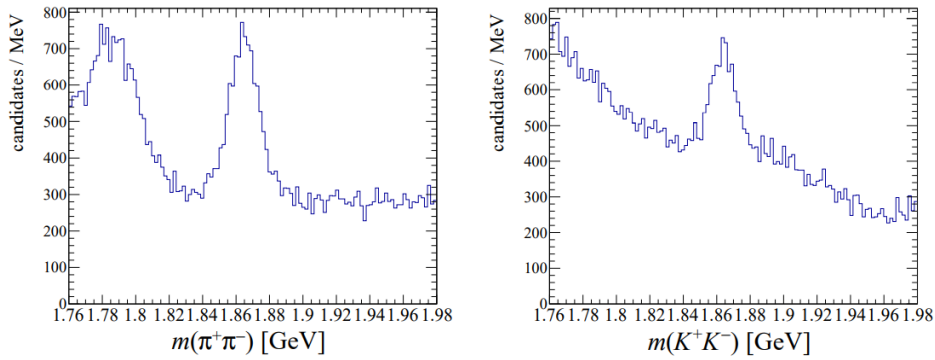


Figura 49 – The $\bar{D}^0 \rightarrow hh$ signal from the $\pi^+K^+\pi^-$ sample after final PID requirements. On the left panel, the $\bar{D}^0 \rightarrow \pi^+\pi^-$ signal with no misID. On the right $\bar{D}^0 \rightarrow K^+K^-$ signal where particle 3 is kaon misidentified as a pion. The plots have the 2016 data and include both polarities.

this, a mass veto of $\pm 60 \text{ MeV}/c^2$ around the B^0 mass is applied. A summary of all cuts used in this analysis is provided in Table 8.

5.3 B^\pm mass fit

This section describes the procedure for fitting the $B^\pm \rightarrow K^\mp K^\pm \pi^\pm$ mass spectrum to determine the total signal yield, raw asymmetry, and background estimates, which will be used as inputs for the Dalitz plot fits in Chapter 8. A simultaneous fit to the B^+ and B^- invariant mass distributions is performed over the range (5080 - 5580) MeV/c^2 . Background sources include combinatorial background, partially reconstructed backgrounds (mainly from four-body decays with a missing particle), and peaking backgrounds with one or more misidentified particles. Peaking and partially reconstructed backgrounds are modeled using MC samples, which are subject to the same selection, stripping, trigger, and offline

Tabela 8 – Summary of all selection stages applied in this analysis.

Trigger requirements as described in section 5.2.1	
Stripping cuts as described in Table 4	
MVA cuts	> -0.07
D0 vetoes as described in section 5.2.8	
Muon veto	Track_isMuon = 0
Veto to $J\psi \rightarrow e^+e^-$	Track_ProbNNe < 0.4
Fiducial cuts	
Track P	< 100 GeV/c
Track pseudorapidity selection	1.5 - 5.5
High invariant mass region veto	
$\sqrt{s_{31}}$ and $\sqrt{s_{23}}$	5.22 - 5.40 GeV/c ²
PID cuts	
$B^\pm \rightarrow K^\mp K^\pm \pi^\pm$	
Track1_ProbNNk	> 0.4
Track2_ProbNNpi	> 0.7
Track2_ProbNNk	< 0.05
Track3_ProbNNk	> 0.6
Track3_ProbNNpi	< 0.2

selection as the data.

5.3.1 Fit model

A simultaneous unbinned extended maximum likelihood fit was applied to the invariant mass distributions of B^+ and B^- . The probability density functions (PDFs) were modeled and fitted using the RooFit C++ framework [50]. The raw charge asymmetry, A_{RAW} , is defined as:

$$A_{RAW} = \frac{N^- - N^+}{N^- + N^+}, \quad (5.2)$$

where N^- and N^+ are the number of B^- and B^+ candidates, respectively. We can represent N^- and N^+ as a function of A_{RAW} and the total number of candidates $N = N^- + N^+$ in the following way:

$$A_{RAW} = \frac{N^- - (N - N^-)}{[N^- + (N - N^-)]} \Rightarrow N^- = \frac{N}{2}(1 + A_{RAW}) \quad (5.3)$$

$$A_{RAW} = \frac{(N - N^+) - N^+}{[(N - N^+) + N^+]} \Rightarrow N^+ = \frac{N}{2}(1 - A_{RAW}) \quad (5.4)$$

Using this definition, we define the mass fit model (F^\pm) for B^\pm samples as:

$$\begin{aligned}
F^\pm &= \left[\frac{N_s}{2} (1 \mp A_{RAW}^S) \right] F_s^\pm + \\
&+ \left[\frac{N_{comb}}{2} (1 \mp A_{RAW}^{comb}) \right] F_{comb}^\pm + \\
&+ \sum_{i=1} \left[\frac{(f_{bkg_i} N_s)}{2} (1 \mp A_{RAW}^{bkg_i}) \right] F_{bkg_i}^\pm,
\end{aligned} \tag{5.5}$$

The term A_{RAW}^S represents the raw asymmetry of the decay channel, encompassing CP, detection, and production asymmetries. $A_{RAW}^{bkg_i}$ corresponds to the asymmetry of peaking or partially reconstructed background, while A_{RAW}^{comb} accounts for any asymmetry in the combinatorial background. N_s and N_{comb} are the total number of signal and combinatorial background events, respectively. F specifies the lineshape function PDF (F_s for signal, F_{comb} for combinatorial background, and F_{bkg_i} for peaking or partial backgrounds). The summation over i considers all background components, with f_{bkg_i} defined as:

$$f_{bkg} = \frac{N_{bkg}}{N_s} = \frac{\mathcal{B}_{bkg}}{\mathcal{B}_s} \times \frac{\epsilon_{bkg}}{\epsilon_s}, \tag{5.6}$$

where \mathcal{B}_{bkg} and \mathcal{B}_s are the branching ratios taken from PDG, and ϵ_{bkg} and ϵ_s are the efficiencies from the MC selection.

5.3.1.1 Signal fit model

The signal PDF (represented by $F_S^\pm(m)$ for B^+ and B^- respectively in Eq. 5.7) model is composed by the sum of a Gaussian plus two Crystal-Balls with common parameters for B^+ and B^- samples. This parametrization is derived from MC studies, which gives a good description of the signal shape and at the same time provides the best stability to data. The two Crystal Balls are needed to account for the non-Gaussian asymmetric tails of the signal, including final state radiation (FSR). One Crystal Ball has its tail on the left and one on the right. The signal PDFs are then defined as:

The signal PDF, represented as $F_S^\pm(m)$ for B^+ and B^- , as shown in Eq. 5.7, is modeled as the sum of a Gaussian and two Crystal-Ball functions with shared parameters for both B^+ and B^- samples. The two Crystal-Ball components account for the non-Gaussian asymmetric tails of the signal, including final state radiation (FSR), with one tail extending to the left and the other to the right. The signal PDFs are expressed as:

$$\begin{aligned}
F_S^+ &= F_S^- = f_G \cdot G(m; m_0, \sigma_G) + \\
&(1 - f_G) \cdot f_{CB_s} \cdot CB_1(m; m_0, n_1, a_1, \sigma_1) + \\
&(1 - f_G) \cdot (1 - f_{CB_s}) \cdot CB_2(m; m_0, n_2, a_2, \sigma_2)
\end{aligned} \tag{5.7}$$

where

$$G(m; m_0, \sigma_G) = \frac{1}{\sqrt{2\pi}} \exp \left[-\frac{(m - m_0)^2}{2\sigma_G^2} \right] \quad (5.8)$$

is the Gaussian distribution. The Crystal Ball functions CB_i ($i = 1, 2$) describe the signal's asymmetric Gaussian behavior, combining a Gaussian peak with a power-law tail. They are defined as:

$$CB_i = \begin{cases} \exp \left[-\frac{(m-m_0)^2}{2\sigma_i^2} \right], & \text{if } \frac{(m-m_0)}{\sigma_i} > -a_i. \\ \left(\frac{n_i}{|a_i|} \right)^{n_i} \left(\frac{n_i - a_i^2}{|a_i|} - \frac{(m-m_0)}{\sigma_i} \right)^{-n_i} \exp \left(\frac{-a_i^2}{2} \right), & \text{if } \frac{(m-m_0)}{\sigma_i} \leq -a_i. \end{cases} \quad (5.9)$$

The tail's power-law behavior is governed by a_i indicating its position relative to the distribution's mean.

5.3.1.2 Background fit models

Combinatorial backgrounds

The high-mass sidebands (above 5440 MeV/ c^2) are primarily dominated by combinatorial background, resulting from random combinations of three unrelated tracks forming a B^\pm vertex. The combinatorial background is modeled using an exponential PDF:

$$F_{comb}(m; b) = e^{[b \cdot (m - 5080 \text{ MeV}/c^2)]} \quad (5.10)$$

with one free parameter b for the slope.

Peaking backgrounds

Peaking backgrounds originate from channels that overlap or lie near the signal region. These include cross-feed backgrounds, where misidentification of final-state particles causes one charmless three-body decay to mimic another, as well as other three-body B decays. Simulated samples are used to estimate their yields relative to the signal and determine their shapes in the B^\pm invariant mass spectrum. These findings are incorporated into the invariant mass fit. The background fraction relative to the signal yield is calculated

Tabela 9 – Branching ratios and fractions of the peaking backgrounds for $B^\pm \rightarrow K^\mp K^\pm \pi^\pm$

Mode	Branching ratio	Fractions from MC 15 - 16
$B^\pm \rightarrow K^\pm K^+ K^-$	$(3.37 \pm 0.22) \times 10^{-5}$	0.0852 ± 0.0139
$B^\pm \rightarrow K^\pm \pi^+ \pi^-$	$(5.10 \pm 0.29) \times 10^{-5}$	0.0958 ± 0.0155
$B^\pm \rightarrow \pi^\pm \pi^+ \pi^-$	$(1.52 \pm 0.14) \times 10^{-5}$	0.0040 ± 0.0009

Tabela 10 – Peaking background parameters extracted from MC studies for $B^\pm \rightarrow K^\mp K^\pm \pi^\pm$.

Final state	μ_i	σ_i	a_1	a_2	n_1	n_2	f_{CB}
$B^\pm \rightarrow K^\pm K^+ K^-$	$5232 \pm$	$20.8 \pm$	$0.07 \pm$	$-2.2 \pm$	$19.4 \pm$	$1.6 \pm$	$0.86 \pm$
	5.1	3.4	0.05	1.5	11.1	2.9	0.11
$B^\pm \rightarrow K^\pm \pi^+ \pi^-$	$5320.9 \pm$	$20.0 \pm$	$1.7 \pm$	$-0.29 \pm$	$1.34 \pm$	$18.4 \pm$	$0.54 \pm$
	2.1	2.0	0.4	0.19	0.71	13.6	0.15
$B^\pm \rightarrow \pi^\pm \pi^+ \pi^-$	$5378.9 \pm$	$16.2 \pm$	$1.3 \pm$	$-0.17 \pm$	$1.84 \pm$	$2.7 \pm$	$0.39 \pm$
	6.1	6.0	1.0	0.55	2.04	15.9	0.32

as shown in Eq. 5.6, with its uncertainty arising from limited simulation statistics and branching fraction errors.

The peaking background lineshapes ($F_{bkg}(m)$) are modeled by two Crystal Ball functions CB_i as defined in Eq. 5.9. This background model is defined as:

$$F_{bkg}^\pm(m) = f_{CB_s} \cdot CB_1(m; \nu_1, n_1, a_1, \sigma_1) + (1 - f_{CB_s}) \cdot CB_2(m; \nu_2, n_2, a_2, \sigma_2) \quad (5.11)$$

The potential sources of peaking backgrounds in the $B^\pm \rightarrow K^\mp K^\pm \pi^\pm$ spectrum, shown in Table 9, were examined. Significant contributions are observed from the $K^\pm \pi^- \pi^\pm$ and $K^+ K^- K^\pm$ final states with one misidentified particle. The $\pi^\pm \pi^- \pi^+$ final state, involving two misidentified pions, contributes around 1% and is absorbed into the combinatorial background, excluding it as a separate fit component. The parameterizations used are listed in Table 10.

Partially-reconstructed backgrounds

Partially reconstructed backgrounds typically arise from 4-body B^\pm decays missing a neutral particle (e.g., π^0 or γ) or from B^0 and B_s^0 decays missing a charged particle. For B^0 and B^\pm decays without misidentification, the background peaks near a high-mass threshold, determined by the mass difference between the B and the pion. In contrast, B_s^0 decays are closer to the signal peak due to the higher B_s^0 mass. These backgrounds are modeled separately in the fit using an Argus function convolved with a Gaussian resolution, where the Argus function is defined as:

Tabela 11 – Fractions of the partially-reconstructed backgrounds, obtained from MC.

Mode	$(B^\pm \rightarrow K^\mp K^\pm \pi^\pm)$
$B^\pm \rightarrow D^0(K^\pm \pi^\mp \pi^0)\pi^\pm$	0.074 ± 0.011
$B^\pm \rightarrow K^{*\pm}(K^\pm \pi^0)K^+K^-$	$< 0.1 \%$
$B^\pm \rightarrow K^{*\pm}(K^\pm \pi^0)\pi^+\pi^-$	0.016 ± 0.003
$B_s^0 \rightarrow D_s^0(K^+K^-\pi^-)\pi^+$	1.13 ± 0.24
$B_s^0 \rightarrow K^{*0}(K^+\pi^-)\phi(K^+K^-)$	$< 0.1 \%$
$B^\pm \rightarrow \eta' K^\pm$	$< 0.1 \%$

$$\mathcal{A}(m; m_t, c, p) = \frac{2^{-p} c^{2(p+1)}}{\Gamma(p+1) - \Gamma(p+1, c^2/2)} \cdot \frac{m}{m_t^2} \left(1 - \frac{m^2}{m_t^2}\right)^p \exp\left[\frac{-1}{2} c^2 \left(1 - \frac{m^2}{m_t^2}\right)\right], \quad (5.12)$$

The Argus function is characterized by three parameters: the upper mass threshold m_t , the curvature c , and the power p , which defines the slope's steepness. During the fit, both the Argus shape parameters and its fractional contribution relative to the signal are treated as free parameters.

The partially reconstructed components, located to the left of the signal peaks, have their normalizations floated during the fit. Table 11 lists the fractions of the studied channels, with B_s^0 decays contributing significantly to the $B^\pm \rightarrow K^\mp K^\pm \pi^\pm$ spectrum. B^0 and B^\pm decays are modeled as a single partially reconstructed four-body component, with a floated fraction in the fit.

5.3.2 Fit procedure and results

The signal PDF shapes are derived from the MC sample, which satisfies the event selection criteria and is triggered by L0 Global TIS or L0 Hadron TOS. These shapes are then applied in the data mass fit. Figure 50 presents the simultaneous mass fits for B^- and B^+ samples in both MC and data.

For the MC fit figures, χ^2/dof covers the full B mass range (5050–5650 MeV/ c^2), while $\chi^2/dof(S)$ focuses on the signal region (5200–5333 MeV/ c^2). Table 12 summarizes the parameters from the MC fit, and Table 13 lists the signal and combinatorial components from the data fit.

5.3.2.1 Signal region

The signal region chosen for the amplitude analysis is selected to be from 5247 to 5315 MeV/ c^2 . In Table 14 is presented the integral of the signal and each background

Tabela 12 – Parameters extracted from the mass fits distribution of MC samples.

Signal component	MC $B^\pm \rightarrow K^\mp K^\pm \pi^\pm$
$m_0[\text{MeV}/c^2]$	5281.0 ± 0.091711
$\sigma[\text{MeV}/c^2]$	14.450 ± 0.66449
$\sigma_3[\text{MeV}/c^2]$	14.868 ± 0.72049
$\sigma_G[\text{MeV}/c^2]$	19.926 ± 1.1883
a_1	1.3846 ± 0.17448
n_1	1.4803 ± 0.11395
a_2	-1.97220 ± 0.20983
n_2	2.1668 ± 0.23755
f_{Gauss}	0.25232 ± 0.071781
f_{CB_s}	0.37223 ± 0.088096
	0.0065401
A_{RAW}	$\pm(-0.0039674,$ $+0.0039636)$
N_{sig}	63626 ± 252.24

Tabela 13 – Parameters extracted from the mass fits distributions of data samples. The numbers followed by a “(C)” were fixed in the corresponding fit. This table presents only the signal and combinatorial components of the fit. This table does not take into account the mass vetoes applied to address the D^0 contamination described in Sec. 5.2.8.

Signal component	Data $B^\pm \rightarrow K^\mp K^\pm \pi^\pm$
$m_0[\text{MeV}/c^2]$	5279.8 ± 0.15009
$\sigma[\text{MeV}/c^2]$	18.837 ± 1.6523
$\sigma_3[\text{MeV}/c^2]$	15.636 ± 1.0735
$\sigma_G[\text{MeV}/c^2]$	17.498 ± 2.4436
a_1	1.3846 (C)
n_1	1.4803 (C)
a_2	-1.97220 (C)
n_2	2.1668 (C)
f_{Gauss}	0.25232 (C)
f_{CB_s}	0.37223 (C)
	-0.131775
A_{RAW}	$\pm(-0.0068116,$ $+0.0067412)$
N_{sig}	32466 ± 296.05
Combinatorial	
shift	5050.0 (C)
b	-0.00254267 ± 0.000084639
A_{comb}	-0.0175048 ± 0.0059264
N_{comb}	59530 ± 1128.1

Tabela 14 – Integral of each component in the signal region of 5247 to 5315 MeV/ c^2 .

Component	$B^\pm \rightarrow K^\mp K^\pm \pi^\pm$
Signal (-)	12606
Signal (+)	16432
Signal (All)	29038
Combinatorial	7320
$B_s \rightarrow 4 - body$	509
Reflection 3	1018
Reflection 4	271
Reflection 5	2

component in this region. The background components named Reflections 3 - 5 are $B^\pm \rightarrow K^\pm \pi^+ \pi^-$, $B^\pm \rightarrow K^\pm K^+ K^-$, $B^\pm \rightarrow \pi^\pm \pi^+ \pi^-$, respectively.

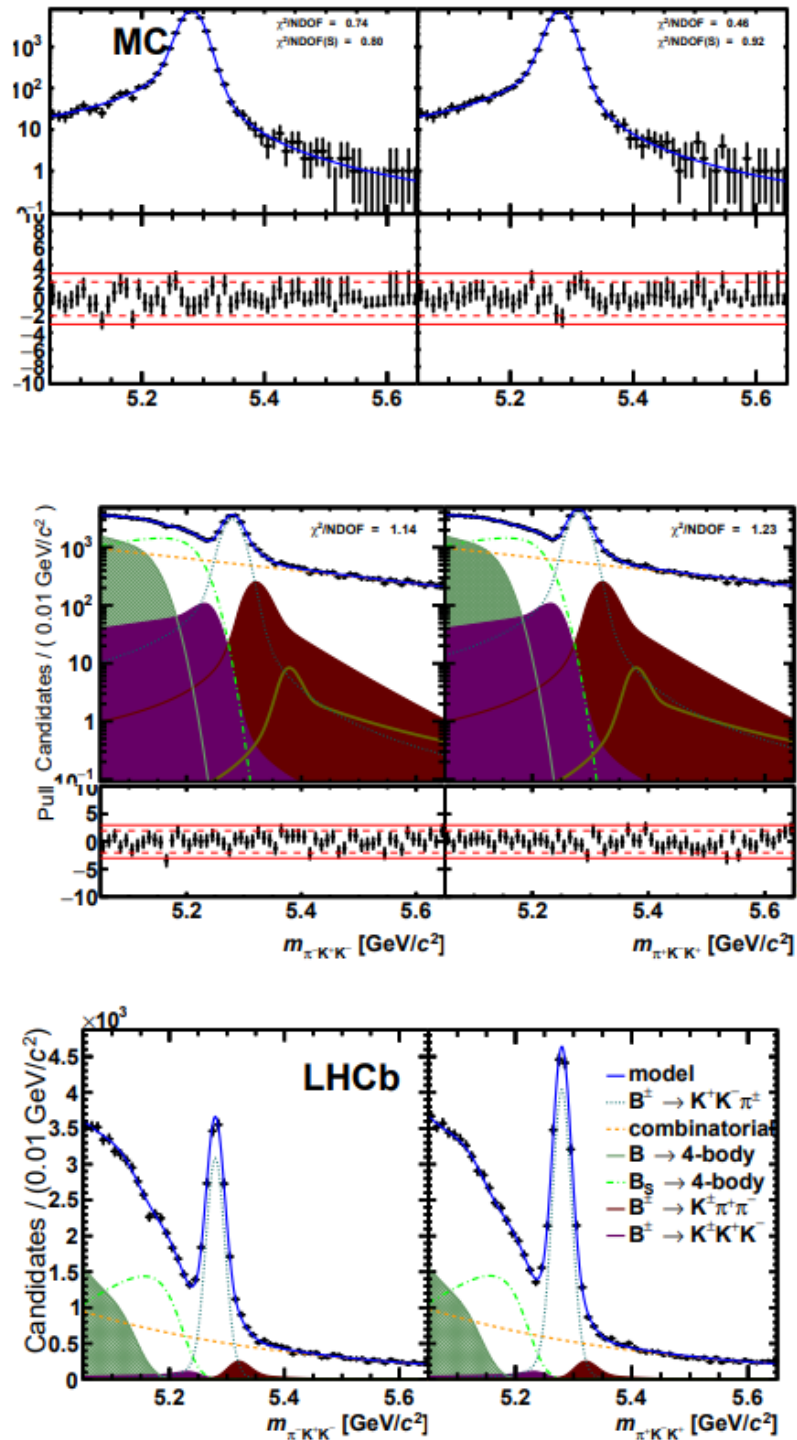


Figure 50 – Invariant mass fits for $B^\pm \rightarrow K^\mp K^\pm \pi^\pm$: (top) MC mass fit result plot using logarithmic scale and pull, (middle) data sample mass fit result plot using logarithmic scale and pull and (bottom) data sample mass fit.

6 The Dalitz Plot: tools and theories

This chapter introduces the Dalitz plot formalism as a framework for analyzing three-body decays, with a focus on the $B^\pm \rightarrow K^\mp K^\pm \pi^\pm$ channel. It highlights the mathematical structure and kinematic boundaries of the Dalitz plot, emphasizing its role in uncovering the dynamics of the decay and identifying resonances. The Isobar model, which will be used for the model-dependent amplitude analysis, is presented, along with discussions on its limitations, alternative approaches for S-wave models, and the impact of rescattering. Dynamical functions are explored to model the resonance contributions.

6.1 The Dalitz Plot description

To illustrate a generic example of a three-body decay, consider Figure 51. In this representation, \vec{P} denotes the 4-momentum vector of the parent particle with mass M , while p_i represents the 4-momentum of each decay product with mass m_i . The decay process complies with the principles of energy and momentum conservation, resulting in the following constraints:

$$E_M = \sum_{i=1}^3 E_i, \quad E_i = m_i^2 + \mathbf{p}_i^2, \quad \vec{p}_M = \sum_{i=1}^3 \mathbf{p}_i = 0, \quad (6.1)$$

In total, there are 12 degrees of freedom (4 for each decay product) due to the 4-momentum vectors. This number is reduced by accounting for three particle masses in the final state (3 degrees of freedom), three Euler angles (3 more degrees of freedom), and the 4 equations for energy and momentum conservation from Eq. 6.1. As a result, only two independent variables remain. These two variables describe the two-dimensional phase space of the decay process, which is visually represented by the *Dalitz plot* (DP).

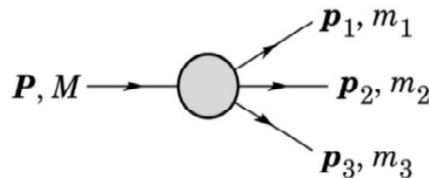


Figure 51 – The scheme for three-body decays. Figure extracted from PDG [10].

By constructing independent variables using the 4-momentum vector of the daughter particles, $\vec{p}_{ij} = \vec{p}_i + \vec{p}_j$ and $m_{ij}^2 = p_{ij}^2$, where i and j stand for any pair combination the daughter particles in the final state, it can be shown, using 4-momentum conservation for the process, that the following relation must be satisfied:

$$M^2 + m_1^2 + m_2^2 + m_3^2 = m_{12}^2 + m_{23}^2 + m_{31}^2 \quad (6.2)$$

Since the momenta of the three daughters are co-planar in the M reference frame, the boundaries of the decay phase space are limited by a maximum and a minimum value of m_{ij}^2 , when the momentum vector \vec{p}_i are parallel or antiparallel to \vec{p}_j . Fig. 52 represents the kinematically allowed phase space in a broader context. These points correspond to configurations where one of the particles is produced at rest in the rest frame of the decaying particle. One can also examine the behavior of the particles in other regions of the Dalitz Plot, such as the middle, where none of the particles are at rest. The shape of the phase-space is intrinsically determined by the kinematics involved in the process, where $m^{max} = M - m_k$ and $m^{min} = m_i + m_j$. The resulting phase space is interpreted as being a scatter plot of any set of m_{ij}^2 variables, m_{12}^2 , m_{23}^2 and m_{31}^2 .

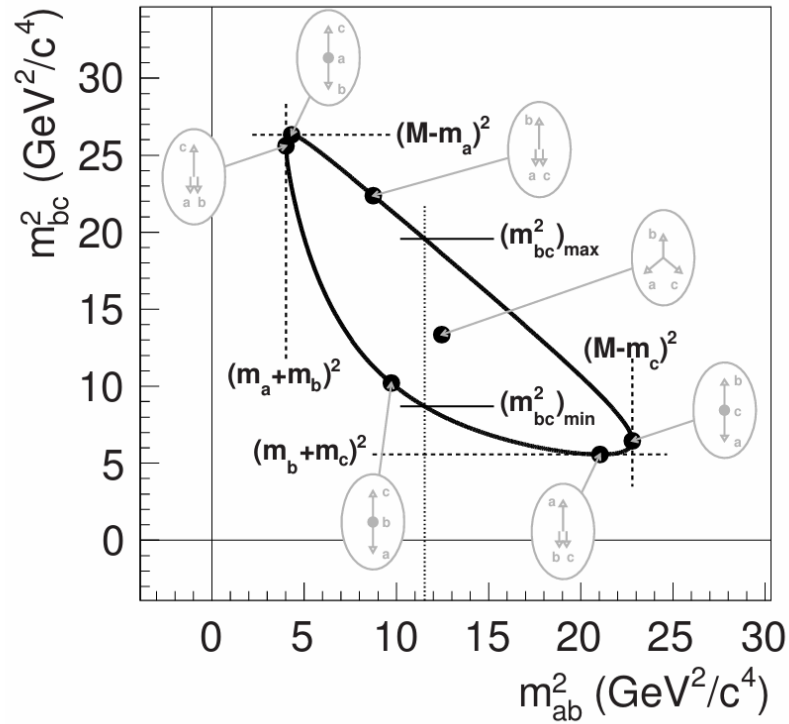


Figura 52 – Kinematic boundaries of the three-body decay phase space, along with a depiction of various kinematic configurations for the final-state particles at representative points on the Dalitz plot. This figure illustrates the phase space for the decay process $B^0 \rightarrow \pi^- \bar{D}^0 K^+$, where $a = \pi^-$, $b = \bar{D}^0$, and $c = K^+$ [11].

Considering the kinematics defined above and the Euler's angle to define the 3-momentum orientation, one can finally write the decay rate for a $M \rightarrow d_1 d_2 d_3$ as

$$d\Gamma = \frac{1}{(2\pi)^3 32M^3} |\mathcal{M}(m_{13}^2, m_{23}^2)|^2 dm_{13}^2 dm_{23}^2, \quad (6.3)$$

Here, \mathcal{M} represents the amplitude of the decay process, which contains information about the dynamics. In contrast, the constant state density term holds the kinematic information. If \mathcal{M} is constant, the Dalitz plot (DP) will show a uniform distribution of events for decays of the type $M \rightarrow d_1 d_2 d_3$. Any asymmetrical distribution of events in the DP indicates the influence of the decay dynamics.

In non-leptonic B meson decays, the DP often displays bands around certain invariant masses of two-particle combinations, suggesting the presence of intermediate states, such as decays of the form $M \rightarrow R d_3$; $R \rightarrow d_1 d_2$, where R is a resonant state. These bands in the DP may interact with each other, revealing interesting patterns that can be examined in the Dalitz plot. Such interactions are studied through amplitude analysis, which is part of the focus of this work.

For the specific case of $B^\pm \rightarrow K^\mp K^\pm \pi^\pm$, Eq. 6.2 can be read as:

$$M_{B^\pm}^2 + m_{K^\pm}^2 + m_{\pi^\pm}^2 + m_{K^\mp}^2 = m_{K^\pm \pi^\pm}^2 + m_{\pi^\pm K^\mp}^2 + m_{K^\mp K^\pm}^2, \quad (6.4)$$

where $m_{K^\pm \pi^\pm}^2$, $m_{\pi^\pm K^\mp}^2$ and $m_{K^\mp K^\pm}^2$ are the invariant masses formed by any two daughters of the decay ($d_1 = K^\pm$, $d_2 = \pi^\pm$, $d_3 = K^\mp$). From the main Feynman contributing diagrams to this process, Tree-level and Penguin shown in Fig. 2, can be noticed that the resonant contributing states are mainly expected in the $m_{\pi^\pm K^\mp}^2$ and $m_{K^\mp K^\pm}^2$ systems. Therefore, these two independent variables form $B^\pm \rightarrow K^\mp K^\pm \pi^\pm$ Dalitz Plot.

For B decays into light mesons, events are mostly distributed near the edges of the Dalitz plot. In the case of $B^\pm \rightarrow K^\mp K^\pm \pi^\pm$, the decay resonances are close to these kinematic boundaries, regions with high sensitivity where significant changes occur within a small area. To avoid information loss in these regions, an alternative representation called the Square Dalitz plot (SDP) can be used. This method transforms the original Dalitz plot into a rectangular plane, removing the curved boundaries and making building the efficiency model for amplitude analysis easier. Additionally, the square variables highlight areas with higher event density, simplifying the parametrization. The transformation equation is given by:

$$dm_{\pi^\pm K^\mp}^2 dm_{K^\mp K^\pm}^2 \rightarrow |\det J| dm' d\theta', \quad (6.5)$$

where $m_{\pi^\pm K^\mp}^2$ and $m_{K^\mp K^\pm}^2$ are the Dalitz plot variables and J is the jacobian of the transformation. The new variables are defined as [51]:

$$m' = \frac{1}{\pi} \arccos \left(2 \frac{m_{\pi^\pm K^\mp}^{max} - m_{\pi^\pm K^\mp}^{min}}{m_{\pi^\pm K^\mp}^{max} + m_{\pi^\pm K^\mp}^{min}} - 1 \right) \quad (6.6)$$

$$\theta' = \frac{1}{\pi} \theta_{\pi^\pm K^\mp}, \quad (6.7)$$

where $m_{\pi^\pm K^\mp}^{min}$ and $m_{\pi^\pm K^\mp}^{max}$ are the kinematics limits of $m_{\pi^\pm K^\mp}$. The $\theta_{\pi^\pm K^\mp}$ is the helicity angle of the “ $\pi^\pm K^\mp$ ” system (angle between the bachelor particle, in this case, “ K^\pm ” and one of the resonance particles produced in the resonance rest frame). The cosine of the helicity angle ($\cos(Hel)$) is a valuable variable for exploring resonant contributions, as the spin of each resonance state exhibits a unique shape on its projection, which is associated with the square of the Legendre polynomial having the same degree as the spin.

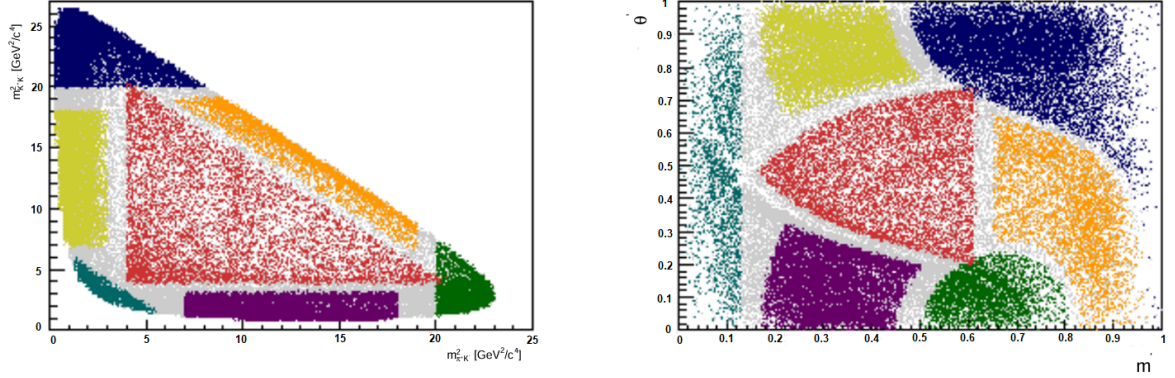


Figure 53 – Simulated data projections in the nominal Dalitz plot (left) and Square Dalitz plot (right) highlighting how each region of the phase space maps from one representation for $B^\pm \rightarrow K^\mp K^\pm \pi^\pm$.

Identifying resonances in the Square Dalitz plot is more challenging than in the standard Dalitz plot. Therefore, in this analysis, the Square Dalitz plot will only be used to compute the efficiency and background models needed for the Dalitz plot fit, rather than for resonance identification. In Figure 53, the standard Dalitz plot is shown with specific regions highlighted in different colors, alongside the corresponding regions in the Square Dalitz plot to illustrate the mapping of distributions. For the $B^\pm \rightarrow K^\mp K^\pm \pi^\pm$ decay, the Monte Carlo (MC) sample that will be used for the acceptance map in the Dalitz Plot fit (see section 7.1) is uniformly generated in the Square Dalitz plot using the $K^+ \pi^+$ variables. The square Dalitz plot variables are dimensionless and range from 0 to 1.

6.2 $B^\pm \rightarrow K^\mp K^\pm \pi^\pm$ decay amplitude

Nonleptonic three-body decays of B and D mesons occur commonly via resonant two-body processes. For decays of a spin-zero particle P such as the B into pseudoscalar final states, the standard theoretical approach to describe the decay amplitude $\mathcal{M}(m_{13}^2, m_{23}^2)$ involves a coherent sum of contributions from two-body resonances (r) and a non-resonant term (NR):

$$\mathcal{M}(m_{13}^2, m_{23}^2) = \sum_{j=1}^N a_j e^{i\phi_j} \mathcal{A}_j(m_{13}^2, m_{23}^2) + a_{NR} e^{i\phi_{NR}} \mathcal{A}_{NR}(m_{13}^2, m_{23}^2). \quad (6.8)$$

Here, a_j (a_{NR}) and ϕ_j (ϕ_{NR}) represent the magnitude and phase (including both weak and strong phases¹) of the amplitude for the j -th resonant (NR) component, respectively. The \mathcal{A}_j and \mathcal{A}_{NR} are the decay amplitudes for each component that describe the dynamics of the decay into multi-body final states. The following section explore the parametrization of $\mathcal{A}_j(m_{13}^2, m_{23}^2)$ within the scope of this thesis.

6.2.1 The Isobar model

One of the simplest and most commonly used approaches for describing the $\mathcal{A}_j(m_{13}^2, m_{23}^2)$ is the Isobar model² formalism. In this context, the \mathcal{A}_j ³ contains the dynamics given by 2-body strong interaction, and it is phenomenological given by:

$$\mathcal{A}_j = F_P \times F_r \times T_r \times W_r, \quad (6.9)$$

The term $T_r \times W_r$ represents the resonance propagator, where T_r corresponds to the dynamical function of the resonance r , and W_r describes the angular distribution of the decay. The dynamical function T_r is typically modeled using a relativistic Breit-Wigner (BW) parameterization, which incorporates a mass-dependent width and will be discussed soon. The Zemach tensor formalism [52][53] are used to describe the W_r , and are given as in the Table 15. These are related to the Legendre polynomials $P_L(\cos \theta_{\text{hel}})$, where the helicity angle θ_{hel} is the angle between \vec{p} and \vec{q} , providing a clear visual representation of the spin of the intermediate state.

The factors F_P and F_r are the Blatt-Weisskopf barrier form factors [54], to consider the penetration effects caused by the finite size of the particles participating in the reaction.

¹ Although the Isobar model does not explicitly account for final-state interactions, these interactions are implicitly incorporated within the strong phase component of ϕ_j .

² The Isobar formalism derives its name from its initial application in describing interactions such as pion-nucleon, nucleon-nucleon, and antinucleon-nucleon processes. The intermediate resonances were identified as isobars of specific nuclear states in these reactions. Over time, this formalism was extended and generalized to describe any three-body final state [11].

³ This description also holds $\bar{\mathcal{A}}_j$.

Resonance Spin	Angular distribution
J = 0	1
J = 1	$-2\vec{p} \cdot \vec{q}$
J = 2	$\frac{4}{3}[3(\vec{p} \cdot \vec{q})^2 - (\vec{p} \vec{q})^2]$
J = 3	$-\frac{24}{15}[5(\vec{p} \cdot \vec{q})^3 - 3(\vec{p} \cdot \vec{q})(\vec{p} \vec{q})^2]$

Tabela 15 – Angular distribution using Zemach tensor formalism.

Spin value	Barrier Factors ($F(z)$)
J = 0	1
J = 1	$\sqrt{\frac{1+z_0^2}{1+z^2}}$
J = 2	$\sqrt{\frac{z_0^4+3z_0^2+9}{z^4+3z^2+9}}$
J = 3	$\sqrt{\frac{z_0^6+6z_0^4+45z_0^2+225}{z^6+6z^4+45z^2+225}}$

Tabela 16 – Blatt-Weisskopf barrier factor used to correct the amplitude for penetration effects where z_0 represents the value of z when the invariant mass is equal to the pole mass of the resonance.

Table 16 shows these factors for various spin values, as a function of a variable z defined as: $z = |\vec{q}|d$ or $z = |\vec{p}|d$, where d is the radius of penetration taken to be $4.0 \text{ GeV}^{-1} \approx 1 \text{ fm}$ [55].

The P - and D -wave components of the decay amplitude are generally well-represented using the BW. The S -wave component of the $B^\pm \rightarrow K^\mp K^\pm \pi^\pm$ amplitude, in both the $K^- K^+$ and $\pi^- K^+$ systems, is characterized by its large magnitude and the presence of multiple overlapping resonances. These broad, overlapping states pose challenges for the isobar model, which often fails to provide an adequate description for such cases. Additionally, it includes effects from rescattering, where particles in the final state interact with each other before reaching the detector and are influenced by thresholds of different decay channels. These factors make modeling the S -wave more complex.

6.2.1.1 Limitations of the Isobar Model

The Isobar Model has certain limitations, some of which are highlighted below:

- The 2+1 (or quasi-two-body) approximation: This approximation assumes that the companion hadron, which does not originate from the resonance decay, does not interact with the other particles in the final state. Any approximation that neglects hadron interactions in multi-hadron decays should be applied cautiously. For instance, the Fermilab E791 and FOCUS experiments conducted amplitude analyses to measure the $K\pi$ S-wave in the $D \rightarrow KK\pi$ decay. Figure 54 illustrates this result compared to the $K\pi$ S-wave measured by the LASS scattering experiment. Notably, both measurements from the decay deviate from the scattering data.

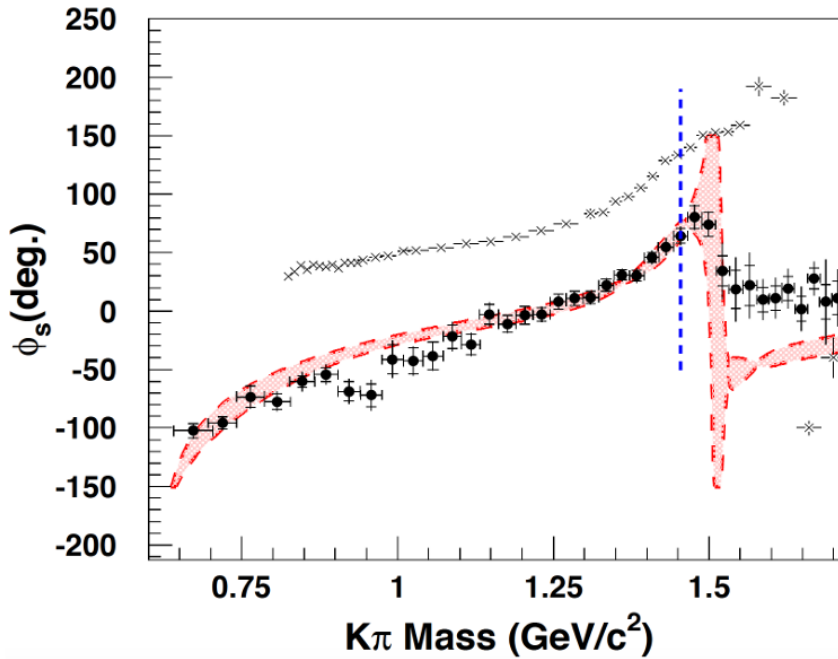


Figure 54 – The S -wave phase as a function of the $K\pi$ invariant mass, extracted from the QMI-PWA analysis of the $D^+ \rightarrow K^+\pi^+\pi^-$ Dalitz plot, is presented in [12]. The shaded region represents the results obtained from the Isobar model fit conducted in a prior study [13]. The dashed vertical line indicates the elastic range as determined by the LASS experiment [14].

Recalling Watson’s theorem, in simpler terms, it posits that swapping two identical particles in a scattering final state results in essentially the same amplitude, modified by a phase factor dependent on the scattering process dynamics. Consequently, the phase behavior should match regardless of whether the production originates from a decay or a scattering process. These observations reinforce the notion that, at least for $D \rightarrow K\pi\pi$ decays, the companion hadron plays a significant role in the final state dynamics. However, this issue is expected to be less problematic for B -meson decays, as the B -decay phase space is significantly larger. In this work, we are particularly interested in the $K\pi$ S -wave, as it will be discussed in greater detail in a subsequent section.

- Resonances shaping: The Breit-Wigner (or its derivatives) approach is known to work well only for narrow resonances and non-overlapping resonances, like the P- and D-waves. But for low-mass broad overlapping resonances (generally the S -wave), this parameterization is not good, which is the kind of component very important or even dominant for B decays.
- Unitarity: assuming that the $2+1$ approximation is exact, the simple sum of Breit-Wigners would not preserve the unitarity of the S -matrix ⁴.

⁴ It still finds support in [56].

To address these limitations, some analyses have adopted alternative methods for parameterizing the S-wave, such as the K-matrix formalism [57]. This method is based on decomposing the physical amplitude into a pole part and a non-pole part (commonly referred to as the Slow Variant Part). The K-matrix formalism ensures that the two-body scattering matrix respects unitarity, a condition that the isobar model does not guarantee.

Another alternative is the (quasi) model-independent partial wave analysis (QMI-PWA). This approach allows the scalar component to be treated in a model-independent manner while retaining a model-based description for the other parts of the amplitude. The S-wave is described by dividing the phase space into bins and introducing a CP-violating complex parameter, which enables the amplitude and phase to be fitted independently in each bin [58].

Despite its approximations, the isobar model remains a simple and elegant framework that continues to offer valuable insights into decay processes. Furthermore, approximations such as the 2+1 approach can still yield remarkably accurate results, especially for non-S-wave contributions, as demonstrated in [59].

6.2.2 Expected resonances

A list of possible resonances for the $B^\pm \rightarrow K^\mp K^\pm \pi^\pm$ decay is presented in 18. However, certain aspects regarding the types of resonances expected for this channel warrant further discussion and are addressed here.

The resonant contributing states are expected in the K^+K^- and $K^-\pi^+$ systems. The diagrams presented in Figure 2 offer valuable insight into the types of resonances that may contribute to the final state. The gluonic penguin diagrams, driven by the quark transition $b \rightarrow d$, indicate that resonances from the K^* family, such as $K^*(892)$, $K_0^*(1430)$, and others, are likely to appear in the $K^\mp \pi^\pm$ sector. These resonances arise due to the rapid decay of K^{*0} into a πK final state. Conversely, tree-level diagrams involving the $b \rightarrow u$ transition suggest the presence of resonances in the K^+K^- system, characterized by the f_x family. These include resonances such as $f_2(1270)$, $f_0(1370)$, and $f_0(980)$.

The so-called OZI rule explains the suppression of certain particle decay processes. Named after Susumu Okubo, George Zweig, and Jugoro Iizuka, who introduced the concept in the 1960s, this rule describes how specific decays are less likely to occur due to disconnected quark diagrams. For instance, the ϕ meson, a vector meson composed of a strange quark (s) and a strange antiquark (\bar{s}), can decay into two kaons (K^+ and K^-) or into (π^+ , π^- , and π^0)

For the decay into kaons, the Feynman diagram involves a strange quark interacting with a gluon, producing an up-anti-up quark pair. Similarly, the strange antiquark interacts with a gluon, which gets absorbed by the newly created up-quark, yielding K^+ and K^-

(see Figure 55 left side). For the decay into pions, the strange and anti-strange quarks annihilate, producing quark-antiquark pairs through interactions with three gluons. These gluons generate down-antidown, up-anti-up, and down-antidown pairs, corresponding to the three pions (see Figure 55 right side).

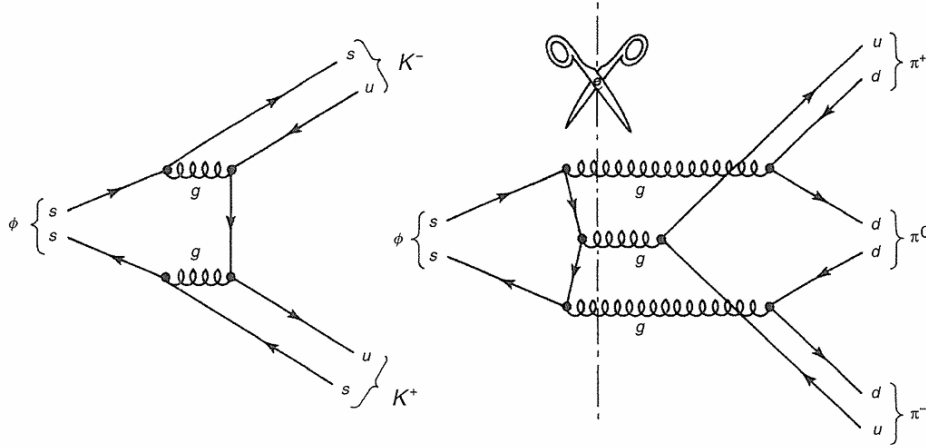


Figure 55 – The OZI rule states that if a Feynman diagram can be divided into two disconnected parts by cutting only gluon lines (without slicing through any external lines), the process is highly suppressed [15]

The Q-value of a decay process measures the energy released or absorbed during the reaction [60]. For the ϕ meson ($m_\phi \approx 1020$ MeV), the Q-values for the decay processes are:

$$\Delta Q_1 = (m_\phi) - (m_{K^+} + m_{K^-}) \approx 30 \text{ MeV} \quad \text{small phase space,} \quad (6.10)$$

$$\Delta Q_2 = (m_\phi) - (m_{\pi^+} + m_{\pi^-} + m_{\pi^0}) \approx 600 \text{ MeV} \quad \text{large phase space.} \quad (6.11)$$

Typically, higher Q-values indicate larger phase spaces, making the process more expected. For pionic decay, the phase space is approximately 20 times larger than that for kaonic decay.

Despite theoretical expectations favoring the pionic decay, experiments reveal that $\sim 50\%$ of phi mesons decay into kaons [61]. This discrepancy led physicists to the OZI rule: if the Feynman diagram of a decay can be separated into initial and final states by cutting only gluon lines, the decay is suppressed.

For the pionic decay, cutting the gluon lines separates the initial and final states entirely, necessitating high-energy gluons to produce hadrons in the final state. In contrast, for the kaonic decay, contributions from the strange quarks in the initial state persist throughout, reducing the required gluon energy. According to QCD's asymptotic freedom, higher-energy gluons couple weakly to quarks, suppressing the pionic decay relative to the kaonic decay.

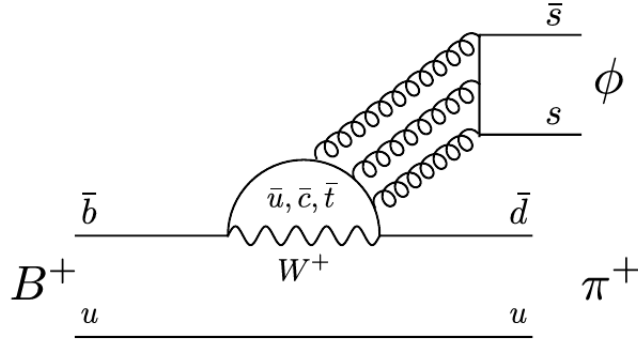


Figura 56 – $B \rightarrow \phi(\rightarrow KK)\pi$ diagram considering the ϕ meson is subject to suppression according to the OZI rule [16].

Figure 56 illustrates the decay diagram for the process $B \rightarrow \phi(\rightarrow KK)\pi$. As can be seen, for this type of decay, it is possible to entirely separate the gluon lines connecting the ϕ meson to the initial state. This characteristic indicates that this decay is suppressed according to the OZI rule.

The OZI rule also plays an important role in suppressing the hadronic decay modes of some charmonia meson, like the χ_{c0} and $J/\psi(1S)$ meson. For instance, the same principle applies, effectively suppressing the $J/\psi(1S) \rightarrow 3\pi$ decay channel and favoring transitions into two charmed D mesons. These D mesons are analogous to kaons but replace the strange quarks with charmed quarks. In this case, the combined mass of two D mesons exceeds the mass of the $J/\psi(1S)$, making the decay $J/\psi(1S) \rightarrow D^+D^-$ kinematically impossible. At the same time, the $J/\psi(1S) \rightarrow 3\pi$ process is strongly suppressed by the OZI rule. This rare combination of kinematic and dynamic factors contributes significantly to the extended lifetime (approximately 10^{-20} sec) of the $J/\psi(1S)$ particle, which is associated with its narrow decay width (approximately 90 KeV) [62].

6.2.3 Dynamical functions

As previously noted, T_r in Eq. 6.9 represents the lineshapes used to describe the resonance's propagator. While there is no single unique parameterization, the Breit-Wigner (BW) remains the primary method for describing resonances and serves as the foundation for other parameterizations. The most relevant parameterizations for this analysis are outlined below.

6.2.3.1 Breit-Wigner

Resonances are characterized by a phase variation that reaches 90° at m_0 (the pole of the resonance) and are typically described by the relativistic Breit-Wigner lineshape [63]. The expression is given by:

$$T_R(m_{ij}) = \frac{1}{m_R^2 - m_{ij}^2 - im_R\Gamma_{ij}(m_{ij})} \quad (6.12)$$

where m_{ij} is the two-body invariant mass corresponding to the two particles to which the resonance decays. The other components are resonance-dependent items, such as the nominal mass (m_R) and the mass-dependent width ($\Gamma_{ij}(m_{ij})$). In general, for a resonance decaying to spinless particles, the width can be expressed as:

$$\Gamma_{ij}(m_{ij}) = \Gamma_R \left(\frac{\vec{q}}{q_R} \right)^{2J+1} \frac{m_R}{m_{ij}} (F^2(|\vec{q}|d)), \quad (6.13)$$

where the $|\vec{q}|$ corresponds to the resonance's daughters momentum and $|q_R|$ is the $|\vec{q}|$ for $m_{ij} = m_R$. The Γ_R corresponds to the nominal width of the resonances and the values of m_R and Γ_R are obtained from the PDG [61].

6.2.3.2 Flatté

To describe resonances with an invariant mass distribution close to a two-particle threshold, the Flatté is often employed [64]. This function is used, for instance, to describe light scalar mesons like $f_0(980)$ and $a_0(980)$. As their mass is slightly below the K^-K^+ threshold, the parameterization is a variation of the relativistic Breit-Wigner distribution. The specific form for $f_0(980)$ is provided by:

$$T_{f_0(980)} = \frac{1}{m_{f_0}^2 - m_{K^-K^+}^2 - i[g_{f_0\pi^+\pi^-}^2 \rho_{\pi^+\pi^-} + g_{f_0K^+K^-}^2 \rho_{K^+K^-}]}, \quad (6.14)$$

where $g_{f_0\pi^+\pi^-} = 0.165$ and $g_{f_0K^+K^-} = 4.21 \times g_{f_0\pi^+\pi^-}$ are the $f_0(980)$ coupling constants to the $\pi^+\pi^-$ and K^-K^+ final states, respectively. The $\rho_{\pi^+\pi^-}$ and $\rho_{K^+K^-}$ are the phase space factors.

6.2.3.3 Gounaris-Sakurai

This parametrization is commonly used to describe broad resonances decaying into two pions, as $\rho^0(770)$, where an analytical dispersive component is incorporated to maintain unitarity at distances far from the pole mass. It is a modification of the Breit-Wigner lineshape, with a width depending on the 2 pions invariant mass computed following the method proposed by [65].

$$T(s) = \frac{1 + \frac{D\Gamma_0}{m_0}}{(m_0^2 - s) + f(s) - im_0\Gamma(s)} \quad (6.15)$$

where $f(s)$ is a mass-dependent term expressed as:

$$f(s) = \frac{\Gamma_0 m_0^2}{q_0^3} \left[q^2 (h(s) - h(m_0^2)) + (m_0^2 - s) q_0^2 \frac{dh}{ds} \Big|_{m_0^2} \right], \quad (6.16)$$

where

$$h(s) = \frac{2q}{\pi\sqrt{s}} \log\left(\frac{\sqrt{s} + 2q}{2m_\pi}\right), \quad (6.17)$$

and

$$\left.\frac{dh}{ds}\right|_{m_0^2} = h(m_0^2) \left[(8q_0^2)^{-1} - (2m_0^2)^{-1} \right] + (2\pi m_0)^{-1}, \quad (6.18)$$

The constant parameter D is given by:

$$D = \frac{3m_\pi^2}{\pi q_0^2} \log\left(\frac{m_0 + 2q_0}{2m_\pi}\right) + \frac{m_0}{2\pi q_0} - \frac{m_\pi^2 m_0}{\pi_0^3}. \quad (6.19)$$

6.2.3.4 Non-resonant contribution

While the BW function is commonly used for resonances, the situation is different for non-resonant contributions. Various empirical approaches can be employed to model non-resonant contributions. For instance, in the case of D -meson decays, where the phase space is relatively small, non-resonant contributions are typically modeled as flat across the Dalitz plot. For B -meson decays, which have significantly larger phase space, exponential form factors are often used [66]. We present some parametrization for this below:

(i) Flat non-resonant

A straightforward approach to parameterize the non-resonant contribution is by employing a flat function that uniformly fills the entire Dalitz Plot. This flat function ignores any dynamics involved in the decay. Nevertheless, it can also be very helpful as it can facilitate the visualization of other lineshapes of resonant states, and non-resonant or rescattering components in the Dalitz plot.

(ii) BelleNR

It represents the simplest empirical non-resonant exponential:

$$R(m) = e^{-\alpha m^2}, \quad (6.20)$$

where the α is a float parameter.

(iii) LASS_NR

The approximation of the BW function is not that good for the $K\pi$ S-wave, which includes the $K_0^*(1430)$ resonance. This resonance strongly interferes with a slowly varying non-resonant term. To address this, the LASS lineshape [14] was introduced to properly combine these amplitudes:

$$T(m) = \frac{m}{q \cot \delta_B - iq} + e^{2i\delta_B} \frac{m_0 \Gamma_0 \frac{m_0}{q_0}}{(m_0^2 - m^2) - im_0 \Gamma_0 \frac{q}{m} \frac{m_0}{q_0}}, \quad (6.21)$$

$$\text{with } \cot \delta_B = \frac{1}{aq} + \frac{1}{2}rq. \quad (6.22)$$

The first term of Eq. 6.21 corresponds to the non-resonant part, while the second term accounts for the resonant contribution. The m_0 and Γ_0 denote the pole mass and width of the $K_0^*(1430)$, respectively, while a and r are parameters defining the shape.

(iv) Polar form factor

A different approach to non-resonant parameterization employs a lineshape with a pole (which is a specific value of the mass where the magnitude reaches its maximum) form factor of the type $(1 + \frac{s}{\Lambda^2})^{-1}$, as proposed in [67]. Following the authors, this form factor offers a phenomenological representation to describe the non-resonant amplitude, highlighting the low-energy production region of the final-state particles. Consequently, this amplitude is more pronounced near the pair threshold and diminished in high-energy regions. The parameterization is expressed as:

$$T_{nr}(m_{ij}^2) = \frac{1}{1 + \frac{m_{ij}^2}{\Lambda^2}}, \quad (6.23)$$

where $\Lambda = 1 \text{ GeV}/c^2$ as default value, taken from the fit to the $B^\pm \rightarrow \pi^\mp \pi^\pm \pi^\pm$ data [68]. This parametrization can be used for both $m_{\pi^\pm K^\mp}^2$ and $m_{K^\pm K^\mp}^2$.

6.2.3.5 The δ formulation

Analytically, in two-body to two-body scattering processes, it can be shown that possible scattering scenarios (such as $\pi\pi$ and $K\pi$) can be divided into elastic and inelastic regions. These regions are represented by a function in the form $\sin(\delta)e^{i\delta}$, where δ is the phase shift. This functional form captures the essential dynamics of scattering processes, allowing for a more accurate representation of the S -wave behavior in the decay analysis. This method enables the observation of phase variations of a complex amplitude within the Dalitz plot for three-body decays using an empirical way.

An important advantage of using the function $\sin(\delta)e^{i\delta}$ over the traditional Breit-Wigner (BW) function should be emphasized. While the BW function effectively captures individual resonances, it fails to account for the regions between resonances, where no peaks are observed. This limitation reduces its accuracy in describing the smooth transitions in these inter-resonance regions. Additionally, a simple sum of BW functions does not preserve the unitarity of the S-matrix, whereas the δ -based formulation inherently ensures unitarity, if we consider only this component.

Two different formats for δ will be used, which are:

- The $\delta_{s_{K\pi}}$: this approach was suggested in [69]. One of the key benefits of the $\delta_{s_{K\pi}}$ model is that it is an empirical method capable of “mimicking” the behavior of a resonance. The $\delta_{s_{K\pi}}$ is defined as:

$$\delta_{s_{K\pi}} = \frac{\pi}{1 + \exp(a(s_{K\pi} - m_0^2))}, \quad (6.24)$$

with a and m_0 as free parameters to be determined in the fit.

- The δ_{Pol} : the primary objective of this alternative approach is to employ a generic function to serve as the phase representation. In this context, we select a fourth-degree polynomial as a function of the mass. It is an effective tool for understanding the data when existing possibilities have been exhausted. By avoiding a predetermined functional form, this approach allows the fit to freely adapt and model the phase in a manner that best aligns with the data. For instance, the δ_{Pol} can be defined as:

$$\delta_{Pol} = A_1 \cdot \text{mass}^4 + B_2 \cdot \text{mass}^3 + C_3 \cdot \text{mass}^2 + D_4 \cdot \text{mass} + E_5 \quad (6.25)$$

The A_1 to E_5 are the free parameters. It is important to note that this approach is generic enough to allow changing the polynomial’s order, if necessary, to achieve a better description of the data.

6.2.3.6 The $\pi\pi \rightarrow KK$ Rescattering

Considering that the rescattering amplitude is not a resonant contribution, yet it is also not classified as a non-resonant contribution (despite fulfilling a similar role from a certain perspective), it is treated in a separate section to emphasize its distinct nature and characteristics.

In characterizing a rescattering amplitude within the framework of three-body decays, it is essential to consider various aspects for its definition. One aspect is the function representing its source (which is essentially the origin of the rescattering), while another is the functional structure of the transition amplitude components. The idea of the rescattering process $\pi\pi \rightarrow KK$ originated from two-body interactions in the context of three-body decays, implying that a meson pair produced in one channel will emerge in the final state of an interconnected channel. The phenomenological form factor that accounts for the source term is introduced in [67]. When aiming to define the rescattering amplitude for the $\pi\pi \rightarrow KK$ process, the source term is formulated as:

$$\mathcal{A}_{source}(m_{K^-K^+}^2) = \frac{1}{1 + \frac{m_{K^-K^+}^2}{\Delta_{\pi\pi}^2}}, \quad (6.26)$$

where $\Delta_{\pi\pi}^2$ is a parameter taken from the fit to the $B^\pm \rightarrow \pi^\mp \pi^\pm \pi^\pm$ [68] and set to $1 \text{ GeV}/c^2$. Similarly, the representation of the source term for the rescattering phenomenon $KK \rightarrow \pi\pi$ will be described by Equation 6.28, using Δ_{KK}^2 instead of $\Delta_{\pi\pi}^2$. We have constrained the amplitude parameterizations used in $\pi\pi - KK$ derived from scattering data [17]. The objective is to characterize the partonic interaction (tree and penguin diagrams at the quark level) that produces the three mesons.

In this study, the authors analyzed $\pi\pi \rightarrow KK$ scattering data, obtaining a set of unconstrained fits (UFD) for each partial wave g_l^I , where l and I represent the angular momentum and isospin, respectively. Of particular interest is the scalar-isoscalar wave g_0^0 , for which they provided two alternative fits, UFD_B and UFD_C, to accommodate two conflicting data sets. They also introduced constrained fits (CFD), which were designed to both describe the data accurately and satisfy theoretical consistency conditions. These constrained parameterizations of the g_0^0 wave, labeled CFD_B and CFD_C, were found to work well across most of the energy range, except very close to the threshold. All these alternative fits will be explored, as detailed in a subsequent section.

This interaction is presumed to differ for the meson pairs $\pi\pi$ and KK . The overall rescattering amplitude in the B three-body decay is thus formulated as:

$$\mathcal{A}_{scatt} = \mathcal{A}_{source} S_{rescattering}, \quad (6.27)$$

$$\mathcal{A}_{scatt} = |g_0^0(s)| e^{i\phi_0^0(s)} \frac{1}{1 + \frac{m_{K-K^+}^2}{\Delta_{KK}^2}}, \quad (6.28)$$

where the $|g_0^0(s)|$ and $\phi_0^0(s)$ are the magnitude and phase, respectively. The $\pi\pi - KK$ amplitude model is divided into two regions. The first one, Region I, from $\sqrt{s_{min,I}} = 2m_K$, which is the KK production threshold, up to $\sqrt{s_{max,I}} = 1.47 \text{ GeV}$, where dispersion relations can be used effectively. The second, Region II, from $\sqrt{s_{min,II}} = 1.47 \text{ GeV}$ up to $\sqrt{s_{max,II}} = 2 \text{ GeV}$ is also modeled, although dispersion relations are not applicable in this region. The magnitude and phase are parameterized as:

$$|g_0^0(s)| = \begin{cases} \sum_{n=0}^3 D_n p_n(x_I(s)) : & \text{Region I} \\ \sum_{n=0}^4 F_n p_n(x_{II}(s)) : & \text{Region II} \end{cases} \quad (6.29)$$

and

$$\phi_0^0(s) = \begin{cases} \sum_{n=0}^3 B_n p_n(x_I(s)) : & \text{Region I} \\ \sum_{n=0}^5 C_n p_n(x_{II}(s)) : & \text{Region II} \end{cases} \quad (6.30)$$

where the p_n are the Chebyshev polynomials, remapping s to lie within the range $[-1, +1]$, in each region. They are given by:

$$\begin{aligned} p_0(x) &= 1, & p_1(x) &= x, \\ p_{n+1}(x) &= 2xp_n(x) - p_{n-1}(x). \end{aligned}$$

Both, the constrained fit to data (CFD) and unconstrained results (UFD) were tested, as will be shown in a further section. The latter do not impose dispersive constraints, while the constrained CFD do. The coefficients B , C , D , and F listed in Table 17 satisfy the continuity conditions between regions:

$$B_0 = \delta_0^{(0)}(s_K) + B_1 - B_2 + B_3 \quad (6.31)$$

$$C_0 = \phi_0^0(s_{max}, I) + C_1 - C_2 + C_3 - C_4 + C_5, \quad (6.32)$$

$$F_0 = |g_0^0(s_{max}, I)| + F_1 - F_2 + F_3 - F_4. \quad (6.33)$$

$$(6.34)$$

Considering the Watson's theorem, at the KK threshold, the $\pi\pi - KK$ scattering phase ϕ_0^0 should match the elastic $\pi\pi - \pi\pi$ phase shift $\delta_0^{(0)} = (226.5 \pm 1.3)^\circ$, which impose the continuity condition B_0 .

Parameter	Value	Parameter	Value ($^\circ$)
D_0	0.59 ± 0.01	δ_{sK}^0	$+226.5 \pm 1.3$
D_1	-0.38 ± 0.01	B_1	23.6 ± 1.3
D_2	0.12 ± 0.01	B_2	29.4 ± 1.3
D_3	-0.09 ± 0.01	B_3	0.6 ± 1.6
F_1	-0.04329 (fixed)	C_1	34.3932 (fixed)
F_2	-0.008 ± 0.009	C_2	4.4 ± 2.6
F_3	-0.028 ± 0.007	C_3	-32.9 ± 5.2
F_4	0.026 ± 0.007	C_4	-16.0 ± 2.2
		C_5	7.4 ± 2.4

Tabela 17 – Parameters and their values extracted from Tables 3 and 4 of [17].

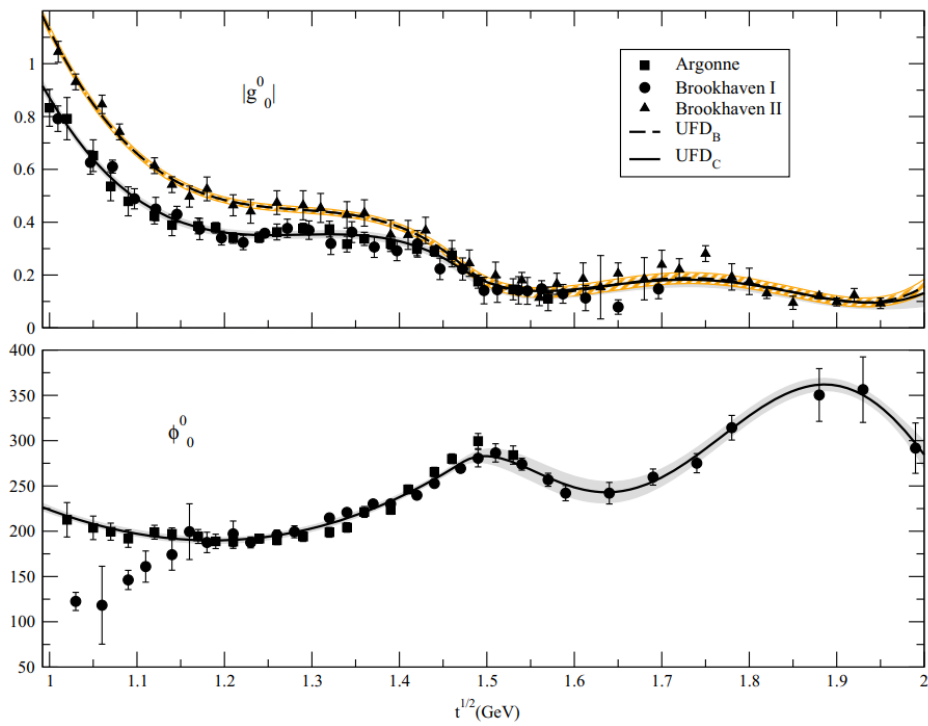


Figura 57 – Upper panel: the modulus of $\pi\pi - KK$ scattering. Lower panel: the phase for $\pi\pi - KK$ scattering. Figure extracted from [17].

7 Dalitz Plot Fit

In this chapter, we will outline the essential components and methods required for constructing and performing a fit, as well as discuss the key metrics used to evaluate the fit results. The aim is to provide a clear understanding of each component involved in the fitting process. Additionally, we will introduce the figures of merit - statistical measures and diagnostic tools - that serve to assess the quality and accuracy of the fit, ensuring that the results are both robust and reliable.

7.1 Acceptance

To accurately determine the physical CP asymmetry, we must correct for differences in detection efficiency and the production rates of B^+ and B^- particles, as these factors are not accounted for in the Monte Carlo (MC) simulations. Such variations can introduce a charge asymmetry that may vary across the Dalitz plot. Therefore, it is crucial to evaluate and correct efficiency differences separately.

Furthermore, the level-0 trigger is not precisely modeled in the MC. To address this, we use absolute trigger efficiencies derived from calibration data. In the decay $B^\pm \rightarrow K^\mp K^\pm \pi^\pm$, both signal and background events are often concentrated near the kinematic boundaries of the phase space. These boundary regions, although covering a small portion of the total phase space, show more pronounced variations in signal efficiency. To improve resolution in these high-sensitivity areas, we employ the Square Dalitz Plot (SDP) representation. This approach expands the corners and edges of the Dalitz plot relative to its less populated center, allowing for finer detail in regions with higher event density.

For this analysis, we apply the phase-space acceptance correction using large, uniformly generated MC samples in the Square Dalitz plot. This ensures that efficiency variations are accurately accounted for across the entire phase space, enhancing the precision of the CP asymmetry measurement.

The acceptance map is generated by year, subsample of L0 trigger configuration. A detailed description of each component is given in the following:

- Year: The acceptance maps are separated by year (2015, 2016, and 2017) to account for differences between the three periods of data taking.
- Polarity: Separated by each magnet polarity to take into account the left-right asymmetry of the detector.

- Trigger configuration: A separation in TOS and TISnotTOS subsamples is performed to account for possible differences between data and MC concerning the *L0Hadron_TOS* trigger efficiency. Once the acceptance maps are generated, a L0 trigger efficiency correction is applied.

Acceptance maps for each subsample are generated using the same selection criteria applied to the data, excluding the PID cuts. PID efficiency weights are derived from the PIDCalib package [70] and are applied to each event. Since the MC generation is not perfectly uniform in the squared Dalitz plot, we also use an unbiased simulated sample generated without any cuts, which is then projected onto a histogram in the square variables and normalized to the actual number of events generated before filtering. Acceptance is then determined by dividing two histograms with the same binning: the histogram with all the selection cuts is divided by the histogram of the uniformly generated events distributed over a 4π solid angle. The binning scheme selected for this process is 30×30 .

7.2 Selection and PID

Since the PID variables are generally not accurately represented in MC simulation samples, a data-driven approach is employed to determine the PID efficiency for the PID cuts listed in Table 6. In MC simulations, factors such as temperature fluctuations, non-linear effects like magnetic field distortions in the detector, and variations in the performance of the RICH detectors across different data recording periods within the year, are not taken into account. This results in an unreliable simulation of the PID variables, leading to significant systematic errors if PID efficiency were derived from them. Therefore, the efficiency for identifying pions and kaons is obtained using the PIDCalib package tools. This package uses a data-driven technique that uses a full set of calibration samples of pions, kaons, and protons from the denominated golden nodes.

It is crucial to consider that track identification depends on its kinematics and that there is a correlation between the kinematic variables of the tracks in the final state. The PID efficiency is therefore determined in bands of kinematic variables, with the most commonly used being momentum (p), pseudorapidity (η), and the number of tracks. However, the latter has proven to be not entirely well-reproduced by simulation samples. For technical reasons, we opted to divide the phase space into bins of p and η (2D-plane) using an appropriate adaptive binning method. This approach aims to achieve a uniform PID efficiency distribution as a function of momentum and pseudorapidity for the cuts applied to pions and kaons. The resulting ntuple from matching the efficiency tables with the analysis sample provides the overall PID efficiency for each event, separated by charge. This efficiency is then used to construct the acceptance maps.

7.2.1 Trigger correction

A correction to the acceptance is performed to account for the differences between data and MC simulations regarding the L0Hadron_TOS trigger efficiency. This correction is applied to the mutually exclusive TOS and TISnotTOS MC subsamples. The process involves calculating the ratio of the L0_Hadron efficiencies for data and MC (data/MC) within the variables of the square Dalitz plot. The L0Hadron efficiency maps are constructed using the $\Lambda_b \beta \rightarrow \Lambda_c(pK\pi)\mu\nu$ Run II data samples. These correction histograms are then applied to the respective acceptance in each category.

The absolute efficiencies for data are obtained from calibration samples. This calculation is based on the track ID, magnet polarity, calorimeter location, and energy deposited, and it also considers the probability of tracks causing overlapping clusters in the calorimeter. The efficiency for a candidate is determined as the probability that at least one track or cluster triggers the calorimeter in the TOS case, and none in the TISnotTOS case. The corresponding MC efficiency is associated with events that fired the trigger.

7.2.2 Total Acceptance Maps

The total acceptance map is constructed by combining the acceptance maps of each category. For each year, the TOS and TISnotTOS histograms are combined in the same proportion as the data while maintaining overall normalization. Thus, a weight factor is defined:

$$w_{TOS}^{year} = R_{TOTAL}^{year} \times \frac{N_{TOS}^{DATA^{year}}}{N_{TOS}^{MC^{year}}}, \quad (7.1)$$

where “year” represents 2015, 2016, or 2017. The R_{TOTAL} is the ratio of the total number of events in the MC sample to the signal data sample. $N_{TOS}^{DATA^{year}}$ is the number of TOS events from the mass fit for the signal data, and $N_{TOS}^{MC^{year}}$ is the corresponding number from the MC sample. The same definition applies to the TISnotTOS configuration. The magnet up and magnet down subsamples are also combined proportionally according to the recorded luminosity for each year.

The total acceptance map by year can be represented as:

$$Acc^{year} = w_{TOS} \times Acc_{TOS}^{(Up+Down)} + w_{TISnotTOS} \times Acc_{TISnotTOS}^{(Up+Down)}, \quad (7.2)$$

where

$$Acc_{TOS}^{(Up+Down)} = w_{Up} Acc_{TOS}^{Up} + (1 - w_{Up}) Acc_{TOS}^{Down}, \quad (7.3)$$

and

$$Acc_{TISnotTOS}^{(Up+Down)} = w_{Up} Acc_{TISnotTOS}^{Up} + (1 - w_{Up}) Acc_{TISnotTOS}^{Down}, \quad (7.4)$$

are the acceptance histograms.

The final acceptance map can be seen in Fig 58 and 59 separated by charge, for B^+ and B^- respectively. As one can see, they are quite similar.

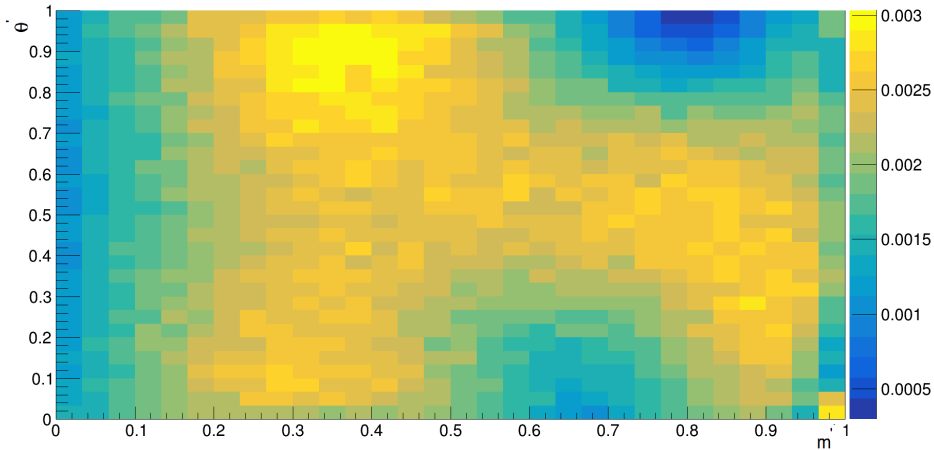


Figura 58 – Overall acceptance map for $B^+ \rightarrow \pi^+ K^+ K^-$.

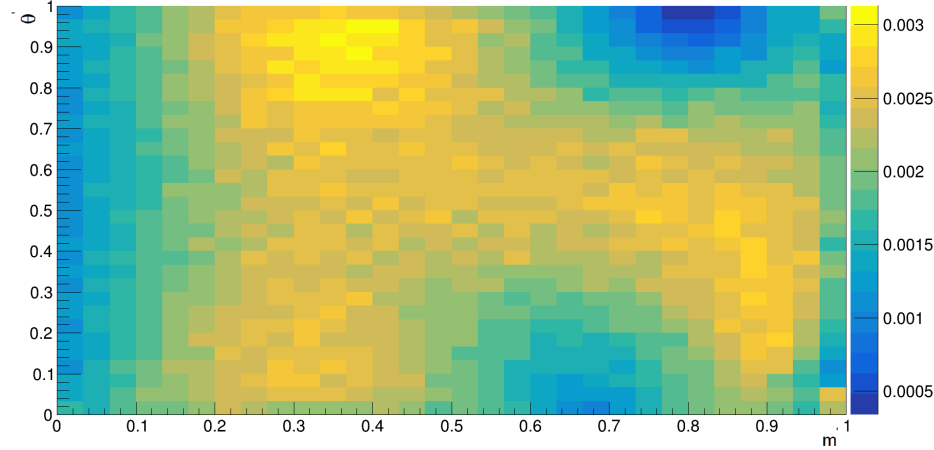


Figura 59 – Overall acceptance map for $B^- \rightarrow \pi^- K^- K^+$.

7.3 Background Models

Incorporating background parametrization is a key component of the Dalitz plot fit. During Run I, the standard method for modeling background across the phase space involved using sidebands. The signal-to-background ratio was determined from the B mass fit and then held constant throughout the amplitude analysis. Since the total background count in a sample is fixed, overestimating background entries in one region will necessarily result in an underestimation in another.

For the previous amplitude analysis of $B^\pm \rightarrow K^\mp K^\pm \pi^\pm$ with Run I data [19], the background model consisted of three main components: combinatorial background, peaking background, and a prompt contribution. The combinatorial background was the largest component, accounting for random combinations of particles. The peaking background aimed to capture reflection events, while the prompt contribution included potential direct entries from decays involving the $\phi(1020)$ resonance.

It's important to recognize that the sidebands often display structures that do not accurately represent the true background. This limitation is especially relevant for $B^\pm \rightarrow K^\mp K^\pm \pi^\pm$, where a large portion of the central region is dominated by background entries, potentially leading to inaccuracies with this approach.

For the Run II data analysis, a new methodology has been introduced [71]. This updated approach constructs the background histogram directly from the signal region, eliminating the reliance on sidebands. The procedure consists of the following steps:

- The Dalitz Plot is divided into bins that are as small as possible, yet sufficiently large to allow for a meaningful fit.
- For each bin, a fit is performed on the B mass projection to estimate the background. The background histogram is then constructed using the fit results.
- It is often challenging to achieve small bins due to the insufficient quantity of entries required to perform a fit. Consequently, different bin configurations were tested, and those not selected were considered for the study of systematic error.
- In cases where larger bins are necessary, the method employs the sPlot tool to enhance the background distribution [72].

This method aims to provide a more accurate background representation by using the signal region and employing advanced statistical tools to address the limitations posed by bin size constraints. The number of bins selected also depends on the number of events in each bin, with the understanding that the number of events per bin is nearly uniform. Various simple functions were used in an attempt to obtain better mass fits within each bin, considering: 1 Gaussian + 1 Crystal-Ball, 2 Gaussians + 1 Crystal-Ball, 2 Gaussians, and 1 Gaussian, all applied separately for B^- and B^+ , for the signal and an exponential for the background.

The binning method employed in this analysis is adaptive, as the bins are distributed according to the number of events in each region. Less populated regions tend to have larger bins, while smaller bins characterize denser regions. The chosen number of bins represents a balance between having sufficient events in each bin, as a low number of events can lead to poorer fits and maintaining a reasonable number of bins that can adequately

describe the phase space. This approach ensures that an insufficient number of bins does not obscure potential imperfections in the background description. Appendix B presents the results of the fits per bin of the Square Dalitz Plot.

7.3.1 Total background model

The final result of the background model used for the Dalitz Plot fits can be seen in Fig 60 and 61, for B^- and B^+ . A yellow streak can be observed in both plots, running diagonally between 0.1 and 0.7 in m' representing the $B \rightarrow K\pi\pi$ reflections. The appearance of this background indicates the new method's ability to capture this contribution without the need for additional background components. In this case, a Gaussian function was used for the signal events within the event window between 5140 and 5450 MeV for each bin.

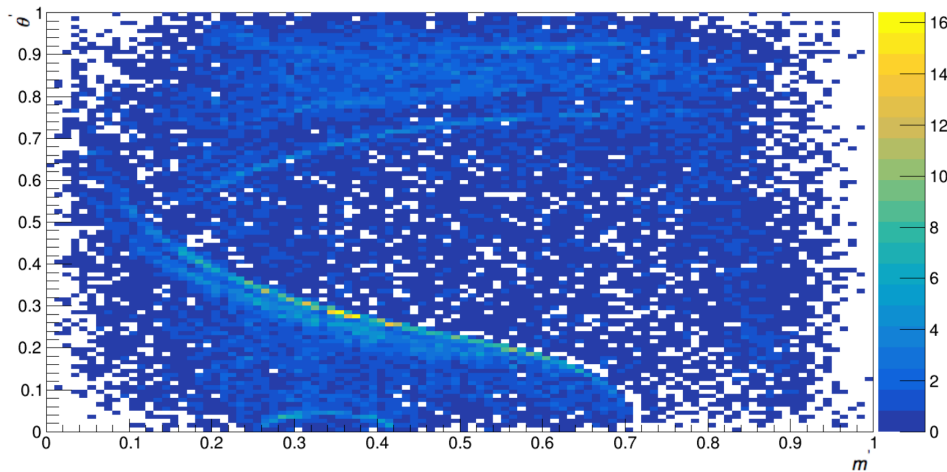


Figura 60 – Background model for $B^- \rightarrow \pi^- K^- K^+$.

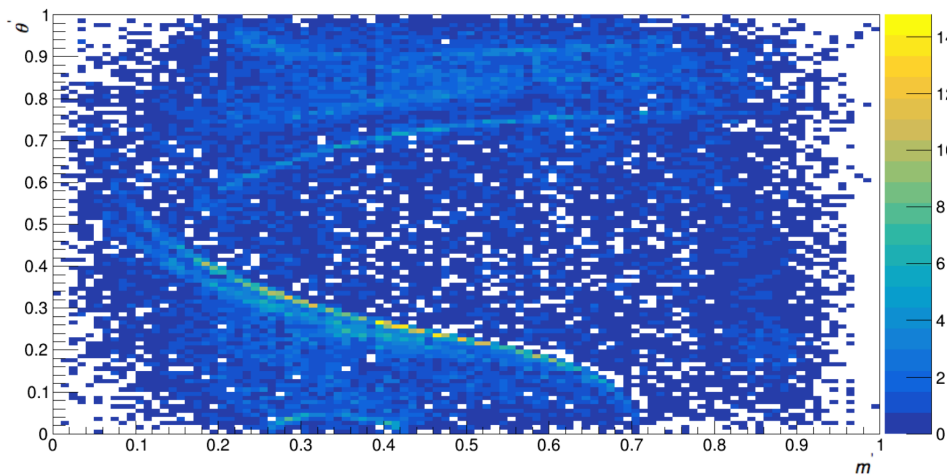


Figura 61 – Background model for $B^+ \rightarrow \pi^+ K^+ K^-$.

7.4 Quantitative metrics for evaluation

Several metrics are utilized to evaluate the results of the Dalitz Plot fits. This section is dedicated to explaining some of these parameters as well as their level of relevance according to the study in question.

7.4.1 The probability density function

To accurately fit the event distribution observed in the Dalitz plot, several key considerations are required. First, each event in the phase space has a certain probability of being either signal or background, which must be accounted for. Second, the complex coefficients c_i need to be properly parameterized to represent the contributions of different resonances. The total decay amplitude model, \mathcal{A} , depends on a set of parameters, whose optimal values are determined by performing a maximum likelihood fit. This fitting method aims to estimate the unknown parameters based on the observed data.

The probability density function (PDF), denoted $P(x|\alpha)$, represents the distribution of the observable data x given a set of parameters α . Here, x represents the event data, and α represents the parameters we aim to estimate. In contrast, the likelihood function $\mathcal{L}(\alpha) = P(x|\alpha)$ is a function of the parameters given the observed data. Considering that the PDF describes the probability distribution of the data, it is normalized to one, while the likelihood function, used for parameter estimation, does not require normalization.

If we have n independent observations of x , we can write the likelihood function for the entire data set as:

$$\mathcal{L}(\alpha) = \prod_i^n P(x_i|\alpha) \quad (7.5)$$

The maximum likelihood estimators for the parameters are those that maximize the likelihood function. In a physical measurement context, this means that these parameter values make it most likely for nature to produce the observed data. To find these optimal values, we minimize twice the negative log-likelihood, $\text{NLL}(\text{or FCN}) = -2 \ln \mathcal{L}$. This approach is chosen for computational efficiency, as the optimization algorithm can handle the log-likelihood more easily. By converting multiplications into sums, calculations are simplified, and the method becomes numerically more stable.

In this analysis, we use the negative log-likelihood function. The optimizer MINUIT, which is specifically designed to minimize function outputs, is employed for this task. MINUIT works in conjunction with the LAURA++ software toolkit [73], which is used to perform the Dalitz plot fit. Minimizing the negative log-likelihood function is equivalent to maximizing the log-likelihood (and hence the likelihood itself), making it an effective approach for parameter estimation. The relationship that $-\ln \mathcal{L}$ must satisfy is:

$$-\frac{\partial}{\partial\alpha}\ln\mathcal{L} = -\frac{\partial}{\partial\alpha}\sum_i^n \ln P(x_i|\alpha) = 0 \quad (7.6)$$

If it were not for the efficiency effects, the signal probability density distribution would be simply given by the square of the total decay amplitude \mathcal{M} , as shown in Eq 6.8. This can be expressed as¹:

$$P_{sig}(m_{\pi^+K^-}^2, m_{K^+K^-}^2 | c_i) = |\mathcal{M}(m_{\pi^+K^-}^2, m_{K^+K^-}^2 | c_i)|^2. \quad (7.7)$$

Due to the effects of the efficiency variations across the Dalitz Plot, the PDF must be corrected for each event. The modified expression for the signal PDF, which accounts for efficiency throughout the phase space, is given by:

$$P_{sig}(m_{\pi^+K^-}^2, m_{K^+K^-}^2, c_i) \propto \epsilon(m_{\pi^+K^-}^2, m_{K^+K^-}^2, c_i) \times P'_{sig}(m_{\pi^+K^-}^2, m_{K^+K^-}^2, c_i). \quad (7.8)$$

The total signal probability density function considering both particle and antiparticle is:

$$P_{sig}(m_{\pi^+K^-}^2, m_{K^+K^-}^2 | c_i) = \frac{\frac{1+q_B}{2}\epsilon(m_{\pi^+K^-}^2, m_{K^+K^-}^2) |\mathcal{A}(m_{\pi^+K^-}^2, m_{K^+K^-}^2)|^2}{N_s} + \frac{\frac{1-q_B}{2}\bar{\epsilon}(m_{\pi^-K^+}^2, m_{K^-K^+}^2) |\bar{\mathcal{A}}(m_{\pi^-K^+}^2, m_{K^-K^+}^2)|^2}{N_s}, \quad (7.9)$$

where the q_B is the charge of the B-meson candidate and ϵ stands for the reconstruction efficiency variations. Each different contribution is individually normalized over the phase space, the N_s is the normalization factor and is given by:

$$N_s = \iint_{DP} \left(\epsilon(m_{\pi^+K^-}^2, m_{K^+K^-}^2) |\mathcal{A}(m_{\pi^+K^-}^2, m_{K^+K^-}^2)|^2 + \left(\bar{\epsilon}(m_{\pi^-K^+}^2, m_{K^-K^+}^2) |\bar{\mathcal{A}}(m_{\pi^-K^+}^2, m_{K^-K^+}^2)|^2 \right) \right) \times d^2m_{\pi^\pm K^\mp} d^2m_{K^+K^-} \quad (7.10)$$

which we calculate using Gauss-Legendre integration methods [74].

The overall probability density function must also consider the background, as mentioned in 7.3. The total PDF is then:

$$P_{total}(m_{\pi^\pm K^\mp}^2, m_{K^+K^-}^2 | c_i) = N_{sig} P_{sig}(m_{\pi^\pm K^\mp}^2, m_{K^+K^-}^2 | c_i) + N_{bkg} P_{bkg}(m_{\pi^\pm K^\mp}^2, m_{K^+K^-}^2 | c_i), \quad (7.11)$$

¹ We have the same for the CP-conjugate process

where the P_{sig} is the signal PDF, the P_{bkg} is the background PDF. N_{sig} and N_{bkg} are the relative contributions number of events of signal and background, respectively, and were obtained from the 1D mass fit. One can notice that the dependence of the complex coefficients c_i is only considered in the signal PDF, once the background modelling is totally fixed in the Dalitz Plot fit.

The Likelihood function for $B^\pm \rightarrow K^\mp K^\pm \pi^\pm$ is constructed using the total probability function referred as in Eq 7.11 and is expressed as:

$$\mathcal{L} = \exp\left(-\sum_k N_k\right) \times \prod_i^N \left(\sum_k N_k P_k^i(m_{\pi^\pm K^\mp}^2, m_{K^+ K^-}^2)\right), \quad (7.12)$$

where the N_k is the yield for the event category k (signal or background), N is the total number of candidates and P_k^i is the PDF for the category k for event i .

The optimal values of the fitted parameters are determined by minimizing the negative log-likelihood, $-2\ln\mathcal{L}$. Due to the multidimensional nature of Dalitz plot analyses, the results can vary depending on the initial parameter values, often converging to a local rather than global minimum of the $-2\ln\mathcal{L}$ function. To seek the global minimum, numerous fits are conducted where the initial values of the complex coefficients c_i of each lineshape are randomized. The fit yielding the smallest $-2\ln\mathcal{L}$ value from this ensemble is then considered the nominal result, taking into account the physical implications as well.

7.4.2 The coefficient c_i

It is important to highlight that c_i is distinct from \bar{c}_i to allow CP violation, and they represent the relative contribution of the component i . These are expressed in the Cartesian convention for CP violation:

$$c_i = (x_i + \Delta x_i) + i(y_i + \Delta y_i), \quad (7.13)$$

$$\bar{c}_i = (x_i - \Delta x_i) + i(y_i - \Delta y_i), \quad (7.14)$$

where x_i , y_i , Δx_i , Δy_i are the CP-conserving (-violating) components of the decay amplitude. Using the Polar coordinate system:

$$c_i = a_i^+ e^{i\delta_i^+}, \quad (7.15)$$

$$\bar{c}_i = a_i^- e^{i\delta_i^-}, \quad (7.16)$$

where the a_i^\pm and δ_i^\pm are the magnitude and phase, respectively, for the component i for B^\pm . The phase δ_i^\pm is composed of the weak and strong phases, while the \mathcal{A}_j (mentioned

in 6.2) can contribute only to the strong phase. The relation between Cartesian and Polar Coordinates, for B^+ and B^- , is:

$$a_i^\pm = \sqrt{(x_i \pm \Delta x_i)^2 + (y_i \pm \Delta y_i)^2}. \quad (7.17)$$

$$\delta_i^\pm = \tan^{-1}\left(\frac{y_i \pm \Delta y_i}{x_i \pm \Delta x_i}\right). \quad (7.18)$$

Typically, using Cartesian coordinates eliminates the issue of positive definite values encountered with polar coordinates. However, this approach results in fitted parameters that are less intuitive to interpret.

7.4.3 Fit Fractions and CP Asymmetry

The main results of the Dalitz-plot fit are the complex Isobar coefficients c_i . However, these coefficients depend on the chosen phase convention, amplitude formalism, and normalization, making direct comparisons between analyses challenging. Therefore, it is more practical to compare fit fractions. These are defined as the integral of the absolute value of the squared amplitude for each intermediate component, i , divided by the integral of the squared coherent matrix element for all intermediate contributions:

$$FF_i = \frac{\iint (|c_i \mathcal{M}_i|^2 + |\bar{c}_i \bar{\mathcal{M}}_i|^2) dm_{\pi^\pm K^\mp}^2 dm_{K^+ K^-}^2}{\iint (|\mathcal{A}|^2 + |\bar{\mathcal{A}}|^2) dm_{\pi^\pm K^\mp}^2 dm_{K^+ K^-}^2} \quad (7.19)$$

Since the denominator comes from the coherent sum of all contributions, these fit fractions do not necessarily sum to unity in the presence of net constructive or destructive interference.

Another powerful tool utilized for analyzing the data is CP asymmetry linked to each resonant state in the model is computed based on its respective magnitudes and phases obtained from the fit, which are dependent on x , y , Δx , Δy . The relationship is expressed as:

$$A_{CP,i} = \frac{|\bar{c}_i|^2 - |c_i|^2}{|\bar{c}_i|^2 + |c_i|^2} = \frac{-2(x_i \Delta x_i + y_i \Delta y_i)}{(x_i)^2 + (\Delta x_i)^2 + (y_i)^2 + (\Delta y_i)^2} \quad (7.20)$$

It is important to mention that CP violation can still occur even when the CP asymmetry parameter A_{CP} is zero, as the difference between \bar{c}_i and c_i can arise from phase differences between components. Since absolute phases cannot be measured, CP violation is detected through these phase differences, which represent the interference between two components of the model.

7.4.4 Multiple solutions

The fit results are highly sensitive to the parameters x_i , y_i , Δx_i , and Δy_i , presented in Section 7.4.2. Therefore, obtaining a coherent set of these parameters is a crucial step in achieving a stable fit. The parameter space is explored by randomizing the initial values of x_i , y_i , Δx_i , and Δy_i . However, depending on the model being fitted to the data, different sets of parameters may emerge as valid solutions. It is in this context that the phenomenon of multiple solutions arises.

In quantum mechanics, observables are connected to the squared modulus of amplitudes, and the total amplitude is determined by the sum of contributions from multiple amplitudes. The mathematical nature of extracting these amplitudes from experimental data often leads to this phenomenon known as multiple solutions. This occurs due to the quadratic relationship between observables and amplitudes, allowing different parameter sets to produce equally valid fits to the data [75].

The method employed in these analyses to select the optimal result in scenarios involving multiple solutions involves randomizing the parameters x_i , y_i , Δx_i , and Δy_i , and evaluating the outcomes based on the lowest NLL values and the most frequently occurring NLLs. Additionally, ideally, if all components correspond to partial waves with distinct quantum numbers, the total fit fractions should sum to 100%. However, in the presence of interference effects among the components, small deviations from 100% are expected. Consequently, results exhibiting total fit fraction sums significantly deviating from 100% may be considered invalid solutions (or non-physical results).

7.4.5 Wilks' Theorem and the Likelihood Ratio Test

As discussed previously, the Negative Log-Likelihood serves as a critical figure of merit for evaluating the outcomes of fits. Generally, physical motivations play a significant role in guiding modifications to models, such as the presence of expected resonances in specific regions of the phase space or the visible agreement between the model and the data in Dalitz Plot projections (see Section 8.2). However, numerical and statistically significant results are equally essential for a robust analysis.

Directly comparing NLL values between models without accounting for changes in degrees of freedom can lead to biased conclusions. Furthermore, there is no universally fixed reference value for differences in NLL units that can be applied to all cases. For instance, if model X shows an improvement of 15 NLL units compared to model Y, how can we determine the statistical relevance of this difference? This is precisely where Wilks' theorem becomes crucial, providing a systematic framework to assess the statistical significance of changes in NLL across models.

The Wilks' Theorem is a statistical result used to determine the significance of

parameters in model fitting by using the Likelihood Ratio Test (LRT) [76]. It states that, under certain conditions, the difference in the log-likelihood values between a complete model and a reduced model follows a chi-square (χ^2) distribution, with degrees of freedom equal to the difference in the number of parameters between the models. This approach enables testing whether the addition of new parameters significantly improves the model fit to the data, thus providing a robust framework for hypothesis testing. The likelihood ratio is defined as:

$$\Lambda = \frac{\mathcal{L}(\theta_0)}{\mathcal{L}(\theta_1)} \quad (7.21)$$

where:

- $\mathcal{L}(\theta_0)$ is the maximum value of the likelihood function under the reduced model (hereafter referred to as θ_0).
- $\mathcal{L}(\theta_1)$ is the maximum value of the likelihood under the complete model (hereafter referred to as θ_1).

Thus, we can define the NLL_{ratio} as:

$$NLL_{ratio} = -2 \ln(\Lambda) = -2 \left(\ln \frac{\mathcal{L}(\theta_0)}{\mathcal{L}(\theta_1)} \right). \quad (7.22)$$

So, to determine whether the complete model significantly improves the fit, we compare $-2 \ln(\Lambda)$ with a critical value from the χ^2 distribution, which depends on *n.d.f.* (number of degrees of freedom) and the desired significance level (2 or 5 σ , for instance). The critical value of a χ^2 distribution is a threshold that determines the point at which the null hypothesis (which in our case is the reduced model) is rejected in a statistical test. It serves as a boundary that distinguishes between retaining or rejecting the null hypothesis, as outlined below:

- If $-2 \ln(\Lambda) \leq$ critical value: We do not reject null hypothesis θ_0 . This means that the simpler model is sufficient to describe the data, and the alternative model does not bring significant improvements.
- If $-2 \ln(\Lambda) >$ critical value: We reject the null hypothesis θ_0 in favor of θ_1 . This implies that the alternative model θ_1 , with additional parameters, significantly improves the fit of the data.

As a practical example, let us consider a scenario where a given reduced model yields a Negative Log-Likelihood (NLL) of -100 , while the complete model (which includes

an additional resonance) produces an NLL of -150 . Using Equation 7.22, the calculation becomes:

$$-2 \ln \Lambda \rightarrow -2 [\ln \mathcal{L}_{\text{reduced}} - \ln \mathcal{L}_{\text{complete}}] = -100 - (-150) = 50 \quad (7.23)$$

By introducing one additional resonance, we effectively add four degrees of freedom to the model (parameters x , y , Δx , Δy , as discussed in Section 7.4.2). Assuming that we aim to evaluate this hypothesis at a 5σ significance level, the statistical implications of the additional parameters can be assessed accordingly. The critical value of the χ^2 distribution corresponding to 4 *n.d.f.* and 5σ significance is 34.5550. If we compare Equation 7.23 with the critical value, we observe that:

$$50 > 34.5550 \quad (7.24)$$

which leads us to conclude that, in this hypothetical case, the null hypothesis should be rejected, and the complete model should be adopted.

However, the Wilk's Theorem has some limitations [77], such as:

- Bounded parameters: for this type, such as those restricted to positive values, the theorem may fail when the parameter lies on the boundary, causing the maximum likelihood estimator (MLE) distribution to split.
- Non-nested models: this case - where one model cannot be derived as a special case of the other — despite both MLEs potentially being Gaussian, they occupy distinct parameter spaces, preventing the test statistic from converging to a chi-square (χ^2) distribution.
- Insufficient data: searches for new physics phenomena, such as dark matter, often involve detecting rare signals against a background that experiments aim to suppress. When the signal is weak or the background level is minimal, there may not be enough data to rely on asymptotic approximations, like those applied in Wilks' theorem.

Therefore, it is important to be aware of some of the limitations associated with the use of Wilks' theorem, as discussed in the case presented in Appendix F. The Appendix G presents a toy study of the Wilks' theorem reliability.

8 Dalitz Plot fit results

This chapter presents the results of the Dalitz plot fits, which were conducted using the Isobar Model formalism. Efficiency and background models, as defined in Sections 7.1 and 7.3 respectively, were incorporated. Events within the designated signal region, as outlined in 5.3.2.1, were used.

The number of signal and background events used for normalizing the Dalitz plot fit is summarized in Table 19, based on the results of the $B^\pm \rightarrow K^\mp K^\pm \pi^\pm$ mass fit. Table 18 presents the resonance line shapes along with the mass and width values [61] used in the Dalitz plot fits. The signal asymmetry is allowed to float in the fit. The combinatorial background asymmetry is fixed to the value obtained from the mass fit presented in Table 13.

8.1 Preliminary observations

Since this is not the first amplitude analysis conducted for this channel, the natural starting point for this study is the results obtained in the Run I analysis [19]. In this

Resonance	Line shape	Mass [MeV]	Width [MeV]
$K^*(892)$	RBW	891.67	51.4
$K_0^*(1430)$	RBW	1425	270
κ	RBW, Pole	845	468
Non-resonant	PolarFFNR, FlatNR	-	-
$\rho(770)$	GS	775.26	147.4
$\rho(1450)$	RBW	1465	400
$\rho(1700)$	RBW	1720	250
$\rho(1900)$	RBW	1909	130
$f_2(1270)$	RBW	1275.5	185.9
$f_0(980)$	Flatté	990	10
$f_0(1370)$	RBW	1370	350
$f_2'(1525)$	RBW	1517.4	86.9
Rescattering	Rescattering	-	-
$\phi(1020)$	RBW	1019.461	4.269
$\chi_{c0}(1P)$	RBW	3414.71	10.5
Lass-NR	LASS	-	-
$J/\psi(1S)$	RBW	3096.9	0.09
$\delta_{S_{K\pi}}$	$\delta_{S_{K\pi}}$	-	-
BelleNR	RBW	-	-
δ_{Pol}	δ_{Pol}	-	-

Tabela 18 – Description of various resonances including their line shapes, masses, and widths.

Category	Number of events
Signal	26443
Background	8350

Tabela 19 – Signal and background events set on the Dalitz plot fit.

section, we will summarize the findings of the previous model, highlighting areas where improvements are necessary and where the additional data collected in Run II provides new opportunities for exploration. As will be detailed later, the chosen approach involves constructing a baseline model with essential updates to the Run I model. From this baseline, we will explore further refinements and address limitations in how the previous model represented the decay dynamics, incorporating insights from the earlier analysis.

There are inherent characteristics of the decay itself that we must consider carefully. Notably, significant integrated CP asymmetry was observed for this channel [1]. Additionally, even more pronounced asymmetries have been identified and reported in specific regions of the phase space. The mass fit performed only in the expected rescattering region ($1 < m^2(K^+K^-) < 2.25$ and $4 < m^2(K^+\pi^-) < 19$) shows a remarkable difference between B^- and B^+ , see Figure 62. The CP asymmetry reported for this region is about -60% [19].

Another notable feature is the strong pattern of destructive interference, which appears as a diagonal slice with almost no events, located in the high mass region of $m_{\pi^\pm K^\mp}^2$ around $15 \text{ GeV}^2/c^4$ and $20 \text{ GeV}^2/c^4$, and for $m_{K^+K^-}^2 < 3.5$, see Figure 63 and 64. From these figures, it is also visually evident that there is a clear difference between B^+ and B^- .

Considering that the total number of events has increased by nearly a factor of seven, the first attempt to model the $B^\pm \rightarrow K^\mp K^\pm \pi^\pm$ resonant structure with Run 1 results, showed itself as not enough. The increased statistic reveals structures that were not possible to identify before. The scrutiny of imperfections will be observed in the projections presented in the next section. This analysis aims to correct such imperfections and update the phenomenological description of the rescattering amplitude following the new model proposed by Pelaez and Rodas [17].

The significant contribution of $\rho(1450)^0$ to the $B^\pm \rightarrow K^\mp K^\pm \pi^\pm$ channel raises questions, especially since a recent study published a fit fraction for $B^\pm \rightarrow \pi^\pm \pi^+ \pi^-$ of about 5% [22], the preferred channel for this resonance. The corresponding $B \rightarrow \rho(1450)^0 \pi$ fit fraction is approximately 30%, an unexpectedly large contribution for the K^+K^- pair, as the dominant decay mode is $\pi\pi$, and the $\rho(1450)^0$ contribution in $B^\pm \rightarrow \pi^\pm \pi^+ \pi^-$ is observed to be much lower.

In general, a refined model will be constructed to account for possible new contributions and attempt to understand the overall dynamics of the decay process more comprehensively. Including these improvements is crucial for refining our theoretical

understanding and ensuring that the model fits the data more accurately and reliably reflects the underlying physical processes.

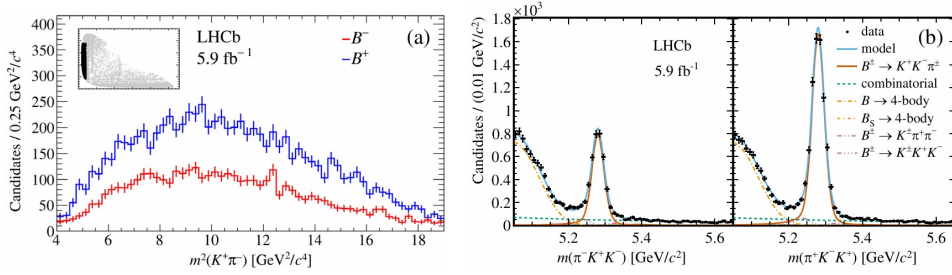


Figure 62 – (a) $m^2(K^+\pi^-)$ projection for the rescattering region with the $B^\pm \rightarrow K^\mp K^\pm \pi^\pm$ mass fits for the (b) region 1 (B^- on the left) [1].

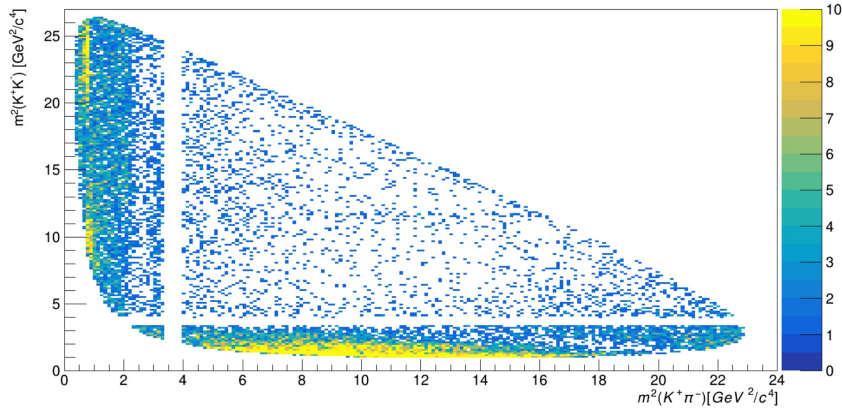


Figure 63 – Dalitz plot distribution for $B^+ \rightarrow K^- K^+ \pi^+$, the color scale indicates the number of events.

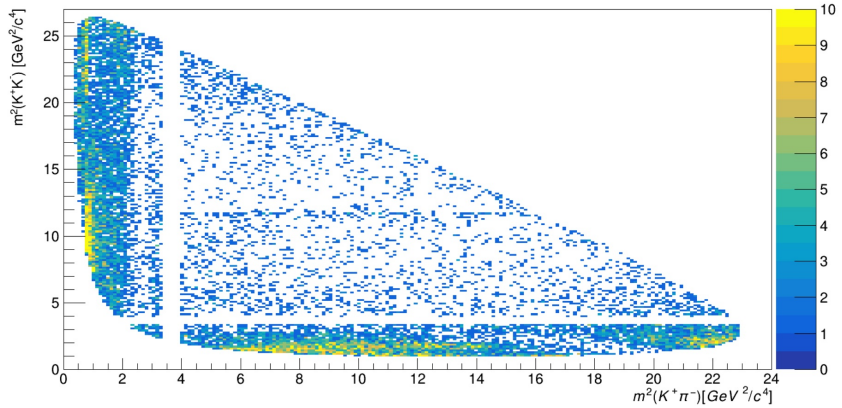


Figure 64 – Dalitz plot distribution for $B^- \rightarrow K^+ K^- \pi^-$, the color scale indicates the number of events.

In the strategy for the Dalitz plot fit, challenges are encountered in the scalar sector, where numerous potential contributions exist, and their signatures are not very clear due to the absence of angular distribution and broad structures. We must be very cautious in including scalar components because it is often possible to achieve better-fit results by allowing many contributions to interplay. However, this approach frequently produces unrealistic interference scenarios that are difficult to interpret.

8.2 Methodology for evaluating fit quality

The results are presented in a table detailing the fit fraction contributions for each resonance within the model, along with their respective magnitudes and phases for both B^+ and B^- , as shown in Sections 7.4.2 and 7.4.3. The direct CP asymmetry for each component is included, calculated according to Eq. 7.20. The $m_{K^-K^+}^2$ and $m_{K^+\pi^-}^2$ projections are compared against the model and background estimations. Additionally, the NLL values for each model, as outlined in Section 7.4.1, and the likelihood ratio results from Section 7.4.5, are employed to evaluate the fits.

This framework combines numerical tools and a visual inspection of how well the model aligns with the Dalitz Plot projections. It is important to emphasize that the decision to include a component will not rely on an isolated evaluation of these tools but rather on a combination of favorable numerical conditions and complementary insights from the physical analysis.

Throughout this analysis, the reference channel is the $K^*(892)K^+$, with its phase set to zero and magnitude allowed to vary freely in the fit. In Cartesian coordinates, this is represented as x fixed at one, y fixed at zero, Δx allowed to vary, and Δy fixed at zero (with the CP asymmetry allowed to vary, noting that Δx and Δy are the CP-violating parameters in the fit, see Eq. 7.18).

A practical approach to qualitatively evaluate how well the data and models align is by examining specific projections in key regions of the Dalitz Plot. These regions are of primary interest because they are where the essential dynamics of the decay are hypothesized to occur. Figure 65 and 66 present the projections of a generic fit result, to highlight the different phase space regions that will be studied and explored in detail.

In the case of Figure 65, the red and blue areas ($\cos Hel23 < 0$ and $\cos Hel23 > 0$ for $m_{K^\pm\pi^\mp}^2$ projection, respectively) highlight the low-mass regions of the $K\pi$ sector, where components such as $K^*(892)$, $K^*(1430)$, and the *PolarFFNR* are located. The light blue and orange areas ($\cos Hel13 > 0$ and $\cos Hel13 < 0$ for $m_{K^+K^-}^2$ projections) show the low-mass regions of the KK sector, where components like the $\rho(1450)$, rescattering, and $f_2(1270)$ are situated. The yellow and green areas show the diagonal projections of the decay. The other two are the $m_{K^\pm\pi^\mp}^2$ and $m_{K^+K^-}^2$ projections with no specific resonance associated. The blue line represents the model, the black dots represent the data, and the red area indicates the background estimation.

For Figure 66, the yellow ($m_{K^\pm\pi^\mp}^2 > 4$), black ($0.9 < m_{K^+K^-}^2 < 1.2$), and purple ($m_{K^\pm\pi^\mp}^2 > 4$) areas highlight the $m_{K^+K^-}^2$ projections directly on the masses of the χ_{c0} , $\phi(1020)$, and the low-mass KK region as a whole, respectively. The blue ($m_{K^+K^-}^2 < 1.4$), green ($1.4 < m_{K^+K^-}^2 < 3.5$) and orange ($4 < m_{K^+K^-}^2 < 5$) lines are the projections for the $m_{K^\pm\pi^\mp}^2$. The pink ($1.2 < m_{K^\pm\pi^\mp}^2 < 3$), light blue ($0.5 < m_{K^\pm\pi^\mp}^2 < 1.2$) and red

($m_{K^+\pi^+}^2 < 5$) lines are the $m_{K^+K^-}^2$ projections. The remaining two, not highlighted in color, show the full KK and $K\pi$ projections using the linear mass rather than the squared mass.

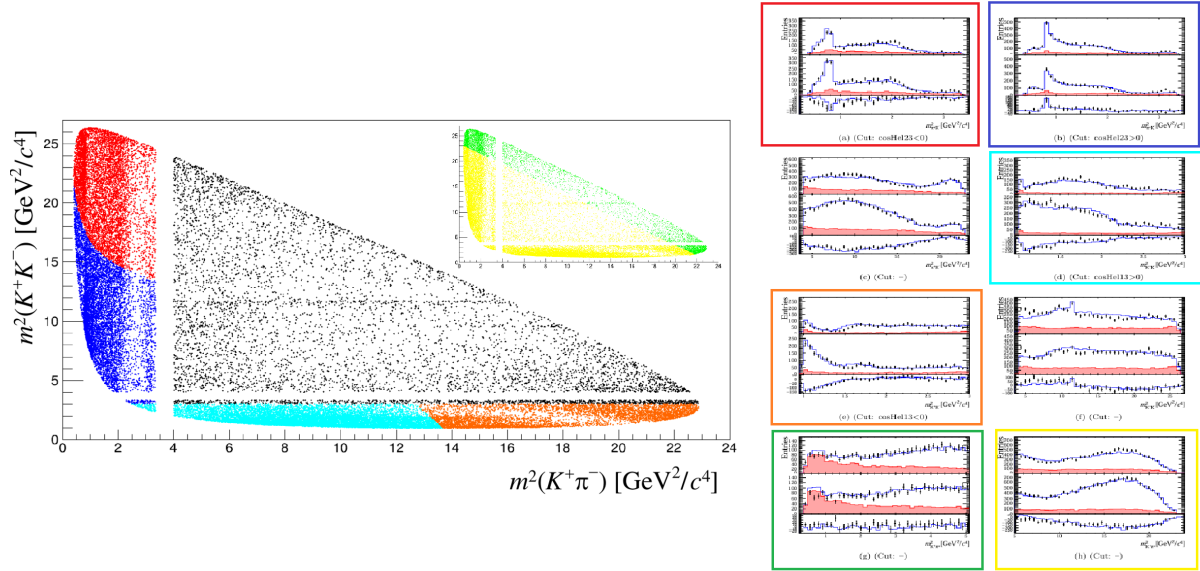


Figure 65 – Colored Dalitz Plot with indications of regions of highest interest.

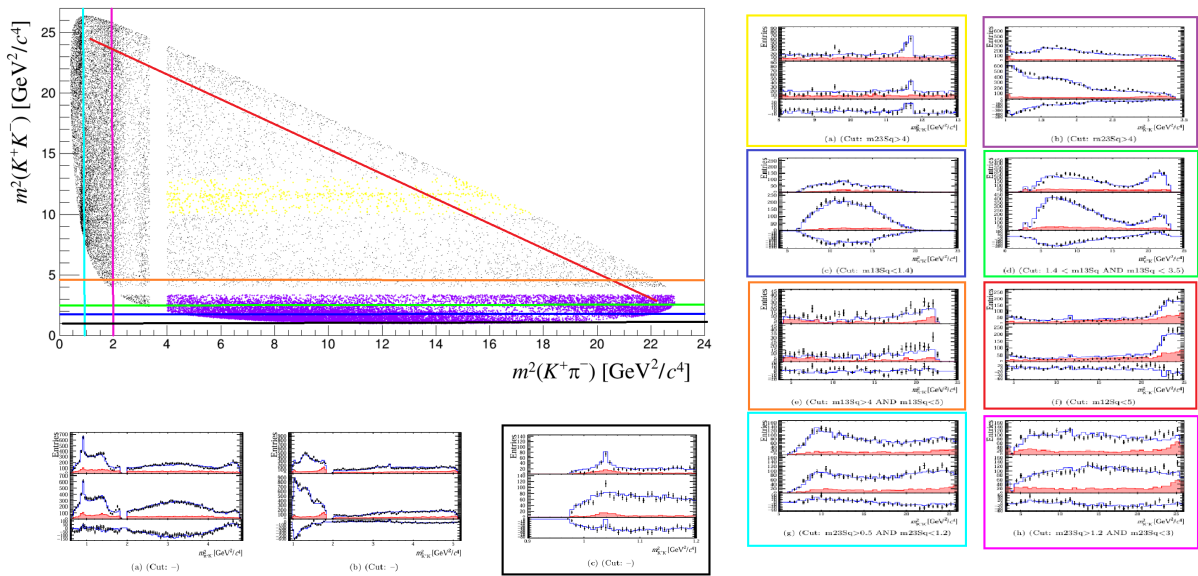


Figure 66 – Colored Dalitz Plot with indications of regions of highest interest.

8.3 Fit Results

Fit 1. Run I model validation

The first step was to validate the previous model using the RUN II data, incorporating new efficiency and background models. The model used as a starting point is the one published in [19].

One can compare the results from Table 20, which presents Run I data using the Run I model, with those from Table 21, which uses the Run I model on Run II data. The findings show good agreement between them. This is a positive indication, demonstrating that the initial model reasonably describes the data although with clear signs of needed improvements. Figure 67, shows the projection of the Run I model on Run II data. It highlights a poor description of the data in panel (a) at $m_{K^+K^-}^2$ around $9 \text{ GeV}^2/c^4$ and $m_{K^+K^-}^2$ around $11 \text{ GeV}^2/c^4$, potentially indicating the presence of the $J/\psi(1S)$ and $\chi_{c0}(1P)$ resonances. Figure 68 also illustrates the discrepancies between data and model.

It is also striking to observe the significant difference in the measured A_{CP} for the $\phi(1020)$ using Run I data compared to the measurement using Run II data. As shown in Figure 69, item c), this appears to be a modeling issue, as the data indicate the presence of the resonance for both charges. However, possibly due to the sharpness of the $\phi(1020)$, whose width is around 7 MeV, the model struggles to capture this feature. This difficulty is likely compounded by the LHCb detector's resolution. Consequently, this limitation might lead to an erroneously large CP violation for this component.

It can also be observed that in certain regions of the phase space, the number of background events exceeds the number of signal events, as shown in item (g) of Figure 67 and item (f) of Figure 68. These regions correspond to the diagonal bands of the Dalitz Plot (see Figures 65 and 66), where little or no contribution from resonances is expected.

Given our particular interest in the S -wave, we will also examine the magnitude and phase motion of the KK and $K\pi$ systems. Figures 70 and 71 present the plots illustrating the magnitude and phase of the S -wave across the phase space. As can be observed, Figure 71 shows a significant difference between the B^+ and B^- components, which is reflected in the measured A_{CP} for the Rescattering contribution presented in Table 21. This type of plot will be revisited in subsequent sections whenever there is interest in evaluating the impact of model modifications.

Tabela 20 – Results of the Dalitz plot fit for the Run I data used as the starting point model, table extracted from [19].

Component	Fit fraction (%)	Magnitude and phase coefficients				A_{CP} (%)
		a_i^-	$\delta_i^- [^\circ]$	a_i^+	$\delta_i^+ [^\circ]$	
$K^*(892)^0$	7.5 ± 0.6	0.94 ± 0.04	0 (fixed)	1.06 ± 0.04	0 (fixed)	$+12.3 \pm 8.7$
$K_0^*(1430)^0$	4.5 ± 0.7	0.74 ± 0.09	-176 ± 10	0.82 ± 0.09	136 ± 11	$+10.4 \pm 14.9$
PolarFFNR	32.3 ± 1.5	2.19 ± 0.13	-138 ± 7	1.97 ± 0.12	166 ± 6	-10.7 ± 5.3
$\rho(1450)^0$	30.7 ± 1.2	2.14 ± 0.11	-175 ± 10	1.92 ± 0.10	140 ± 13	-10.9 ± 4.4
$f_2(1270)$	7.5 ± 0.8	0.86 ± 0.09	-106 ± 11	1.13 ± 0.08	-128 ± 11	$+26.7 \pm 10.2$
Rescattering	16.4 ± 0.8	1.91 ± 0.09	-56 ± 12	0.86 ± 0.07	-81 ± 14	-66.4 ± 3.8
$\phi(1020)$	0.3 ± 0.1	0.20 ± 0.07	-52 ± 23	0.22 ± 0.06	107 ± 33	$+9.8 \pm 43.6$
Fit Fraction Sum	99.2					

Tabela 21 – Results of the Dalitz plot Fit 1 for the Run II data using the starting point model.

[NLL -142446] Component	Fit fraction (%)		Magnitude and phase coefficients				A_{CP} (%)
	B^-	B^+	a_i^+	$\delta_i^+ [^\circ]$	a_i^-	$\delta_i^- [^\circ]$	
$K^*(892)$	6.6 ± 0.3	4.9 ± 0.3	0.99 ± 0.02	0 ± 0	1.01 ± 0.02	0 ± 0	1.1 ± 4.0
$K_0^*(1430)$	6.7 ± 0.6	4.0 ± 0.6	0.91 ± 0.06	11 ± 4	1.02 ± 0.05	-21 ± 3	11.6 ± 7.5
<i>PolarFFNR</i>	38.4 ± 2.6	32.8 ± 2.0	2.59 ± 0.08	28 ± 2	2.43 ± 0.10	-11 ± 3	-6.1 ± 2.0
$\rho(1450)$	31.5 ± 2.0	27.6 ± 2.2	2.37 ± 0.13	157 ± 4	2.20 ± 0.08	124 ± 2	-7.4 ± 2.6
$f_2(1270)$	9.9 ± 0.7	5.3 ± 0.4	1.04 ± 0.04	47 ± 4	1.23 ± 0.04	33 ± 4	16.9 ± 4.0
Re-scattering	7.3 ± 0.5	23.6 ± 1.2	2.19 ± 0.05	110 ± 4	1.06 ± 0.03	86 ± 5	-62.3 ± 1.5
$\phi(1020)$	1.0 ± 0.1	0.01 ± 0.02	0.05 ± 0.05	-111 ± 62	0.40 ± 0.02	111 ± 8	97.4 ± 5.4
Fit Fraction Sum	101.2	98.2					

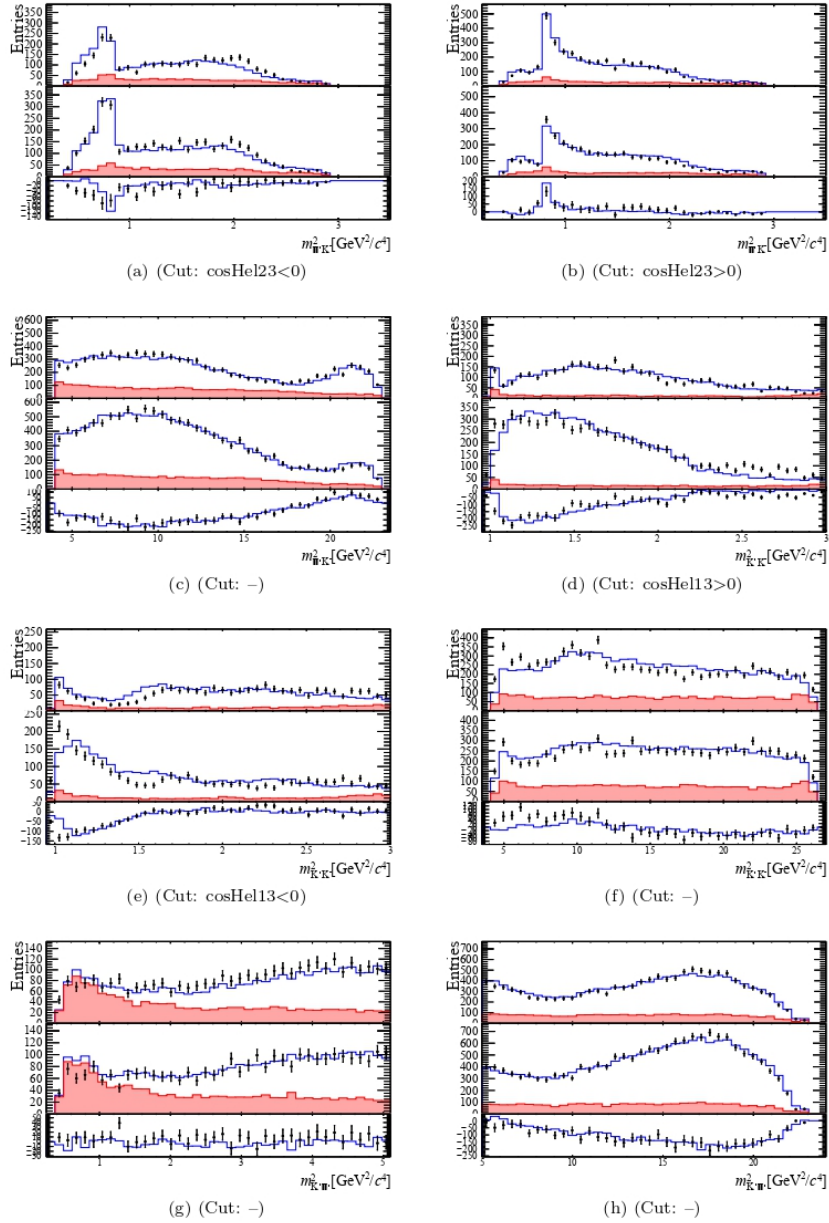


Figura 67 – Fit 1 results, for each plot B^- (top), B^+ (middle) and the difference ($B^- - B^+$, bottom). The a) ($\cos\text{Hel}23 < 0$), b) ($\cos\text{Hel} > 0$), and c) are showing the $m^2_{K^\pm\pi^\mp}$ in a different region. The d) ($\cos\text{Hel}13 > 0$), e) ($\cos\text{Hel}13 < 0$), and f) are the projections for the $m^2_{K^+K^-}$. For the g) and h) we have the diagonal projections $m^2_{K^+\pi^+}$. The line in blue represents the model, the black dots represent the data, and the region in red is the background estimation. All plots were produced using 40 bins.

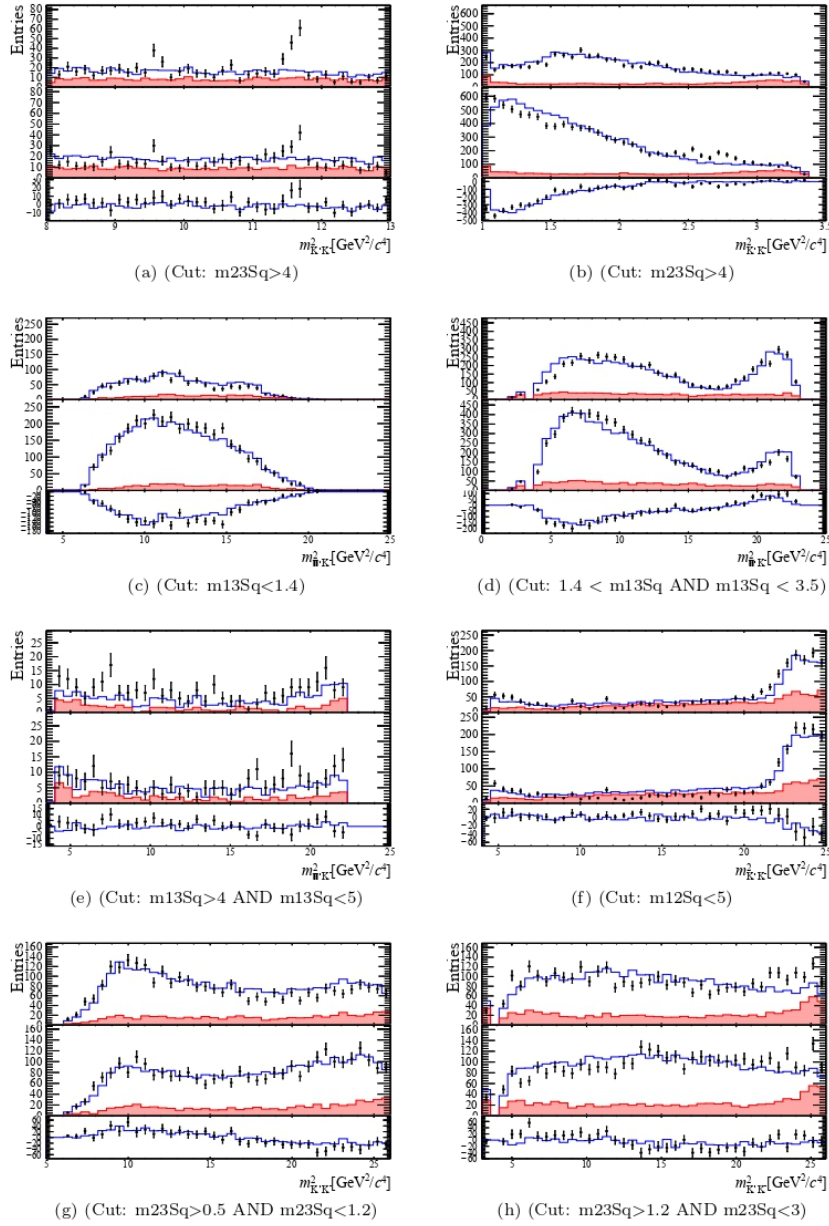


Figure 68 – Fit 1 results, for each plot B^- (top), B^+ (middle) and the difference ($B^- - B^+$, bottom). The a) ($m_{K^\pm\pi^\mp}^2 > 4$, specially for the $\chi_{c0}(1P)$), b) ($m_{K^\pm\pi^\mp}^2 > 4$) are showing the $m_{K^+K^-}^2$ in different regions. The c) ($m_{K^+K^-}^2 < 1.4$), d) ($1.4 < m_{K^+K^-}^2 < 3.5$), and e) ($4 < m_{K^+K^-}^2 < 5$) are the projections for the $m_{K^\pm\pi^\mp}^2$. For the f) ($m_{K^+\pi^+}^2 < 5$), g) ($0.5 < m_{K^\pm\pi^\mp}^2 < 1.2$) and h) ($1.2 < m_{K^\pm\pi^\mp}^2 < 3$) we have the $m_{K^+K^-}^2$ projections. The line in blue represents the model, the black dots represent the data, and the region in red is the background estimation. All plots were produced using 40 bins.

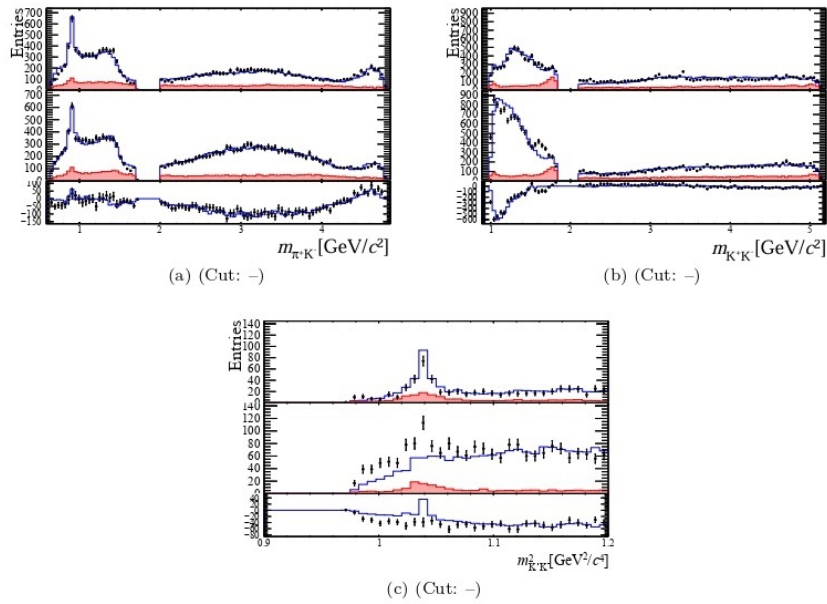


Figura 69 – Fit 1 results, for each plot B^- (top), B^+ (middle) and the difference ($B^- - B^+$, bottom). The a) and b) show the full projections of $m_{K^\pm\pi^\mp}$ and $m_{K^+K^-}$ produced using 100 bins, respectively. It is important to note that in these two cases, the mass is not squared. The c) is the $0.9 < m_{K^+K^-}^2 < 1.2$ to zoom in on the $\phi(1020)$, using 40 bins. The line in blue represents the model, the black dots represent the data, and the region in red is the background estimation.

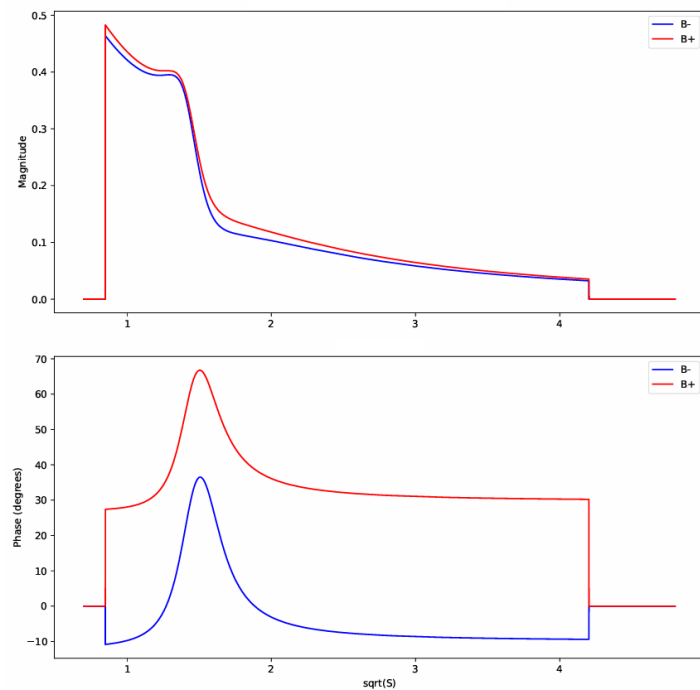


Figura 70 – Magnitude and phase of the $K\pi$ S-wave resulting from Fit 1 using $K_0^*(1430)$ and PolarFFNR.

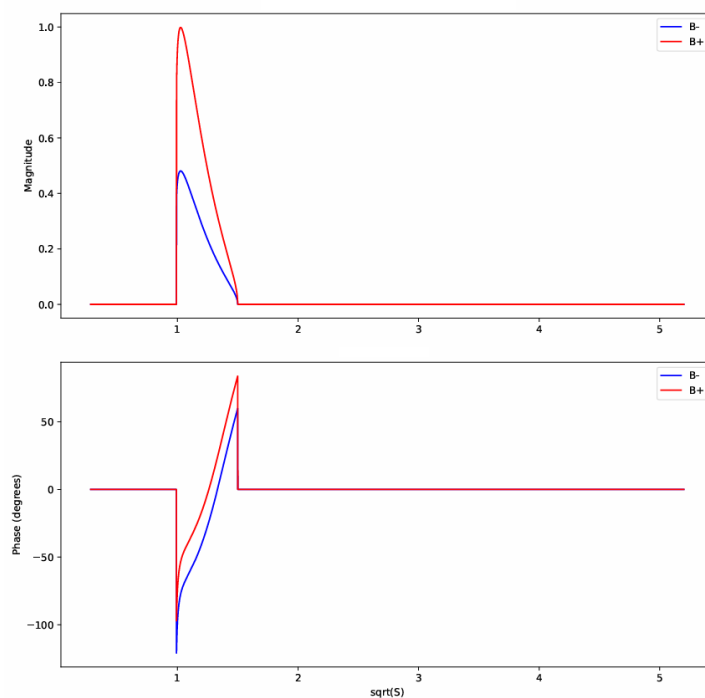


Figura 71 – Magnitude and phase of the KK S-wave resulting from Fit 1 using Rescattering.

Fit 2. Adding the $\chi_{c0}(1P)$ resonance

Figure 68 item *a*) highlights the clear need to include the $\chi_{c0}(1P)$ resonance in our model, as the data strongly indicates its presence around $11.5 \text{ GeV}^2/c^4$. As can be seen, the A_{CP} for the $\chi_{c0}(1P)$ in this model presents a value compatible with zero. Figure 72 illustrates the impact on the model when adding this component. Due to its narrow width, the $\chi_{c0}(1P)$ interferes minimally with other resonances, resulting in only minor changes to the parameters of the other components in the model, see Table 22.

Using the tools outlined in Section 8.2, we verified that $\Delta_{NLL} = 103$, considering Fit 1 - Fit 2¹, and applying the likelihood ratio technique $103 > 34.55^2$. Thus, all indicators strongly support the inclusion of this resonance in the model.

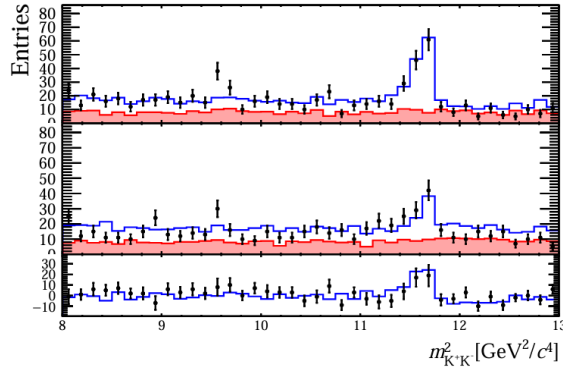
(a) (Cut: $m_{23S} > 4$)

Figure 72 – Fit 2 results for the $m_{K^+K^-}$ projection with the $m_{K^\pm\pi^\mp}^2 > 4$. Signature of $J/\psi(1S)$ and $\chi_{c0}(1P)$ around $9.5 \text{ GeV}^2/c^4$ and $11.6 \text{ GeV}^2/c^4$, respectively.

Tabela 22 – Results of the Dalitz plot Fit 2 considering the addition of $\chi_{c0}(1P)$.

[NLL -142549] Component	Fit fraction (%)		Magnitude and phase coefficients				A_{CP} (%)
	B^-	B^+	a_i^+	$\delta_i^+ [^\circ]$	a_i^-	$\delta_i^- [^\circ]$	
$K^*(892)$	6.8 ± 0.3	4.9 ± 0.3	0.99 ± 0.02	0 ± 0	1.01 ± 0.02	0 ± 0	1.7 ± 3.9
$K_0^*(1430)$	7.5 ± 0.6	4.2 ± 0.3	0.92 ± 0.04	11 ± 4	1.06 ± 0.05	-19 ± 4	14.2 ± 5.4
<i>PolarFFNR</i>	37.2 ± 1.0	32.5 ± 0.7	2.55 ± 0.06	28 ± 3	2.37 ± 0.06	-10 ± 3	-7.2 ± 1.8
$\rho(1450)$	31.6 ± 0.7	27.6 ± 0.6	2.35 ± 0.05	158 ± 4	2.18 ± 0.05	127 ± 4	-7.2 ± 1.7
$f_2(1270)$	9.7 ± 0.5	5.3 ± 0.4	1.03 ± 0.04	49 ± 4	1.21 ± 0.04	36 ± 4	16.5 ± 4.1
Re-scattering	7.3 ± 0.3	23.6 ± 0.4	2.17 ± 0.05	111 ± 4	1.05 ± 0.03	89 ± 5	-62.3 ± 1.5
$\phi(1020)$	1.0 ± 0.1	0.01 ± 0.02	0.05 ± 0.05	-110 ± 63	0.39 ± 0.02	115 ± 9	97.5 ± 5.3
χ_{c0}	1.3 ± 0.1	0.6 ± 0.1	0.35 ± 0.03	112 ± 8	0.44 ± 0.03	46 ± 8	21.5 ± 8.3
Fit Fraction Sum	102.2	98.8					

¹ We will adopt as the standard for calculating Δ_{NLL} the convention of using the previous fit as the baseline and subtracting the subsequent fit.

² Considering 4 degrees of freedom and a 5σ threshold, the critical χ^2 value is 34.55, which serves as the reference for some subsequent studies.

Fit 3. *Low mass $K\pi$*

The PolarFFNR component, which was used as the standard non-resonant contribution during the Run 1 analysis, will also serve as the default non-resonant component in this study. As in the previous study, the existence of a second solution (i.e., different results for the a^\pm and δ^\pm , A_{CP} , and Fit Fraction) exhibited non-physical behavior, being a fitter-created outcome, resulting from the large interference of scalars in the $K\pi$ sector, particularly caused by the interference between the $K_0^*(1430)$ and the PolarFFNR. In essence, this reflects a scenario of multiple solutions, where different parameter sets can explain the experimental data, as explained in the section 7.4.4.

To address this issue, we conducted a study (see details in Appendix D) where we fitted the Λ parameter of the PolarFFNR. The fitted value was $\Lambda = 1.22 \pm 0.03$, and this value will be fixed in the fits from now on. Table 23 presents the results of fitting the Λ value. For this case, $\Delta_{NLL} = 31$, with the critical value for a χ^2 distribution being 25^3 , thus $31 > 25$. Therefore, the indicators also support the modification applied in this scenario.

Tabela 23 – Results of the Dalitz plot Fit 3 fitting $\Lambda = 1.22 \pm 0.03$.

[NLL -142580] Component	Fit fraction (%)		Magnitude and phase coefficients				A_{CP} (%)
	B^-	B^+	a_i^+	$\delta_i^+ [^\circ]$	a_i^-	$\delta_i^- [^\circ]$	
$K^*(892)$	7.0 ± 0.4	5.3 ± 0.3	1.00 ± 0.02	0 ± 0	1.00 ± 0.02	0 ± 0	0.3 ± 3.8
$K_0^*(1430)$	9.2 ± 0.7	5.4 ± 0.4	1.02 ± 0.04	22 ± 4	1.15 ± 0.05	-12 ± 4	12.6 ± 4.9
<i>PolarFFNR</i>	38.7 ± 1.0	33.1 ± 0.8	2.51 ± 0.06	29 ± 3	2.36 ± 0.06	-11 ± 3	-5.9 ± 1.8
$\rho(1450)$	31.1 ± 0.7	27.1 ± 0.6	2.27 ± 0.05	158 ± 4	2.12 ± 0.05	128 ± 4	-6.9 ± 1.7
$f_2(1270)$	9.3 ± 0.5	4.9 ± 0.3	0.96 ± 0.04	50 ± 4	1.16 ± 0.04	38 ± 4	18.1 ± 4.2
Re-scattering	7.0 ± 0.3	23.4 ± 0.4	2.11 ± 0.05	112 ± 4	1.00 ± 0.03	90 ± 5	-63.1 ± 1.5
$\phi(1020)$	1.0 ± 0.1	0.01 ± 0.02	0.04 ± 0.05	-104 ± 59	0.38 ± 0.02	115 ± 9	97.5 ± 5.5
χ_{c0}	1.3 ± 0.1	0.6 ± 0.1	0.34 ± 0.03	114 ± 7	0.43 ± 0.02	49 ± 8	21.9 ± 8.2
Fit Fraction Sum	105.0	99.9					

Fit 4. *Rescattering update*

As mentioned in Section 6.2.3.6, an update to the phenomenological description of the $\pi\pi \rightarrow KK$ rescattering was conducted, following [17]. This element is one of the main parts of this analysis, as it exhibits one of the largest CP violations observed in a single component.

Considering the available parameter options, we tested several sets, including CFD_b , CFD_c , UFD_b , and UFD_c . Based on the results, we decided to proceed with the UFD_b parameters for the remainder of the analysis, as they provided the most consistent performance. Detailed results of the other parameter sets are presented in the Appendix C.

³ Considering 1 degree of freedom and a 5σ threshold, the critical χ^2 value is 25.

Figures 73, 74 and 75 present the new projections of the Dalitz plot regions after the rescattering update. Attention is particularly drawn to the areas surrounding this new component due to its changes, especially in the KK projections between $1 \text{ GeV}^2/c^4$ and $2 \text{ GeV}^2/c^4$. Notably, items d) and e) in Figure 73 underwent considerable changes compared to the same items in the previous Run I model results, as shown in Figure 67. The model's behavior after the update appears to be more consistent with the data. However, specifically for item d) in 73, the results seem to be worse between 1.6 and 2 GeV^2/c^4 . For this case, $\Delta_{NLL} = 148$.

Tabela 24 – Dalitz Plot Fit 4 results using UFD_b parameters for the Rescattering component.

[NLL -142728] Component	Fit fraction (%)		Magnitude and phase coefficients				A_{CP} (%)
	B^-	B^+	a_i^+	$\delta_i^+ [^\circ]$	a_i^-	$\delta_i^- [^\circ]$	
$K^*(892)$	7.1 ± 0.3	5.1 ± 0.3	0.99 ± 0.02	0 ± 0	1.01 ± 0.02	0 ± 0	2.1 ± 3.8
$K_0^*(1430)$	9.3 ± 0.7	5.8 ± 0.4	1.05 ± 0.04	18 ± 3	1.16 ± 0.05	-13 ± 4	9.7 ± 4.9
<i>PolarFFNR</i>	39.8 ± 1.0	33.7 ± 0.8	2.54 ± 0.06	29 ± 3	2.40 ± 0.06	-10 ± 3	-5.6 ± 1.8
$\rho(1450)$	33.5 ± 0.7	26.8 ± 0.5	2.26 ± 0.05	178 ± 259	2.20 ± 0.05	141 ± 5	-2.7 ± 1.7
$f_2(1270)$	8.5 ± 0.5	3.8 ± 0.3	0.85 ± 0.04	78 ± 5	1.11 ± 0.04	49 ± 5	26.1 ± 4.3
Re-scattering	6.7 ± 0.3	24.1 ± 0.4	2.14 ± 0.05	-173 ± 5	0.99 ± 0.03	141 ± 6	-65.1 ± 1.4
$\phi(1020)$	0.9 ± 0.1	0.01 ± 0.02	0.05 ± 0.03	38 ± 39	0.37 ± 0.02	171 ± 9	97.0 ± 4.2
χ_{c0}	1.3 ± 0.1	0.7 ± 0.1	0.35 ± 0.03	115 ± 7	0.44 ± 0.02	52 ± 7	21.2 ± 8.1
Fit Fraction Sum	107.1	100.0					

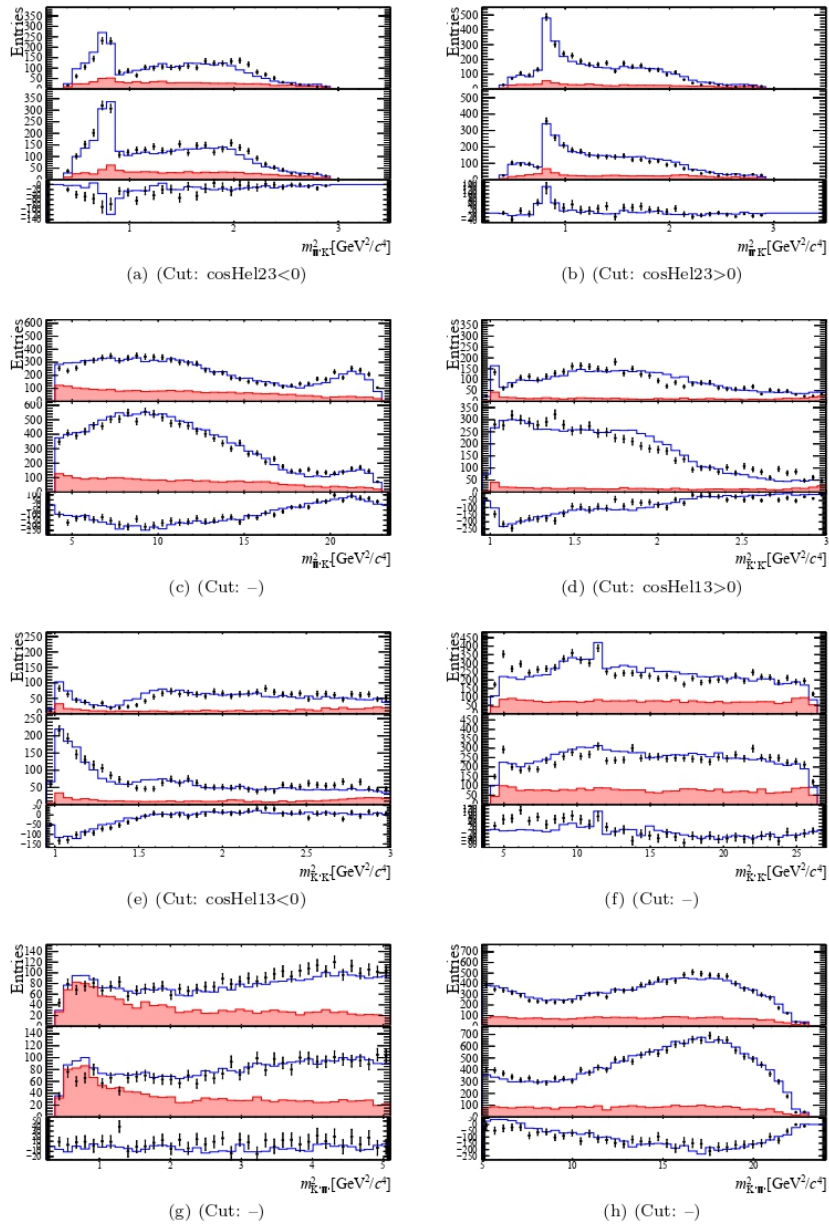


Figure 73 – Fit 4 using UFD_b parameters, for each plot B^- (top), B^+ (middle) and the difference ($B^- - B^+$, bottom). The a) ($\cos\text{Hel}23 < 0$), b) ($\cos\text{Hel} > 0$), and c) are showing the $m_{K^\pm\pi^\mp}^2$ in a different region. The d) ($\cos\text{Hel}13 > 0$), e) ($\cos\text{Hel}13 < 0$), and f) are the projections for the $m_{K^+K^-}^2$. For the g) and h) we have the diagonal projections $m_{K^+\pi^+}^2$. The line in blue represents the model, the black dots represent the data, and the region in red is the background estimation. All plots were produced using 40 bins.

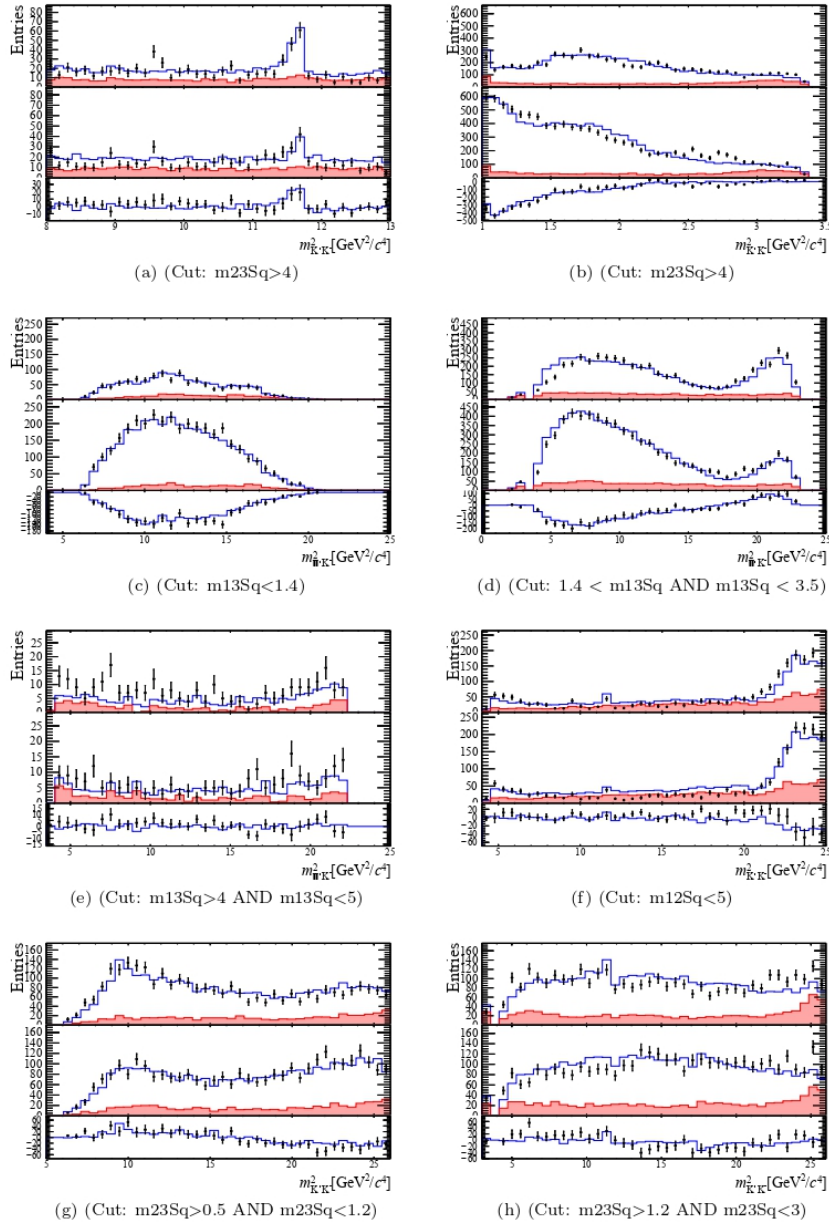


Figura 74 – Fit 4 using UFD_b parameters, for each plot B^- (top), B^+ (middle) and the difference ($B^- - B^+$, bottom). The a) ($m_{K^\pm\pi^\mp}^2 > 4$, specially for the $\chi_{c0}(1P)$), b) ($m_{K^\pm\pi^\mp}^2 > 4$) are showing the $m_{K^+K^-}^2$ in different regions. The c) ($m_{K^+K^-}^2 < 1.4$), d) ($1.4 < m_{K^+K^-}^2 < 3.5$), and e) ($4 < m_{K^+K^-}^2 < 5$) are the projections for the $m_{K^\pm\pi^\mp}^2$. For the f) ($m_{K^+\pi^+}^2 < 5$), g) ($0.5 < m_{K^\pm\pi^\mp}^2 < 1.2$) and h) ($1.2 < m_{K^\pm\pi^\mp}^2 < 3$) we have the $m_{K^+K^-}^2$ projections. The line in blue represents the model, the black dots represent the data, and the region in red is the background estimation. All plots were produced using 40 bins.

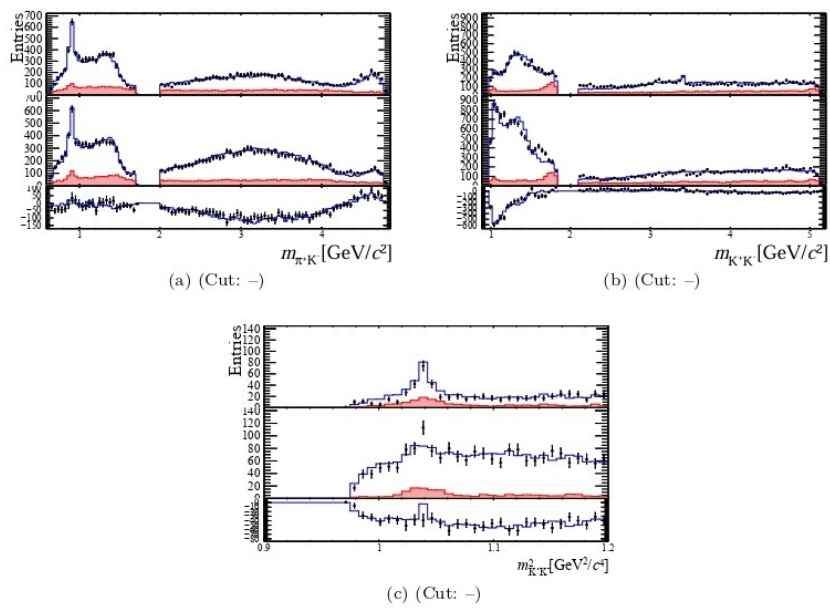


Figura 75 – Fit 4 using UFD_b parameters, for each plot B^- (top), B^+ (middle) and the difference ($B^- - B^+$, bottom). The a) and b) show the full projections of $m_{K^\pm\pi^\mp}$ and $m_{K^+K^-}$ produced using 100 bins, respectively. It is important to note that in these two cases, the mass is not squared. The c) is the $0.9 < m_{K^+K^-}^2 < 1.2$ to zoom in on the $\phi(1020)$, using 40 bins. The line in blue represents the model, the black dots represent the data, and the region in red is the background estimation.

Fit 5. *Floating mass and width of $\rho^0(1450)$*

Following studies of the previous analysis, the mass and width of the $\rho^0(1450)$ amplitude were allowed to float ⁴. Table 25 shows the fit results obtained by floating the mass and width of the $\rho^0(1450)$, being these of 1.546 ± 0.005 GeV/ c^2 and 0.452 ± 0.018 GeV/ c^2 , respectively. As can be seen, there is an improvement in the NLL compared to the previous results in Table 24. Additionally, a significant change in the A_{CP} values can be noted, showing how sensitive and yet unstable the system remains.

Tabela 25 – Dalitz Plot Fit 5 results with mass and width of the $\rho^0(1450)$ floating.

[NLL -142808] Component	Fit fraction (%)		Magnitude and phase coefficients				A_{CP} (%)
	B^-	B^+	a_i^+	$\delta_i^+ [^\circ]$	a_i^-	$\delta_i^- [^\circ]$	
$K^*(892)$	6.0 ± 0.3	5.1 ± 0.3	1.03 ± 0.02	0 ± 0	0.97 ± 0.02	0 ± 0	-5.1 ± 3.9
$K_0^*(1430)$	5.9 ± 0.5	6.0 ± 0.4	1.12 ± 0.04	16 ± 3	0.97 ± 0.04	-24 ± 4	-14.2 ± 5.0
<i>PolarFFNR</i>	34.8 ± 1.1	33.8 ± 0.8	2.64 ± 0.07	28 ± 3	2.35 ± 0.06	5 ± 3	-11.7 ± 2.0
$\rho(1450)$	41.0 ± 0.8	27.6 ± 0.6	2.39 ± 0.05	-172 ± 4	2.55 ± 0.06	-111 ± 4	6.6 ± 1.7
$f_2(1270)$	10.2 ± 0.5	4.1 ± 0.3	0.92 ± 0.04	73 ± 4	1.27 ± 0.04	126 ± 4	31.7 ± 4.1
Re-scattering	9.2 ± 0.4	24.4 ± 0.5	2.25 ± 0.05	-165 ± 5	1.21 ± 0.04	-115 ± 5	-55.1 ± 1.7
$\phi(1020)$	0.8 ± 0.1	0.07 ± 0.04	0.12 ± 0.03	39 ± 15	0.35 ± 0.03	-69 ± 9	78.7 ± 10.3
χ_{c0}	1.3 ± 0.1	0.7 ± 0.1	0.37 ± 0.03	115 ± 7	0.46 ± 0.03	68 ± 7	21.5 ± 8.2
Fit Fraction Sum	110.3	101.5					

Fit 6. *Improving KK P -wave*

Due to the previous fit, we conducted a test by adding the $\rho^0(1700)$ together with the $\rho^0(1450)$ but keeping their masses and widths at the original values. Indeed, when the $\rho^0(1700)$ was included, the fit improved, indicating that there are likely two distinct ρ resonances. If we compare this result with the Fit 1, we notice a significant improvement in the NLL, with a $\Delta_{NLL} = 373$. This observation will be further discussed, along with other characteristics of the baseline model, in the next section. This model will be regarded as our baseline, serving as the foundation for subsequent enhancements.

⁴ The standard values for the $\rho^0(1450)$ are 1465 ± 25 MeV for the mass and 400 ± 60 MeV for the width [61].

8.3.1 The baseline model

Future improvements will be systematically developed and evaluated based on the results presented here. By using this baseline as a reference point, we can accurately evaluate the effects of different modifications, ensuring solid model development. In this section, we will also analyze the partial results obtained thus far.

Table 26 presents the results after the addition of the $\rho^0(1700)$ to the model. A drastic difference in the total sum of the Fit Fraction is noteworthy, especially for the case of the $\rho^0(1450)$, which experienced a reduction in its contribution by nearly 20% compared to the previous result, likely due to a constructive interference between the $\rho^0(1450)$ and $\rho^0(1700)$. Figures 78, 79, and 80 show the new projections of the phase space regions, and it can be seen that the addition of the $\rho^0(1700)$ has a positive impact. Specifically, note item *d*) in Figure 79, which shows improvement compared to the previous result between 1.6 and 2 GeV^2/c^4 .

Tabela 26 – Dalitz Plot Fit 6 results after adding the $\rho^0(1700)$.

[NLL -142819] Component	Fit fraction (%)		Magnitude and phase coefficients				A_{CP} (%)
	B^-	B^+	a_i^+	$\delta_i^+ [^\circ]$	a_i^-	$\delta_i^- [^\circ]$	
$K^*(892)$	6.3 ± 0.3	5.0 ± 0.3	1.01 ± 0.02	0 ± 0	0.99 ± 0.02	0 ± 0	-1.4 ± 3.9
$K_0^*(1430)$	5.8 ± 0.5	5.6 ± 0.4	1.07 ± 0.04	15 ± 3	0.95 ± 0.04	-25 ± 4	-11.9 ± 5.3
<i>PolarFFNR</i>	37.8 ± 1.2	34.3 ± 0.8	2.65 ± 0.07	29 ± 3	2.43 ± 0.06	2 ± 3	-8.5 ± 2.0
$\rho(1700)$	3.6 ± 0.5	2.9 ± 0.5	0.76 ± 0.07	-99 ± 8	0.75 ± 0.06	-84 ± 6	-2.2 ± 11.2
$\rho(1450)$	22.4 ± 1.2	16.6 ± 0.9	1.84 ± 0.06	177 ± -123	1.87 ± 0.06	-141 ± 7	1.5 ± 3.9
$f_2(1270)$	9.8 ± 0.5	3.9 ± 0.3	0.89 ± 0.04	81 ± 5	1.24 ± 0.04	113 ± 5	31.9 ± 4.2
Re-scattering	8.7 ± 0.4	24.6 ± 0.5	2.24 ± 0.05	-162 ± 6	1.16 ± 0.04	-132 ± 6	-57.6 ± 1.7
$\phi(1020)$	0.8 ± 0.1	0.07 ± 0.04	0.12 ± 0.03	46 ± 15	0.35 ± 0.03	-91 ± 10	77.4 ± 10.6
χ_{c0}	1.4 ± 0.1	0.7 ± 0.1	0.37 ± 0.03	115 ± 7	0.46 ± 0.03	66 ± 7	22.5 ± 8.0
Fit Fraction Sum	96.5	93.5					

The signature of a possible $J/\psi(1S)$ resonance at $9.5 \text{ GeV}^2/c^4$ can be observed (see item *a*) Fig 79), warranting further studies and special attention in the following sections. Additionally, in the same figure and item, the model (blue line) appears to overestimate the number of entries compared to the data (black points), especially for the B^+ (middle layer). This suggests that improvements are needed around the $\chi_{c0}(1P)$, particularly concerning broad contributions with tails extending across the phase space. This is evident in non-resonant contributions like the PolarFFNR or the $K_0^*(1430)^0$. Figure 80 item *c*) shows that the issue remains unresolved in the fit of the $\phi(1020)$, as the model continues to struggle with accurately fitting the sharp $\phi(1020)$ resonance, resulting in an erroneously large CP violation. Attempts to modify the width of the $\phi(1020)$ were made, but without positive results. The difficulty in achieving a good result regarding the width of this component is related to the LHCb energy resolution, as already mentioned.

Since this is the baseline model, it is also insightful to examine again the behavior of the S -wave magnitude and phase across the phase space. Figures 76 and 77 present the magnitude and phase motion for the KK and $K\pi$ S -wave. It can be observed that the $K\pi$

S -wave behavior has remained almost unchanged so far, as seen when comparing Figure 76 with Figure 70. On the other hand, after the Rescattering update, the KK S -wave exhibits significant differences, particularly in the phase behavior of the rescattering component, alongside the inclusion of the χ_{c0} resonance, comparing Figure 77 with Figure 71. However, it is important to emphasize that the large difference in magnitude remains similar. Such an analysis provides a reference point for understanding how modifications in alternative models may impact these plots.

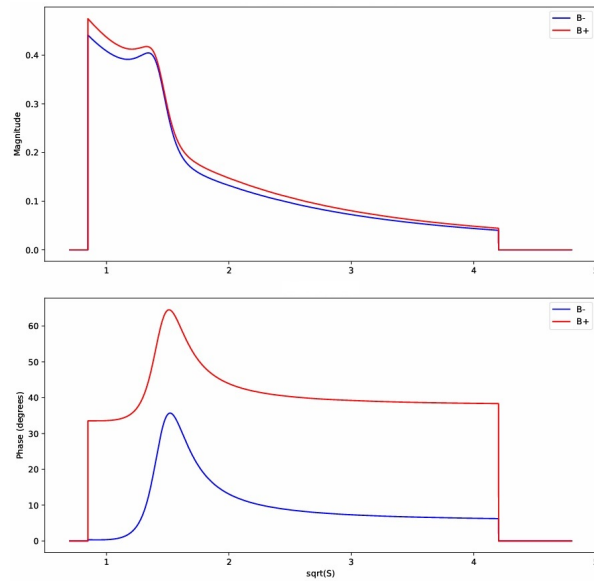


Figure 76 – Magnitude and phase of the $K\pi$ S -wave resulting from Fit 6 using $K_0^*(1430)$ and PolarFFNR.

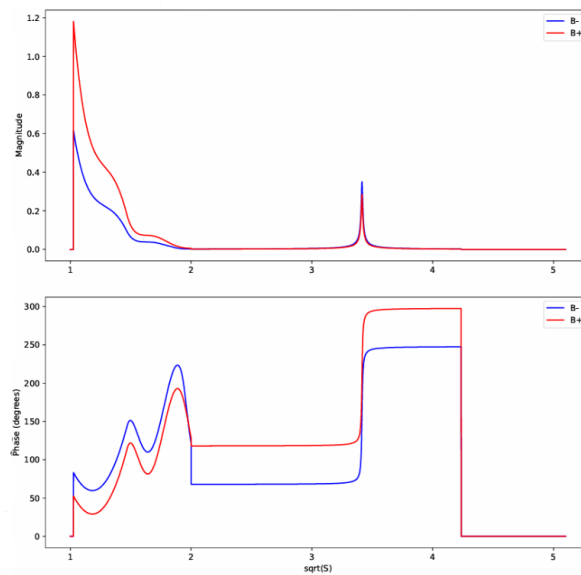


Figure 77 – Magnitude and phase of the KK S -wave resulting from Fit 6 using Rescattering and χ_{c0} .

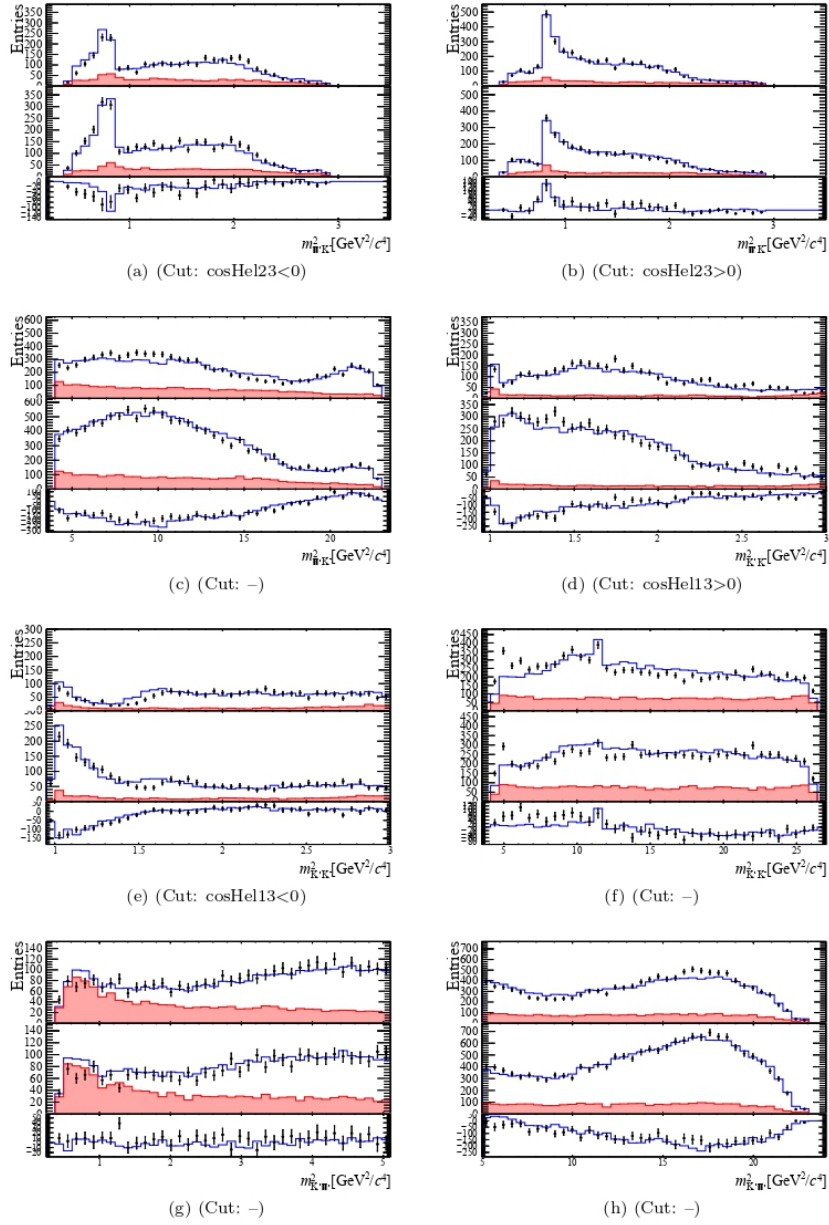


Figure 78 – Fit 6, for each plot B^- (top), B^+ (middle) and the difference ($B^- - B^+$, bottom). The a) ($\cos\text{Hel}23 < 0$), b) ($\cos\text{Hel} > 0$), and c) are showing the $m_{K^{\pm}\pi^{\mp}}^2$ in a different region. The d) ($\cos\text{Hel}13 > 0$), e) ($\cos\text{Hel}13 < 0$), and f) are the projections for the $m_{K^+K^-}^2$. For the g) and h) we have the diagonal projections $m_{K^+\pi^+}^2$. The line in blue represents the model, the black dots represent the data, and the region in red is the background estimation. All plots were produced using 40 bins.

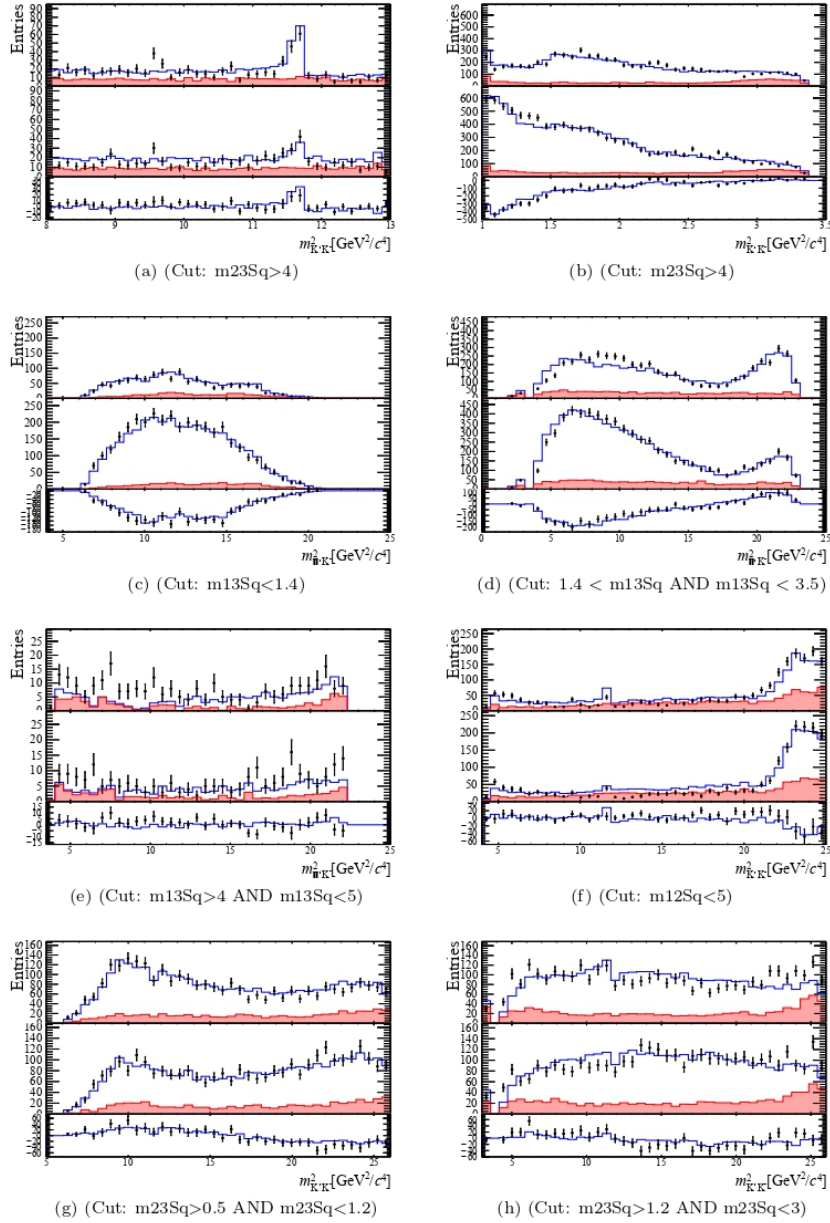


Figure 79 – Fit 6, for each plot B^- (top), B^+ (middle) and the difference ($B^- - B^+$, bottom). The a) ($\cos Hel_{23} < 0$), b) ($\cos Hel > 0$), and c) are showing the $m_{K^\pm\pi^\mp}^2$ in a different region. The d) ($\cos Hel_{13} > 0$), e) ($\cos Hel_{13} < 0$), and f) are the projections for the $m_{K^+K^-}$. For the g) and h) we have the diagonal projections $m_{K^+\pi^+}^2$. The line in blue represents the model, the black dots represent the data, and the region in red is the background estimation. All plots were produced using 40 bins.

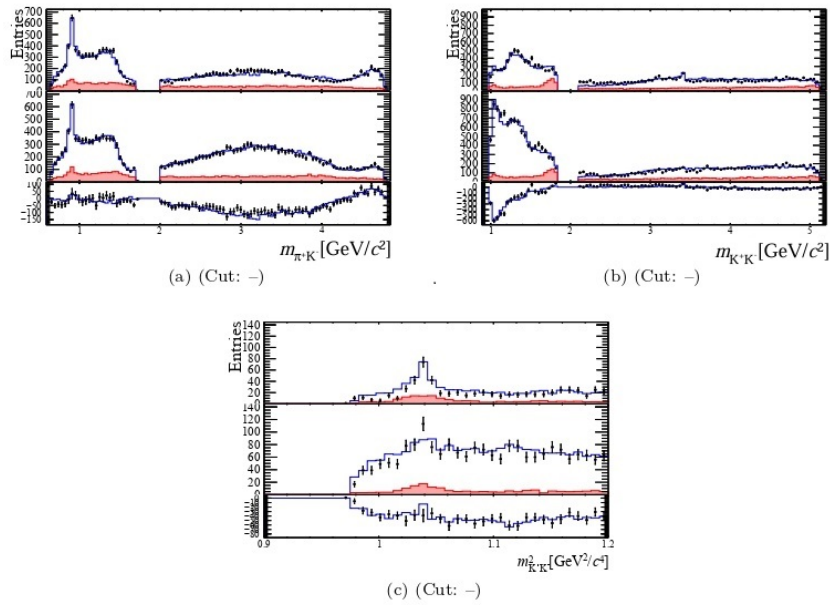


Figura 80 – Fit 6, for each plot B^- (top), B^+ (middle) and the difference ($B^- - B^+$, bottom). The a) and b) show the full projections of $m_{K^\pm\pi^\mp}$ and $m_{K^+K^-}$ produced using 100 bins, respectively. It is important to note that in these two cases, the mass is not squared. The c) is the $0.9 < m_{K^+K^-}^2 < 1.2$ to zoom in on the $\phi(1020)$, using 40 bins. The line in blue represents the model, the black dots represent the data, and the region in red is the background estimation.

Fit 7. *Further $K\pi$ improvements - $\delta s_{K\pi}$ formulation*

We also considered an alternative parametrization for the low-mass $K\pi$ region using the δ formulation, as discussed in the section 6.2.3.5.

The primary difference between the PolarFFNR and δ options lies in their formulations. While the PolarFFNR is a real contribution without phase (aside from the one directly from the Isobar model), the δ is a unitary formulation that includes phase motion. It is important to note that obtaining a precise measurement of the phase of the $K\pi$ S -wave is particularly challenging. This difficulty arises because it is located in regions far from other resonances, and as a result, it does not intersect with the neighboring elements.

Table 27 presents the results of replacing the PolarFFNR by the $\delta s_{K\pi}$, allowing the m_0 and a parameters to float. The resulting values were:

$$m_0 = 0.86 \pm 0.03 \quad \text{and} \quad a = -1.14 \pm 0.03.$$

It can be observed that the total sum of the Fit Fractions in this case is notably large, which raises concerns about the validity of this attempt. Additionally, the NLL showed a significant deterioration compared to the previous model, increasing by nearly 200 units.

Tabela 27 – Dalitz Plot Fit 7 results using the $\delta s_{K\pi}$ as parametrization for the $K\pi$ low mass.

[NLL -142632] Component	Fit fraction (%)		Magnitude and phase coefficients				A_{CP} (%)
	B^-	B^+	a_i^+	$\delta_i^+ [^\circ]$	a_i^-	$\delta_i^- [^\circ]$	
$K^*(892)$	5.88 ± 0.34	4.58 ± 0.27	1.002 ± 0.020	0 ± 0	0.998 ± 0.020	0 ± 0	-0.3 ± 4.0
$K_0^*(1430)$	45.82 ± 1.73	45.83 ± 1.28	3.169 ± 0.093	144 ± 3	2.786 ± 0.092	96 ± 4	-12.8 ± 2.1
$\delta(s_{K\pi})$	35.02 ± 2.38	39.76 ± 1.86	2.952 ± 0.109	-83 ± 4	2.435 ± 0.111	-124 ± 4	-19.0 ± 3.2
$\rho(1700)$	2.21 ± 0.46	1.95 ± 0.33	0.654 ± 0.057	153 ± 9	0.612 ± 0.064	42 ± 10	-6.8 ± 13.3
$\rho(1450)$	24.75 ± 1.39	15.83 ± 0.95	1.863 ± 0.063	104 ± 6	2.048 ± 0.066	56 ± 7	9.4 ± 3.6
$f_2(1270)$	9.58 ± 0.51	4.66 ± 0.33	1.011 ± 0.039	-4 ± 5	1.274 ± 0.039	-46 ± 7	22.8 ± 3.9
Re-scattering	6.98 ± 0.36	23.18 ± 0.67	2.254 ± 0.051	111 ± 6	1.088 ± 0.033	53 ± 8	-62.2 ± 1.4
$\phi(1020)$	0.79 ± 0.10	0.03 ± 0.02	0.082 ± 0.030	-43 ± 22	0.367 ± 0.025	84 ± 10	90.5 ± 7.0
χ_{c0}	0.67 ± 0.10	0.20 ± 0.05	0.208 ± 0.024	-109 ± 14	0.337 ± 0.027	-114 ± 14	44.6 ± 10.7
Fit Fraction Sum	148.4	152.5					

Fit 8. *Further $K\pi$ improvements - δ_{Pol} formulation*

The same considerations applied to Fit 7 are also valid in this case. We included the version of the generic function mentioned in section 6.2.3.5, using a second-degree polynomial in the format:

$$\delta_{Pol} = A_1 mass^2 + B_2 mass + C_3 \quad (8.1)$$

where $A_1 = -0.137 \pm 0.002$ (floating) and $C_3 = 1.19 \pm 0.03$ (floating), while the $B_2 = 1$ (fixed).

Table 28 presents the results of replacing the PolarFFNR by the δ_{Pol} . These results, along with the previous findings in Table 26, show that the outcomes remain stable and consistent, reinforcing that the δ_{Pol} is a reliable option for this role.

Tabela 28 – Dalitz Plot Fit 7 results using the δ_{Pol} as parametrization for the $K\pi$ low mass.

[NLL -142915] Component	Fit fraction (%)		Magnitude and phase coefficients				A_{CP} (%)
	B^-	B^+	a_i^+	$\delta_i^+ [^\circ]$	a_i^-	$\delta_i^- [^\circ]$	
$K^*(892)$	6.97 ± 0.36	5.04 ± 0.30	0.997 ± 0.019	0 ± 0	1.003 ± 0.019	0 ± 0	0.6 ± 3.9
$K_0^*(1430)$	8.81 ± 0.77	7.85 ± 0.67	1.245 ± 0.064	46 ± 4	1.128 ± 0.056	6 ± 4	-9.8 ± 6.2
δ_{Pol}	42.79 ± 1.45	39.70 ± 1.06	2.799 ± 0.073	-90 ± 5	2.485 ± 0.068	-121 ± 3	-11.9 ± 2.4
$\rho(1700)$	2.31 ± 0.49	3.26 ± 0.77	0.802 ± 0.090	-33 ± 15	0.577 ± 0.063	-43 ± 9	-31.8 ± 13.1
$\rho(1450)$	27.01 ± 1.41	20.53 ± 1.10	2.013 ± 0.069	-140 ± 13	1.974 ± 0.062	-129 ± 8	-1.9 ± 3.8
$f_2(1270)$	11.71 ± 0.60	4.84 ± 0.38	0.977 ± 0.041	124 ± 13	1.300 ± 0.042	132 ± 6	27.8 ± 4.0
Re-scattering	8.65 ± 0.44	26.12 ± 1.15	2.270 ± 0.052	-121 ± 15	1.117 ± 0.036	-115 ± 7	-61.0 ± 1.6
$\phi(1020)$	0.78 ± 0.12	0.10 ± 0.05	0.142 ± 0.032	87 ± 19	0.336 ± 0.027	-76 ± 12	69.8 ± 12.4
χ_{c0}	1.02 ± 0.19	0.69 ± 0.09	0.369 ± 0.025	154 ± 8	0.383 ± 0.036	57 ± 13	3.6 ± 11.3
Fit Fraction Sum	100.1	102.2					

Figures 76 and 81 present the resulting amplitudes and phases motion from the PDFs of $K\pi$ S -wave of the fits using $K_0^*(1430)$ together with PolarFFNR, and $K_0^*(1430)$ together with δ_{Pol} , respectively. As previously mentioned, the PolarFFNR contributes only a constant phase, while the δ_{Pol} introduces a varying phase that increases across the phase space. On the other hand, the amplitudes exhibit very similar shapes. Figures 82, 83 and 84 present the projections of the Dalitz Plot using the δ_{Pol} . For this case, $\Delta_{NLL} = 96$.

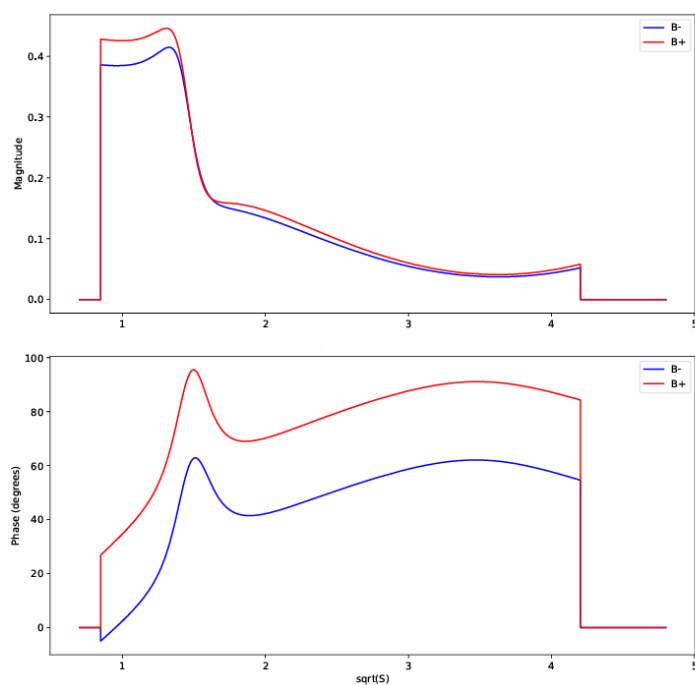


Figura 81 – Magnitude and phase of the $K\pi$ S-wave resulting from Fit 7 using $K_0^*(1430)$ and δ_{Pol2} .

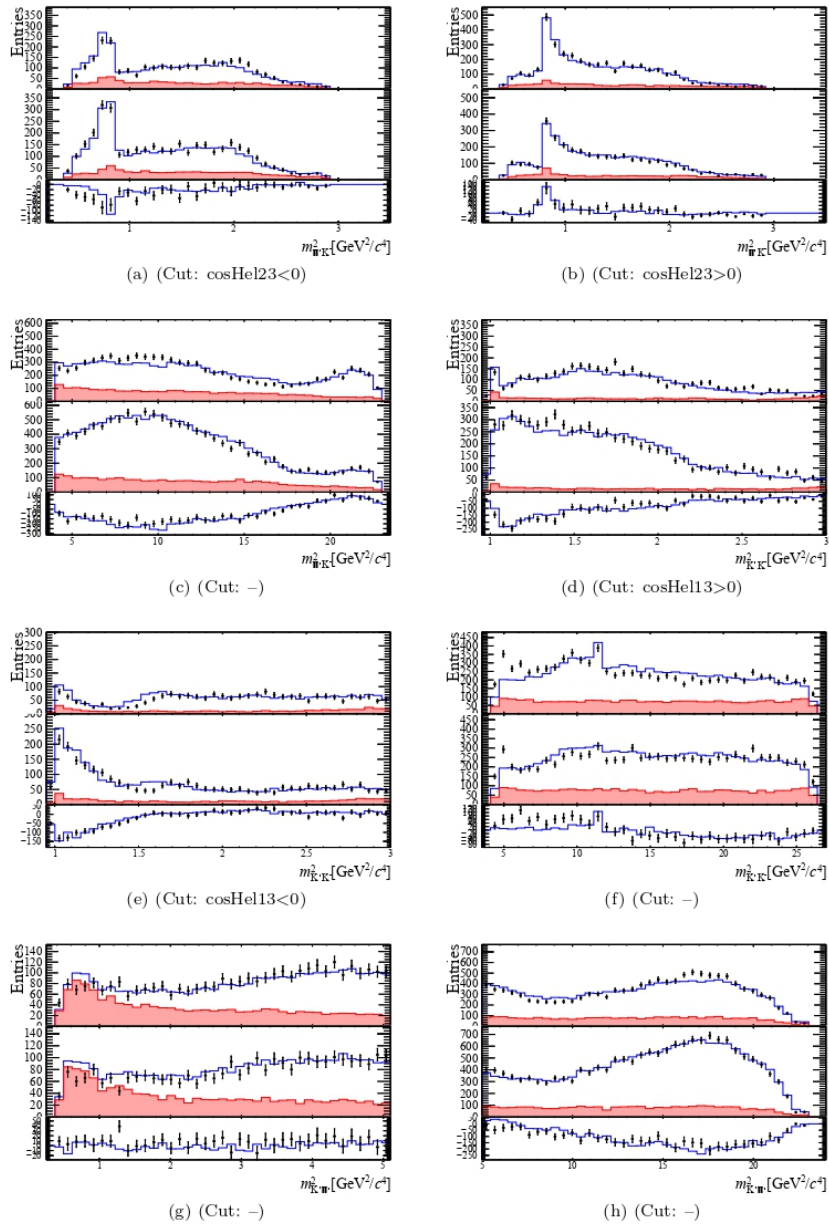


Figura 82 – Fit 7, for each plot B^- (top), B^+ (middle) and the difference ($B^- - B^+$, bottom). The a) ($\cos\text{Hel}23 < 0$), b) ($\cos\text{Hel} > 0$), and c) are showing the $m_{K^{\pm}\pi^{\mp}}^2$ in a different region. The d) ($\cos\text{Hel}13 > 0$), e) ($\cos\text{Hel}13 < 0$), and f) are the projections for the $m_{K^+K^-}^2$. For the g) and h) we have the diagonal projections $m_{K^+\pi^+}^2$. The line in blue represents the model, the black dots represent the data, and the region in red is the background estimation. All plots were produced using 40 bins.

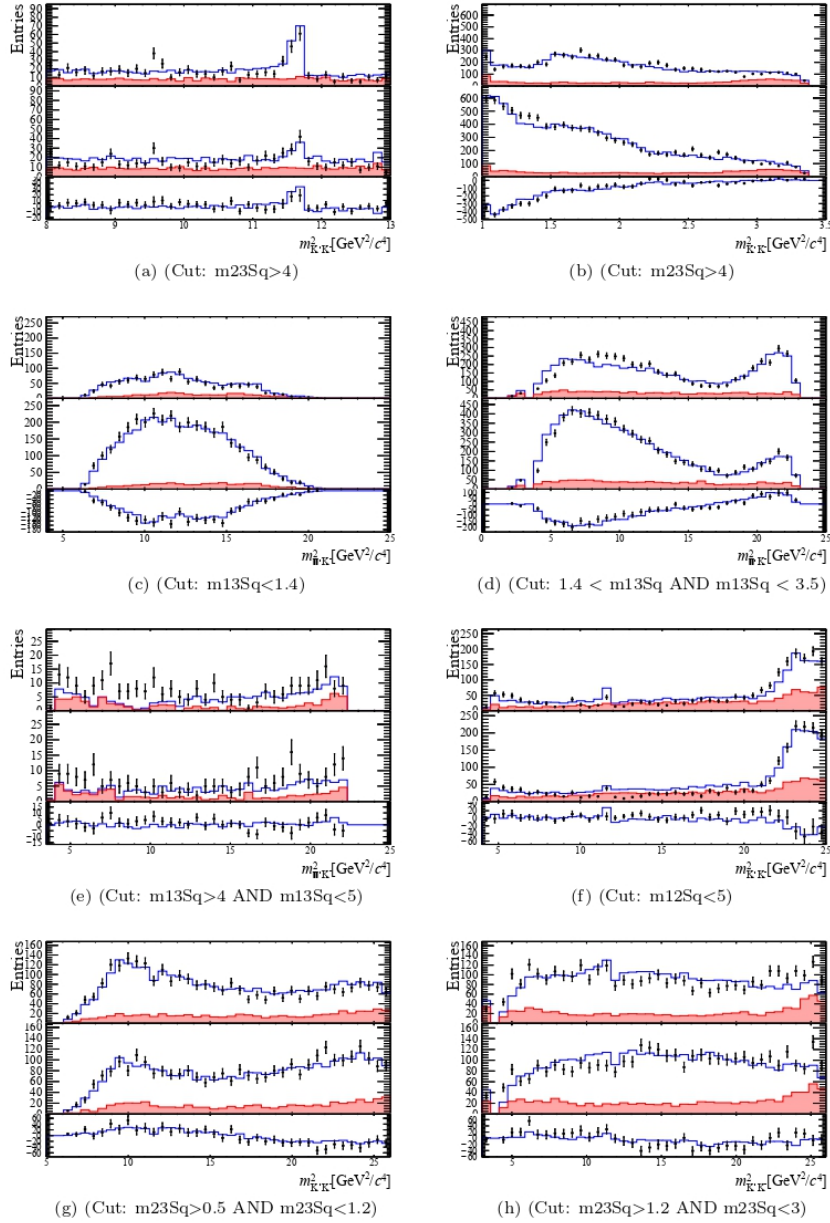


Figura 83 – Fit 7, for each plot B^- (top), B^+ (middle) and the difference ($B^- - B^+$, bottom). The a) ($\cos Hel_{23} < 0$), b) ($\cos Hel > 0$), and c) are showing the $m_{K^\pm\pi^\mp}^2$ in a different region. The d) ($\cos Hel_{13} > 0$), e) ($\cos Hel_{13} < 0$), and f) are the projections for the $m_{K^+K^-}$. For the g) and h) we have the diagonal projections $m_{K^+\pi^+}^2$. The line in blue represents the model, the black dots represent the data, and the region in red is the background estimation. All plots were produced using 40 bins.

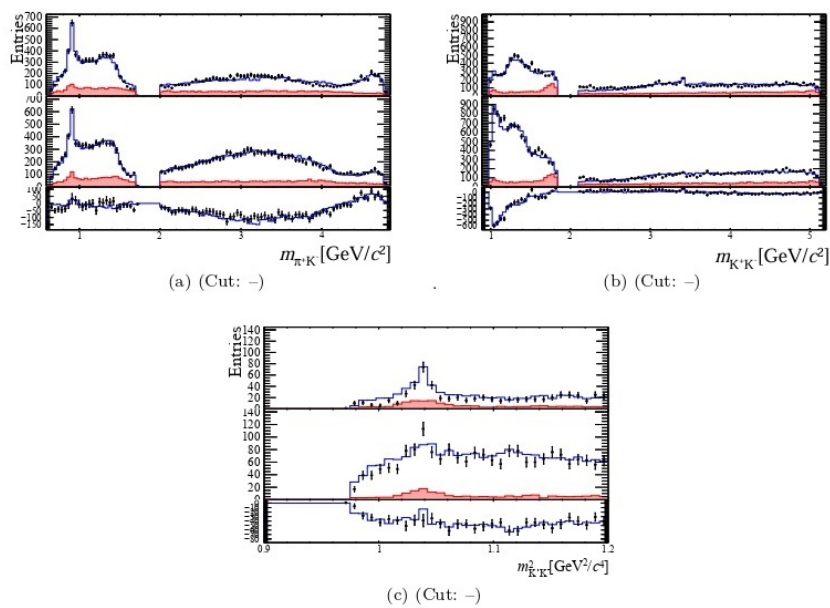


Figura 84 – Fit 7, for each plot B^- (top), B^+ (middle) and the difference ($B^- - B^+$, bottom). The a) and b) show the full projections of $m_{K^\pm\pi^\mp}$ and $m_{K^+K^-}$ produced using 100 bins, respectively. It is important to note that in these two cases, the mass is not squared. The c) is the $0.9 < m_{K^+K^-}^2 < 1.2$ to zoom in on the $\phi(1020)$, using 40 bins. The line in blue represents the model, the black dots represent the data, and the region in red is the background estimation.

Fit 9. Including the $J/\psi(1S)$

After the modifications made to the Fit 7, the addition of the $J/\psi(1S)$ component was tested, as there appear to be indications of its presence (as discussed in Fit 2). Table 29 presents the fit results after including the J/ψ , and Figure 85 shows the region where this component is located. As can be seen, there is almost no impact on the Dalitz plot projection, and the Fit Fraction shows a very low value of around 0.1%. Using the likelihood ratio, we find that the inclusion of the $J/\psi(1S)$ in this case does not have appreciable statistical significance since $NLL_{\text{ratio}} = 33$, and $33 < 34.55$. A study with toys generated including the $J/\psi(1S)$ is presented in Appendix G, exploring different configurations.

Tabela 29 – Dalitz Plot Fit 9 results including the J/ψ .

[NLL -142848] Component	Fit fraction (%)		Magnitude and phase coefficients				A_{CP} (%)
	B^-	B^+	a_i^+	$\delta_i^+ [^\circ]$	a_i^-	$\delta_i^- [^\circ]$	
$K^*(892)$	6.42 ± 0.34	4.95 ± 0.28	1.002 ± 0.020	0 ± 0	0.998 ± 0.020	0 ± 0	-0.4 ± 3.9
$K_0^*(1430)$	6.02 ± 0.49	5.64 ± 0.41	1.069 ± 0.044	15 ± 3	0.966 ± 0.043	-25 ± 4	-10.1 ± 5.3
$PolarFFNR$	38.39 ± 1.14	34.15 ± 0.76	2.632 ± 0.064	29 ± 3	2.440 ± 0.062	1 ± 3	-7.6 ± 1.9
$\rho(1700)$	3.51 ± 0.53	3.05 ± 0.51	0.786 ± 0.068	-96 ± 10	0.738 ± 0.059	-90 ± 6	-6.3 ± 11.3
$\rho(1450)$	22.43 ± 1.22	16.83 ± 0.92	1.848 ± 0.062	177 ± -120	1.865 ± 0.063	-145 ± 7	0.9 ± 3.8
$f_2(1270)$	9.83 ± 0.51	3.92 ± 0.29	0.891 ± 0.038	80 ± 6	1.235 ± 0.041	109 ± 5	31.5 ± 4.2
Re-scattering	8.52 ± 0.39	24.47 ± 0.46	2.228 ± 0.049	-164 ± 6	1.150 ± 0.036	-136 ± 6	-57.9 ± 1.7
$\phi(1020)$	0.77 ± 0.11	0.07 ± 0.04	0.120 ± 0.031	42 ± 16	0.346 ± 0.026	-96 ± 10	78.5 ± 10.4
χ_{c0}	1.39 ± 0.14	0.66 ± 0.09	0.367 ± 0.025	115 ± 7	0.464 ± 0.026	66 ± 7	23.1 ± 7.9
J/ψ	0.20 ± 0.09	0.01 ± 0.02	0.053 ± 0.035	52 ± 37	0.177 ± 0.040	161 ± 11	83.5 ± 22.3
Fit Fraction Sum	97.5	93.7					

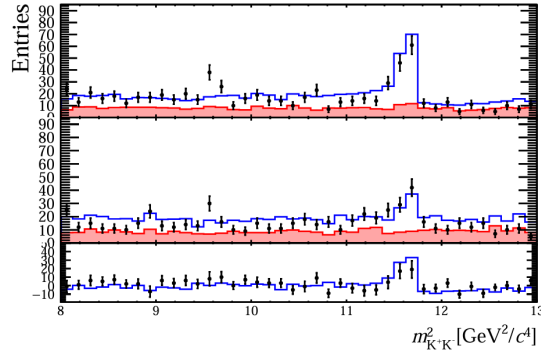
(a) (Cut: $m_{23S} > 4$)

Figura 85 – Fit 9 results for the m_{K+K-}^2 projection with the $m_{K\pm\pi\mp}^2 > 4$. Signature of $J/\psi(1S)$ around $9.5 \text{ GeV}^2/c^4$.

Fit 10. *Trials to include the $f'_2(1525)$*

The objective of this test is to evaluate the possibility of replacing (or including) the tensor resonance in the decay with the $f'_2(1525)$. This proposal is based on [61], which shows that the dominant decay channel for the $f'_2(1525)$ is 87.6%, while for the $f_2(1270)$, it is 4.6% for the $K\bar{K}$ system.

Table 30 presents the results of the attempt to replace $f_2(1270)$ with $f'_2(1525)$. As observed, the impact on the NLL value is significantly negative if compared to the previous result Fit 6. Various regions of the phase space were adversely affected by this change. Figures 86, 87, and 88 display the Dalitz Plot projections. For instance, in Figure 87, item c), the negative impact of this modification is evident.

Attempts were also made to include both resonances ($f_2(1270)$ and $f'_2(1525)$). Table 31 presents the results of including both resonances. Figures 89, 90, and 91 display the Dalitz Plot projections for this scenario. No noticeable positive or negative impact from the addition of $f'_2(1525)$ was observed in the projections. However, using the likelihood ratio for this case, the $NLL_{\text{ratio}} = 66$. Since $34.55 < 66$, the addition of $f'_2(1525)$ in this model demonstrates positive statistical significance. In the other hand one can also observe the low contribution of the $f'_2(1525)$ to the decay, around 0.5% of total Fit Fraction. Due to these ambiguities, we decided not to proceed with the inclusion of the $f'_2(1525)$ in the final model.

Tabela 30 – Dalitz Plot Fit 10 results replacing $f_2(1270)$ with $f'_2(1525)$.

[NLL -142442] Component	Fit fraction (%)		Magnitude and phase coefficients				A_{CP} (%)
	B^-	B^+	a_i^+	$\delta_i^+ [^\circ]$	a_i^-	$\delta_i^- [^\circ]$	
$K^*(892)$	6.12 ± 0.32	4.94 ± 0.29	1.009 ± 0.020	0 ± 0	0.991 ± 0.020	0 ± 0	-1.9 ± 4.0
$K_0^*(1430)$	7.13 ± 0.53	4.08 ± 0.33	0.918 ± 0.042	19 ± 4	1.069 ± 0.045	-20 ± 4	15.2 ± 5.4
<i>PolarFFNR</i>	32.77 ± 1.07	34.87 ± 0.76	2.683 ± 0.067	32 ± 3	2.292 ± 0.063	0 ± 3	-15.6 ± 2.0
$\rho(1700)$	2.17 ± 0.48	2.80 ± 0.49	0.760 ± 0.069	-96 ± 8	0.590 ± 0.068	-91 ± 7	-24.8 ± 13.4
$\rho(1450)$	30.76 ± 1.49	16.00 ± 0.87	1.818 ± 0.061	175 ± 4	2.221 ± 0.071	-88 ± 5	19.8 ± 3.5
$f'_2(1525)$	5.68 ± 0.38	0.96 ± 0.14	0.444 ± 0.033	-163 ± 8	0.954 ± 0.037	-53 ± 5	64.4 ± 4.7
Re-scattering	13.94 ± 0.42	26.78 ± 0.44	2.351 ± 0.052	171 ± 5	1.495 ± 0.039	-95 ± 5	-42.4 ± 1.5
$\phi(1020)$	0.77 ± 0.11	0.07 ± 0.04	0.120 ± 0.032	9 ± 15	0.351 ± 0.027	-53 ± 8	79.2 ± 10.2
χ_{c0}	1.21 ± 0.13	0.10 ± 0.04	0.144 ± 0.026	-24 ± 18	0.440 ± 0.026	59 ± 8	80.8 ± 6.5
Fit Fraction Sum	100.5	90.6					

Tabela 31 – Dalitz Plot Fit 10 results adding $f_2(1270)$ together with $f_2'(1525)$.

[NLL -142885] Component	Fit fraction (%)		Magnitude and phase coefficients				A_{CP} (%)
	B^-	B^+	a_i^+	$\delta_i^+ [^\circ]$	a_i^-	$\delta_i^- [^\circ]$	
$K^*(892)$	6.25 ± 0.34	4.93 ± 0.29	1.008 ± 0.020	0 ± 0	0.992 ± 0.020	0 ± 0	-1.6 ± 4.0
$K_0^*(1430)$	5.79 ± 0.47	5.45 ± 0.40	1.060 ± 0.045	16 ± 3	0.955 ± 0.043	-24 ± 4	-10.4 ± 5.3
<i>PolarFFNR</i>	37.69 ± 1.30	34.25 ± 0.76	2.656 ± 0.066	30 ± 3	2.436 ± 0.065	2 ± 3	-8.6 ± 2.1
$\rho(1700)$	3.62 ± 0.55	3.16 ± 0.52	0.807 ± 0.069	-97 ± 9	0.755 ± 0.060	-78 ± 6	-6.6 ± 11.2
$\rho(1450)$	22.48 ± 1.35	16.34 ± 0.91	1.835 ± 0.063	174 ± 5	1.881 ± 0.070	-135 ± 9	2.5 ± 4.2
$f_2(1270)$	7.90 ± 0.54	3.53 ± 0.30	0.853 ± 0.040	71 ± 5	1.116 ± 0.044	109 ± 6	26.2 ± 5.1
$f_2'(1525)$	0.92 ± 0.24	0.18 ± 0.07	0.192 ± 0.038	-166 ± 13	0.380 ± 0.050	-118 ± 12	59.4 ± 15.4
Re-scattering	9.18 ± 0.46	24.55 ± 0.46	2.249 ± 0.050	-168 ± 6	1.202 ± 0.041	-127 ± 7	-55.5 ± 1.9
$\phi(1020)$	0.79 ± 0.11	0.07 ± 0.04	0.120 ± 0.032	37 ± 16	0.353 ± 0.027	-82 ± 10	79.1 ± 10.2
χ_{c0}	1.36 ± 0.14	0.09 ± 0.03	0.139 ± 0.026	-29 ± 18	0.463 ± 0.026	65 ± 7	83.5 ± 5.8
Fit Fraction Sum	96.0	92.6					

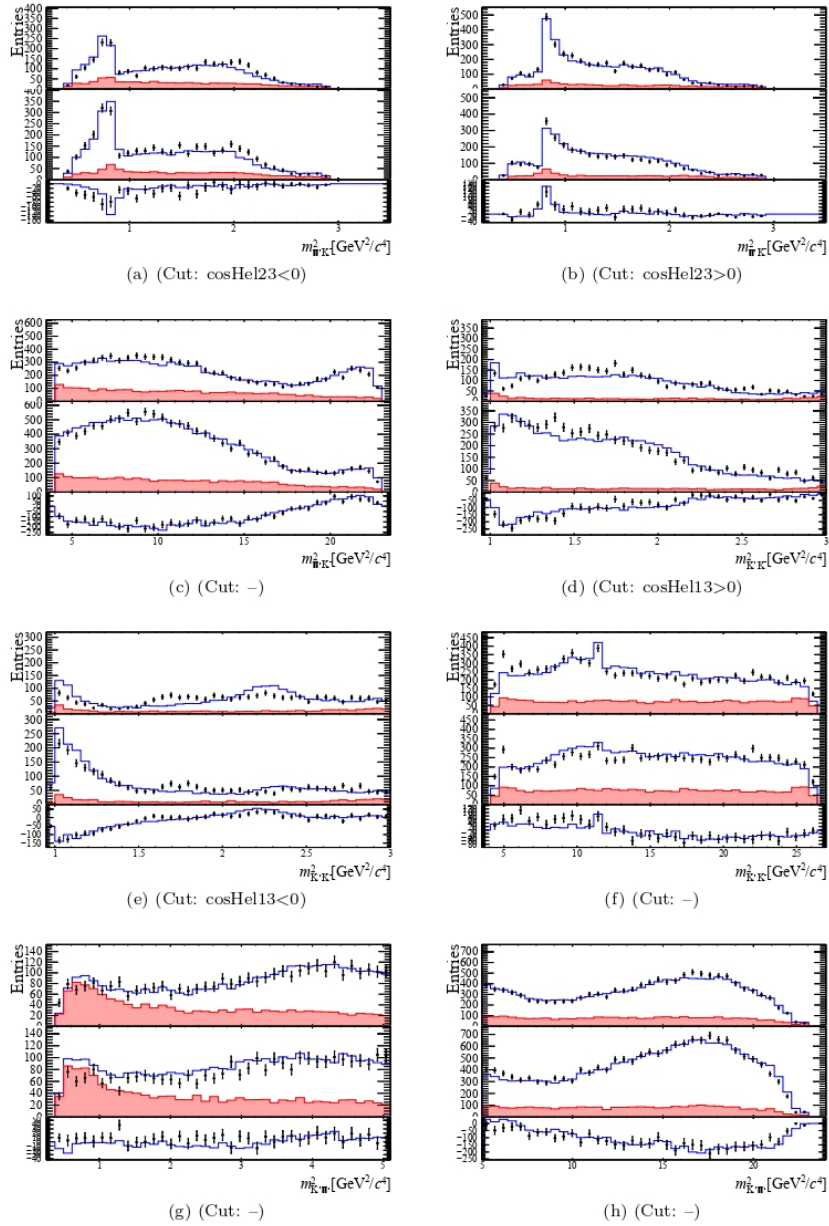


Figura 86 – Fit 10 replacing the $f_2(1270)$ with $f_2'(1525)$, for each plot B^- (top), B^+ (middle) and the difference ($B^- - B^+$, bottom). The a) ($\cos\text{Hel}23 < 0$), b) ($\cos\text{Hel} > 0$), and c) are showing the $m_{K^\pm\pi^\mp}^2$ in a different region. The d) ($\cos\text{Hel}13 > 0$), e) ($\cos\text{Hel}13 < 0$), and f) are the projections for the $m_{K^+K^-}^2$. For the g) and h) we have the diagonal projections $m_{K^+\pi^+}^2$. The line in blue represents the model, the black dots represent the data, and the region in red is the background estimation. All plots were produced using 40 bins.

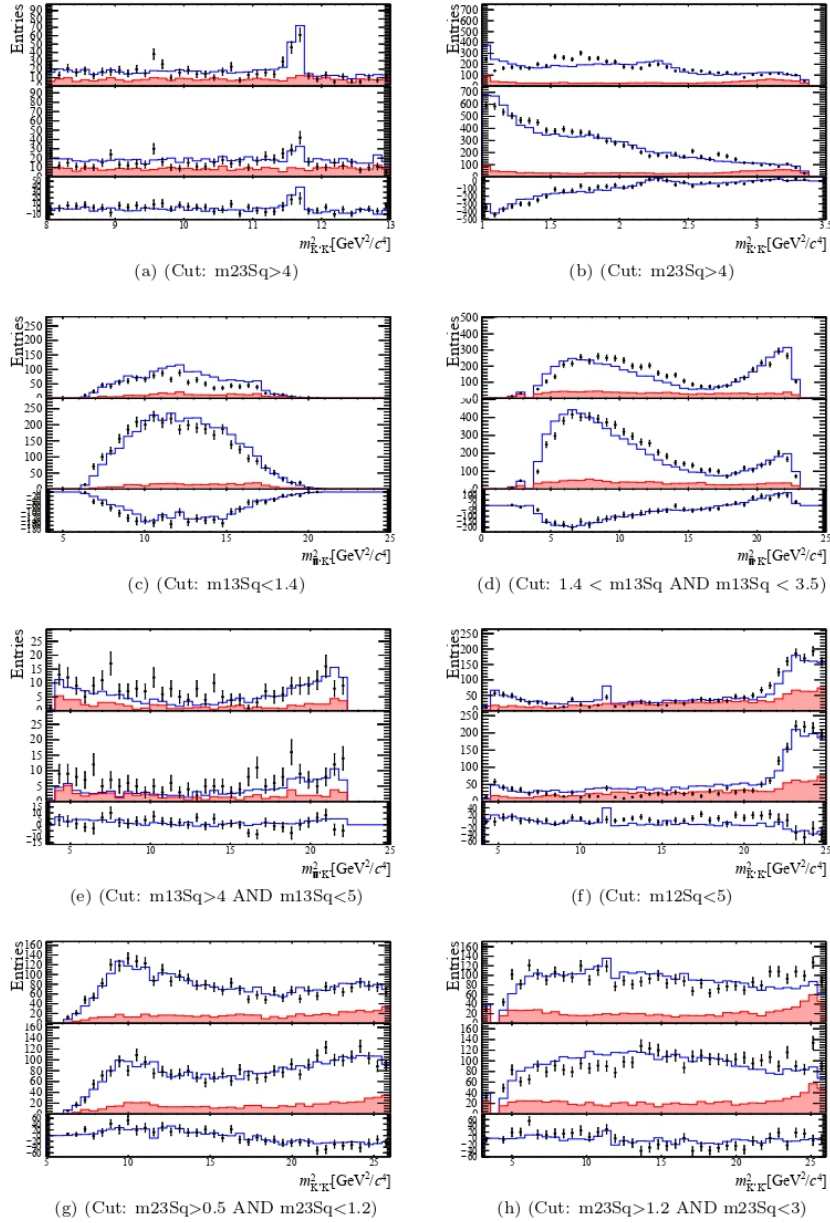


Figura 87 – Fit 10 replacing the $f_2(1270)$ with $f'_2(1525)$, for each plot B^- (top), B^+ (middle) and the difference ($B^- - B^+$, bottom). The a) ($\cos Hel_{23} < 0$), b) ($\cos Hel_{23} > 0$), and c) are showing the $m_{K^\pm\pi^\mp}^2$ in a different region. The d) ($\cos Hel_{13} > 0$), e) ($\cos Hel_{13} < 0$), and f) are the projections for the $m_{K^+K^-}^2$. For the g) and h) we have the diagonal projections $m_{K^+\pi^+}^2$. The line in blue represents the model, the black dots represent the data, and the region in red is the background estimation. All plots were produced using 40 bins.

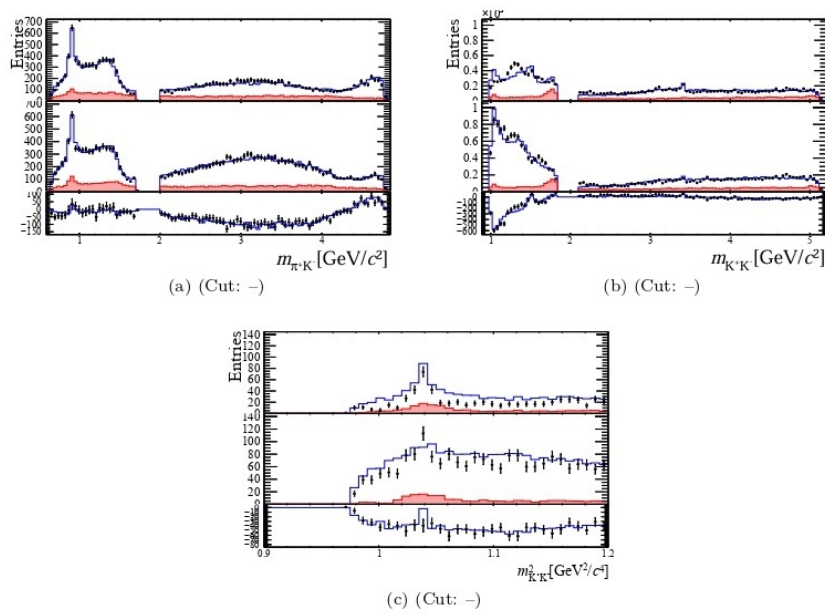


Figura 88 – Fit 10 replacing the $f_2(1270)$ with $f_2'(1525)$, for each plot B^- (top), B^+ (middle) and the difference ($B^- - B^+$, bottom). The a) and b) show the full projections of $m_{K^\pm\pi^\mp}$ and $m_{K^+K^-}$ produced using 100 bins, respectively. It is important to note that in these two cases, the mass is not squared. The c) is the $0.9 < m_{K^+K^-}^2 < 1.2$ to zoom in on the $\phi(1020)$, using 40 bins. The line in blue represents the model, the black dots represent the data, and the region in red is the background estimation.

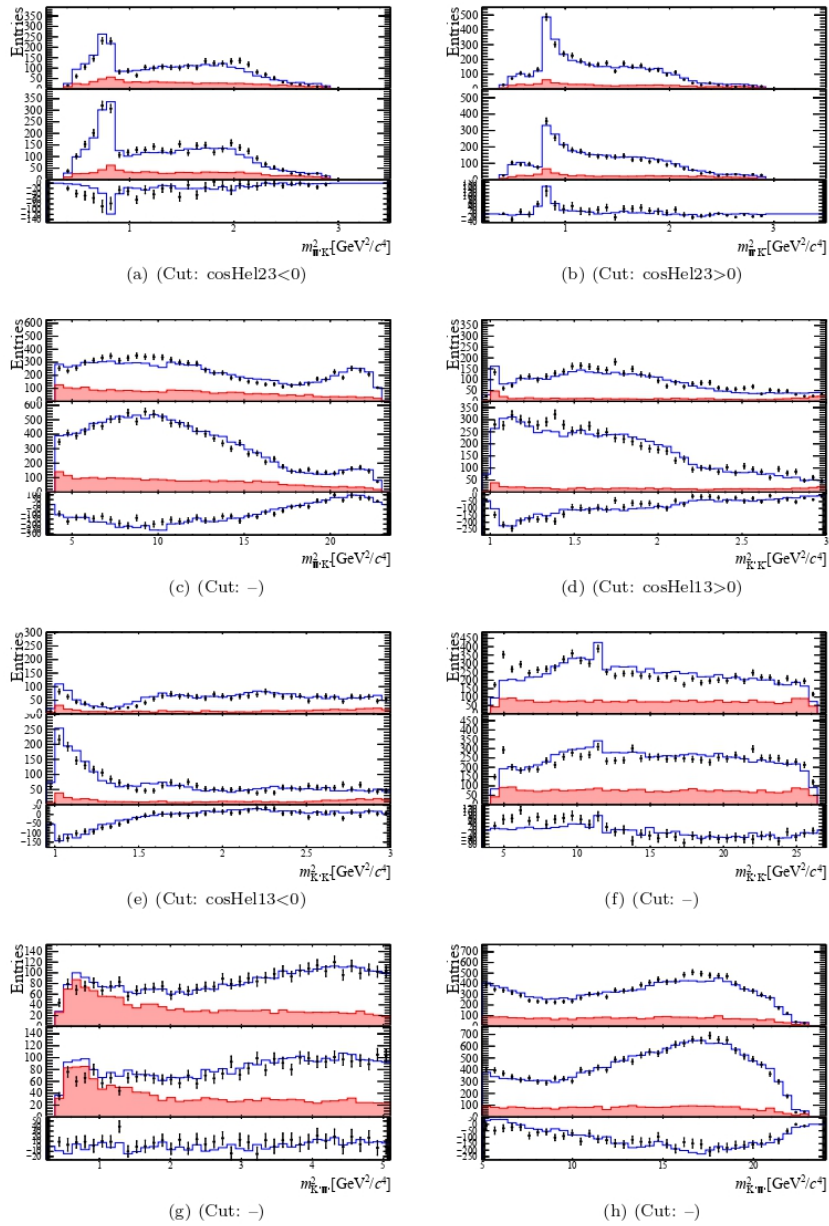


Figura 89 – Fit 10 adding the $f_2(1270)$ together with $f_2'(1525)$, for each plot B^- (top), B^+ (middle) and the difference ($B^- - B^+$, bottom). The a) ($\cos\text{Hel}23 < 0$), b) ($\cos\text{Hel} > 0$), and c) are showing the $m_{K^\pm\pi^\mp}^2$ in a different region. The d) ($\cos\text{Hel}13 > 0$), e) ($\cos\text{Hel}13 < 0$), and f) are the projections for the $m_{K^+K^-}^2$. For the g) and h) we have the diagonal projections $m_{K^+\pi^+}^2$. The line in blue represents the model, the black dots represent the data, and the region in red is the background estimation. All plots were produced using 40 bins.

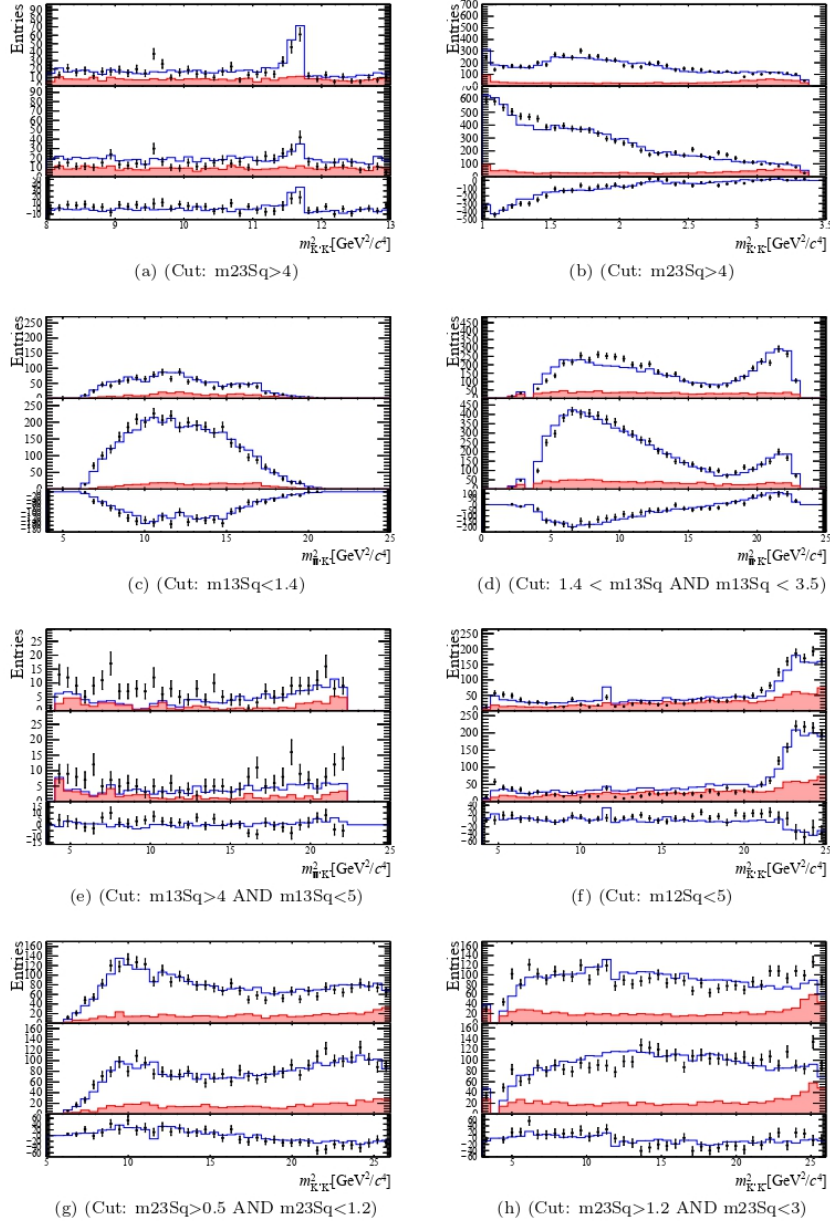


Figura 90 – Fit 10 adding the $f_2(1270)$ together with $f_2'(1525)$, for each plot B^- (top), B^+ (middle) and the difference ($B^- - B^+$, bottom). The a) ($\cos Hel_{23} < 0$), b) ($\cos Hel_{23} > 0$), and c) are showing the $m_{K^\pm\pi^\mp}^2$ in a different region. The d) ($\cos Hel_{13} > 0$), e) ($\cos Hel_{13} < 0$), and f) are the projections for the $m_{K^+K^-}^2$. For the g) and h) we have the diagonal projections $m_{K^+\pi^+}^2$. The line in blue represents the model, the black dots represent the data, and the region in red is the background estimation. All plots were produced using 40 bins.

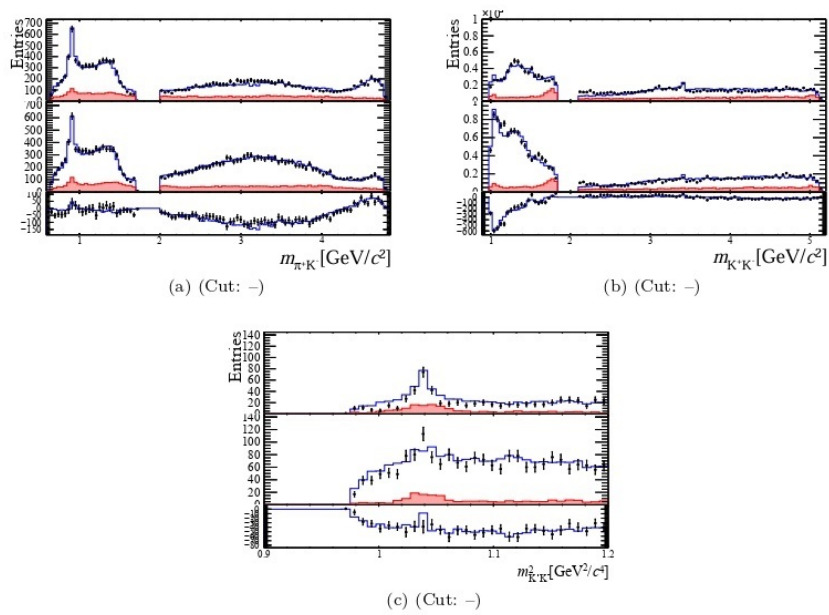


Figura 91 – Fit 10 adding the $f_2(1270)$ together with $f_2'(1525)$, for each plot B^- (top), B^+ (middle) and the difference ($B^- - B^+$, bottom). The a) and b) show the full projections of $m_{K^{\pm}\pi^{\mp}}$ and $m_{K^+K^-}$ produced using 100 bins, respectively. It is important to note that in these two cases, the mass is not squared. The c) is the $0.9 < m_{K^+K^-}^2 < 1.2$ to zoom in on the $\phi(1020)$, using 40 bins. The line in blue represents the model, the black dots represent the data, and the region in red is the background estimation.

Fit 11. *Alternative model*

As an alternative model, studies were conducted involving the substitution of the two main S -wave components for the KK and $K\pi$ systems: the $f_0(980)$ replacing the Rescattering component, and the δ_{Pol4} replacing the PolarFFNR. In this case, a fourth-degree polynomial is used to describe the phase, expressed as:

$$\delta_{Pol4} = A_1 mass^4 + B_2 mass^3 + C_3 mass^2 + D_4 mass + E_5 \quad (8.2)$$

with all parameters free to vary, the measured values are: $A_1 = -3.01 \times 10^{-2} \pm 2.11 \times 10^{-4}$, $B_2 = 2.97 \times 10^{-1} \pm 9.84 \times 10^{-4}$, $C_3 = -1.07 \pm 4.41 \times 10^{-3}$, $D_4 = 1.97 \pm 2.90 \times 10^{-2}$ and $E_5 = 1.25 \pm 7.54 \times 10^{-2}$.

As shown in Figures 92, 93, and 94, the results of these modifications are presented. In the $c)$ of Figure 94, the negative impact on the model can be observed in the region where the $f_0(980)$ is located (see the same item Figure 84 for comparison). Other regions of the Dalitz plot experienced minimal or no changes.

Figures 95 and 96 present the phase and amplitude motion for this case. It can be observed that for the $K\pi$ S -wave, the difference between using a second-degree or fourth-degree polynomial introduces more intense variations in the phase (compared to Figure 81). As we can see, the δ_{Pol} approach is flexible and adapts to different scenarios. On the other hand, the KK S -wave shows significant differences (compared to Figure 77), as expected, given that the Rescattering modeling is substantially different from the Flatté parameterization used for the $f_0(980)$.

Tabela 32 – Dalitz Plot Fit 11 results using $f_0(980)$ replacing the Rescattering and the δ_{Pol4} replacing the PolarFFNR.

[NLL -142909] Component	Fit fraction (%)		Magnitude and phase coefficients				A_{CP} (%)
	B^-	B^+	a_i^+	$\delta_i^+ [^\circ]$	a_i^-	$\delta_i^- [^\circ]$	
$K^*(892)$	6.07 ± 0.33	4.49 ± 0.26	1.012 ± 0.020	0 ± 0	0.988 ± 0.020	0 ± 0	-2.3 ± 3.9
$K_0^*(1430)$	8.19 ± 0.69	6.89 ± 0.63	1.253 ± 0.059	43 ± 3	1.148 ± 0.052	-1 ± 4	-8.7 ± 5.7
δ_{Pol4}	31.34 ± 1.13	29.00 ± 1.04	2.571 ± 0.073	-110 ± 4	2.246 ± 0.065	-139 ± 4	-13.4 ± 2.5
$\rho(1700)$	1.67 ± 0.39	1.13 ± 0.29	0.508 ± 0.067	-56 ± 11	0.519 ± 0.063	-35 ± 10	2.2 ± 16.1
$\rho(1450)$	24.42 ± 1.27	15.81 ± 0.88	1.899 ± 0.060	-111 ± 6	1.983 ± 0.064	-104 ± 6	4.3 ± 3.6
$f_2(1270)$	9.09 ± 0.52	3.21 ± 0.31	0.856 ± 0.046	141 ± 6	1.210 ± 0.042	149 ± 5	33.3 ± 5.0
$f_0(980)$	16.52 ± 0.62	38.63 ± 0.70	2.967 ± 0.066	-44 ± 6	1.631 ± 0.044	-48 ± 5	-53.6 ± 1.4
$\phi(1020)$	0.70 ± 0.10	0.04 ± 0.03	0.096 ± 0.035	52 ± 19	0.336 ± 0.026	-108 ± 9	85.0 ± 10.5
χ_{c0}	0.90 ± 0.12	0.41 ± 0.09	0.307 ± 0.034	155 ± 15	0.381 ± 0.026	77 ± 9	21.2 ± 12.2
Fit Fraction Sum	101.6	107.8					

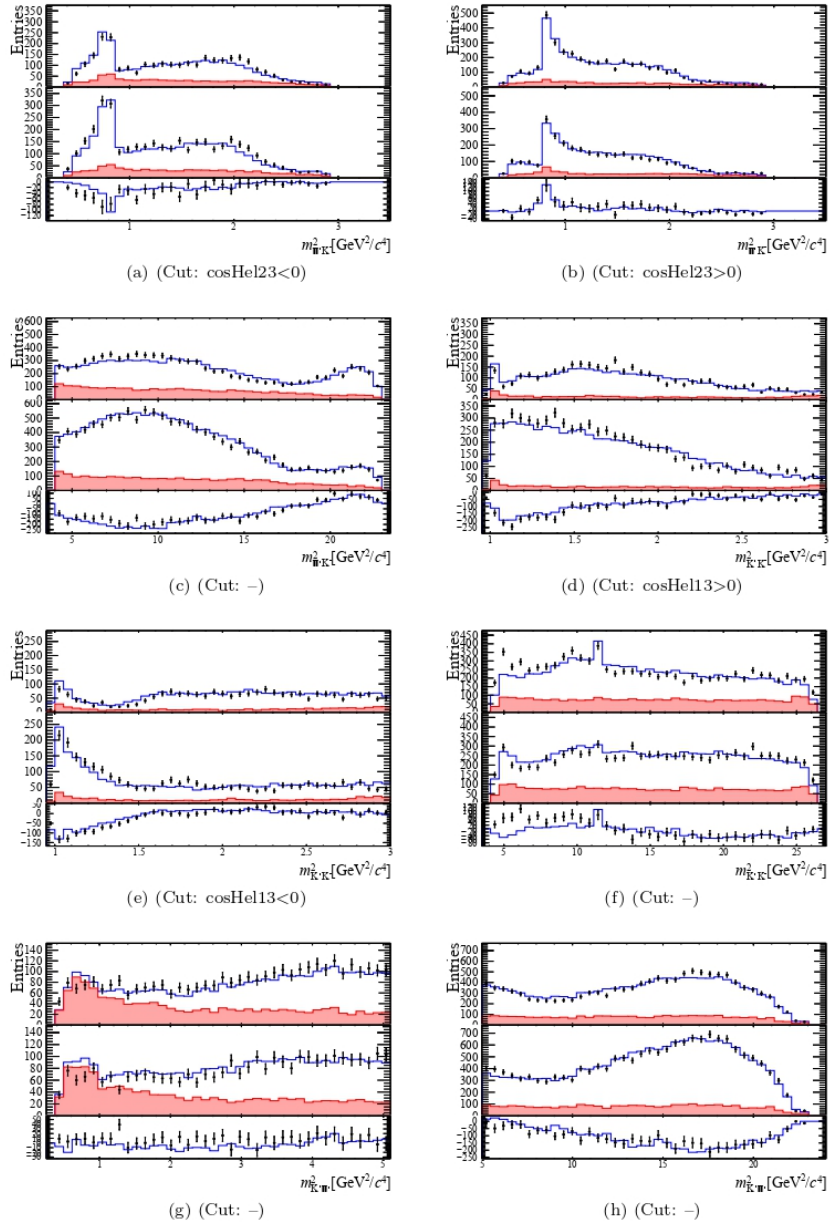


Figura 92 – Fit 11 using $f_0(980)$ in place of Rescattering and δ_{Pol4} for PolarFFNR, for each plot B^- (top), B^+ (middle) and the difference ($B^- - B^+$, bottom). The a) ($\cos\text{Hel}23 < 0$), b) ($\cos\text{Hel} > 0$), and c) are showing the $m_{K^\pm\pi^\mp}^2$ in a different region. The d) ($\cos\text{Hel}13 > 0$), e) ($\cos\text{Hel}13 < 0$), and f) are the projections for the $m_{K^+K^-}^2$. For the g) and h) we have the diagonal projections $m_{K^+\pi^+}^2$. The line in blue represents the model, the black dots represent the data, and the region in red is the background estimation. All plots were produced using 40 bins.

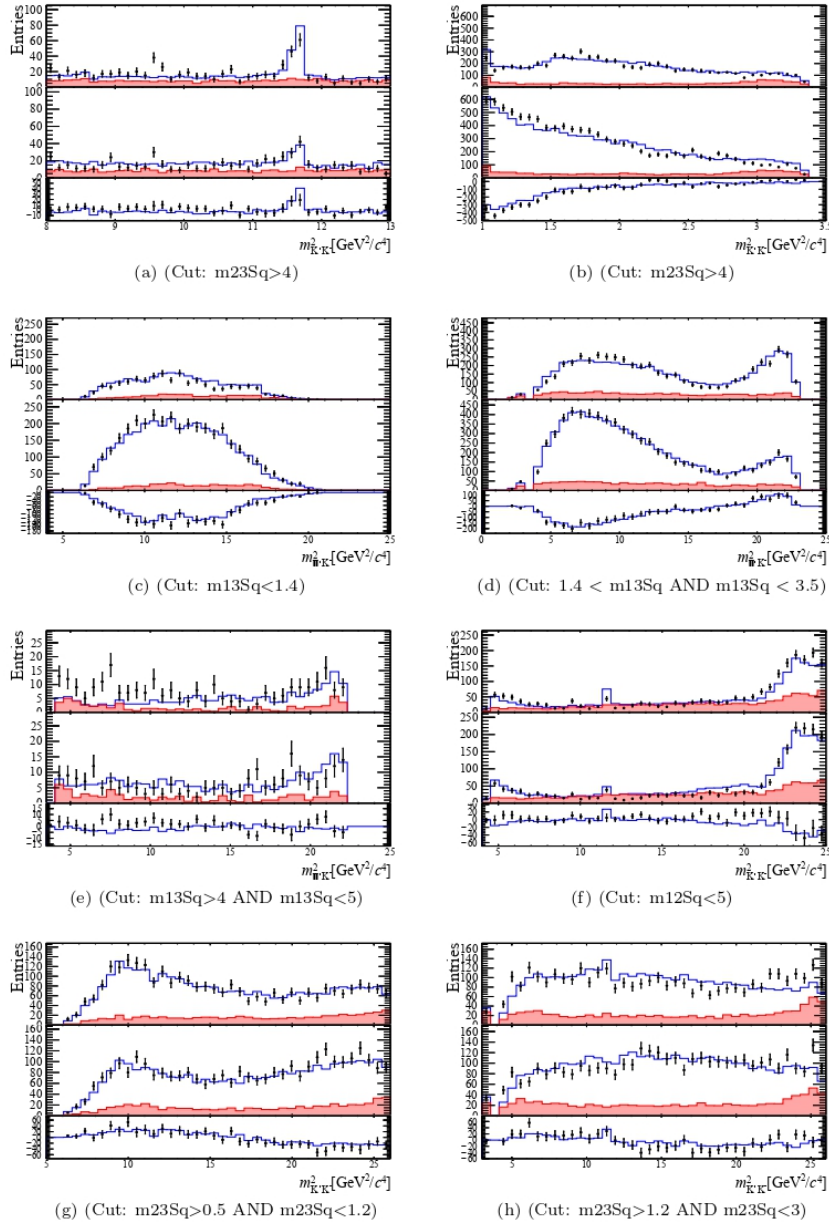


Figura 93 – Fit 11 using $f_0(980)$ in place of Rescattering and δ_{Pol4} for PolarFFNR, for each plot B^- (top), B^+ (middle) and the difference ($B^- - B^+$, bottom). The a) ($\cos Hel_{23} < 0$), b) ($\cos Hel_{23} > 0$), and c) are showing the $m_{K^\pm\pi^\mp}^2$ in a different region. The d) ($\cos Hel_{13} > 0$), e) ($\cos Hel_{13} < 0$), and f) are the projections for the $m_{K^+K^-}^2$. For the g) and h) we have the diagonal projections $m_{K^+\pi^+}^2$. The line in blue represents the model, the black dots represent the data, and the region in red is the background estimation. All plots were produced using 40 bins.

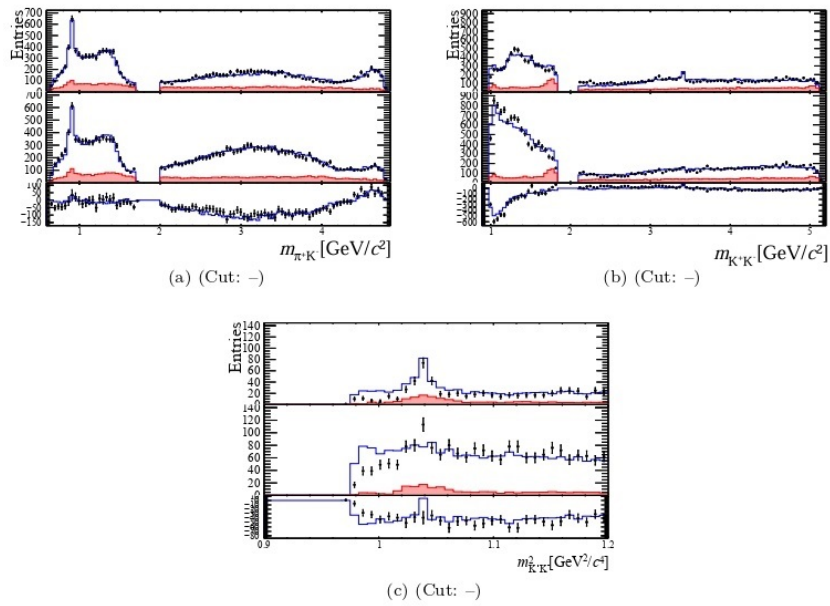


Figura 94 – Fit 11 using $f_0(980)$ in place of Rescattering and δ_{Pol4} for PolarFFNR, for each plot B^- (top), B^+ (middle) and the difference ($B^- - B^+$, bottom). The a) and b) show the full projections of $m_{K^\pm\pi^\mp}$ and $m_{K^+K^-}$ produced using 100 bins, respectively. It is important to note that in these two cases, the mass is not squared. The c) is the $0.9 < m_{K^+K^-}^2 < 1.2$ to zoom in on the $\phi(1020)$, using 40 bins. The line in blue represents the model, the black dots represent the data, and the region in red is the background estimation.

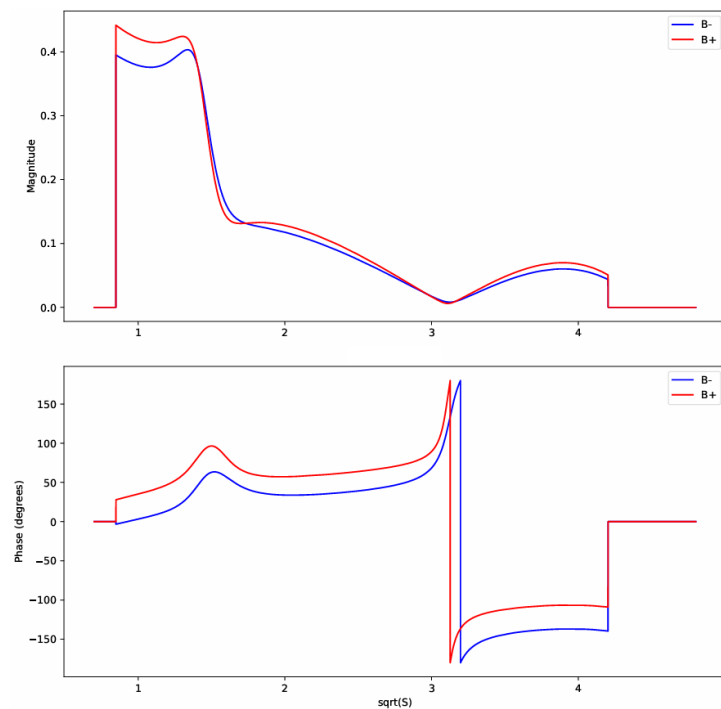


Figura 95 – Amplitude and phase of the $K\pi$ S-wave resulting from Fit 11 using $K_0^*(1430)$ and δ_{Pol4} .

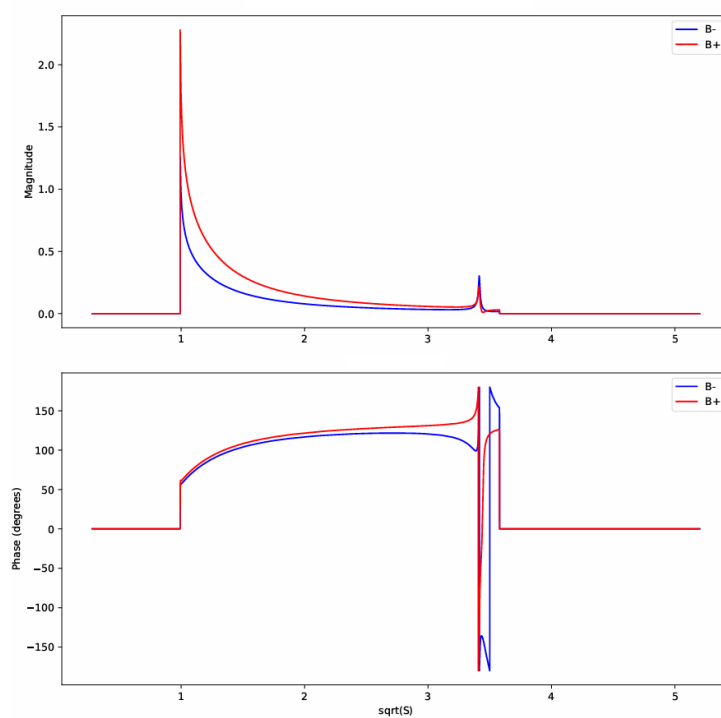


Figura 96 – Amplitude and phase of the KK S-wave resulting from Fit 11 using $f_0(980)$ and χ_{c0} .

8.4 Summary

As discussed in the previous section, various contributions were tested for the decay composition. The highlighted results presented represent only the most notable outcomes. Additional attempts that did not yield satisfactory results are detailed in Appendix H. The final results comprise the baseline model Fit 6 and the version Fit 8. It is worth noting that the attempts including the J/ψ and $f'_2(1525)$ resonances are not entirely dismissible and could be revisited in future studies with larger datasets. We also have an alternative model Fit 11 considering the substitution of all S-waves to different components.

Appendix E also introduces an alternative approach to Dalitz plot cropping, reducing the full phase space to regions of particular interest. This method prioritizes resonances localized in these regions, such as χ_c and J/ψ , enhancing the focus on their contributions.

9 Future systematic uncertainties studies

The evaluation of systematic uncertainties has not yet been carried out, as it depends on finalizing and agreeing upon the baseline model for the paper. Consequently, this section currently focuses on describing the possible sources of uncertainty.

Several sources are considered for systematic uncertainties, including the signal-to-background ratio derived from the B mass fit, efficiency variations across the phase space, and the background distribution within the SDP, among others. Systematic uncertainties are evaluated for each parameter of the baseline result. These parameters include FF^\pm , the Isobar coefficients a^\pm and δ^\pm , the A_{CP} , and the total fit fraction of each resonant state in the model. The total systematic uncertainty is determined by summing in quadrature the contributions from all these sources.

As a concrete example of a source of systematic uncertainties, one can consider variations in the functions used to fit the mass bins forming the background model presented in section 7.3. Additionally, the number of bins employed in these background models can also be varied to assess their impact on the results.

Another example lies in the variation of the acceptance presented in section 7.1. As observed, the current study does not account for the acceptance corresponding to the data collected in 2018. We can also consider, as a source of systematic uncertainties, the different sets of parameters provided by the authors for the parameterization of the Rescattering process, as presented in section 6.2.3.6.

Additionally, the choice of resonance used as a reference in the model can also influence the systematic uncertainties. Until now, the $K^*(892)$ has been used as the reference resonance. However, alternative resonances such as the $\rho(1450)$, which interacts significantly with many structures across the Dalitz Plot, could also be considered to evaluate their impact on the results.

10 Conclusions

This study provides a comprehensive amplitude analysis of the $B^\pm \rightarrow K^\mp K^\pm \pi^\pm$ decay channel using the complete LHCb Run II dataset, addressing key issues identified in previous analyses and enhancing our understanding of CP violation mechanisms in charmless B meson decays. Resonances are expected in the KK and $K\pi$ pairs and linked to specific quark transitions in the decay process. The penguin diagrams ($b \rightarrow d$) suggest contributions from the K^* family, such as $K^*(892)$, $K_0^*(1430)$, while tree-level transitions ($b \rightarrow u$) indicate resonances in the K^+K^- system, such as $f_2(1270)$, $f_0(1370)$, and $f_0(980)$.

The analysis highlighted several challenges, such as the need for improved parametrization of the Rescattering region and the clarification of unexpected resonances, for instance, $\phi(1020)$, $\rho(1450)$, and $f_2(1270)$. Certain resonances, such as $\phi(1020)$, are strongly suppressed due to the OZI rule. Others, like $f_2(1270)$ and $\rho(1450)$, have smaller contributions than expected due to low branching fractions to KK . The rescattering region, which previously lacked a robust description, has been updated. Our revisited model has also clarified the roles of the $\rho(1450)$ and $f_2(1270)$ resonances. Contrary to initial expectations, $\rho(1450)$ contributes distinctly in the $B^\pm \rightarrow K^\mp K^\pm \pi^\pm$ channel, while $f_2(1270)$ serves as the principal tensor contribution. Adding the $\rho^0(1700)$ resonance to the model has also proven advantageous, especially by improving the fit fraction balance and reducing the $\rho^0(1450)$ contribution. This change is indicative of constructive interference between the $\rho^0(1450)$ and $\rho^0(1700)$ resonances.

Furthermore, the complex modeling of the S-wave component remains an intricate aspect of the analysis. The S-wave model, which comprises approximately 60% of the decay amplitude, now offers an improved fit along the densely populated Dalitz plot edges, where prior analyses faced substantial modeling challenges. The introduction of the δ_{Pol} parametrization as an alternative to the PolarFFNR has provided a more accurate model of the $K\pi$ low mass region, introducing a unitary formulation with phase motion. This approach has demonstrated stable and consistent results, thereby establishing δ_{Pol} as a reliable alternative. This development is particularly valuable given the challenges associated with measuring the phase of the $K\pi$ S-wave.

A novel approach to modeling the background, developed by the CBPF group, was introduced and demonstrated to be highly promising. This method consolidates all background contributions of the channel into a single framework, which could potentially reduce the impact of systematic uncertainties.

Different studies of Dalitz plot fits are presented in the appendix, including methods based on cropped Dalitz plots and Likelihood Ratio. The latter is highlighted as a reliable

method for statistical evaluation, serving as a foundation for future analyses.

The results obtained were evaluated both through physical principles and in light of the statistical tools discussed. We present two reliable models that differ only in their treatment of non-resonant contributions, specifically by including either the δ_{Pol2} or the PolarFFNR component. The baseline model incorporates $K^*(892)$, $K_0^*(1430)$, and PolarFFNR as components of the KK system, alongside $\rho(1700)$, $\rho(1450)$, $f_2(1270)$, Rescattering, $\phi(1020)$, and χ_{c0} resonances for the $K\pi$ system. The second model essentially introduces the phase motion allowed by δ_{Pol} , which offers a more dynamic representation of the $K\pi$ low-mass region. There are also indications of the presence of the $J/\psi(1S)$ and $f_2'(1525)$. However, possibly due to the limited number of events, it was not possible to draw definitive conclusions about these resonances.

In both models, the significant CP violation is confined primarily to the rescattering component, suggesting a unique dynamic effect in this region that warrants further investigation. Notably, this measurement represents one of the largest CP violations observed in a single component. On the other hand, no CP violation was identified in the charmonium resonances. The updated models provide crucial insights into the resonant structures and CP asymmetries in charmless B decays, setting a robust benchmark for future investigations and offering potential pathways to identify new physics beyond the Standard Model.

The results leave the matter open for future analyses, such as a simultaneous amplitude analysis of the strongly coupled channels $B \rightarrow K^+K^-\pi^\pm$ and $B \rightarrow \pi^+\pi^-\pi^\pm$. This study could provide a more precise understanding of unresolved questions regarding the origin of resonant processes in the three-body decays of massive mesons. Through this analysis, it will be possible to differentiate between contributions to the amplitudes arising from the direct coupling of the weak process and those resulting from hadron-hadron rescattering occurring after the decay process.

This work also contributes to the LHCb Upgrade I, specifically in the commissioning of the new SciFi Tracker. Contributions were made to the Read-out Box (RoB) test system, including active participation in drafting a technical note.

The findings presented in this thesis are also included in the complete analysis note, which is currently undergoing internal scrutiny within the LHCb collaboration as part of the publication process. During this review phase, systematic studies will be conducted to determine the uncertainties associated with the fit results.

References

- 1 AAIJ, R. et al. *Direct CP violation in charmless three-body decays of B^\pm mesons*. arXiv, 2022. Disponível em: <<https://arxiv.org/abs/2206.07622>>.
- 2 FLEISCHER, R. B physics and cp violation. In: _____. *Heavy Quark Physics*. Berlin, Heidelberg: Springer Berlin Heidelberg, 2004. p. 42–77. ISBN 978-3-540-40975-5. Disponível em: <https://doi.org/10.1007/978-3-540-40975-5_2>.
- 3 AAIJ, R. et al. (LHCb Collaboration). Direct cp violation in charmless three-body decays of b mesons. *Physical Review D*, American Physical Society (APS), v. 108, n. 1, jul. 2023. ISSN 2470-0029. Disponível em: <<http://dx.doi.org/10.1103/PhysRevD.108.012008>>.
- 4 BORSATO, M.; VIDAL, X.; TSAI, Y.; SIERRA, C.; ZURITA, J.; ALONSO-ÁLVAREZ, G.; BOYARSKY, A.; RODRÍGUEZ, A. B.; FRANZOSI, D. B.; CACCIAPAGLIA, G.; VIDAL, A. C.; DU, M.; ELOR, G.; ESCUDERO, M.; FERRETTI, G.; FLACKE, T.; FOLDENAUER, P.; HAJER, J.; HENRY, L.; ZUPAN, J. *Unleashing the full power of LHCb to probe Stealth New Physics*. 2021.
- 5 BETETA, C. A.; ATZENI, M.; BATTISTA, V.; BURSCHE, A.; DEY, B.; SUAREZ, A. D.; ELSASSER, C.; PRIETO, A. F.; FU, J.; GRAVERINI, E.; KOMAROV, I.; CID, E. L.; LIONETTO, F.; MAURI, A.; MERLI, A.; PAIS, P.; TRIGO, E. P.; REGALES, M. del P. P.; STEFKO, P.; STEINKAMP, O.; STORACI, B.; TOBIN, M.; WEIDEN, A. Monitoring radiation damage in the lhcb tracker turicensis. *Journal of Instrumentation*, v. 15, n. 08, p. P08016, aug 2020. Disponível em: <<https://dx.doi.org/10.1088/1748-0221/15/08/P08016>>.
- 6 ALVES JR., A. A. et al. The LHCb Detector at the LHC. *JINST*, v. 3, p. S08005, 2008.
- 7 AAIJ, R. et al. (LHCb Collaboration). Design and performance of the lhcb trigger and full real-time reconstruction in run 2 of the lhc. *Journal of Instrumentation*, IOP Publishing, v. 14, n. 04, p. P04013–P04013, abr. 2019. ISSN 1748-0221. Disponível em: <<http://dx.doi.org/10.1088/1748-0221/14/04/P04013>>.
- 8 AAIJ, R. et al. (LHCb Collaboration). The lhcb upgrade i. *Journal of Instrumentation*, IOP Publishing, v. 19, n. 05, p. P05065, maio 2024. ISSN 1748-0221. Disponível em: <<http://dx.doi.org/10.1088/1748-0221/19/05/P05065>>.
- 9 COLLABORATION, L. *LHCb Tracker Upgrade Technical Design Report*. [S.l.], 2014. Disponível em: <<https://cds.cern.ch/record/1647400>>.
- 10 OLIVE, K. A. et al. *Review of particle physics*. *Chin. Phys.*, C38, p. 090001, 2014.
- 11 BEVAN, A. J. et al. The physics of the b factories. *The European Physical Journal C*, Springer Science and Business Media LLC, v. 74, n. 11, nov. 2014. ISSN 1434-6052. Disponível em: <<http://dx.doi.org/10.1140/epjc/s10052-014-3026-9>>.

- 12 AITALA, E. M. et al. Model-independent measurement of s -wave $K^-\pi^+$ systems using $D^+ \rightarrow k\pi\pi$ decays from fermilab e791. *Phys. Rev. D*, American Physical Society, v. 73, p. 032004, Feb 2006. Disponível em: <<https://link.aps.org/doi/10.1103/PhysRevD.73.032004>>.
- 13 AITALA, E. M. et al. Dalitz plot analysis of the decay $D^+ \rightarrow K^-\pi^+\pi^+$ and indication of a low-mass scalar $k\pi$ resonance. *Phys. Rev. Lett.*, American Physical Society, v. 89, p. 121801, Aug 2002. Disponível em: <<https://link.aps.org/doi/10.1103/PhysRevLett.89.121801>>.
- 14 ASTON, D. et al. A Study of $K^- \pi^+$ Scattering in the Reaction $K^- p \rightarrow K^- \pi^+ n$ at 11-GeV/c. *Nucl. Phys. B*, v. 296, p. 493–526, 1988.
- 15 GRIFFITHS, D. J. *Introduction to elementary particles; 2nd rev. version*. New York, NY: Wiley, 2008. (Physics textbook). Disponível em: <<https://cds.cern.ch/record/111880>>.
- 16 ET AL, R. A. Measurement of the charge asymmetry in $b^\pm \rightarrow k^\pm$ and search for $b^\pm \rightarrow \pm$ decays. *Physics Letters B*, v. 728, p. 85–94, 2014. ISSN 0370-2693. Disponível em: <<https://www.sciencedirect.com/science/article/pii/S0370269313009398>>.
- 17 PELÁEZ, J.; RODAS, A. $\pi\pi \rightarrow k\bar{k}$ scattering up to 1.47 gev with hyperbolic dispersion relations. *The European Physical Journal C*, v. 78, 11 2018.
- 18 JACOBSSON, R. Performance of the LHCb Detector During the LHC Proton Runs 2010 - 2012. Geneva, 2013. LHCb-PROC-2013-030, CERN-LHCb-PROC-2013-030. Disponível em: <<http://cds.cern.ch/record/1550771>>.
- 19 AAIJ, R. et al. Amplitude analysis of $B^\pm \rightarrow \pi^\pm K^+ K^-$ decays. *Phys. Rev. Lett.*, American Physical Society, v. 123, p. 231802, Dec 2019. Disponível em: <<https://link.aps.org/doi/10.1103/PhysRevLett.123.231802>>.
- 20 AAIJ, R. et al. Measurements of cp violation in the three-body phase space of charmless B^\pm decays. *Phys. Rev. D*, American Physical Society, v. 90, p. 112004, Dec 2014. Disponível em: <<https://link.aps.org/doi/10.1103/PhysRevD.90.112004>>.
- 21 AAIJ, R. et al. Amplitude analysis of the $B^+ \rightarrow \pi^+\pi^+\pi^-$ decay. *Phys. Rev. D*, American Physical Society, v. 101, p. 012006, Jan 2020. Disponível em: <<https://link.aps.org/doi/10.1103/PhysRevD.101.012006>>.
- 22 AAIJ, R. et al. Amplitude analysis of the $B^+ \rightarrow \pi^+\pi^+\pi^-$ decay. *Phys. Rev. D*, American Physical Society, v. 101, p. 012006, Jan 2020. Disponível em: <<https://link.aps.org/doi/10.1103/PhysRevD.101.012006>>.
- 23 AAIJ, R. et al. Measurement of the charge asymmetry in $B^\pm \rightarrow \phi k^\pm$ and search for $B^\pm \rightarrow \phi\pi^\pm$ decays. *Physics Letters B*, v. 728, p. 85–94, 2014. ISSN 0370-2693. Disponível em: <<https://www.sciencedirect.com/science/article/pii/S0370269313009398>>.
- 24 WOLFENSTEIN, L. Parametrization of the kobayashi-maskawa matrix. *Phys. Rev. Lett.*, American Physical Society, v. 51, p. 1945–1947, Nov 1983. Disponível em: <<https://link.aps.org/doi/10.1103/PhysRevLett.51.1945>>.

- 25 BEDIAGA, I.; GÖBEL, C. Direct CP violation in beauty and charm hadron decays. *Progress in Particle and Nuclear Physics*, v. 114, p. 103808, 2020. ISSN 0146-6410. Disponível em: <<http://www.sciencedirect.com/science/article/pii/S0146641020300557>>.
- 26 BIGI, I. I.; SANDA, A. I. *CP violation*. [S.l.]: Cambridge University Press, 2009. v. 9. ISBN 978-0-511-57728-4, 978-0-521-84794-0, 978-1-107-42430-2.
- 27 BANDER, M.; SILVERMAN, D.; SONI, A. CP noninvariance in the decays of heavy charged quark systems. *Phys. Rev. Lett.*, American Physical Society, v. 43, p. 242–245, Jul 1979. Disponível em: <<https://link.aps.org/doi/10.1103/PhysRevLett.43.242>>.
- 28 HARRISON P.F., e.; QUINN HELEN R., e.; /SLAC. The babar physics book: Physics at an asymmetric b factory. Disponível em: <<https://www.osti.gov/biblio/979931>>.
- 29 CHENG, H.-Y.; CHUA, C.-K.; SONI, A. Final state interactions in hadronic b decays. *Physical Review D*, American Physical Society (APS), v. 71, n. 1, jan. 2005. ISSN 1550-2368. Disponível em: <<http://dx.doi.org/10.1103/PhysRevD.71.014030>>.
- 30 GERARD, J.-M.; HOU, W.-S. CP violation in inclusive and exclusive charmless B decays. *Phys. Rev. D*, v. 43, p. 2909–2930, 1991.
- 31 BEDIAGA, I.; FREDERICO, T.; LOURENÇO, O. Cp violation and cpt invariance in b decays with final state interactions. *Physical Review D*, American Physical Society (APS), v. 89, n. 9, maio 2014. ISSN 1550-2368. Disponível em: <<http://dx.doi.org/10.1103/PhysRevD.89.094013>>.
- 32 NOGUEIRA, J. H. A.; BEDIAGA, I.; CAVALCANTE, A. B. R.; FREDERICO, T.; cO, O. Louren. *cp violation: Dalitz interference, cpt, and final state interactions*. *Phys. Rev. D*, American Physical Society, v. 92, p. 054010, Sep 2015. Disponível em: <<https://link.aps.org/doi/10.1103/PhysRevD.92.054010>>.
- 33 AAMODT, K. . et al. (ALICE Collaboration). The ALICE experiment at the CERN LHC. *Journal of Instrumentation*, IOP Publishing, v. 3, n. 08, p. S08002–S08002, aug 2008. Disponível em: <<https://doi.org/10.1088/1748-0221/3/8/S08002>>.
- 34 AAD, G. et al. (ATLAS Collaboration). The ATLAS experiment at the CERN large hadron collider. *Journal of Instrumentation*, IOP Publishing, v. 3, n. 08, p. S08003–S08003, aug 2008. Disponível em: <<https://doi.org/10.1088/1748-0221/3/8/S08003>>.
- 35 CHATRCHYAN, S. et al. (CMS Collaboration). The CMS Experiment at the CERN LHC. *JINST*, v. 3, p. S08004, 2008.
- 36 LUMINOSITY: Taking a closer look at LHC. <http://lhc-closer.es/taking_a_closer_look_at_lhc/0.luminosity>.
- 37 FOLLIN, F.; JACQUET, D. Implementation and experience with luminosity levelling with offset beam. 2014. ArXiv:1410.3667. Disponível em: <<https://cds.cern.ch/record/1955354>>.
- 38 AAIJ, R. et al. Performance of the LHCb vertex locator. *Journal of Instrumentation*, IOP Publishing Ltd., v. 9, n. 9, set. 2014. ISSN 1748-0221.

- 39 AAIJ, R. et al. Measurement of the track reconstruction efficiency at LHCb. *Journal of Instrumentation*, Iop Publishing Ltd, Bristol, v. 10, p. 23. P02007, 2015. Disponible em: <http://infoscience.epfl.ch/record/208556>.
- 40 LHCb COLLABORATION. *LHCb: Inner tracker technical design report*. 2002. CERN-LHCC-2002-029.
- 41 LHCb COLLABORATION. *LHCb: Outer tracker technical design report*. 2001. CERN-LHCC-2001-024.
- 42 LHCb COLLABORATION. *LHCb magnet: Technical design report*. 2000. CERN-LHCC-2000-007.
- 43 LHCb COLLABORATION. *LHCb calorimeters: Technical design report*. 2000. CERN-LHCC-2000-036.
- 44 LHCb COLLABORATION. *LHCb muon system technical design report*. 2001. CERN-LHCC-2001-010.
- 45 COS, J. M. D. PACIFIC : The readout ASIC for the SciFi Tracker planned for the upgrade of the LHCb detector. 2015. Disponible em: <https://cds.cern.ch/record/2061576>.
- 46 WYLLIE, K.; ALESSIO, F.; GASPAR, C.; JACOBSSON, R.; GAC, R. L.; NEUFELD, N.; SCHWEMMER, R. *Electronics Architecture of the LHCb Upgrade*. Geneva, 2013. Previous version: 01/03/2013 Current version: 18/06/2013 (version 2.6) based on LHCb-INT-2011-006 (removed from CDS). Disponible em: <https://cds.cern.ch/record/1340939>.
- 47 WILLIAMS, M.; GLIGOROV, V.; THOMAS, C.; DIJKSTRA, H.; NARDULLI, J.; SPRADLIN, P. The HLT2 Topological Lines. 1 2011.
- 48 HULSBERGEN, W. D. Decay chain fitting with a kalman filter. *Nuclear Instruments and Methods in Physics Research Section A: Accelerators, Spectrometers, Detectors and Associated Equipment*, Elsevier BV, v. 552, n. 3, p. 566–575, nov 2005. Disponible em: <https://doi.org/10.1016%2Fj.nima.2005.06.078>.
- 49 ANDERLINI, L.; CONTU, A.; JONES, C. R.; MALDE, S. S.; MULLER, D.; OGILVY, S.; GOICOCHEA, J. M. O.; PEARCE, A.; POLYAKOV, I.; QIAN, W.; SCIASCIA, B.; GOMEZ, R. V.; ZHANG, Y. *The PIDCalib package*. Geneva, 2016. Disponible em: <http://cds.cern.ch/record/2202412>.
- 50 VERKERKE, W.; KIRKBY, D. *The RooFit toolkit for data modeling*. arXiv, 2003. Disponible em: <https://arxiv.org/abs/physics/0306116>.
- 51 AUBERT, B. et al. Amplitude analysis of the decay $B^\pm \rightarrow \pi^\pm \pi^\pm \pi^\mp$. *Phys. Rev. D*, v. 72, p. 052002, 2005.
- 52 ZEMACH, C. Three-pion decays of unstable particles. *Phys. Rev.*, American Physical Society, v. 133, p. B1201–B1220, Mar 1964. Disponible em: <https://link.aps.org/doi/10.1103/PhysRev.133.B1201>.
- 53 ZEMACH, C. Use of angular-momentum tensors. *Phys. Rev.*, American Physical Society, v. 140, p. B97–B108, Oct 1965. Disponible em: <https://link.aps.org/doi/10.1103/PhysRev.140.B97>.

- 54 BLATT, J. M.; WEISSKOPF, V. F. *Theoretical nuclear physics*. New York: Springer, 1952. ISBN 978-0-471-08019-0.
- 55 AAIJ, R. et al. Dalitz plot analysis of $b_s^0 \rightarrow \bar{D}^0 k^- \pi^+$. *Physical Review D*, American Physical Society (APS), v. 90, n. 7, out. 2014. ISSN 1550-2368. Disponível em: <<http://dx.doi.org/10.1103/PhysRevD.90.072003>>.
- 56 SVEC, M. Unitarity and interfering resonances in $\pi\pi$ scattering and in pion production $\pi n \rightarrow \pi\pi n$. *Physical Review D*, American Physical Society (APS), v. 64, n. 9, out. 2001. ISSN 1089-4918. Disponível em: <<http://dx.doi.org/10.1103/PhysRevD.64.096003>>.
- 57 CHUNG, S. U.; BROSE, J.; HACKMANN, R.; KLEMPT, E.; SPANIER, S.; STRASSBURGER, C. Partial wave analysis in K matrix formalism. *Annalen Phys.*, v. 4, p. 404–430, 1995.
- 58 AUBERT, B. et al. Dalitz plot analysis of $D_s^+ \rightarrow \pi^+ \pi^- \pi^+$. *Phys. Rev. D*, American Physical Society, v. 79, p. 032003, Feb 2009. Disponível em: <<https://link.aps.org/doi/10.1103/PhysRevD.79.032003>>.
- 59 AAIJ, R. et al. Search for direct cp violation in charged charmless $b \rightarrow pv$ decays. *Phys. Rev. D*, American Physical Society, v. 108, p. 012013, Jul 2023. Disponível em: <<https://link.aps.org/doi/10.1103/PhysRevD.108.012013>>.
- 60 LAW, J.; RENNIE, R. *A Dictionary of Physics*. Oxford University Press, 2015. ISBN 9780191783036. Disponível em: <<https://www.oxfordreference.com/view/10.1093/acref/9780198714743.001.0001/acref-9780198714743>>.
- 61 WORKMAN, R. L. et al. Review of Particle Physics. *PTEP*, v. 2022, p. 083C01, 2022.
- 62 LIAO, L.; WANG, S.; LI, G.; ZHANG, Z.; SONG, W. Update of hadronic decays of j/ψ and $\psi(2s)$ through virtual photons. *Phys. Rev. D*, American Physical Society, v. 107, p. 112007, Jun 2023. Disponível em: <<https://link.aps.org/doi/10.1103/PhysRevD.107.112007>>.
- 63 JACKSON, J. D. Remarks on the phenomenological analysis of resonances. *Nuovo Cim.*, v. 34, p. 1644–1666, 1964.
- 64 FLATTÉ, S. Coupled-channel analysis of the $\bar{K}^0 K^0$ and $K^+ K^-$ systems near $K\bar{K}$ threshold. *Physics Letters B*, v. 63, n. 2, p. 224–227, 1976. ISSN 0370-2693. Disponível em: <<https://www.sciencedirect.com/science/article/pii/0370269376906547>>.
- 65 GOUNARIS, G. J.; SAKURAI, J. J. Finite-width corrections to the vector-meson-dominance prediction for $\rho \rightarrow e^+ e^-$. *Phys. Rev. Lett.*, American Physical Society, v. 21, p. 244–247, Jul 1968. Disponível em: <<https://link.aps.org/doi/10.1103/PhysRevLett.21.244>>.
- 66 GARMASH, A. et al. Dalitz analysis of the three-body charmless decays $b^+ \rightarrow k^+ \pi^+ \pi^-$ and $b^+ \rightarrow k^+ k^+ k^-$. *Physical Review D*, American Physical Society (APS), v. 71, n. 9, maio 2005. ISSN 1550-2368. Disponível em: <<http://dx.doi.org/10.1103/PhysRevD.71.092003>>.

- 67 NOGUEIRA, J. A.; BEDIAGA, I.; CAVALCANTE, A.; FREDERICO, T.; LOURENÇO, O. Cp violation: Dalitz interference, cpt and fsi. *Physical Review D*, American Physical Society (APS), v. 92, n. 5, set. 2015. ISSN 1550-2368. Disponível em: <<http://dx.doi.org/10.1103/PhysRevD.92.054010>>.
- 68 HICKMAN, I. D. B.; NETO, A. G. D. S.; MAGALHAES, P. C.; MIRANDA, J. M. D.; RODRIGUES, F. L. F.; DALSENO, J. P.; RADEMACKER, J.; BACK, J. J.; GERSHON, T.; LATHAM, T. E.; O'HANLON, D. P.; QIAN, W. $B^\pm \rightarrow \pi^\pm \pi^+ \pi^-$ amplitude analysis on Run 1 data. 2017. Disponível em: <<https://cds.cern.ch/record/2258554>>.
- 69 BEDIAGA, I.; MIRANDA, J. M. de. Complex amplitude phase motion in dalitz plot heavy meson three body decay. *Physics Letters B*, Elsevier BV, v. 550, n. 3–4, p. 135–139, dez. 2002. ISSN 0370-2693. Disponível em: <[http://dx.doi.org/10.1016/S0370-2693\(02\)02983-0](http://dx.doi.org/10.1016/S0370-2693(02)02983-0)>.
- 70 ANDERLINI, L.; CONTU, A.; JONES, C. R.; MALDE, S. S.; MULLER, D.; OGILVY, S.; GOICOCHEA, J. M. O.; PEARCE, A.; POLYAKOV, I.; QIAN, W.; SCIASCIA, B.; GOMEZ, R. V.; ZHANG, Y. *The PIDCalib package*. Geneva, 2016. Disponível em: <<https://cds.cern.ch/record/2202412>>.
- 71 GOICOCHEA, J. M. O. *A new method to build background histograms*. Disponível em: <<https://indico.cern.ch/event/1142606/contributions/4798386/attachments/2414752/4131842/BkgStudyOverDP.pdf>>.
- 72 PIVK, M.; Le Diberder, F. Plots: A statistical tool to unfold data distributions. *Nuclear Instruments and Methods in Physics Research Section A: Accelerators, Spectrometers, Detectors and Associated Equipment*, v. 555, n. 1, p. 356–369, 2005. ISSN 0168-9002. Disponível em: <<https://www.sciencedirect.com/science/article/pii/S0168900205018024>>.
- 73 BACK, J.; GERSHON, T.; HARRISON, P.; LATHAM, T.; O'HANLON, D.; QIAN, W.; SANCHEZ, P. del A.; CRAIK, D.; ILIC, J.; GOICOCHEA, J. M. O.; PUCCIO, E.; COUTINHO, R. S.; WHITEHEAD, M. Laura++: A dalitz plot fitter. *Computer Physics Communications*, Elsevier BV, v. 231, p. 198–242, out. 2018. ISSN 0010-4655. Disponível em: <<http://dx.doi.org/10.1016/j.cpc.2018.04.017>>.
- 74 PRESS, W.; OTHER. *Numerical Recipes in C*. [S.l.]: Cambridge University Press, 1998.
- 75 YUAN, C. Z.; MO, X. H.; WANG, P. Multiple solutions in extracting physics information from experimental data. *International Journal of Modern Physics A*, World Scientific Pub Co Pte Lt, v. 25, n. 32, p. 5963–5972, dez. 2010. ISSN 1793-656X. Disponível em: <<http://dx.doi.org/10.1142/S0217751X10051153>>.
- 76 WILKS, S. S. The large-sample distribution of the likelihood ratio for testing composite hypotheses. *The Annals of Mathematical Statistics*, Institute of Mathematical Statistics, v. 9, n. 1, p. 60–62, 1938. ISSN 00034851, 21688990. Disponível em: <<http://www.jstor.org/stable/2957648>>.
- 77 ALGERI, S.; AALBERS, J.; MORÅ, K. D.; CONRAD, J. Searching for new phenomena with profile likelihood ratio tests. *Nature Reviews Physics*, Springer Science and Business Media LLC, v. 2, n. 5, p. 245–252, abr. 2020. ISSN 2522-5820. Disponível em: <<http://dx.doi.org/10.1038/s42254-020-0169-5>>.

- 78 GARROTE, R. Álvarez; CUERVO, J.; MAGALHÃES, P.; PELÁEZ, J. Dispersive $\rightarrow k k^-$ amplitude and giant cp violation in b to three light-meson decays at lhcb. *Physical Review Letters*, American Physical Society (APS), v. 130, n. 20, maio 2023. ISSN 1079-7114. Disponível em: <<http://dx.doi.org/10.1103/PhysRevLett.130.201901>>.

A Appendix: Components

In Figures 97, 98, 99 and 100 we present simulations showing the Dalitz plot distributions for possible components involved in the decay $B^\pm \rightarrow K^\mp K^\pm \pi^\pm$. Each resonance displays a distinct lineshape, as previously described. Figures 97 and 98 show all resonances modeled with the Breit-Wigner lineshape, which is commonly used to represent resonance behavior in particle decays.

In contrast, Figure 99 explores alternative parametrizations: the flat non-resonant lineshape, the Flatté lineshape, the non-resonant polar form factor, and the rescattering lineshape, shown sequentially from top to bottom.

All resonances in these simulations were generated using only signal events. In each figure, the first column displays the Dalitz plot distribution, providing a two-dimensional view of the invariant mass combinations. The second column shows the distribution projected onto $m_{\pi^\pm K^\mp}^2$, while the third column presents the projection onto $m_{K^+ K^-}^2$. These projections allow us to observe the component structures and mass dependencies in specific two-body subsystems, offering additional insights into the decay dynamics.

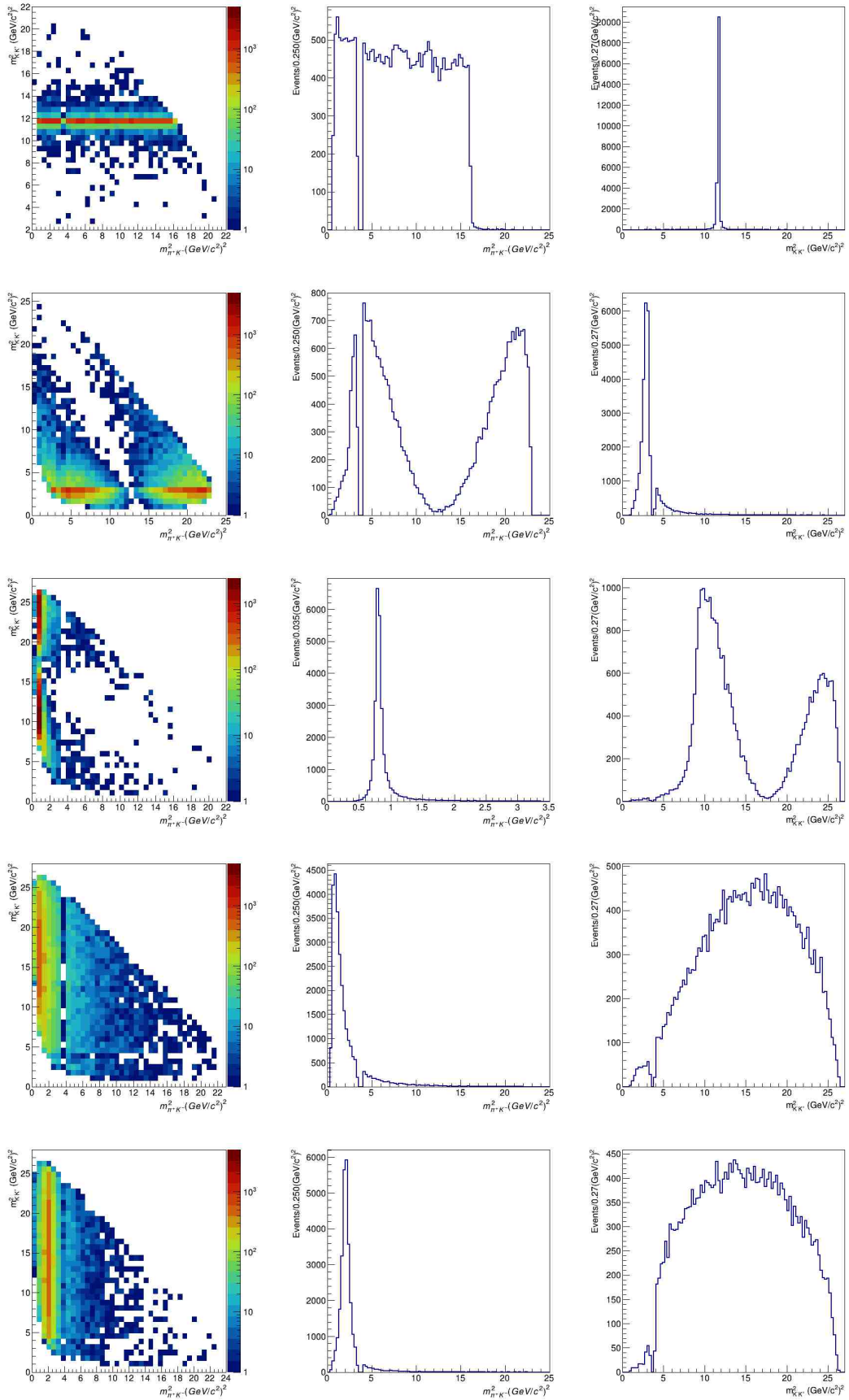


Figure 97 – Possible components contributions in the $B^\pm \rightarrow K^\mp K^\pm \pi^\pm$ phase space. Components are parameterized using the Breit-Wigner lineshape. The first line shows $\chi_{c0}(1P)$, the second line shows $\rho(1700)$, the third line shows $K^*(892)$, the fourth line shows κ , and the fifth line shows $K_0^*(1430)$.

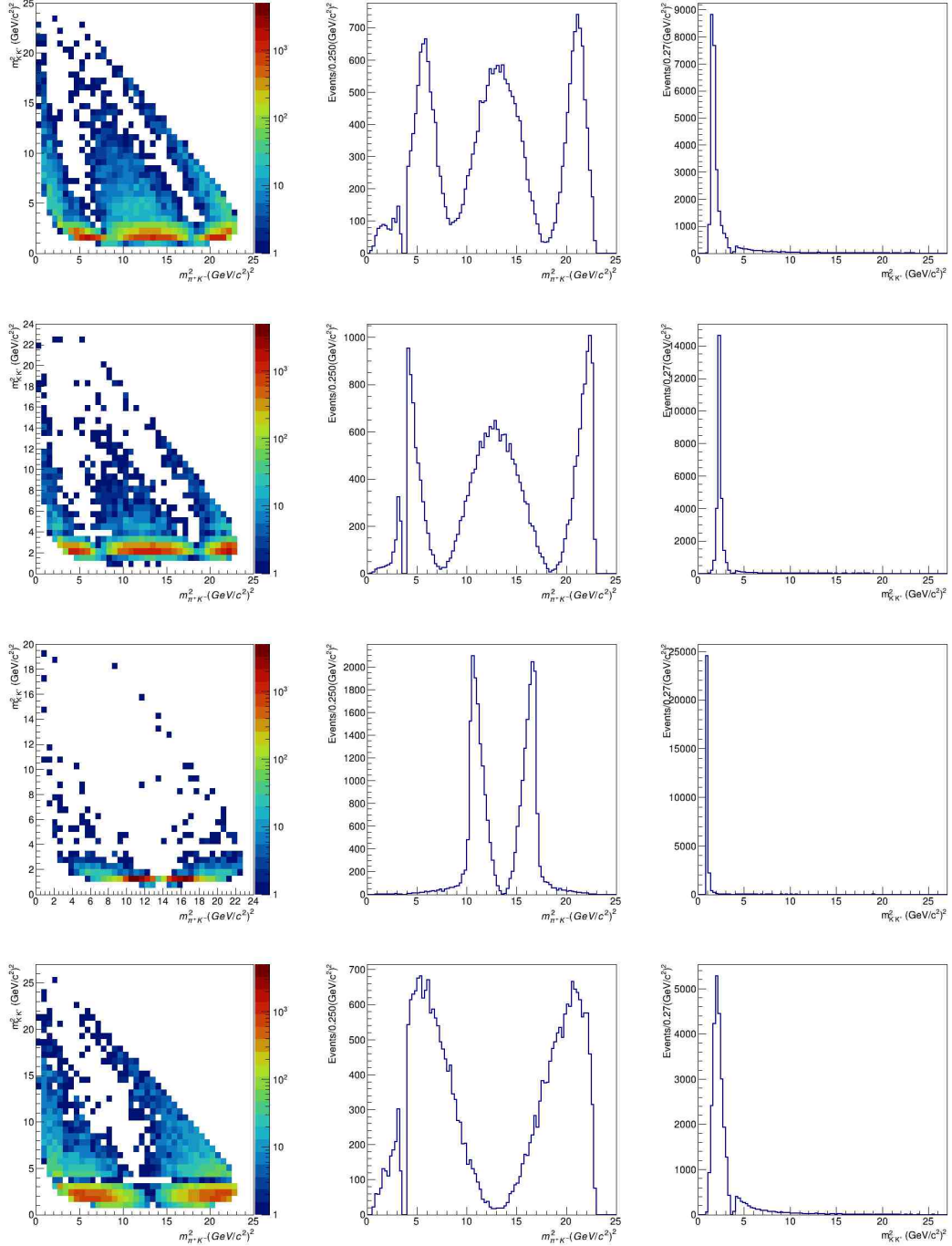


Figure 98 – Possible components contributions in the $B^\pm \rightarrow K^\mp K^\pm \pi^\pm$ phase space. Components are parameterized using the Breit-Wigner lineshape. The first line shows $f_2(1270)$, the second line shows $f_2'(1525)$, the third line shows $\phi(1020)$, and the fourth line shows $\rho(1450)$.

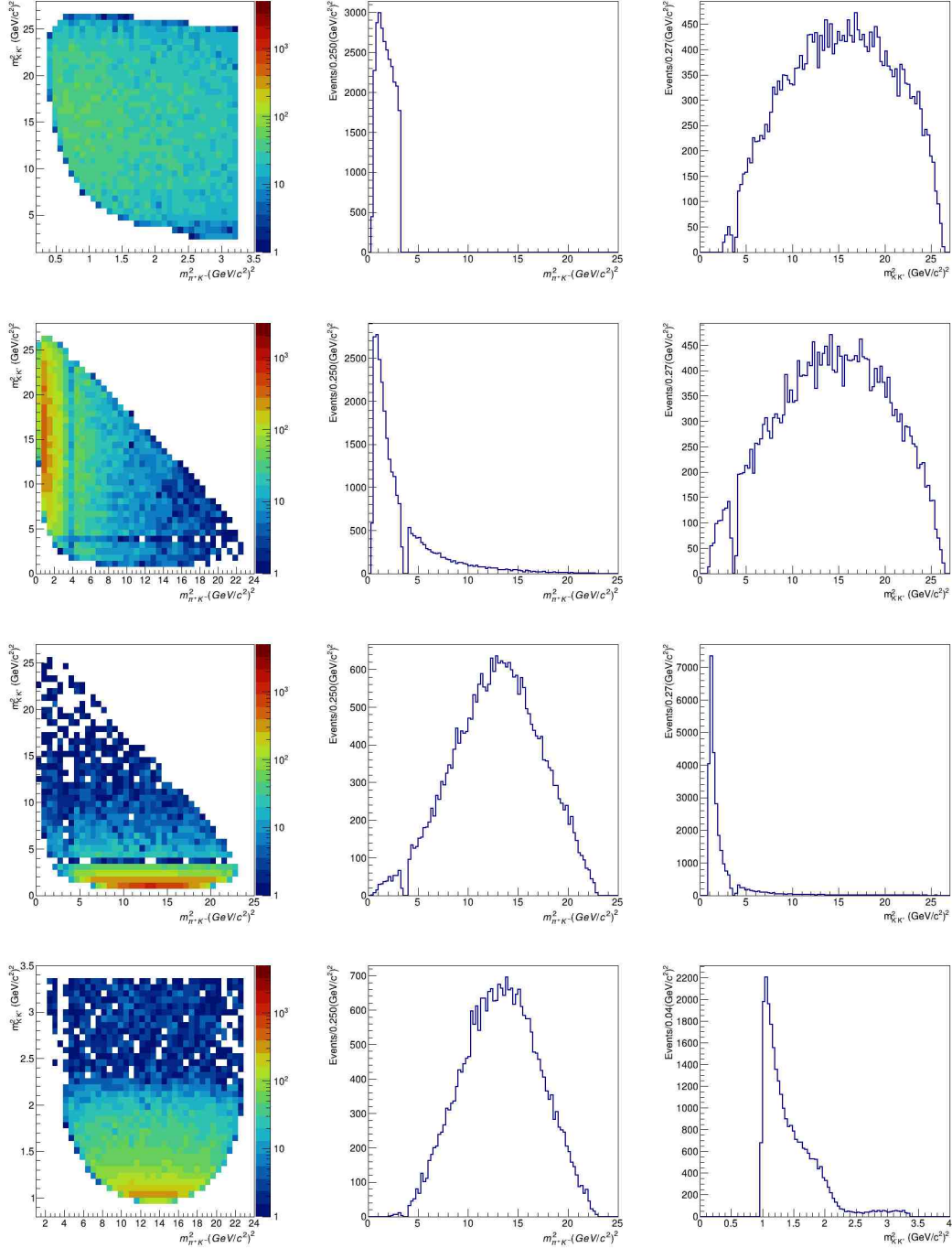


Figure 99 – Possible components contributions in the $B^\pm \rightarrow K^\mp K^\pm \pi^\pm$ phase space. Components are parameterized using different lineshapes. The first line shows a Non-Resonant using LASS, the second line shows the PolarFFNR, the third line shows $f_0(980)$ using Flattè, and the fourth line shows the Rescattering.

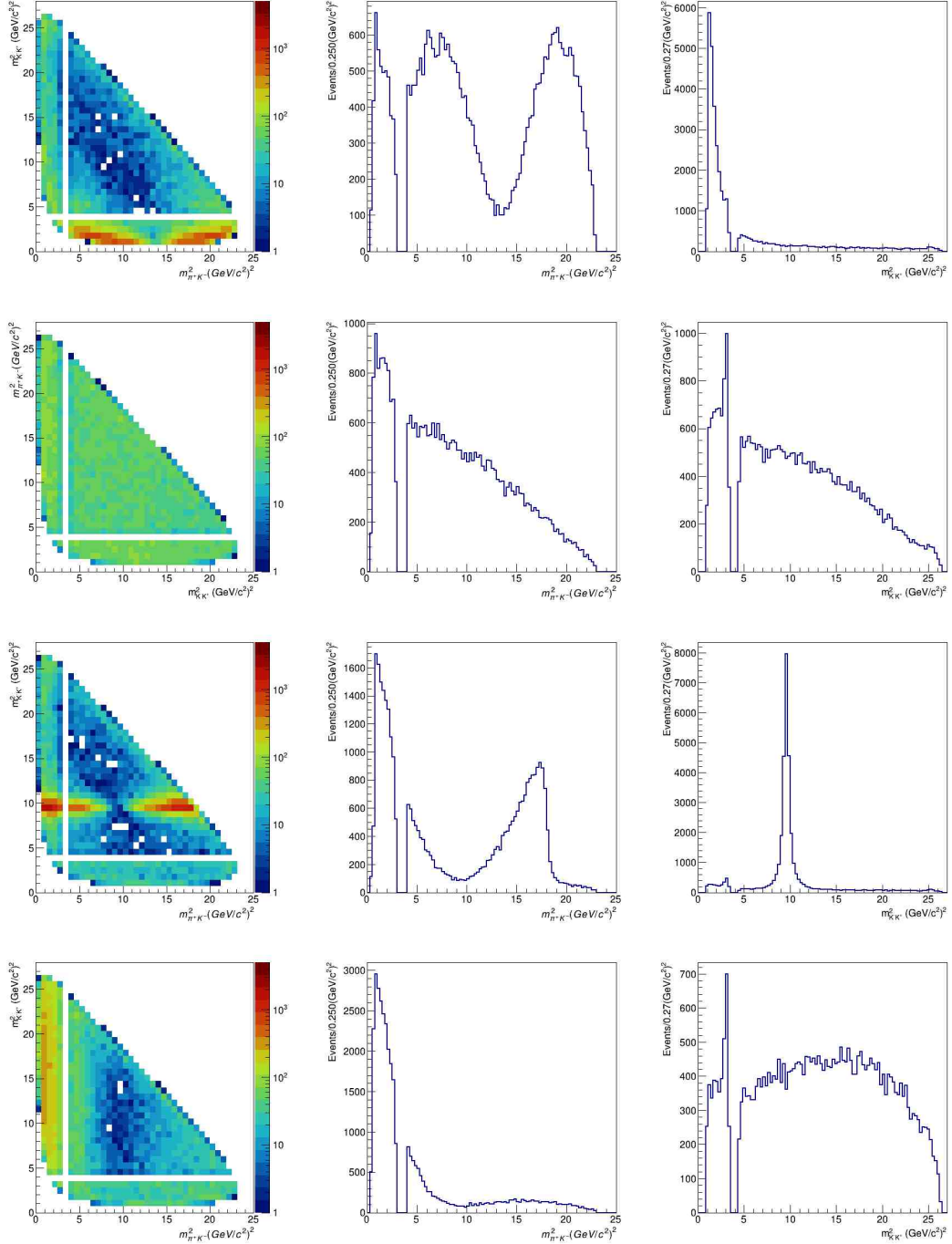


Figure 100 – Possible components contributions in the $B^\pm \rightarrow K^\mp K^\pm \pi^\pm$ phase space. Components are parameterized using different lineshapes. The first line shows $\rho(770)$ using Gounaris-Sakurai, the second line shows the BelleNR, the third line shows J/ψ , and the fourth line shows the δ_{Pol2} .

B Appendix: Fits per bin

In this appendix, we present the fits per bin of the Dalitz Plot that form the background model used for the amplitude analysis, where only a single Gaussian was employed. It can be observed that some plots exhibit different distributions, and in many cases, a mass peak does not even appear. This occurs because these bins contain almost no signal events.

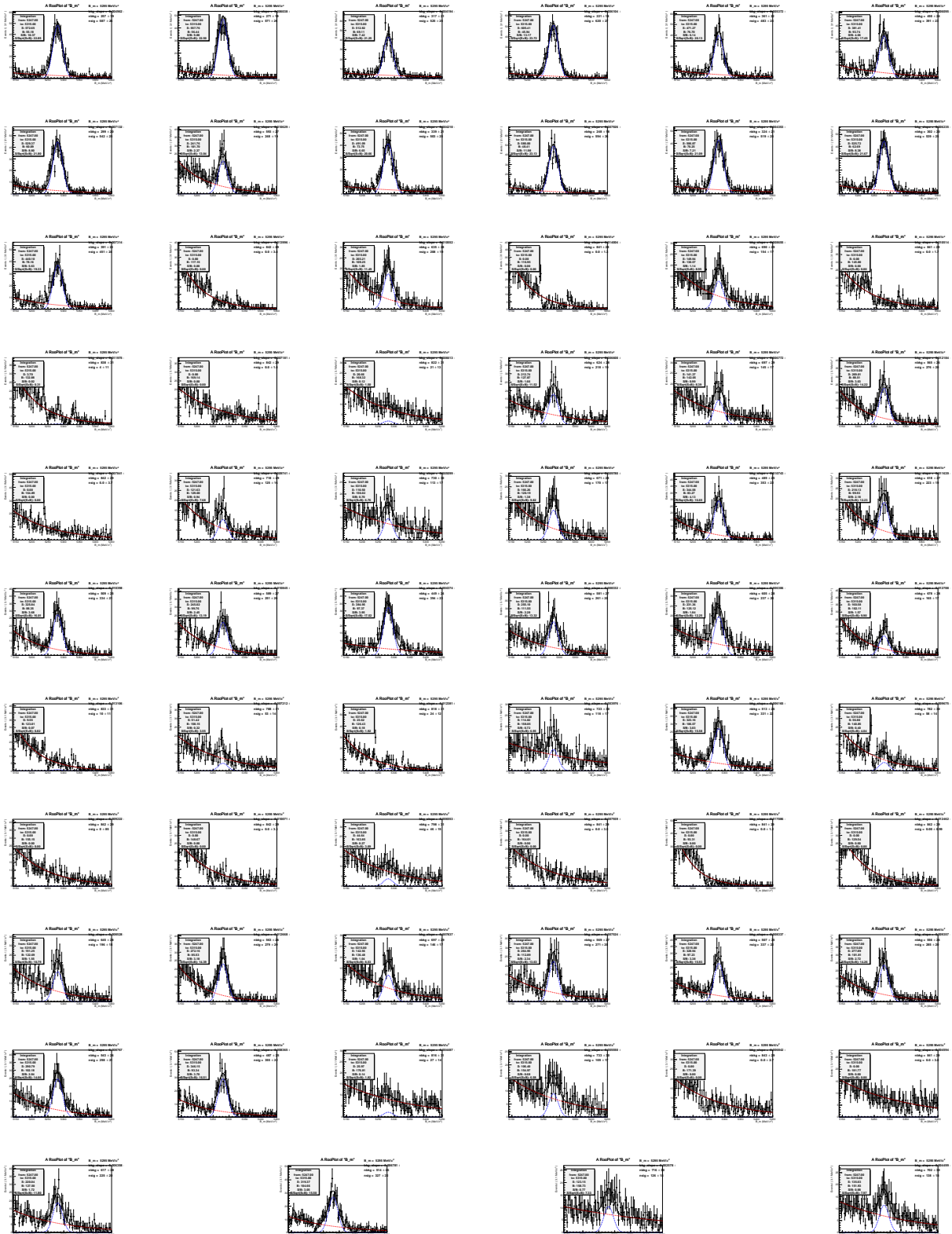


Figure 101 – Fits for B^+ for all 64 bins of the background model.

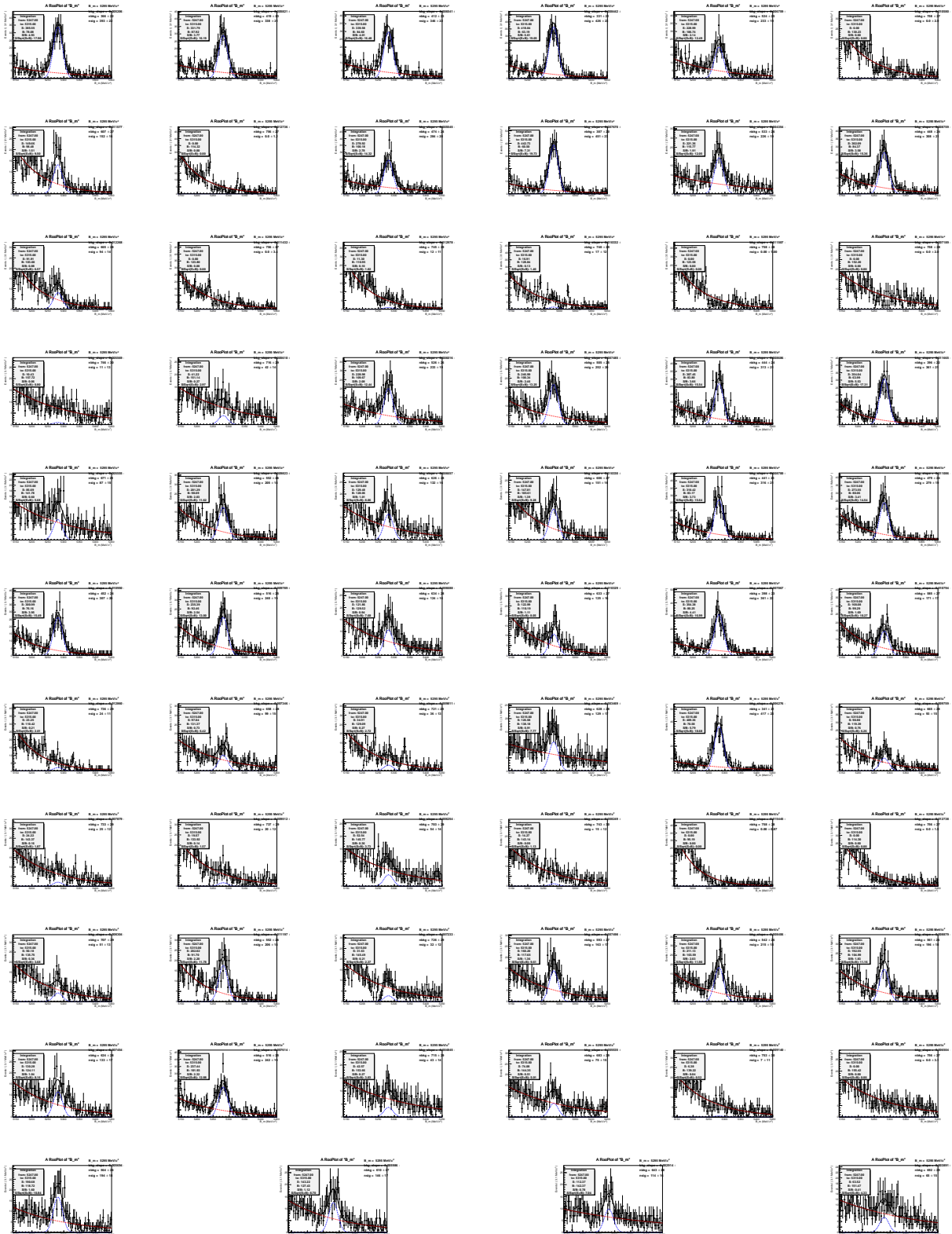


Figure 102 – Fits for B^- for all 64 bins of the background model.

C Appendix: Comparative analysis of Rescattering parameter sets

The full results of the Dalitz Plot fits considering the parameter options presented in [17], including CFD_b , CFD_c , UFD_b , and UFD_c , are detailed in Tables 34, 33, 36 and 35. As can be seen, the results are similar, with subtle variations in the a^\pm and δ^\pm parameters. The decision to proceed with the UFD_b parameters was based on a comparison of NLL values and Fit Fractions, which indicated that UFD_b provided the most stable and consistent results for further analysis.

Tabela 33 – Dalitz Plot fit results using CFD_c parameters for the Rescattering component.

[NLL -142584] Component	Fit fraction (%)		Magnitude and phase coefficients				A_{CP} (%)
	B^-	B^+	a_i^+	$\delta_i^+ [^\circ]$	a_i^-	$\delta_i^- [^\circ]$	
$K^{*0}(892)$	6.35 ± 0.34	5.08 ± 0.29	1.014 ± 0.020	0 ± 0	0.986 ± 0.020	0 ± 0	-2.8 ± 3.9
$K_0^*(1430)$	5.88 ± 0.50	5.74 ± 0.41	1.078 ± 0.044	16 ± 3	0.949 ± 0.043	-24 ± 4	-12.7 ± 5.3
<i>Polar FFNR</i>	38.45 ± 1.11	34.56 ± 0.78	2.645 ± 0.065	30 ± 3	2.426 ± 0.063	3 ± 3	-8.6 ± 1.9
$\rho(1450)$	39.19 ± 0.87	26.62 ± 0.56	2.322 ± 0.053	-168 ± 5	2.449 ± 0.060	-124 ± 6	5.3 ± 1.8
$f_2(1270)$	8.88 ± 0.54	3.41 ± 0.27	0.830 ± 0.038	97 ± 5	1.166 ± 0.042	129 ± 5	32.7 ± 4.5
Re-scattering	9.37 ± 0.46	25.55 ± 0.53	2.274 ± 0.050	-152 ± 6	1.198 ± 0.040	-123 ± 6	-56.6 ± 1.8
$\phi(1020)$	0.96 ± 0.12	0.03 ± 0.03	0.077 ± 0.032	60 ± 24	0.384 ± 0.025	-86 ± 9	92.3 ± 6.4
χ_{c0}	1.41 ± 0.15	0.67 ± 0.09	0.368 ± 0.026	116 ± 7	0.464 ± 0.026	66 ± 7	22.8 ± 8.0
Fit Fraction Sum	110.5	101.7					

Tabela 34 – Dalitz Plot fit results using CFD_b parameters for the Rescattering component.

[NLL -142587] Component	Fit fraction (%)		Magnitude and phase coefficients				A_{CP} (%)
	B^-	B^+	a_i^+	$\delta_i^+ [^\circ]$	a_i^-	$\delta_i^- [^\circ]$	
$K^{*0}(892)$	6.55 ± 0.68	5.14 ± 0.31	1.011 ± 0.032	0 ± 0	0.989 ± 0.032	0 ± 0	-2.3 ± 6.3
$K_0^*(1430)$	6.33 ± 1.26	5.73 ± 0.40	1.068 ± 0.046	18 ± 4	0.971 ± 0.082	-25 ± 5	-9.5 ± 9.9
<i>Polar FFNR</i>	38.88 ± 2.88	33.85 ± 0.77	2.596 ± 0.074	30 ± 3	2.408 ± 0.072	2 ± 5	-7.5 ± 3.5
$\rho(1450)$	38.19 ± 3.26	26.55 ± 0.54	2.299 ± 0.062	-180 ± 49	2.386 ± 0.159	-133 ± 35	3.7 ± 6.0
$f_2(1270)$	9.19 ± 0.68	3.44 ± 0.27	0.828 ± 0.039	86 ± 6	1.171 ± 0.041	121 ± 29	33.4 ± 4.4
Re-scattering	8.85 ± 1.44	24.54 ± 0.46	2.210 ± 0.059	-166 ± 7	1.149 ± 0.116	-132 ± 33	-57.5 ± 5.3
$\phi(1020)$	0.95 ± 0.13	0.02 ± 0.02	0.070 ± 0.027	48 ± 25	0.377 ± 0.030	-95 ± 35	93.4 ± 5.7
χ_{c0}	1.42 ± 0.15	0.65 ± 0.09	0.360 ± 0.026	116 ± 7	0.461 ± 0.025	66 ± 7	24.2 ± 8.1
Fit Fraction Sum	110.4	99.9					

Tabela 35 – Dalitz Plot fit results using UFD_c parameters for the Rescattering component.

[NLL -142620] Component	Fit fraction (%)		Magnitude and phase coefficients				A_{CP} (%)
	B^-	B^+	a_i^+	$\delta_i^+ [^\circ]$	a_i^-	$\delta_i^- [^\circ]$	
$K^{*0}(892)$	6.43 ± 0.35	5.08 ± 0.29	1.011 ± 0.020	0 ± 0	0.989 ± 0.020	0 ± 0	-2.3 ± 4.0
$K_0^*(1430)$	6.00 ± 0.51	5.81 ± 0.41	1.082 ± 0.044	16 ± 3	0.955 ± 0.044	-25 ± 4	-12.4 ± 5.4
<i>Polar FFNR</i>	38.71 ± 1.14	34.52 ± 0.78	2.637 ± 0.065	29 ± 3	2.425 ± 0.062	3 ± 3	-8.4 ± 2.0
$\rho(1450)$	38.78 ± 0.92	26.79 ± 0.55	2.323 ± 0.053	-169 ± 5	2.427 ± 0.061	-128 ± 6	4.4 ± 1.8
$f_2(1270)$	9.21 ± 0.54	3.59 ± 0.28	0.850 ± 0.038	92 ± 5	1.183 ± 0.042	125 ± 6	31.9 ± 4.4
Re-scattering	9.09 ± 0.46	25.12 ± 0.48	2.250 ± 0.049	-158 ± 6	1.175 ± 0.040	-125 ± 7	-57.1 ± 1.9
$\phi(1020)$	0.96 ± 0.12	0.02 ± 0.02	0.058 ± 0.031	50 ± 32	0.382 ± 0.025	-90 ± 10	95.5 ± 4.9
χ_{c0}	1.41 ± 0.15	0.67 ± 0.09	0.367 ± 0.025	116 ± 7	0.463 ± 0.026	66 ± 7	23.0 ± 8.0
Fit Fraction Sum	110.6	101.6					

Tabela 36 – Dalitz Plot fit results using UFD_b parameters for the Rescattering component.

[NLL -142728] Component	Fit fraction (%)		Magnitude and phase coefficients				A_{CP} (%)
	B^-	B^+	a_i^+	δ_i^+ [°]	a_i^-	δ_i^- [°]	
$K^{*0}(892)$	7.07 ± 0.34	5.14 ± 0.29	0.990 ± 0.019	0 ± 0	1.010 ± 0.019	0 ± 0	2.1 ± 3.8
$K_0^*(1430)$	9.29 ± 0.67	5.80 ± 0.40	1.051 ± 0.042	18 ± 3	1.158 ± 0.047	-13 ± 4	9.7 ± 4.9
<i>PolarFFNR</i>	39.76 ± 0.99	33.74 ± 0.77	2.535 ± 0.061	29 ± 3	2.396 ± 0.059	-10 ± 3	-5.6 ± 1.8
$\rho(1450)$	33.45 ± 0.68	26.76 ± 0.54	2.257 ± 0.049	178 ± -101	2.197 ± 0.049	141 ± 5	-2.7 ± 1.7
$f_2(1270)$	8.54 ± 0.46	3.80 ± 0.29	0.850 ± 0.036	78 ± 5	1.110 ± 0.036	49 ± 5	26.1 ± 4.3
Re-scattering	6.73 ± 0.30	24.09 ± 0.43	2.142 ± 0.045	-173 ± 5	0.985 ± 0.029	141 ± 6	-65.1 ± 1.4
$\phi(1020)$	0.93 ± 0.12	0.01 ± 0.02	0.045 ± 0.029	38 ± 39	0.365 ± 0.024	171 ± 9	97.0 ± 4.2
χ_{c0}	1.31 ± 0.14	0.65 ± 0.09	0.351 ± 0.025	115 ± 7	0.435 ± 0.024	52 ± 7	21.2 ± 8.1
Fit Fraction Sum	107.1	100.0					

D Appendix: PolarFFNR Λ fitting

The issue of the unphysical result mentioned previously is closely related to the $K\pi$ S-wave in the decay. Since it exhibits little distinction between the angular distributions, it becomes difficult to differentiate and identify the possible scalar resonances that might contribute to the decay. Moreover, being generally broad, these resonances interfere with each other. As a consequence of the difficulty in dealing with the S-wave of the $K\pi$ system, the results of the fits using the Run I model on the Run II data showed large fluctuations in the fit fractions. This problem, known as multiple solutions, arises from the lack of stability in the fit when randomizing the initial parameters x_i , y_i , Δx_i , and Δy_i . When these parameters were randomized, many different local minima existed, producing non-physical results.

To address this problem, we fitted the Λ parameter of the PolarFFNR component, which has the largest contribution to the decay. Simultaneously, we randomized the initial parameters x_i , y_i , Δx_i , and Δy_i . By doing so, we were able to find a set of initial parameters along with the value of Λ that provided stability to the fit. Figure 103 shows the large number of different results (NLL) for different fitted values of Λ . It can be seen that there are some Λ values (between 1.05 and 1.25) that produce lower NLL values, indicating a better-fit result. On the other hand, Figure 104 shows that the highest frequency of Λ values is around 1.22. From this study, we concluded that the best value for Λ is 1.22, and the result where $\Lambda = 1.22$ appeared almost 40% of the time. By fixing the fit at this value, it becomes stable as it represents the best and most frequent NLL.

Table 23 presents the results of using the most frequent values of Λ , x_i , y_i , Δx_i , and Δy_i . Depending on these parameters, it can lead to a local minimum with non-physical results. These parameters were used throughout the entire analysis.

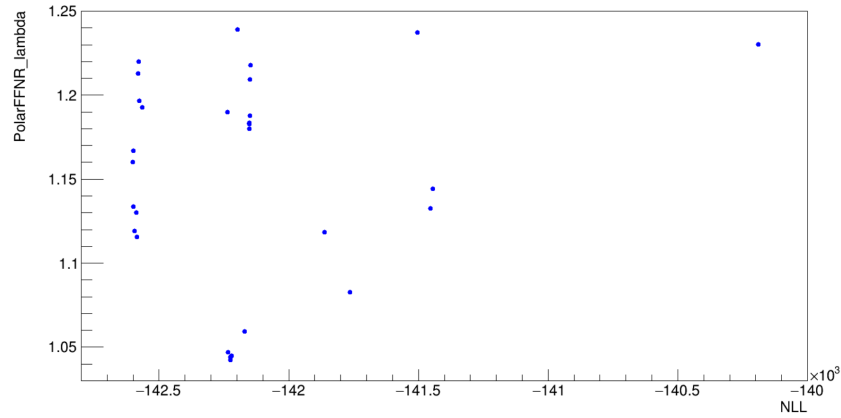


Figura 103 – Scatter plot showing the relationship between NLL and Λ from PolarFFNR from a total of 100 fits. Each point represents a different local minimum for each fitted value of Λ .

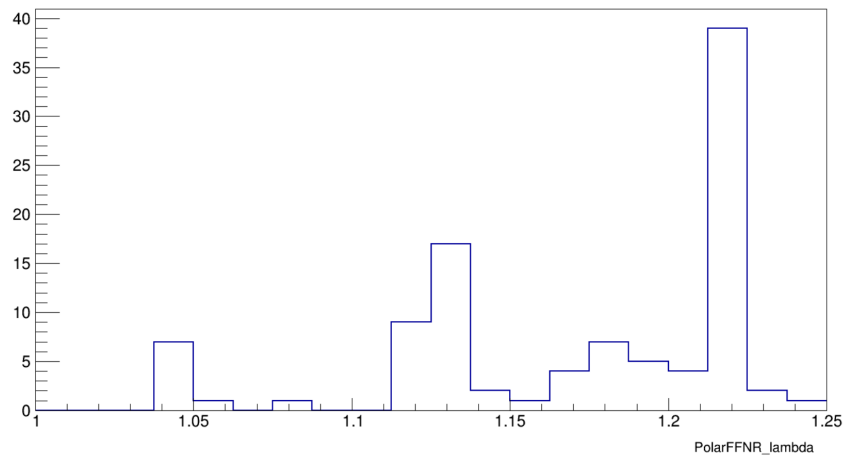


Figura 104 – Histogram showing the distribution of Λ from PolarFFNR values from a total of 100 fits. This histogram highlights that the preferred value for Λ is around 1.22

E Appendix: Cropped Dalitz Plot Fit studies

In this appendix, results from studies on Dalitz Plot fits for specific regions of the phase space, referred to as “cropped Dalitz Plots”, are presented. The purpose of this study is to investigate whether it is feasible to perform Dalitz Plot fits on selected regions of the phase space and still obtain results consistent with those derived from the complete Dalitz Plot.

The underlying idea is that by isolating regions of the phase space densely populated with resonances from those with fewer contributions, we could focus on the less crowded regions (or those with resonances contributing minimally to the total), thereby enabling a more accurate measurement in those areas. This approach aims to enhance precision in regions of the Dalitz Plot where the complexity is lower, offering a clearer insight into the dynamics of the decay process.

Furthermore, the study explores the possibility of partitioning the phase space into two distinct sections: one corresponding to the $K\pi$ system and the other to the KK system. This division is potentially viable since the resonances associated with both systems tend to occupy the boundaries of the Dalitz Plot. The results and implications of this approach are examined in detail within this appendix.

E.1 First approach: generated toys and individual contributions

What we aim to verify is whether it will be possible to recover the original result (used as input for generating the toys) in the fits of the Dalitz plot restricted regions (A_{CP} and Fit Fraction). To achieve this, the study will involve generating 100 toys, each with 100,000 events. Initially, these toys are based on a simplified model counting only with some resonances. Figure 105 illustrates the resonances included in this study and the regions of the phase space they occupy, proportionally to their respective fit fractions (these resonances were generated individually without background). It is also noteworthy that not all resonances are distributed across the entire Dalitz Plot, as expected. Figure 106 illustrates the regions of greatest interest, where the Dalitz Plot will be cropped. It is important to highlight that the regions, named according to the cropping, will be referenced throughout the remainder of this work. Table 37 presents the model being used as the basis for this study. Note that the contributions of this model do not necessarily correspond to real data, as some resonances had their contributions artificially enhanced to facilitate the study (e.g., χ_c and J/ψ).

First, a consistency test was performed to verify whether the input parameters

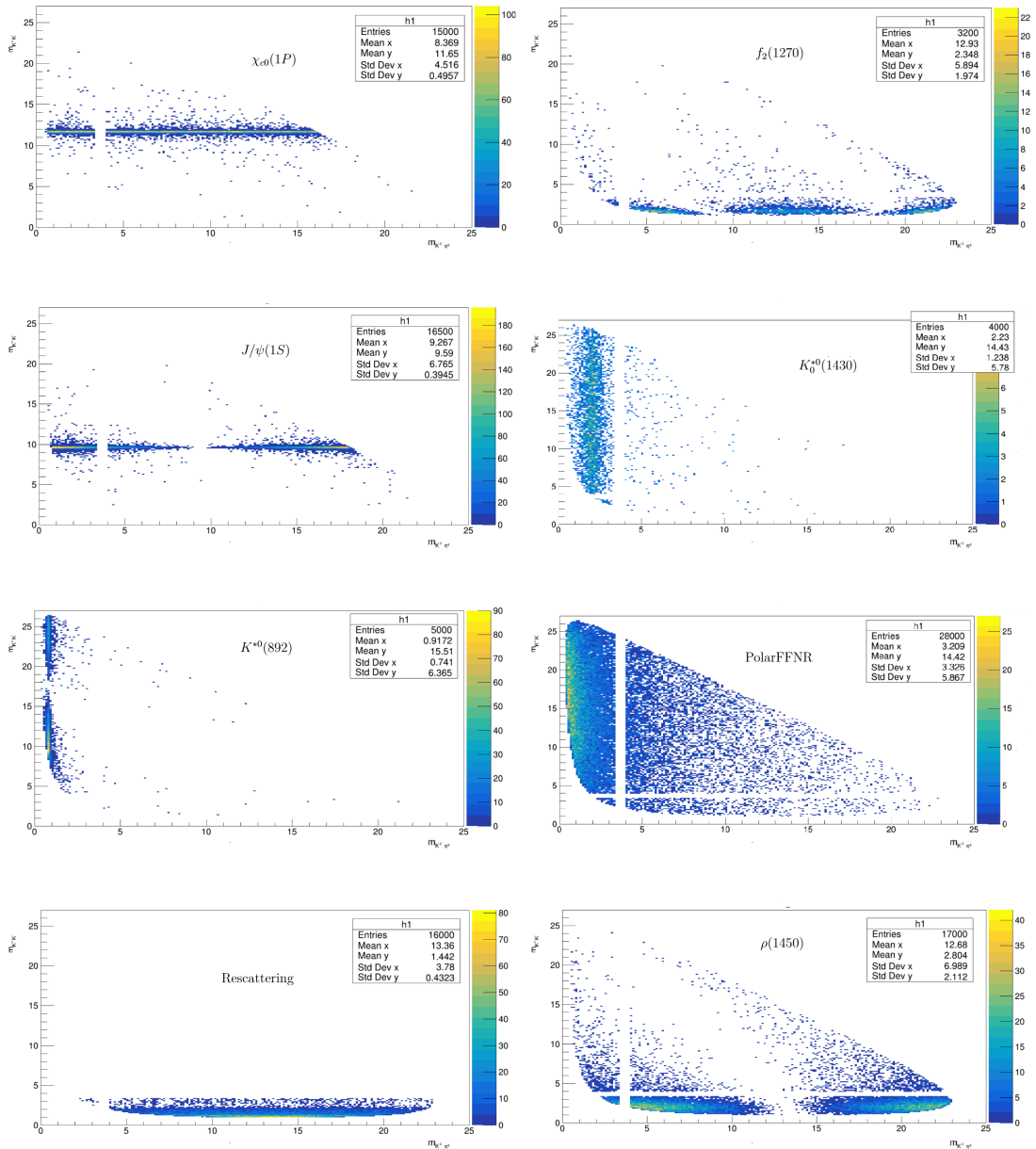


Figure 105 – Resonances generated without background contributions, proportional to their respective fit fractions.

Tabela 37 – Model given as input for the generation of 100 toys.

Component	Fit fraction (%)		A_{CP} (%)
	B^-	B^+	
$K^*(892)$	4.4	5.2	-2.9
$K_0^*(1430)$	4.0	3.3	14.5
<i>PolarFFNR</i>	23.5	32.9	-11.1
$\rho(1450)$	18.8	14.9	17.0
$f_2(1270)$	3.9	2.8	21.3
Re-scattering	5.6	26.6	-61.6
χ_{c0}	18.1	11.4	28.0
J/ψ	27.1	6.2	65.9

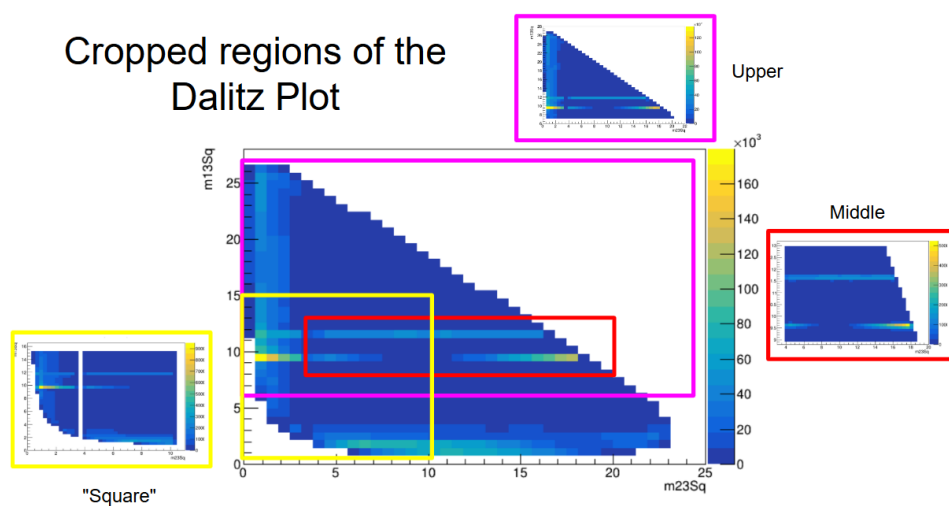


Figure 106 – Cropped regions of the Dalitz Plot.

used for the toy generation could be recovered in the fits. To this end, a simple test was conducted by fitting the 100 generated toys. Figures 107, 108, and 109 present the results for the A_{CP} and Fit Fraction, where the red bin represents the true value (input parameter), and the blue bins represent the fit results. As can be observed, there is a clear Gaussian behavior centered around the red bin, which is a positive indication that the input parameters are being successfully recovered by the fit. It is worth noting that, in this initial test, no cropped regions were applied to the Dalitz plot, and the entire phase space was fitted. The amplitudes considered in this study are:

- $A_0 = K^{*0}(892)$ $A_1 = K_0^*(1430)$ $A_2 = \text{PolarFFNR}$ $A_3 = \rho(1450)$
- $A_4 = f_2(1270)$ $A_5 = \text{Re-scattering}$ $A_6 = \chi_{c0}$ $A_7 = J/\psi$

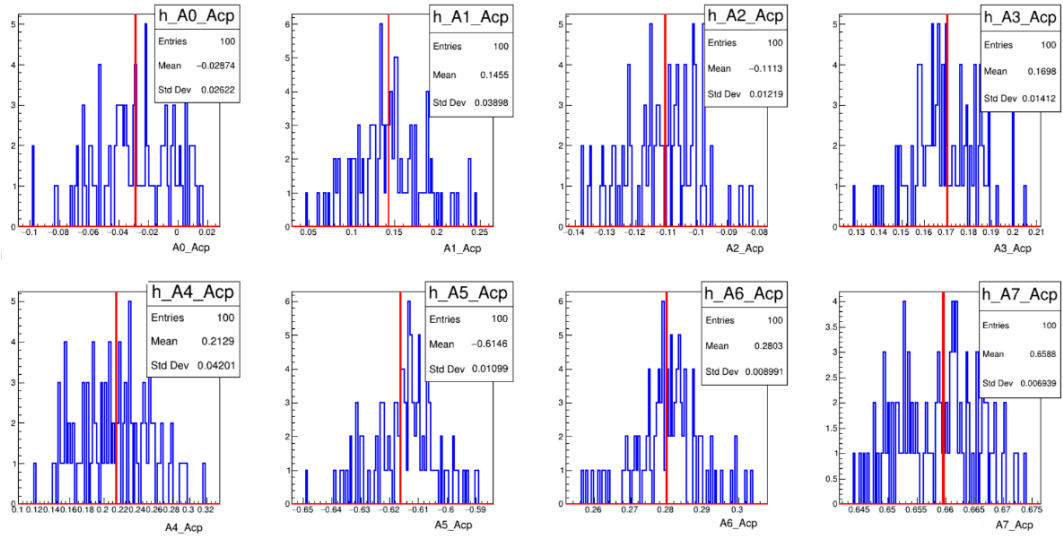


Figure 107 – Fitted A_{CP} distribution from the 100 generated toys, with the reference value shown in red.

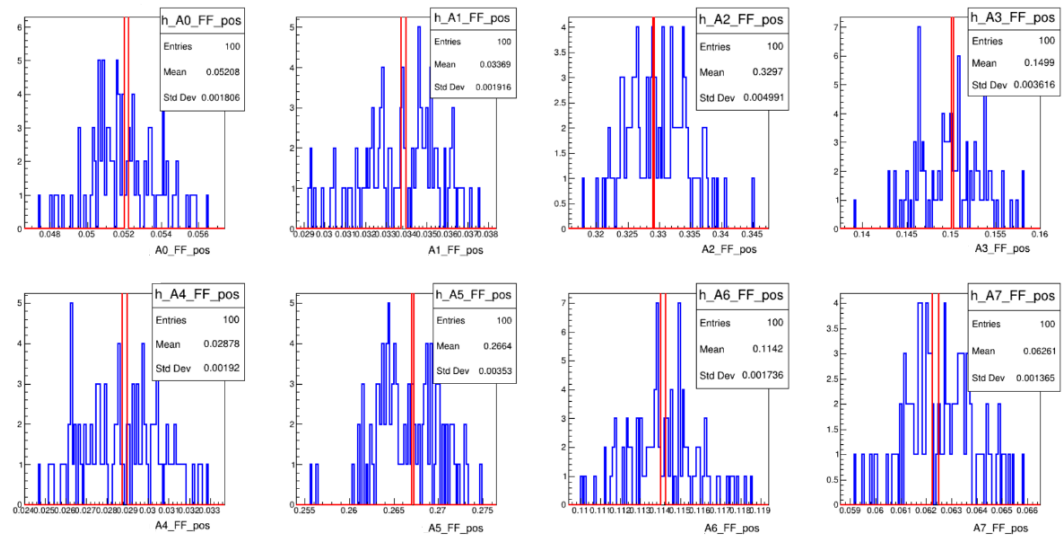


Figure 108 – Fitted positive fit fraction distribution from the 100 generated toys, with the reference value shown in red.

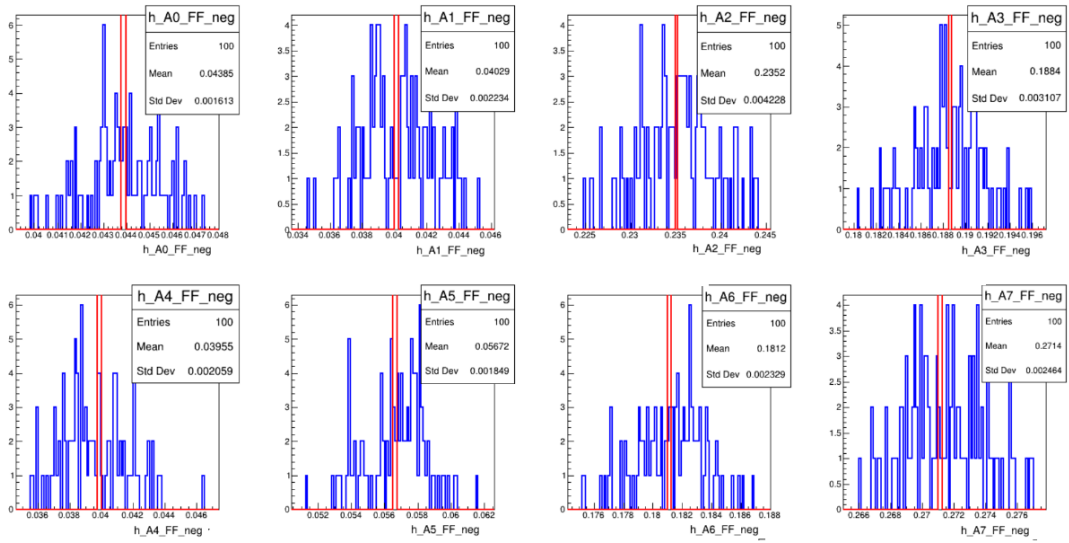


Figure 109 – Fitted negative fit fraction distribution from the 100 generated toys, with the reference value shown in red.

E.2 “Square” cropped region

The first version of the cropped Dalitz plot is referred to as the “square” where the cuts are applied at $KK < 15$ and $K\pi < 10$. This reduction results in approximately 45,000 events remaining in the phase space. This format was chosen because it allows for the inclusion of all resonances. Thus, despite being a cropped version, we will test the hypothesis that it is still possible to recover the results of the full phase space analysis, even with a reduced dataset.

Figures 110, 111, and 112 present the results of the fits performed on the 100 generated toys. It is noticeable that there is a bias between the reference values and the distributions, which are no longer centered around the reference value. This discrepancy arises due to the impact of the difference in the background level. In this first version, we assumed that the background level in this cropped region was equal to or very close to the background level of the full phase space, which is 76% of purity.

Figures 113, 114, and 115 present the results after correcting the background level. As observed, there is no bias in this case. By applying the correct background level for this region (approximately 80% of purity), it is possible to recover the input values. This result demonstrates that it is feasible to crop the Dalitz plot and still obtain results consistent with those from the full Dalitz plot analysis. The final results are summarized in Table 38. Considering this result, the studies in the following sections already account for the correct background contribution according to the cropped region.

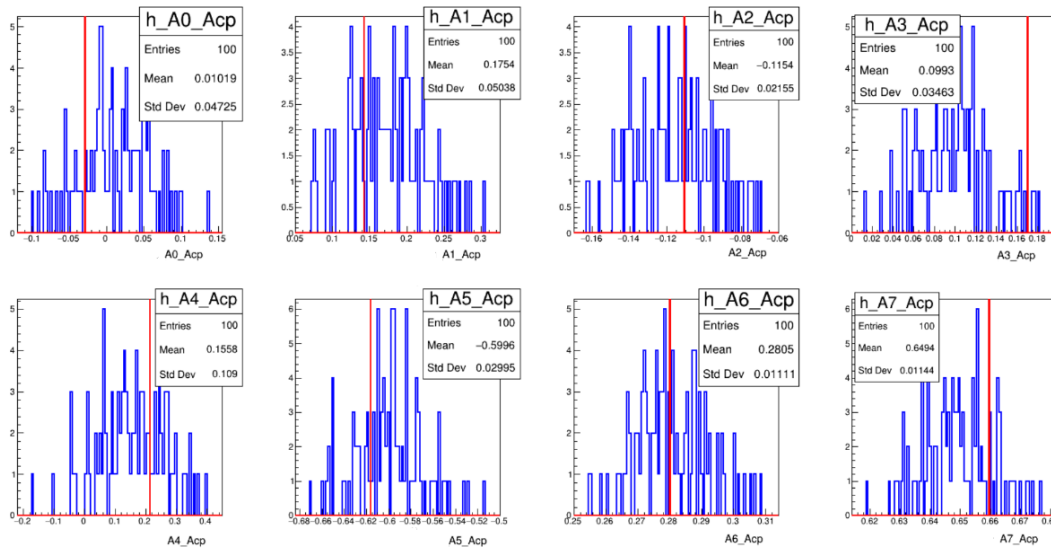


Figure 110 – Fitted A_{CP} distribution from the 100 generated toys for the square cropped region of the Dalitz Plot. There is a clear bias between the reference value shown in red and the distribution of the fits depicted in blue.

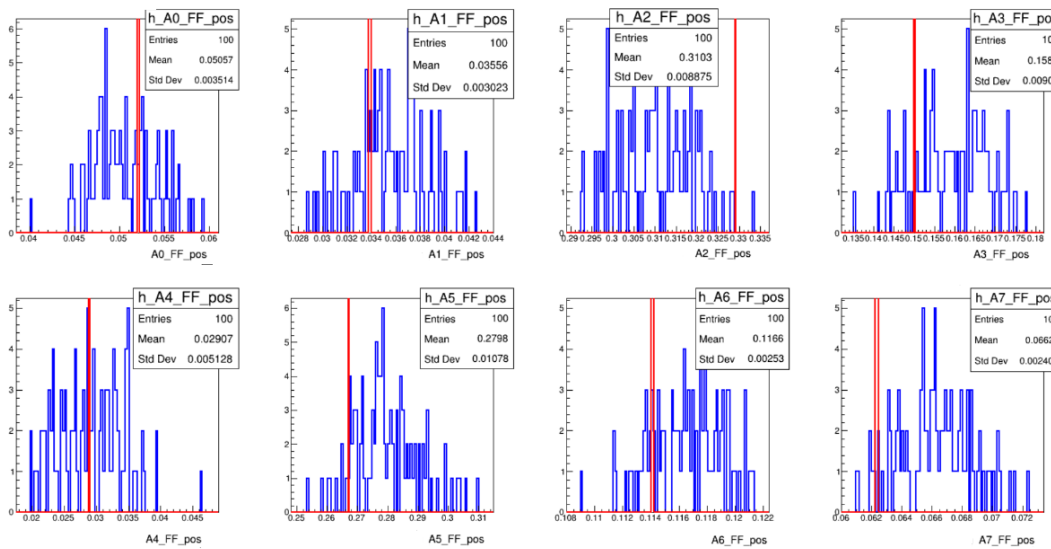


Figure 111 – Fitted positive fit fraction distribution from the 100 generated toys for the square cropped region of the Dalitz Plot. There is a clear bias between the reference value shown in red and the distribution of the fits depicted in blue.

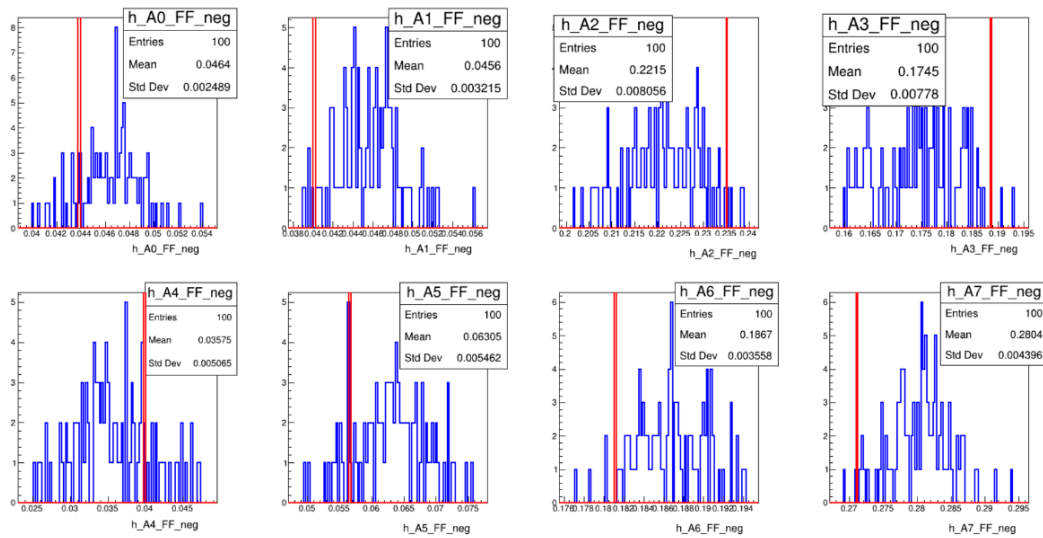


Figure 112 – Fitted negative fit fraction distribution from the 100 generated toys for the square cropped region of the Dalitz Plot. There is a clear bias between the reference value shown in red and the distribution of the fits depicted in blue.

Tabela 38 – Results of the square cropped Dalitz Plot after the correction of the background level.

Component	Fit fraction (%)		A_{CP} (%)
	B^-	B^+	
$K^{*0}(892)$	4.4	5.2	1.0 ± 4.7
$K_0^*(1430)$	4.0	3.3	17.5 ± 5.0
$PolarFFNR$	23.5	32.9	-11.5 ± 2.1
$\rho(1450)$	18.8	14.9	10.0 ± 3.5
$f_2(1270)$	3.9	2.8	15.6 ± 11
Re-scattering	5.6	26.6	-60.0 ± 3.0
χ_{c0}	18.1	11.4	28.0 ± 1.1
J/ψ	27.1	6.2	65.0 ± 1.1

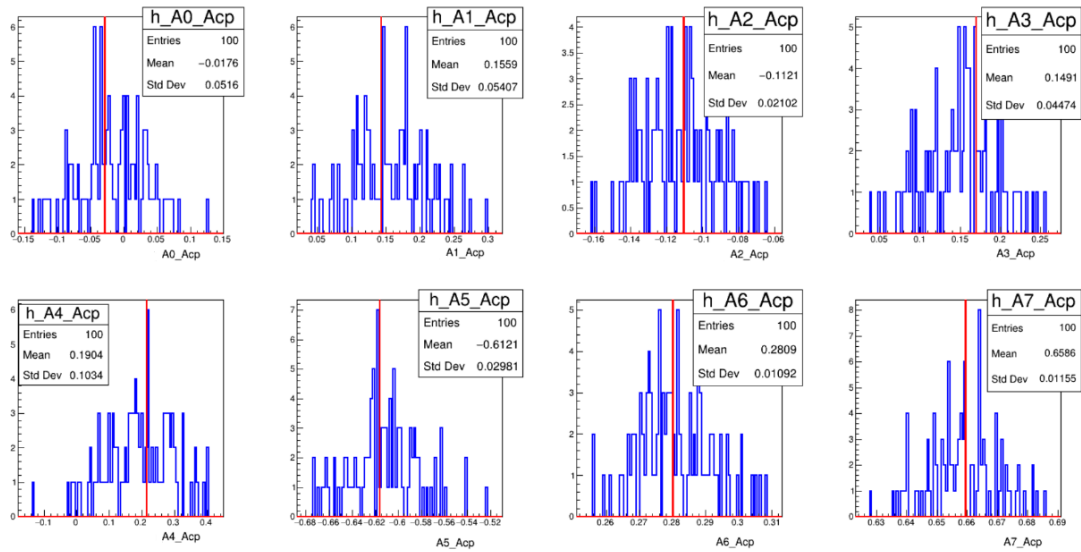


Figure 113 – Fitted A_{CP} distribution from the 100 generated toys for the square cropped region of the Dalitz Plot. There is no bias between the reference value shown in red and the distribution of the fits depicted in blue after correcting the background level.

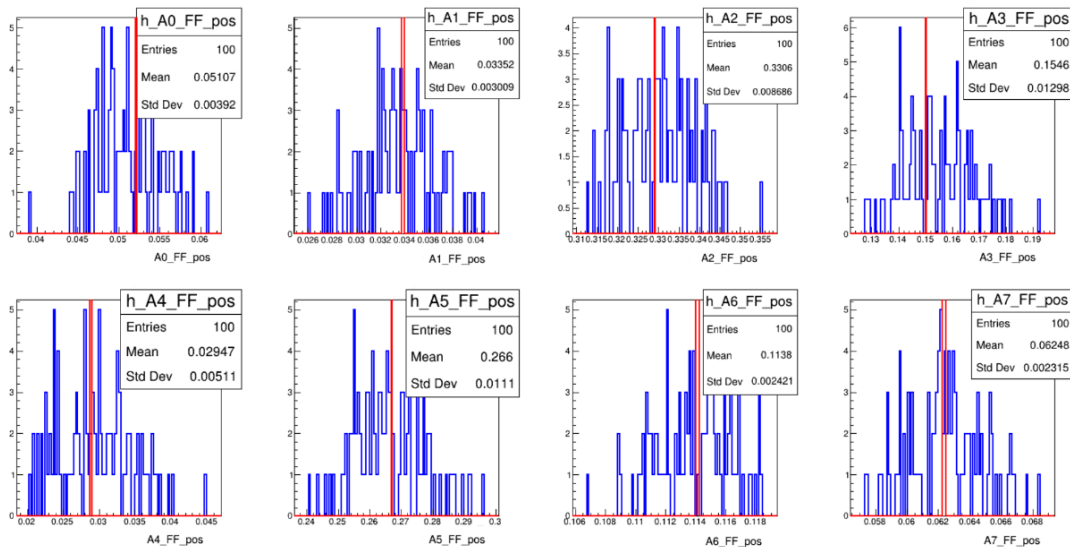


Figure 114 – Fitted positive fit fraction distribution from the 100 generated toys for the square cropped region of the Dalitz Plot. There is no bias between the reference value shown in red and the distribution of the fits depicted in blue after correcting the background level.

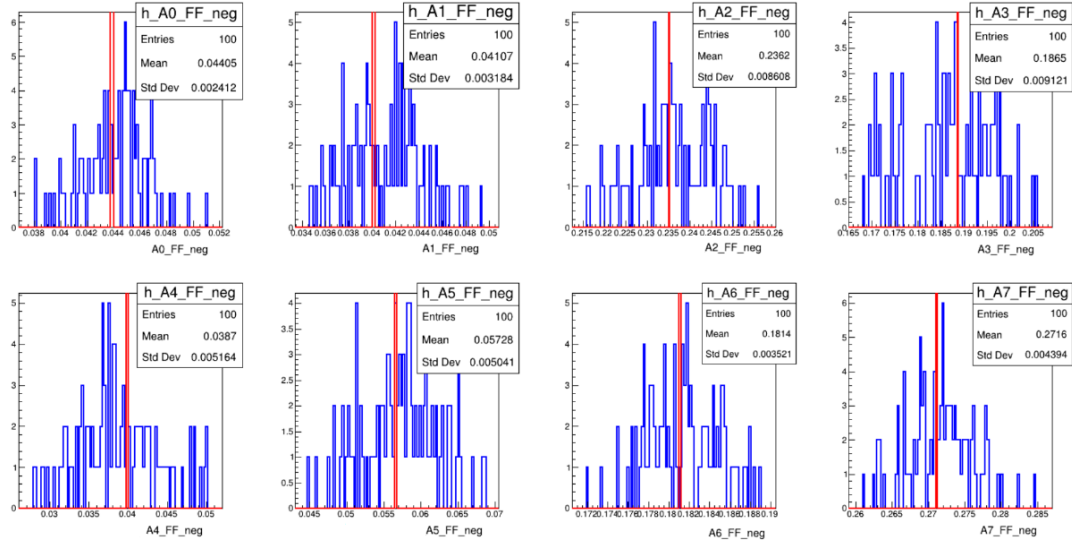


Figure 115 – Fitted negative fit fraction distribution from the 100 generated toys for the square cropped region of the Dalitz Plot. There is no bias between the reference value shown in red and the distribution of the fits depicted in blue after correcting the background level.

E.3 Upper cropped region

For this region, a cut was applied to the Dalitz Plot at $KK < 6$. This region contains approximately 65,000 events with a purity of 79%. It was selected because, above $6 \text{ GeV}^2/c^4$, there should be no contribution from the Rescattering process, and little to no contribution from the $\rho(1450)$ and $f_2(1270)$ resonances (see Figure 105). This step aims to reinforce the hypothesis that it may be possible to entirely exclude a specific contribution from the fit while still recovering the input information provided.

Figures 116, 117, and 118 present the results for the 100 fitted toys, which in this case were fitted considering only $K^*0(892)$, $K^*0(1430)$, PolarFFNR, χ_c , and J/ψ to test the hypothesis. As expected, the fit fractions were significantly altered compared to the reference values, since cropping the Dalitz Plot changes the proportion of the resonances. Additionally, the A_{CP} values were also considerably different from the original ones.

Considering that the observed changes in the results were a consequence of removing the $\rho(1450)$, $f_2(1270)$, and Rescattering contributions, we tested the impact of removing only the Rescattering amplitude. This choice is justified as the Rescattering amplitude extends at most up to $4 \text{ GeV}^2/c^4$. Thus, by excluding the Rescattering component from the fit model and applying it to a dataset cropped accordingly, it is expected that the results will not deviate from the original input values. Figures 119, 120, and 121 show the results of this test, with only the Rescattering contribution removed. As observed, the distributions exhibit the expected behavior, spreading Gaussian-like around the central

value. From this step, we conclude that while $\rho(1450)$ and $f_2(1270)$ still need to be included in the fit model due to their small contributions to the upper Dalitz Plot, it is feasible to exclude the Rescattering amplitude, as it does not contribute to this region. The table 39 presents the results after the removal of only the Rescattering component.

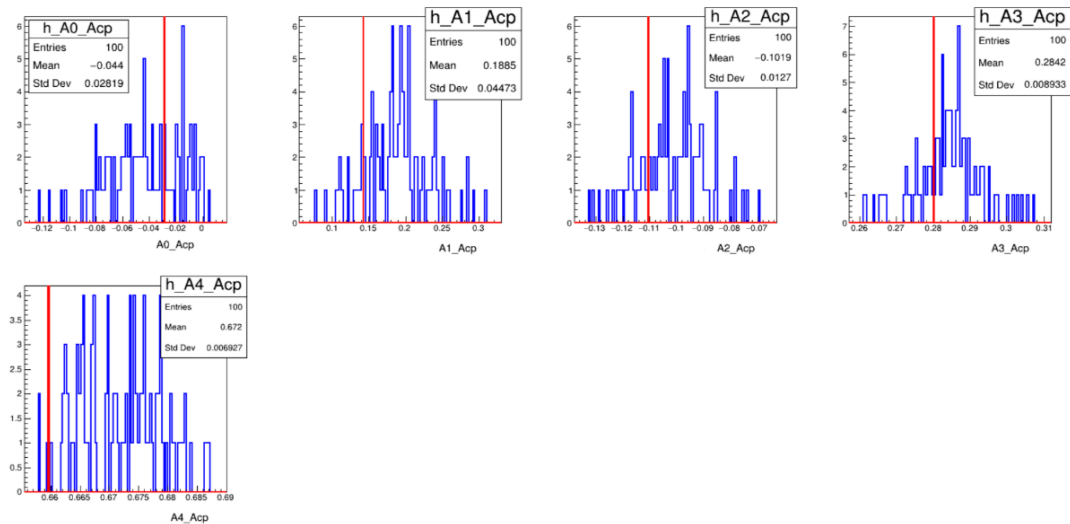


Figure 116 – Fitted A_{CP} distribution from the 100 generated toys for the Upper cropped region of the Dalitz Plot. The impact of removing three resonances on the fitted values (in blue) can be observed by comparing them with the reference values (in red).

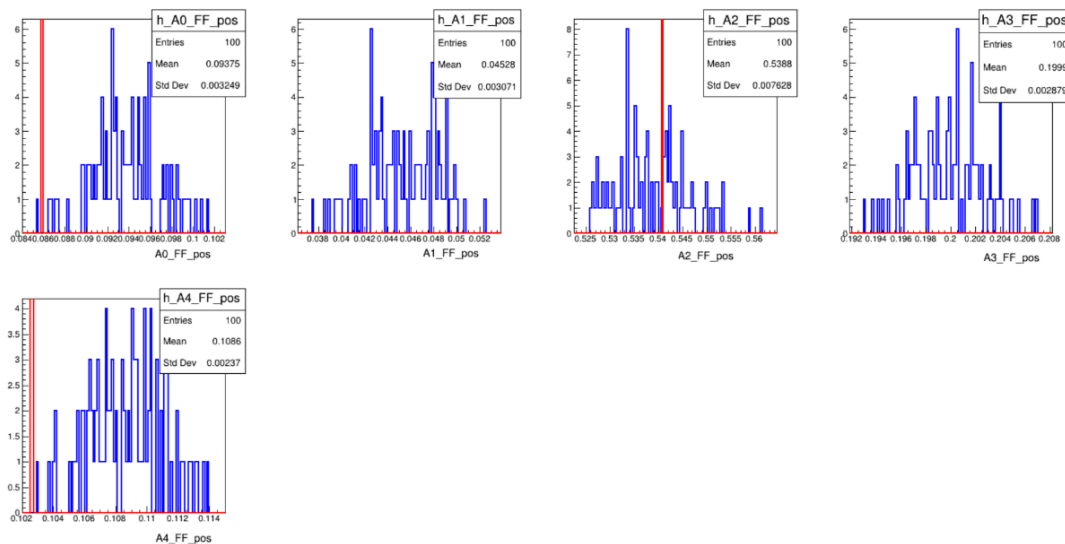


Figure 117 – Fitted positive fit fraction distribution from the 100 generated toys for the Upper cropped region of the Dalitz Plot. The impact of removing three resonances on the fitted values (in blue) can be observed by comparing them with the reference values (in red).

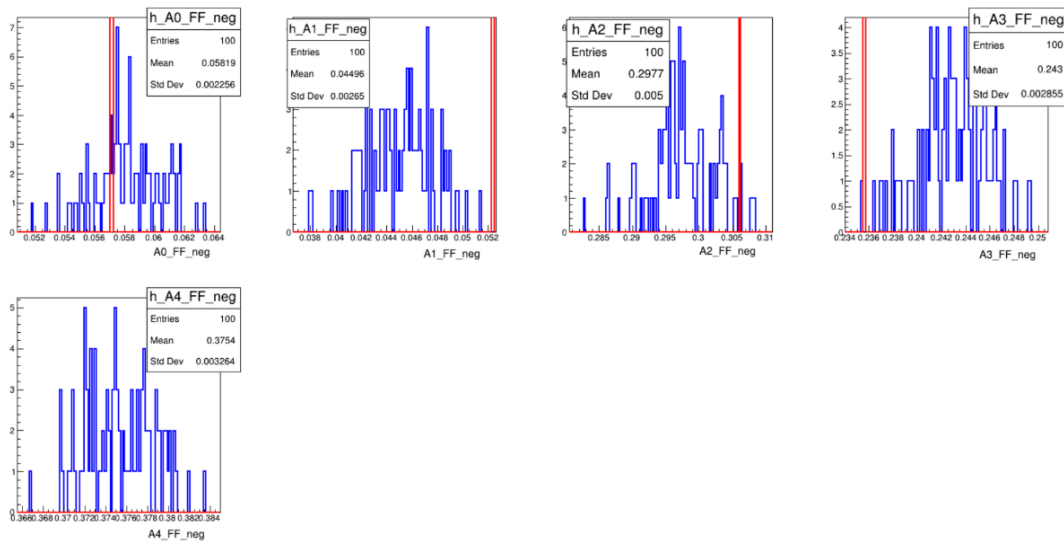


Figure 118 – Fitted negative fit fraction distribution from the 100 generated toys for the Upper cropped region of the Dalitz Plot. The impact of removing three resonances on the fitted values (in blue) can be observed by comparing them with the reference values (in red).

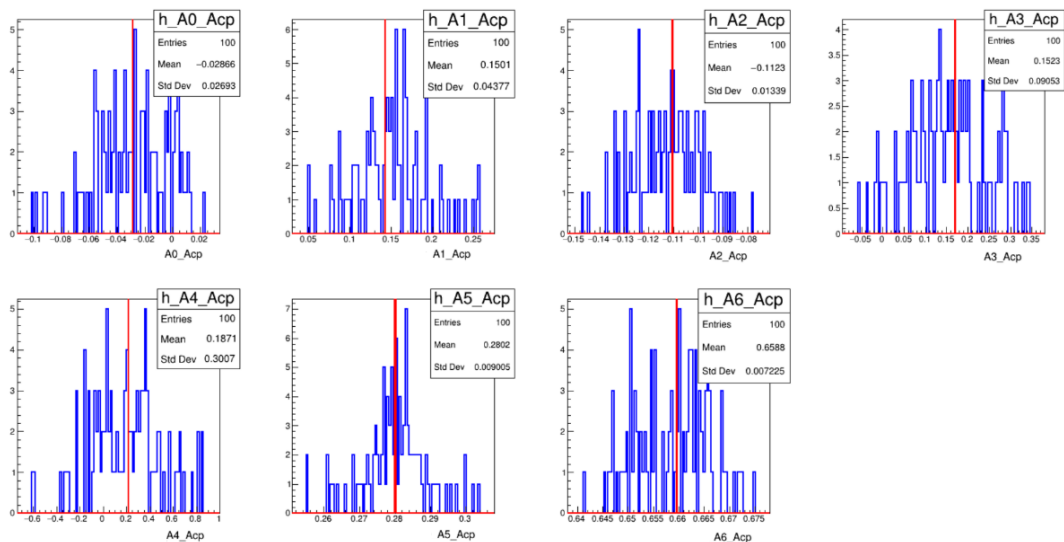


Figure 119 – Fitted A_{CP} distribution from the 100 generated toys for the Upper cropped region of the Dalitz Plot. After removing only the rescattering, the distributions (in blue) align consistently with the reference values (in red).

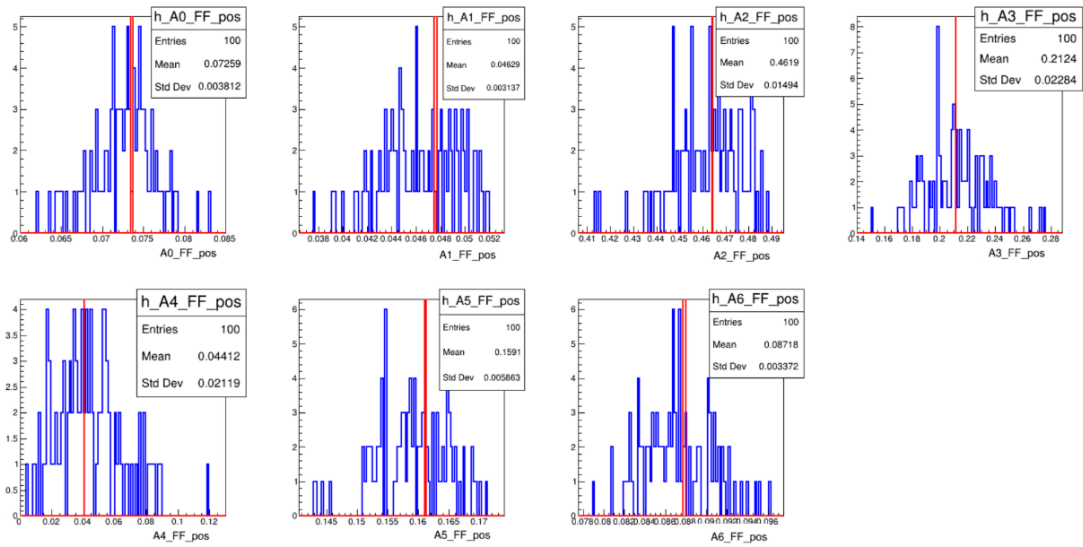


Figure 120 – Fitted positive fit fraction distribution from the 100 generated toys for the Upper cropped region of the Dalitz Plot. After removing only the rescattering, the distributions (in blue) align consistently with the reference values (in red)..

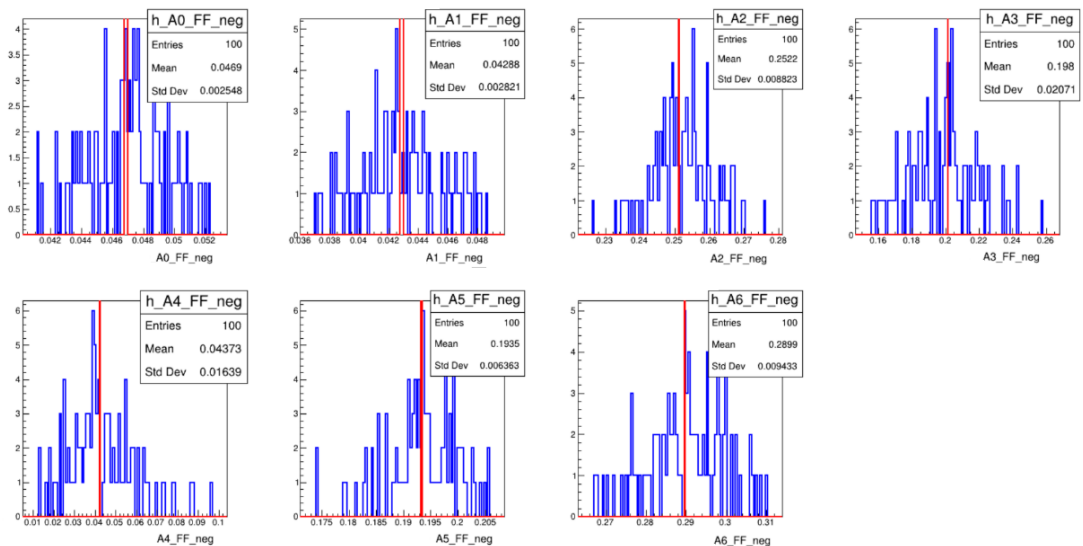


Figure 121 – Fitted negative fit fraction distribution from the 100 generated toys for the Upper cropped region of the Dalitz Plot. After removing only the rescattering, the distributions (in blue) align consistently with the reference values (in red).

Tabela 39 – Results of the upper cropped Dalitz Plot after removing only the Rescattering.

Component	Fit fraction (%)		A_{CP} (%)
	B^-	B^+	
$K^{*0}(892)$	4.6	7.2	-2.9 ± 2.7
$K_0^*(1430)$	4.3	4.6	15.0 ± 4.4
<i>PolarFFNR</i>	25.2	46.1	-11.3 ± 1.3
$\rho(1450)$	20.0	21.2	15.2 ± 9.0
$f_2(1270)$	4.4	4.4	18.7 ± 30
χ_{c0}	19.3	15.9	28.0 ± 0.9
J/ψ	30.0	8.7	65.9 ± 0.7

E.4 Middle cropped region

The aim of this study, involving cropped Dalitz Plots, is to perform Dalitz Plot fits in regions where certain resonances contribute significantly more than others, thus allowing them to be prioritized. For the “Middle” region, the focus is on obtaining a more accurate A_{CP} measurement for χ_c and J/ψ , as these resonances are very narrow and involve fewer events. This cropped region was defined with $13 \text{ GeV}^2/c^4 > KK > 9 \text{ GeV}^2/c^4$ and $K\pi > 4 \text{ GeV}^2/c^4$, containing approximately 20,000 events per toy with a purity of about 93%. Since only the PolarFFNR component, in addition to χ_c and J/ψ , significantly contributes to this region, it was also included in the fit model.

As seen in the previous section, since the Fit Fraction values are always altered according to the region, these plots will not be presented here as their effect is already well understood. Figure 122 shows the result of the fits for 100 toys, keeping only PolarFFNR, χ_c , and J/ψ in the model, where $A_0 = \text{PolarFFNR}$, $A_1 = \chi_c$, and $A_2 = J/\psi$. The A_{CP} values exhibit some deviations from the reference values, which may be due to the absence of certain contributions in the Middle region. Consequently, the same study was repeated, this time including $\rho(1450)$, which contributes significantly to this region.

The figure 123 presents the results for the fits of the 100 toys, this time considering $A_0 = \text{PolarFFNR}$, $A_1 = \rho(1450)$, $A_2 = \chi_c$, and $A_3 = J/\psi$. As observed, there is a good agreement between the fit distributions and the reference values. However, some bias is still present, particularly in PolarFFNR, likely due to the absence of another resonance not accounted for in this region.

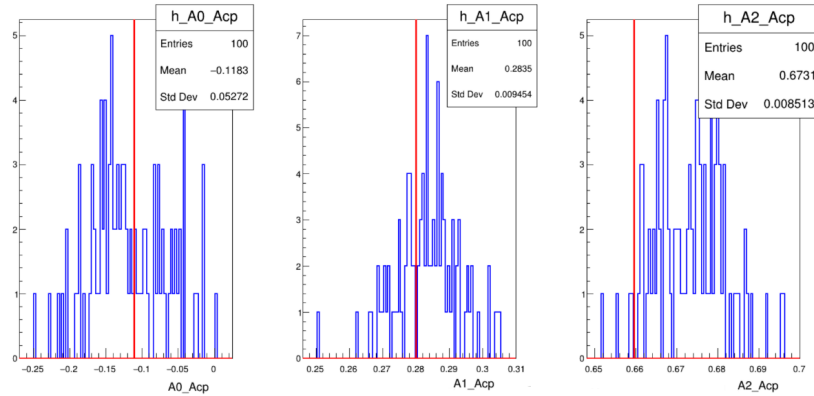


Figure 122 – Fitted A_{CP} distribution from the 100 generated toys for the Middle cropped region of the Dalitz Plot. Keeping only PolarFFNR, χ_c , and J/ψ , there appears to be a bias in the A_{CP} values when comparing the reference value (in red) with the distribution (in blue).

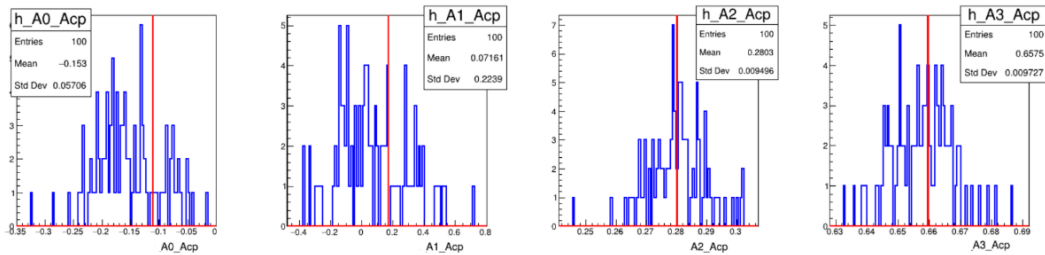


Figure 123 – Fitted A_{CP} distribution from the 100 generated toys for the Middle cropped region of the Dalitz Plot, after adding the $\rho(1450)$.

E.4.1 Studies with a realistic model for the Middle cropped region

The studies conducted thus far have involved simulations of the real data using a model that was not entirely realistic with respect to the contributions of the resonances J/ψ and χ_c . This approach was initially adopted to simplify the process of verifying, in a first approximation, whether it would be possible to recover the values provided as input, although under the assumption that these resonances contributed more significantly than they do in reality.

In this subsection, we will employ a more realistic model, where the contributions of these resonances will exhibit behavior closer to that observed in the real data. In other words, a new set of 100 toys, each containing 100,000 events, was generated with contributions more realistic. Table 40 presents the input values used for the toy generation.

Note that this model does not exactly replicate the one extracted from the data; it merely adjusts the contributions of the two resonances that were artificially amplified in the previous study. It should be emphasized that the A_{CP} values of these two contributions

remain quite large, while the fit fractions have been significantly altered. Under these new conditions, the cropped region now contains approximately 3,600 events with a purity of 63%, which is drastically different from the previous study.

Tabela 40 – A more realistic model used as input for the generation of the new set of toys.

Component	Fit fraction (%)		A_{CP} (%)
	B^-	B^+	
$K^{*0}(892)$	7.6	6.2	-2.7
$K_0^*(1430)$	7.1	4.1	14.3
<i>PolarFFNR</i>	41.1	39.2	-11.0
$\rho(1450)$	32.9	17.8	17.1
$f_2(1270)$	7.0	3.4	21.3
Rescattering	9.9	31.7	-61.5
χ_{c0}	1.2	0.7	86.3
J/ψ	1.6	1.1	82.3

Figure 124 presents the results of the new set of 100 fitted toys for the Middle region, with $A_0 = \text{PolarFFNR}$, $A_1 = \rho(1450)$, $A_2 = \chi_c$, and $A_3 = J/\psi$. In this case, although all fits converged, 83% of them reached parameter limits, which is a negative indicator. As shown, there is a clear bias in this scenario, with no agreement between the reference values and the distributions. This discrepancy arises due to the low number of events in the region along with the absence of other resonances that might contribute to this region.

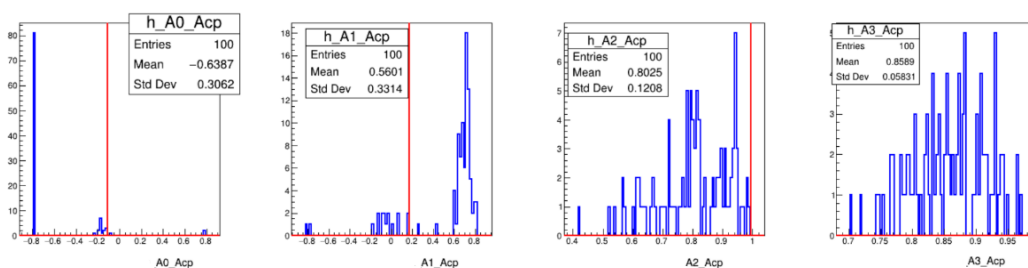


Figure 124 – Fitted A_{CP} distribution from the new 100 generated toys for the Middle cropped region of the Dalitz Plot.

E.5 Limitations and insights from Cropped Dalitz Plot Analysis

This study involving cropped regions of the Dalitz Plot suggests that it is possible to correlate fits from cropped regions with the full phase space. Initial results demonstrated that, depending on the resonances included in the fit model and the specific region of the

phase space being cropped, consistency in the results can be achieved if the contributing resonances to that region are well understood.

On the other hand, it was also observed that in regions with a low number of events and resonances that, although isolated, still interact with larger resonances spreading throughout the phase space, obtaining accurate results becomes challenging. Therefore, specifically for $B \rightarrow KK\pi$, it is not feasible to achieve precise results for χ_c and J/ψ using the cropped Dalitz Plot method.

F Appendix: Impact of Rescattering Model Variations on NLL

As observed throughout this analysis, the metric used to evaluate the quality of a fit is the negative log-likelihood (NLL). The NLL value allows us to quantify numerically how much a fit has improved and to assess whether one model might be superior to another. However, this metric does not have an associated uncertainty, meaning that when we observe an improvement in the NLL between models, it remains unclear if, despite the progress, the models may still be statistically compatible.

As described in section 7.4.5, generally, to evaluate the statistical significance of adding a component to a model (or a degree of freedom in a broader sense), the Wilks' Theorem is applied. However, there are some limitations like non-nested models and bounded parameters. Both situations limit the applicability of Wilks' theorem in studying the case of Rescattering, as this amplitude includes bounded parameters, and the use of either Rescattering(2018) or Rescattering(2023) results in non-nested models, as will be presented.

Therefore, as an alternative for evaluating the NLL in this case, simulations can be used. The motivation for this appendix study lies in the attempt to provide users of this metric with insights into how meaningful an improvement in NLL may be. Through this investigation, we aim to clarify the interpretive value of changes in NLL, enhancing the understanding of model comparison based on this metric.

To achieve this, we employ two different rescattering models: one referred to as Rescattering(2018), based on the work of [17], and the other referred to as Rescattering(2023), derived from [78]. The primary distinction between these two models lies in their suitability for the specific decay environment. Rescattering(2018) is more appropriate for use within the isobar model framework, as it describes two-body scattering. In contrast, Rescattering(2023) is formulated for direct three-body scattering, making it incompatible with the isobar model's "quasi-two-body" or "2+1" approximation, which treats the decay as two quasi-independent two-body processes.

Thus, the study presented here compares these two distinct rescattering models to observe how the NLL value changes with each. By comparing the impact of Rescattering(2018) and Rescattering(2023) on the model, we aim to identify how many units of NLL shift with each model, providing insight into the effect of fundamentally different rescattering assumptions on model quality.

As a first step in this study, we applied the same model to fit the data, differing

Tabela 41 – Dalitz Plot fit results using the Rescattering(2018).

[NLL -146056] Component	Fit fraction (%)		Magnitude and phase coefficients				A_{CP} (%)
	B^-	B^+	a_i^+	$\delta_i^+ [^\circ]$	a_i^-	$\delta_i^- [^\circ]$	
$K^*(892)$	5.1 ± 0.5	6.1 ± 0.4	0.99 ± 0.02	0 ± 0	1.01 ± 0.02	0 ± 0	2.8 ± 4.1
$K_0^*(1430)$	3.6 ± 0.5	4.5 ± 0.3	0.81 ± 0.04	4 ± 4	0.87 ± 0.04	-30 ± 4	7.7 ± 5.8
<i>PolarFFNR</i>	36.9 ± 1.5	38.9 ± 1.3	2.81 ± 0.07	36 ± 3	2.56 ± 0.06	3 ± 3	-9.3 ± 1.9
$\rho(1700)$	4.2 ± 0.8	4.3 ± 0.7	1.03 ± 0.06	-47 ± 6	0.75 ± 0.06	-92 ± 6	-31.0 ± 8.4
$\rho(1450)$	18.9 ± 1.2	23.4 ± 1.0	1.86 ± 0.07	-121 ± 7	1.98 ± 0.07	-135 ± 5	6.3 ± 3.8
$f_2(1270)$	6.5 ± 0.7	8.4 ± 0.6	1.28 ± 0.06	132 ± 6	1.26 ± 0.05	117 ± 4	24.2 ± 4.4
Re-scattering	19.5 ± 0.8	8.7 ± 0.7	2.48 ± 0.06	-104 ± 6	2.11 ± 0.04	-131 ± 5	-61.5 ± 1.6
$\phi(1020)$	0.4 ± 0.1	0.8 ± 0.1	0.12 ± 0.03	93 ± 15	0.37 ± 0.03	-89 ± 9	79.9 ± 9.0
χ_{e0}	1.0 ± 0.2	1.4 ± 0.2	0.40 ± 0.03	125 ± 6	0.48 ± 0.03	67 ± 6	18.3 ± 7.8
Fit Fraction Sum	96.0	96.6					

Tabela 42 – Dalitz Plot fit results using the Rescattering(2023).

[NLL -145838] Component	Fit fraction (%)		Magnitude and phase coefficients				A_{CP} (%)
	B^-	B^+	a_i^+	$\delta_i^+ [^\circ]$	a_i^-	$\delta_i^- [^\circ]$	
$K^*(892)$	5.1 ± 0.5	6.0 ± 0.4	0.99 ± 0.02	0 ± 0	1.01 ± 0.02	0 ± 0	2.1 ± 4.1
$K_0^*(1430)$	3.3 ± 0.3	4.3 ± 0.3	0.76 ± 0.04	7 ± 4	0.85 ± 0.04	-29 ± 4	11.5 ± 6.0
<i>PolarFFNR</i>	37.3 ± 1.4	39.2 ± 1.2	2.84 ± 0.07	36 ± 3	2.58 ± 0.07	3 ± 3	-9.8 ± 1.8
$\rho(1700)$	4.6 ± 0.8	3.2 ± 0.7	1.13 ± 0.07	-38 ± 6	0.74 ± 0.06	-89 ± 6	-40.2 ± 8.1
$\rho(1450)$	18.3 ± 1.1	24.5 ± 1.3	1.75 ± 0.07	-120 ± 6	2.04 ± 0.07	-130 ± 5	15.0 ± 4.1
$f_2(1270)$	5.3 ± 0.8	8.4 ± 0.7	0.88 ± 0.06	136 ± 6	1.26 ± 0.04	143 ± 5	36.0 ± 4.9
Re-scattering	22.3 ± 0.9	9.4 ± 0.7	2.68 ± 0.06	-104 ± 5	1.26 ± 0.04	-143 ± 5	-63.7 ± 1.5
$\phi(1020)$	0.6 ± 0.1	1.0 ± 0.3	0.25 ± 0.03	112 ± 12	0.41 ± 0.03	-84 ± 12	46.7 ± 11.6
χ_{e0}	1.0 ± 0.2	1.4 ± 0.2	0.40 ± 0.03	124 ± 6	0.48 ± 0.03	67 ± 7	18.1 ± 7.9
Fit Fraction Sum	97.9	97.4					

only in the choice of rescattering model. Table 41 presents the results for the fit using Rescattering(2018), and Table 42 shows the fit results with Rescattering(2023). As can be observed, both results are quite similar in terms of A_{CP} , Fit Fractions, a_i , and δ_i . The most noticeable difference lies in the NLL value, which varies between the two models.

A set of 500 samples was generated based on the solution using the Rescattering(2018) model, which will be referred to as the “mother solution” from here onward. First, we calculated¹ the NLL values by “fitting” the mother solution directly to these datasets. We then recalculated the NLL values by applying variations of the mother solution, created by randomizing all parameters according to Gaussian distributions centered on their values and uncertainties from the mother solution — a method we will refer to as “shaking” For instance, if the central value of a_i for $K^*(892)$ is 0.99 with an error of 0.02, these parameters select a randomized value within a Gaussian distribution. Parameter variations were applied in Cartesian coordinates rather than polar coordinates, based on the results of this fit.

Figure 125 presents the result after a single “shaking” of the mother solution. The NLL distribution calculated with the parameters of the mother solution is shown in blue, while the NLL distribution calculated after shaking the parameters is shown in red. It

¹ “Calculating the NLL” refers to performing the fit with all parameters fixed, except for the number of signal events.

can be observed that, in this first test, the difference between the mean NLL values is approximately 200 units. In other words, after Gaussian randomization of the parameters according to the mother solution, the NLL distribution of the new solution differs by around 200 units.

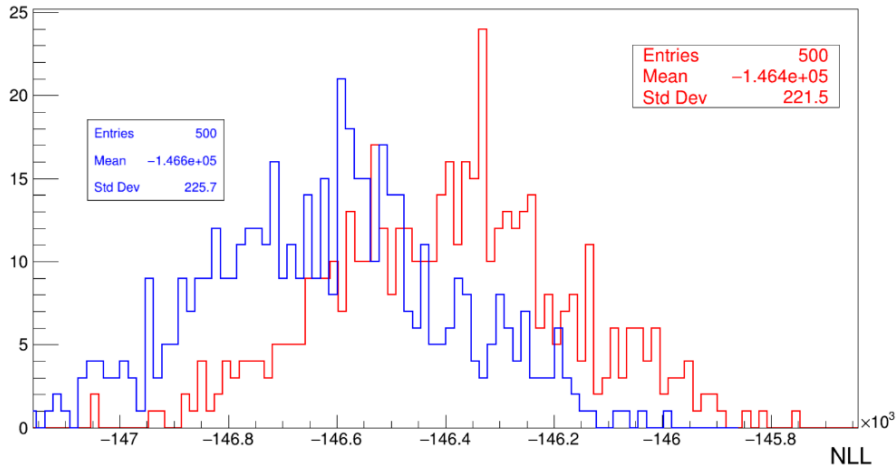


Figure 125 – NLL distribution for the mother solution (in blue) and the parameters after one shaking (in red).

The next step was to shake the mother solution 500 times, allowing us to observe the behavior of the distribution of the shaken solutions. Figure 126 presents the results, in blue, we once again show the NLL distribution calculated from the parameters of the mother solution. In red, we display the NLL distribution after shaking the parameters 500 times.

It can be observed that the Gaussian distributions of the mother solution parameters and the shaken parameters are compatible. The standard deviation of the Gaussian in blue is due to statistical error, while the standard deviation of the Gaussian in red results from a convolution of statistical and model errors. From this, we conclude that a 200-unit difference in NLL does not appear sufficient to distinguish between models.

The next test aims to estimate the difference in NLL units between the Rescattering(2023) and Rescattering(2018) models. To do this, we generated 500 simulations using the Rescattering(2018) solution and 500 simulations with the Rescattering(2023) solution. Figure 127 presents the distributions of the NLL values calculated in four distinct ways: first, we calculated the NLL for the Rescattering(2018)-generated set by applying the model containing Rescattering(2018) itself (in blue), and then by applying the model containing Rescattering(2023) (in red). Next, for the Rescattering(2023)-generated set, we calculated the NLL first with Rescattering(2023) (in pink) and then with the model using Rescattering(2018) (in green).

As shown, all distributions are compatible with each other, and a difference of around 200 NLL units does not seem sufficient to distinguish between the models. We

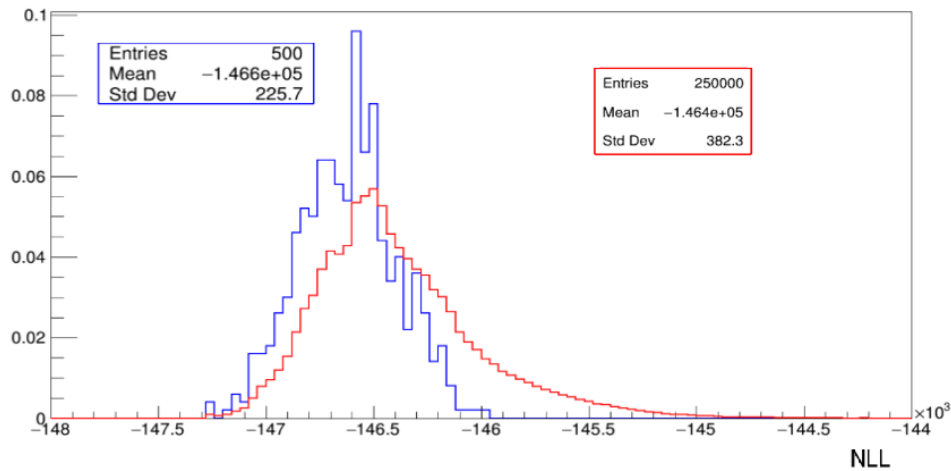


Figure 126 – NLL distribution for the mother solution (in blue) and the parameters after 500 shakings (in red).

conclude that, while Rescattering(2018) yields results with better NLL values and is more suitable for this analysis, Rescattering(2023) should not be entirely disregarded. Additionally, incorporating correlation matrices between parameters would lead to more accurate results, as “shaking” the mother solution without considering correlations risks ignoring the effect that changes in one parameter may have on another, especially when they are strongly correlated.

It is important to note that this study is not general. In considering a 200-unit difference in NLL as insufficient to distinguish between models, we do not imply this threshold applies to any possible modification within this analysis. This evaluation is specific to the two rescattering options under consideration, where we conclude there is insufficient evidence to exclude one model in favor of the other. We have chosen to proceed with Rescattering(2018) due to its greater suitability for use within the isobar model framework.

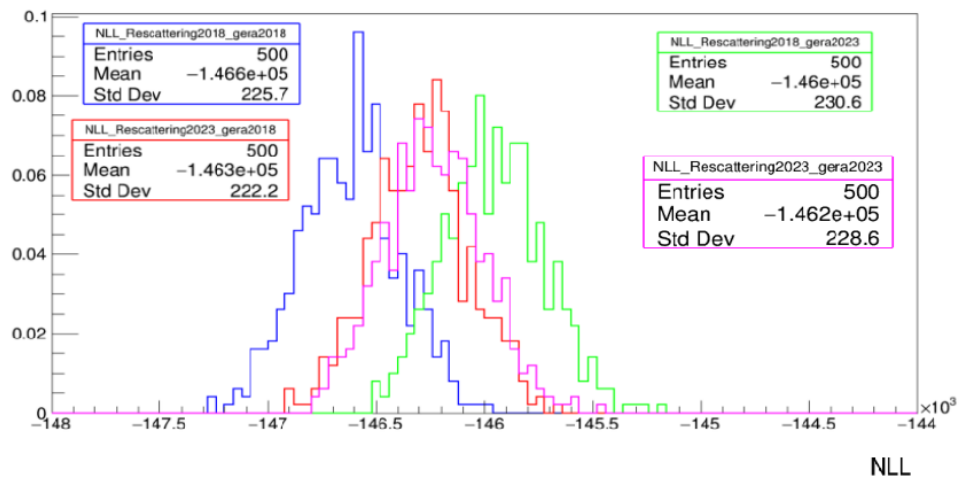


Figure 127 – Distribution of NLL values calculated for four different cases: 500 simulations generated with Rescattering(2018), calculated with Rescattering(2018) and Rescattering(2023) shown in blue and red, respectively. 500 simulations generated with Rescattering(2023), calculated with Rescattering(2018) and Rescattering(2023) shown in green and pink, respectively.

G Appendix: testing Wilk's Theorem with toys

In this appendix, toy studies are presented to evaluate the validity of Wilks' Theorem. A toy dataset was generated with 100,000 events and a purity of 76%. Various scenarios were evaluated, including vector and tensor resonances with both broader and narrower widths. All the generated toys were based on the baseline model presented in Section 8.3.1. For each individual case, the resonance under investigation, aimed at determining its statistical significance, was added to the model. In all cases, 4 degrees of freedom will be added in this appendix. For this scenario, considering 5σ , the critical value of a χ^2 distribution is 34.55. Therefore, this will serve as the reference value for all subsequent studies.

G.1 The vector $J/\psi(1S)$ resonance

Due to its extremely narrow width (approximately 90 KeV), two scenarios were tested: one with its width increased to 9 MeV and another using its real width.

- $J/\psi(1S)$ with width 9 MeV:

The Table 44 presents the real model used for the generation of the toy for this case, considering the addition of the $J/\psi(1S)$ resonance with total fit fraction of 0.2%. Table 43 present the result after removing the $J/\psi(1S)$ from the fit model. Considering that $NLL_{\text{ratio}} = 66$, and since $34.55 < 66$, the inclusion of the J/ψ in this context does have appreciable statistical significance.

Tabela 43 – Dalitz Plot fit result for a toy dataset generated with the $J/\psi(1S)$ having an increased width and not included in the fit model.

[NLL -514517] Component	Fit fraction (%)		Magnitude and phase coefficients				A_{CP} (%)
	B^-	B^+	a_i^+	$\delta_i^+ [^\circ]$	a_i^-	$\delta_i^- [^\circ]$	
$K(892)$	5.94 ± 0.19	5.06 ± 0.16	1.028 ± 0.011	0 ± 0	0.972 ± 0.011	0 ± 0	-5.6 ± 2.3
$K_0^*(1430)$	5.55 ± 0.27	5.90 ± 0.24	1.109 ± 0.027	14 ± 2	0.940 ± 0.025	-22 ± 2	-16.5 ± 3.1
$PolarFFNR$	37.94 ± 0.61	33.93 ± 0.45	2.661 ± 0.038	31 ± 2	2.457 ± 0.037	6 ± 2	-8.0 ± 1.1
$\rho^0(1700)$	3.91 ± 0.33	2.61 ± 0.25	0.738 ± 0.037	-99 ± 5	0.788 ± 0.035	-72 ± 4	6.6 ± 6.5
$\rho^0(1450)$	22.00 ± 0.72	16.28 ± 0.52	1.844 ± 0.036	-176 ± 3	1.871 ± 0.038	-137 ± 3	1.5 ± 2.3
$f_2(1270)$	9.57 ± 0.29	4.04 ± 0.18	0.919 ± 0.023	82 ± 3	1.234 ± 0.024	119 ± 3	28.7 ± 2.5
Re-scattering	9.07 ± 0.24	24.62 ± 0.28	2.267 ± 0.029	-159 ± 3	1.201 ± 0.022	-126 ± 3	-56.1 ± 1.0
$\phi(1020)$	0.82 ± 0.07	0.09 ± 0.02	0.137 ± 0.017	56 ± 9	0.361 ± 0.015	-79 ± 5	74.9 ± 5.7
χ_{co}	1.38 ± 0.09	0.61 ± 0.05	0.357 ± 0.015	116 ± 4	0.469 ± 0.016	62 ± 5	26.6 ± 4.9
Fit Fraction Sum	96.2	93.1					

Tabela 44 – Dalitz Plot fit result for a toy dataset generated with the $J/\psi(1S)$ having an increased width and included in the fit model.

[NLL -514583] Component	Fit fraction (%)		Magnitude and phase coefficients				A_{CP} (%)
	B^-	B^+	a_i^+	$\delta_i^+ [^\circ]$	a_i^-	$\delta_i^- [^\circ]$	
$K^*(892)$	5.98 ± 0.19	5.03 ± 0.16	1.024 ± 0.012	0 ± 0	0.976 ± 0.012	0 ± 0	-4.9 ± 2.3
$K_0^*(1430)$	5.91 ± 0.29	5.79 ± 0.24	1.100 ± 0.027	14 ± 2	0.970 ± 0.026	-21 ± 2	-12.5 ± 3.1
<i>Polar</i> FFNR	38.21 ± 0.60	33.72 ± 0.45	2.653 ± 0.038	31 ± 2	2.466 ± 0.037	4 ± 2	-7.3 ± 1.1
$\rho^0(1700)$	3.86 ± 0.33	2.55 ± 0.25	0.730 ± 0.037	-98 ± 5	0.784 ± 0.035	-81 ± 4	7.1 ± 6.6
$\rho^0(1450)$	22.20 ± 0.72	16.49 ± 0.52	1.855 ± 0.036	-177 ± 3	1.880 ± 0.038	-141 ± 3	1.3 ± 2.3
$f_2(1270)$	9.45 ± 0.29	4.01 ± 0.18	0.915 ± 0.023	82 ± 3	1.226 ± 0.024	114 ± 3	28.5 ± 2.5
Re-scattering	8.87 ± 0.23	24.64 ± 0.28	2.268 ± 0.029	-160 ± 3	1.189 ± 0.021	-132 ± 3	-56.9 ± 1.0
$\phi(1020)$	0.84 ± 0.07	0.09 ± 0.02	0.139 ± 0.017	55 ± 9	0.365 ± 0.015	-85 ± 5	74.8 ± 5.7
χ_{c0}	1.40 ± 0.09	0.61 ± 0.05	0.357 ± 0.015	116 ± 4	0.472 ± 0.016	62 ± 4	27.2 ± 4.9
J/ψ	0.27 ± 0.06	0.09 ± 0.03	0.138 ± 0.021	45 ± 8	0.205 ± 0.023	151 ± 6	37.8 ± 16.0
Fit Fraction Sum	97.0	93.0					

- $J/\psi(1S)$ with width 90 KeV:

The Table 46 presents the real model used for the generation of the toy for this case, considering the addition of the $J/\psi(1S)$ resonance with total fit fraction of 0.2%. Table 45 present the result after removing the $J/\psi(1S)$ from the fit model. Considering that $NLL_{\text{ratio}} = 496$, and since $34.55 < 496$, the inclusion of the J/ψ in this context does have appreciable statistical significance.

Tabela 45 – Dalitz Plot fit result for a toy dataset generated with the $J/\psi(1S)$ having the real width and not included in the fit model.

[NLL -514285] Component	Fit fraction (%)		Magnitude and phase coefficients				A_{CP} (%)
	B^-	B^+	a_i^+	$\delta_i^+ [^\circ]$	a_i^-	$\delta_i^- [^\circ]$	
$K^*(892)$	6.02 ± 0.19	5.03 ± 0.16	1.021 ± 0.011	0 ± 0	0.979 ± 0.011	0 ± 0	-4.2 ± 2.3
$K_0^*(1430)$	5.78 ± 0.28	5.83 ± 0.24	1.100 ± 0.027	14 ± 2	0.959 ± 0.025	-22 ± 2	-13.7 ± 3.1
<i>Polar</i> FFNR	38.42 ± 0.61	33.91 ± 0.45	2.652 ± 0.038	31 ± 2	2.473 ± 0.037	4 ± 2	-7.0 ± 1.1
$\rho^0(1700)$	3.78 ± 0.32	2.58 ± 0.25	0.731 ± 0.037	-99 ± 5	0.776 ± 0.035	-82 ± 4	5.9 ± 6.5
$\rho^0(1450)$	22.19 ± 0.71	16.45 ± 0.52	1.847 ± 0.036	-177 ± 3	1.879 ± 0.037	-141 ± 3	1.7 ± 2.3
$f_2(1270)$	9.37 ± 0.29	4.01 ± 0.18	0.912 ± 0.023	82 ± 3	1.221 ± 0.024	115 ± 3	28.4 ± 2.5
Re-scattering	8.81 ± 0.23	24.66 ± 0.28	2.262 ± 0.029	-159 ± 3	1.184 ± 0.021	-131 ± 3	-57.0 ± 1.0
$\phi(1020)$	0.84 ± 0.07	0.09 ± 0.02	0.136 ± 0.017	56 ± 9	0.365 ± 0.015	-85 ± 5	75.6 ± 5.6
χ_{c0}	1.38 ± 0.09	0.61 ± 0.05	0.356 ± 0.015	116 ± 4	0.469 ± 0.016	60 ± 5	27.0 ± 4.9
Fit Fraction Sum	96.6	93.2					

Tabela 46 – Dalitz Plot fit result for a toy dataset generated with the $J/\psi(1S)$ having the real width and included in the fit model.

[NLL -514781] Component	Fit fraction (%)		Magnitude and phase coefficients				A_{CP} (%)
	B^-	B^+	a_i^+	$\delta_i^+ [^\circ]$	a_i^-	$\delta_i^- [^\circ]$	
$K^*(892)$	6.01 ± 0.19	5.02 ± 0.16	1.022 ± 0.011	0 ± 0	0.978 ± 0.011	0 ± 0	-4.3 ± 2.3
$K_0^*(1430)$	5.96 ± 0.28	5.86 ± 0.24	1.103 ± 0.027	14 ± 2	0.974 ± 0.026	-21 ± 2	-12.4 ± 3.1
<i>Polar</i> FFNR	37.97 ± 0.61	33.86 ± 0.45	2.652 ± 0.038	31 ± 2	2.459 ± 0.037	4 ± 2	-7.5 ± 1.1
$\rho^0(1700)$	3.80 ± 0.32	2.54 ± 0.25	0.726 ± 0.037	-99 ± 5	0.778 ± 0.035	-81 ± 4	7.0 ± 6.6
$\rho^0(1450)$	22.11 ± 0.71	16.48 ± 0.52	1.850 ± 0.036	-177 ± 3	1.877 ± 0.037	-140 ± 3	1.4 ± 2.3
$f_2(1270)$	9.43 ± 0.29	4.02 ± 0.18	0.914 ± 0.023	82 ± 3	1.226 ± 0.024	115 ± 3	28.5 ± 2.5
Re-scattering	8.81 ± 0.23	24.63 ± 0.28	2.262 ± 0.029	-160 ± 3	1.185 ± 0.021	-131 ± 3	-56.9 ± 1.0
$\phi(1020)$	0.83 ± 0.07	0.09 ± 0.02	0.136 ± 0.017	56 ± 9	0.364 ± 0.015	-84 ± 5	75.6 ± 5.6
χ_{c0}	1.38 ± 0.09	0.61 ± 0.05	0.356 ± 0.015	116 ± 4	0.469 ± 0.016	62 ± 5	27.0 ± 4.9
J/ψ	0.38 ± 0.03	0.05 ± 0.01	0.101 ± 0.011	39 ± 26	0.245 ± 0.012	148 ± 27	70.8 ± 6.1
Fit Fraction Sum	96.7	93.2					

G.1.1 Adding no $J/\psi(1S)$

In this study, we used a toy generated as previously, but this time without including the $J/\psi(1S)$. The Table 47 presents the real model used for the generation. Table 48 present the result after removing the $J/\psi(1S)$ from the fit model. Considering that $\text{NLL}_{\text{ratio}} = 2$, and since $34.55 > 2$, the inclusion of the J/ψ in this context does not have appreciable statistical significance. This approach aims to reinforce the idea that the method is unbiased.

Tabela 47 – Dalitz Plot fit result for a toy dataset generated without the $J/\psi(1S)$ and not included in the fit model.

[NLL -514626] Component	Fit fraction (%)		Magnitude and phase coefficients				A_{CP} (%)
	B^-	B^+	a_i^+	$\delta_i^+ [^\circ]$	a_i^-	$\delta_i^- [^\circ]$	
$K^*(892)$	6.02 ± 0.19	5.03 ± 0.16	1.022 ± 0.011	0 ± 0	0.978 ± 0.011	0 ± 0	-4.5 ± 2.3
$K_0^*(1430)$	5.99 ± 0.28	5.86 ± 0.24	1.103 ± 0.027	14 ± 2	0.975 ± 0.026	-21 ± 2	-12.3 ± 3.1
<i>PolarFFNR</i>	38.16 ± 0.61	33.86 ± 0.45	2.652 ± 0.038	31 ± 2	2.462 ± 0.037	4 ± 2	-7.4 ± 1.1
$\rho^0(1700)$	3.84 ± 0.32	2.60 ± 0.26	0.734 ± 0.037	-98 ± 5	0.781 ± 0.035	-81 ± 4	6.1 ± 6.5
$\rho^0(1450)$	22.16 ± 0.71	16.42 ± 0.52	1.847 ± 0.036	-177 ± 3	1.876 ± 0.037	-141 ± 3	1.6 ± 2.3
$f_2(1270)$	9.44 ± 0.29	4.03 ± 0.18	0.915 ± 0.023	82 ± 3	1.225 ± 0.024	114 ± 3	28.4 ± 2.5
Re-scattering	8.86 ± 0.23	24.67 ± 0.28	2.263 ± 0.029	-160 ± 3	1.186 ± 0.021	-132 ± 3	-56.9 ± 1.0
$\phi(1020)$	0.84 ± 0.07	0.09 ± 0.02	0.139 ± 0.017	55 ± 9	0.364 ± 0.015	-85 ± 5	74.6 ± 5.7
χ_{c0}	1.38 ± 0.09	0.61 ± 0.05	0.356 ± 0.015	117 ± 4	0.468 ± 0.016	61 ± 5	26.8 ± 4.9
Fit Fraction Sum	96.7	93.2					

Tabela 48 – Dalitz Plot fit result for a toy dataset generated without the $J/\psi(1S)$ and included in the fit model.

[NLL -514628] Component	Fit fraction (%)		Magnitude and phase coefficients				A_{CP} (%)
	B^-	B^+	a_i^+	$\delta_i^+ [^\circ]$	a_i^-	$\delta_i^- [^\circ]$	
$K^*(892)$	6.00 ± 0.19	5.02 ± 0.16	1.023 ± 0.011	0 ± 0	0.977 ± 0.011	0 ± 0	-4.5 ± 2.3
$K_0^*(1430)$	5.97 ± 0.29	5.82 ± 0.24	1.101 ± 0.027	14 ± 2	0.975 ± 0.026	-21 ± 2	-12.1 ± 3.1
<i>PolarFFNR</i>	38.09 ± 0.61	33.83 ± 0.45	2.653 ± 0.038	31 ± 2	2.463 ± 0.037	4 ± 2	-7.4 ± 1.1
$\rho^0(1700)$	3.83 ± 0.33	2.58 ± 0.26	0.733 ± 0.038	-98 ± 5	0.780 ± 0.035	-81 ± 4	6.3 ± 6.6
$\rho^0(1450)$	22.17 ± 0.72	16.48 ± 0.52	1.852 ± 0.036	-178 ± 3	1.879 ± 0.038	-141 ± 3	1.5 ± 2.3
$f_2(1270)$	9.45 ± 0.29	4.02 ± 0.18	0.915 ± 0.023	81 ± 3	1.226 ± 0.024	115 ± 3	28.5 ± 2.5
Re-scattering	8.87 ± 0.23	24.67 ± 0.28	2.266 ± 0.029	-160 ± 3	1.188 ± 0.021	-131 ± 3	-56.9 ± 1.0
$\phi(1020)$	0.83 ± 0.07	0.09 ± 0.02	0.140 ± 0.017	55 ± 9	0.365 ± 0.015	-85 ± 5	74.4 ± 5.7
χ_{c0}	1.38 ± 0.09	0.61 ± 0.05	0.356 ± 0.015	116 ± 4	0.469 ± 0.016	61 ± 5	26.9 ± 4.9
J/ψ	0.00 ± 0.01	0.01 ± 0.01	0.038 ± 0.020	34 ± 31	0.021 ± 0.018	28 ± 57	-53.1 ± 68.3
Fit Fraction Sum	96.6	93.1					

G.2 The tensor $f_2'(1525)$ resonance

In this study, we evaluate the statistical impact of including or excluding the tensor resonance $f_2'(1525)$ in the fit model, in a toy dataset generated including it. The Table 49 presents the real model used for the generation of the toy for this case, considering the addition of the $f_2'(1525)$ resonance with total fit fraction of 0.04%. Table 50 present the result after removing the $f_2'(1525)$ from the fit model. Considering that $\text{NLL}_{\text{ratio}} = 12$, and since $34.55 > 12$, the inclusion of the $f_2'(1525)$ in this context does not have appreciable statistical significance.

It is important to emphasize that the method does not confirm or exclude the presence of any resonance; it only evaluates the statistical significance of adding a resonance. This distinction is crucial because, as in the case of $f_2'(1525)$, even though it is known to exist (as it was included in the generation model), the method indicates that its addition lacks statistical relevance. In other words, Wilks' theorem concludes that the inclusion of $f_2'(1525)$ is statistically insignificant. This result aligns with expectations since, despite its inclusion in the toy generation, $f_2'(1525)$ contributes only marginally (with just 0.05% fit fraction).

Tabela 49 – Dalitz Plot fit result for a toy dataset generated with the $f_2'(1525)$ and included in the fit model.

[NLL -514440] Component	Fit fraction (%)		Magnitude and phase coefficients				A_{CP} (%)
	B^-	B^+	a_i^+	$\delta_i^+ [^\circ]$	a_i^-	$\delta_i^- [^\circ]$	
$K^*(892)$	6.01 ± 0.19	5.02 ± 0.16	1.021 ± 0.011	0 ± 0	0.979 ± 0.011	0 ± 0	-4.1 ± 2.3
$K_0^*(1430)$	5.97 ± 0.29	5.84 ± 0.24	1.101 ± 0.027	14 ± 2	0.976 ± 0.026	-21 ± 2	-12.0 ± 3.1
<i>PolarFFNR</i>	37.89 ± 0.60	33.85 ± 0.45	2.651 ± 0.038	31 ± 2	2.459 ± 0.037	4 ± 2	-7.5 ± 1.1
$\rho^0(1700)$	3.80 ± 0.33	2.63 ± 0.26	0.739 ± 0.037	-99 ± 5	0.778 ± 0.035	-81 ± 4	5.2 ± 6.5
$\rho^0(1450)$	22.30 ± 0.71	16.37 ± 0.53	1.844 ± 0.036	-177 ± 3	1.886 ± 0.037	-141 ± 3	2.3 ± 2.3
$f_2(1270)$	9.41 ± 0.30	4.04 ± 0.18	0.916 ± 0.023	81 ± 3	1.225 ± 0.025	115 ± 3	28.3 ± 2.6
$f_2'(1525)$	0.07 ± 0.03	0.01 ± 0.01	0.053 ± 0.024	63 ± 25	0.108 ± 0.024	103 ± 12	60.9 ± 31.7
Re-scattering	8.76 ± 0.23	24.64 ± 0.28	2.262 ± 0.029	-160 ± 3	1.183 ± 0.021	-132 ± 3	-57.1 ± 1.0
$\phi(1020)$	0.83 ± 0.07	0.09 ± 0.02	0.136 ± 0.017	55 ± 9	0.365 ± 0.015	-85 ± 5	75.6 ± 5.6
χ_{c0}	1.38 ± 0.09	0.61 ± 0.05	0.357 ± 0.015	117 ± 4	0.470 ± 0.016	62 ± 4	26.7 ± 4.9
Fit Fraction Sum	96.4	93.1					

Tabela 50 – Dalitz Plot fit result for a toy dataset generated with the $f_2'(1525)$ and not included in the fit model.

[NLL -514428] Component	Fit fraction (%)		Magnitude and phase coefficients				A_{CP} (%)
	B^-	B^+	a_i^+	$\delta_i^+ [^\circ]$	a_i^-	$\delta_i^- [^\circ]$	
$K^*(892)$	6.06 ± 0.19	5.02 ± 0.16	1.019 ± 0.011	0 ± 0	0.981 ± 0.011	0 ± 0	-3.9 ± 2.3
$K_0^*(1430)$	6.05 ± 0.29	5.79 ± 0.24	1.095 ± 0.026	14 ± 2	0.980 ± 0.026	-21 ± 2	-11.1 ± 3.1
<i>PolarFFNR</i>	38.04 ± 0.61	33.94 ± 0.45	2.650 ± 0.038	31 ± 2	2.458 ± 0.037	4 ± 2	-7.5 ± 1.1
$\rho^0(1700)$	3.96 ± 0.33	2.68 ± 0.26	0.744 ± 0.037	-98 ± 5	0.793 ± 0.035	-81 ± 4	6.3 ± 6.4
$\rho^0(1450)$	22.26 ± 0.71	16.34 ± 0.52	1.839 ± 0.036	-177 ± 3	1.880 ± 0.037	-142 ± 3	2.2 ± 2.3
$f_2(1270)$	9.32 ± 0.29	4.00 ± 0.18	0.910 ± 0.023	80 ± 3	1.217 ± 0.024	112 ± 3	28.2 ± 2.5
Re-scattering	8.75 ± 0.23	24.64 ± 0.28	2.258 ± 0.029	-160 ± 3	1.179 ± 0.021	-134 ± 3	-57.1 ± 1.0
$\phi(1020)$	0.84 ± 0.07	0.09 ± 0.02	0.134 ± 0.017	54 ± 9	0.365 ± 0.015	-86 ± 5	76.2 ± 5.5
χ_{c0}	1.39 ± 0.09	0.61 ± 0.05	0.357 ± 0.015	117 ± 4	0.469 ± 0.016	62 ± 4	26.8 ± 4.9
Fit Fraction Sum	96.7	93.1					

H Appendix: Alternative models

An amplitude analysis is highly sensitive to the components tested. Therefore, in this appendix, we present a series of tests conducted with alternative resonances. These studies were based on the Baseline Model 6, with occasional modifications where established resonances in the analysis were replaced one at a time. The tests focused on low-mass components that could appear in the decay, particularly for the $K\pi$ S-wave. Only the tables with the numerical results will be presented. These alternatives will also be used for systematic error studies in this analysis.

Tabela 51 – Dalitz Plot Fit replacing the PolarFFNR with the BelleNR.

[NLL -142795] Component	Fit fraction (%)		Magnitude and phase coefficients				A_{CP} (%)
	B^-	B^+	a_i^+	$\delta_i^+ [^\circ]$	a_i^-	$\delta_i^- [^\circ]$	
$K(892)$	5.91 ± 0.30	4.33 ± 0.25	0.992 ± 0.019	0 ± 0	1.008 ± 0.019	0 ± 0	1.7 ± 3.8
$K_0^*(1430)$	7.01 ± 0.58	5.80 ± 0.50	1.148 ± 0.052	28 ± 3	1.098 ± 0.048	-10 ± 4	-4.4 ± 4.9
<i>BelleNR</i>	36.29 ± 0.94	32.83 ± 0.69	2.730 ± 0.068	34 ± 3	2.498 ± 0.063	1 ± 3	-8.8 ± 2.1
$\rho(1700)$	4.05 ± 0.56	4.24 ± 0.48	0.981 ± 0.059	-54 ± 7	0.835 ± 0.061	-101 ± 6	-16.0 ± 8.8
$\rho(1450)$	22.81 ± 1.31	15.45 ± 0.94	1.873 ± 0.067	-116 ± 6	1.981 ± 0.070	-126 ± 5	5.6 ± 4.0
$f_2(1270)$	8.81 ± 0.48	4.01 ± 0.31	0.954 ± 0.042	131 ± 5	1.231 ± 0.042	121 ± 5	25.0 ± 4.4
Re-scattering	8.19 ± 0.37	25.00 ± 0.58	2.382 ± 0.052	-109 ± 6	1.187 ± 0.035	-127 ± 5	-60.2 ± 1.5
$\phi(1020)$	0.80 ± 0.10	0.02 ± 0.02	0.073 ± 0.032	84 ± 22	0.371 ± 0.025	-88 ± 9	92.5 ± 6.5
χ_{c0}	1.21 ± 0.13	0.60 ± 0.08	0.369 ± 0.025	118 ± 7	0.457 ± 0.025	64 ± 7	21.1 ± 7.9
Fit Fraction Sum	105.1	103.1					

Tabela 52 – Dalitz Plot Fit replacing the PolarFFNR with the κ .

[NLL -141872] Component	Fit fraction (%)		Magnitude and phase coefficients				A_{CP} (%)
	B^-	B^+	a_i^+	$\delta_i^+ [^\circ]$	a_i^-	$\delta_i^- [^\circ]$	
$K(892)$	7.62 ± 0.83	0.17 ± 0.07	0.400 ± 0.076	180 ± 0	2.400 ± 0.076	0 ± 0	94.6 ± 1.6
$K_0^*(1430)$	17.66 ± 0.73	9.80 ± 0.64	3.060 ± 0.148	-97 ± 3	3.653 ± 0.137	0 ± 4	17.5 ± 3.6
κ	8.32 ± 0.46	12.48 ± 0.46	3.454 ± 0.129	158 ± 5	2.507 ± 0.115	-112 ± 3	-31.0 ± 3.0
$\rho(1700)$	3.77 ± 0.58	3.31 ± 0.46	1.780 ± 0.139	-106 ± 7	1.688 ± 0.144	-92 ± 6	-5.3 ± 10.1
$\rho(1450)$	28.70 ± 1.37	19.03 ± 1.05	4.266 ± 0.196	-135 ± 6	4.657 ± 0.188	-78 ± 3	8.8 ± 3.7
$f_2(1270)$	11.50 ± 0.54	5.60 ± 0.40	2.313 ± 0.112	106 ± 5	2.949 ± 0.123	176 ± 4	23.8 ± 4.1
Re-scattering	8.45 ± 0.37	29.17 ± 0.52	5.281 ± 0.188	-133 ± 4	2.527 ± 0.101	-81 ± 5	-62.7 ± 1.4
$\phi(1020)$	0.94 ± 0.12	0.03 ± 0.02	0.163 ± 0.070	64 ± 23	0.845 ± 0.060	-49 ± 8	92.8 ± 6.1
χ_{c0}	0.98 ± 0.12	0.37 ± 0.07	0.597 ± 0.058	-21 ± 14	0.862 ± 0.058	114 ± 9	35.3 ± 9.3
Fit Fraction Sum	88.0	80.0					

Tabela 53 – Dalitz Plot Fit replacing the PolarFFNR with the LASS.

[NLL -142367] Component	Fit fraction (%)		Magnitude and phase coefficients				A_{CP} (%)
	B^-	B^+	a_i^+	$\delta_i^+ [^\circ]$	a_i^-	$\delta_i^- [^\circ]$	
$K(892)$	6.21 ± 0.33	4.91 ± 0.27	1.002 ± 0.020	0 ± 0	0.998 ± 0.020	0 ± 0	-0.4 ± 3.9
$K_0^*(1430)$	35.78 ± 1.24	8.69 ± 0.65	1.333 ± 0.056	37 ± 3	2.396 ± 0.067	24 ± 3	52.7 ± 3.0
NR(LASS)	12.27 ± 0.70	23.30 ± 1.11	2.182 ± 0.069	8 ± 3	1.403 ± 0.052	-53 ± 3	-41.5 ± 3.1
$\rho(1700)$	3.73 ± 0.61	2.31 ± 0.43	0.687 ± 0.066	-89 ± 9	0.774 ± 0.067	-82 ± 8	11.8 ± 12.4
$\rho(1450)$	29.95 ± 1.40	22.21 ± 1.08	2.131 ± 0.066	-92 ± 7	2.192 ± 0.067	-52 ± 6	2.8 ± 3.4
$f_2(1270)$	10.50 ± 0.50	5.06 ± 0.37	1.017 ± 0.043	158 ± 7	1.298 ± 0.041	-154 ± 6	23.9 ± 4.2
Re-scattering	8.35 ± 0.34	29.14 ± 0.49	2.441 ± 0.051	-88 ± 7	1.157 ± 0.032	-55 ± 7	-63.3 ± 1.3
$\phi(1020)$	0.91 ± 0.11	0.01 ± 0.02	0.053 ± 0.030	120 ± 35	0.382 ± 0.025	-26 ± 10	96.3 ± 4.5
χ_{c0}	0.77 ± 0.10	0.52 ± 0.07	0.325 ± 0.024	142 ± 11	0.352 ± 0.023	141 ± 11	8.2 ± 9.5
Fit Fraction Sum	108.5	96.2					

Tabela 54 – Dalitz Plot Fit replacing the PolarFFNR with the non-resonant flat contribution.

[NLL -141778] Component	Fit fraction (%)		Magnitude and phase coefficients				A_{CP} (%)
	B^-	B^+	a_i^+	$\delta_i^+ [^\circ]$	a_i^-	$\delta_i^- [^\circ]$	
$K(892)$	7.70 ± 0.37	6.80 ± 0.30	1.034 ± 0.016	0 ± 0	0.966 ± 0.016	0 ± 0	-6.9 ± 3.3
$K_0^*(1430)$	24.75 ± 1.17	26.19 ± 0.79	2.030 ± 0.050	60 ± 3	1.731 ± 0.053	4 ± 4	-15.8 ± 2.8
NR (Flat)	29.76 ± 0.81	21.79 ± 0.62	1.852 ± 0.044	31 ± 3	1.898 ± 0.045	-9 ± 5	2.5 ± 2.1
$\rho(1700)$	3.65 ± 0.59	1.11 ± 0.30	0.419 ± 0.057	-25 ± 8	0.665 ± 0.056	-90 ± 7	43.1 ± 12.8
$\rho(1450)$	32.32 ± 1.50	23.08 ± 1.08	1.906 ± 0.056	-13 ± 4	1.978 ± 0.057	-49 ± 5	3.7 ± 3.3
$f_2(1270)$	8.27 ± 0.49	5.03 ± 0.39	0.890 ± 0.038	-125 ± 5	1.001 ± 0.035	-152 ± 6	11.7 ± 4.9
Re-scattering	17.50 ± 0.55	38.72 ± 0.63	2.469 ± 0.047	-9 ± 4	1.456 ± 0.033	-47 ± 6	-48.4 ± 1.4
$\phi(1020)$	0.77 ± 0.11	0.01 ± 0.01	0.042 ± 0.027	-171 ± 146	0.306 ± 0.023	-11 ± 9	96.2 ± 4.8
χ_{c0}	1.22 ± 0.13	0.57 ± 0.08	0.298 ± 0.022	122 ± 9	0.385 ± 0.021	66 ± 8	24.9 ± 8.3
Fit Fraction Sum	125.9	123.3					